Proceedings of Surgetica 2019 - Computer-Assisted Medical Interventions: scientific problems, tools and clinical applications

Pascal Haigron, Antoine Simon

SURGETICA 2019

June 17-18

Rennes, France

Computer-Assisted Medical Interventions: scientific problems, tools and clinical applications

Proceedings

Editors: Pascal Haigron, Antoine Simon

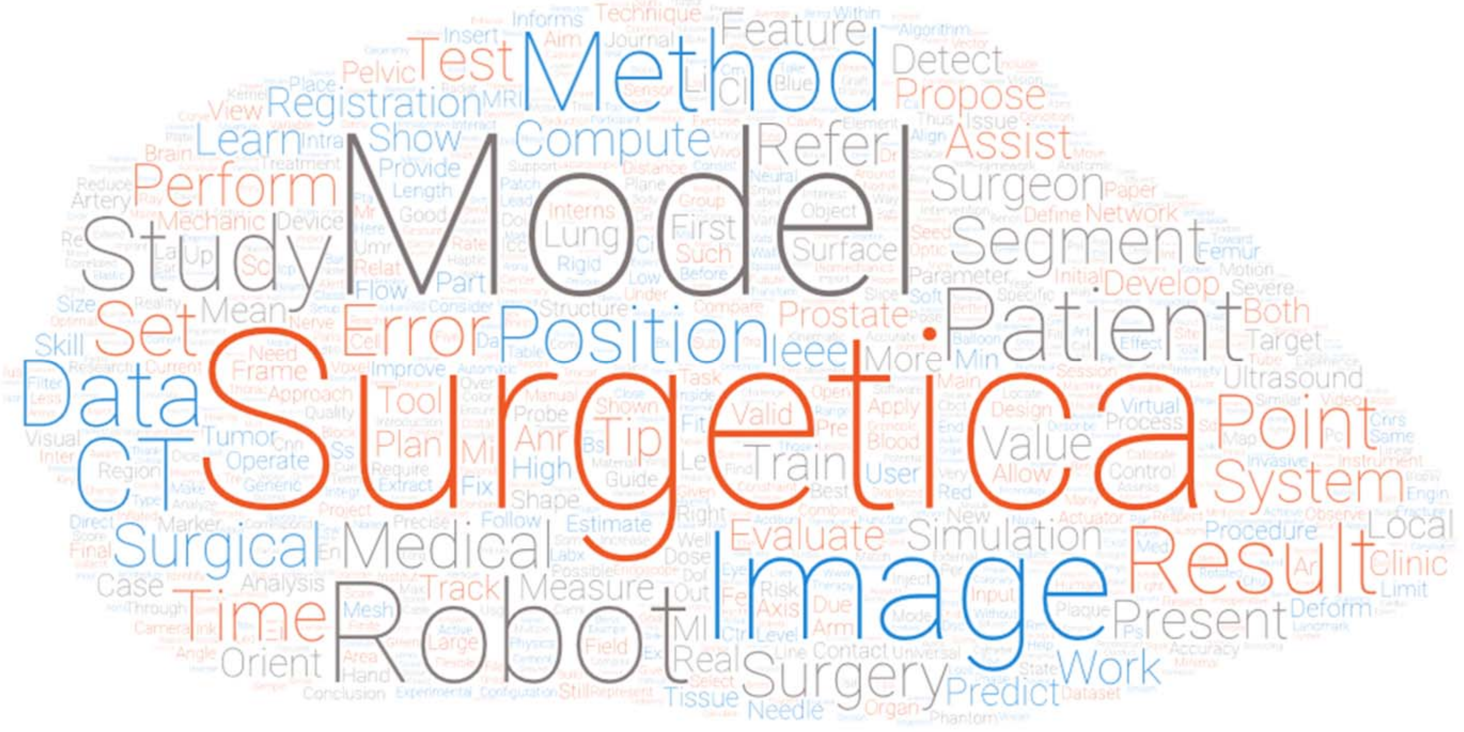

CAMI
COMPUTER ASSISTED
MEDICAL INTERVENTIONS

AGENCE NATIONALE DE LA RECHERCHE
ANR

INVESTISSEMENTS D'AVENIR

The 6th edition of SURGETICA conference was held in Rennes (France) from June 17th to 18th, in conjunction with CARS2019. Organized by Labex CAMI members, this international event brought together around 100 participants including academics, clinicians and MedTech professionals acting in the field of Computer Assisted Medical Interventions (CAMI). In an atmosphere favoring thinking, the *Couvent des Jacobins*, the conference particularly promoted scientific exchanges within the community. The program was composed of 23 oral presentations, including invited and keynote lectures, and 27 poster presentations. SURGETICA thus provided the opportunity to examine progresses beyond state-of-the-art, to formulate new hypotheses where experimental support is yet preliminary, and to discuss new CAMI tools and their clinical applications.

Scientific topics included but were not limited to:

- Image processing and registration for Computer Assisted Medical Interventions
- Modeling and simulation in Computer Assisted Medical Interventions
- Data fusion and augmented reality for Computer Assisted Medical Interventions
- Medical robotics and navigation systems
- Sensors and instrumentation for Computer Assisted Medical Interventions
- Specific man-machine interfaces for Computer Assisted Medical Interventions
- Protocol encoding and recognition in Computer Assisted Medical Interventions
- Clinical evaluation of CAMI systems

Pascal Haigron, Antoine Simon, Pierre Jannin
LTSI, INSERM, University of Rennes 1, France

Organizing committee:

Chairs: Pascal Haigron, Antoine Simon, Pierre Jannin
LTSI, INSERM, University of Rennes 1

Jocelyne Troccaz, TIMC-IMAG, CNRS, Grenoble
Jérôme Szewczyk, ISIR, Sorbonne Universités – UPMC
Jean-Philippe Verhoye, LTSI, Rennes University Hospital
Pierre Renaud, ICUBE, INSA Strasbourg
Matthieu Chabanas, TIMC-IMAG, Grenoble Alpes University
Guillaume Dardenne, LATIM, Brest University Hospital
Jean Louis Dillenseger, LTSI, University of Rennes 1
Marie-Aude Vitrani, ISIR, Sorbonne Universités - UPMC
Nabil Zemiti, LIRMM, University of Montpellier

Program committee:

Salih Abdelaziz, LIRMM, University of Montpellier
Bernard Bayle, ICUBE, University of Strasbourg
Julien Bert, LATIM, Brest University Hospital
Ivan Bricault, TIMC-IMAG, Grenoble Alpes University Hospital
Matthieu Chabanas, TIMC-IMAG, Grenoble Alpes University
Mohamed Taha Chikhaoui, TIMC-IMAG, CNRS, Grenoble
Philippe Cinquin, TIMC-IMAG, Grenoble Alpes University Hospital
Rolf Clackdoyle, TIMC-IMAG, CNRS, Grenoble
Hadrien Courtecuisse, ICUBE, University of Strasbourg
Guillaume Dardenne, LATIM, Brest University Hospital
Laurent Desbat, TIMC-IMAG, Grenoble Alpes University
Jean Louis Dillenseger, LTSI, University of Rennes 1
Gaelle Fiard, Grenoble Alpes University Hospital
Mireille Garreau, LTSI, University of Rennes 1
Bernard Gibaud, LTSI, Inserm, Rennes
Yassine Haddab, LIRMM, University of Montpellier
Pascal Haigron, LTSI, University of Rennes 1
Antoine Lucas, LTSI, Rennes University Hospital
Guillaume Morel, ISIR, Sorbonne Universités – UPMC
Pierre Mozer, ISIR, La Pitié Salpêtrière Hospital, Paris
Florent Nageotte, ICUBE, University of Strasbourg
Philippe Poignet, LIRMM, University of Montpellier
Pierre Renaud, ICUBE, INSA Strasbourg
Benoit Rosa, ICUBE, University of Strasbourg
Romuald Seizeur, LATIM, Brest University Hospital - UBO
Lotfi Senhadji, LTSI, University of Rennes 1
Antoine Simon, LTSI, University of Rennes 1
Jérôme Szewczyk, ISIR, Sorbonne Universités – UPMC
Jocelyne Troccaz, TIMC-IMAG, CNRS, Grenoble
Jean-Philippe Verhoye, LTSI, Rennes University Hospital
Dimitris Visvikis, LATIM, Inserm, Brest
Marie-Aude Vitrani, ISIR, Sorbonne Universités - UPMC
Sandrine Voros, TIMC-IMAG, Inserm, Grenoble
Nabil Zemiti, LIRMM, University of Montpellier

6TH SURGETICA

Le Couvent des Jacobins, Rennes, France, June 17-18, 2019

Conference chairs: Pascal Haigron (FR), Antoine Simon (FR), Pierre Jannin (FR)

Monday, June 17, 2019

08:00 Registration

08:30 Opening Session

Jocelyne Troccaz, Pascal Haigron (FR)

08:40 Modeling and simulation

Session chair: Nabil Zemiti (FR)

Modeling the non-linearities of flexible endoscopes using machine learning
Rafael Aleluia Porto, Florent Nageotte and Michel De Mathelin; ICube - Laboratoire des sciences de l'ingénieur, de l'informatique et de l'imagerie

Kernel selection in statistical femur modeling
Alireza Asvadi, Guillaume Dardenne, Aziliz Guezou-Philippe, Asma Salhi, Bhushan Borotikar, Jocelyne Troccaz and Valérie Burdin; Univ of Western Brittany, LaTIM INSERM U1101; IMT Atlantique, Mines Telecom Institute; Univ Grenoble Alpes, CNRS, Grenoble INP, TIMC-IMAG

Pre-operative planning in acetabular and pelvic ring surgery: the first biomechanical model
Mehdi Boudissa, Matthieu Chabanas, Hadrien Oliveri, Gaetan Bahl and Jérôme Tonetti; Orthopedic and Traumatology Surgery Department, Grenoble University Hospitals; TIMC-IMAG lab, Univ. Grenoble Alpes, CNRS UMR 5525

Biomechanical modeling of the lung deflation during minimally-invasive surgery
Anne Cécile Lesage, Kristy Brock, David Rice, Bastien Rigaud, Alda Tam and Guillaume Cazoulat; The University of Texas MD Anderson Cancer Center

10:00 Coffee break

10:30 Keynote lecture

Chair: Jocelyne Troccaz (FR)

Image guided surgery - inside and outside the OR
Ingerid Reinertsen; SINTEF Digital, Dpt. of Health Research, Norway

11:30 Medical procedures: analysis and evaluation

Session chair: Guillaume Dardenne (FR)

Situation awareness in the "Virtual Operating Room of Errors": a pilot study
Marie-Stephanie Bracq, Marie Le Duff, Estelle Michinov, Bruno Arnaldi, Valérie Gouranton and Pierre Jannin ; Univ Rennes, LP3C (EA 1285); Univ Rennes, Inserm, LTSI - UMR 1099; Univ Rennes, INSA Rennes, Inria, CNRS, IRISA

Preliminary evaluation of haptic guidance for pre-positioning a comanipulated needle
Hadrien Gurnel, Maud Marchal, Laurent Launay, Luc Beuzit and Alexandre Krupa ; Univ. Rennes, IRISA, Inria, INSA Rennes, IRT b<>com

Analyzing the practice of expert surgeons based on video spatial features
Arthur Derathé, Sandrine Voros, Fabian Reche, Pierre Jannin, Alexandre Moreau-Gaudry and Bernard Gibaud; CNRS, UGA, Grenoble INP, TIMC-IMAG, CHU de Grenoble, CIC-IT, INSERM, Univ Rennes 1, LTSI

12:30 Lunch

13:30 Data fusion and augmented reality

Session chair: Matthieu Chabanas (FR)

Intraoperative Ultrasound-based Augmented Reality Guidance
Jun Shen, Nabil Zemiti, Christophe Taoum, Jean-Louis Dillenseger, Philippe Rouanet and Philippe Poignet; Inserm, U1099, Rennes, France; Université de Rennes 1, LTSI; LIRMM, Université de Montpellier; Institut du Cancer de Montpellier Val d'Aurelle

3D landmark detection for augmented reality based otologic procedures
Raabid Hussain, Caroline Guigou, Kibrom Berihu Girum, Alain Lalande and Alexis Bozorg Grayeli; ImViA Laboratory, Universite de Bourgogne Franche-Comté

Fusion of X-Ray and patient specific model to assist cardiac resynchronisation therapy
Nicolas Courtial, Antoine Simon, Sophie Bruge, Mathieu Lederlin, Erwan Donal, Christophe Leclercq and Mireille Garreau; Univ Rennes, CHU Rennes, Inserm, LTSI - UMR 1099

14:30 Keynote lecture

Chair: Jérôme Szewczyk (FR)

Driving and controlling flexible surgical instruments - new developments and challenges
Emmanuel Vander Poorten; Dept. of Mechanical Engineering, division PMA, KU Leuven, Belgium

15:30 Coffee break & Poster session

16:00 Poster session

17:10 Robotics and mechatronics

Session chair: Pierre Renaud (FR)

X-ray free breach detection in robot-assisted spine surgery with real-time conductivity sensing

Jimmy Da Silva, Florian Richer, Valentin Kespern, Thibault Chandanson and Guillaume Morel; SpineGuard, Institut des Systèmes Intelligents et de Robotique (ISIR)

Toward a design method for tensegrity-based medical robots

Jérémy Begey, Marc Vedrines, Nicolas Andreff and Pierre Renaud; ICube, University of Strasbourg, CNRS, INSA Strasbourg; IRCAD; Femto-ST, University of Franche-Comté, CNRS

Bright pill: ingestible biorobot using light to control therapeutic molecule release produced by embarked bacteria

Thomas Soranzo, Guillaume Aiche, Clément Caffaratti, Don Martin, Philippe Cinquin and Yassine Haddab; University Grenoble Alpes, TIMC-IMAG - UMR 5525; University of Montpellier, LIRMM - UMR 5506

18:30 Surgetica Welcome Reception

20:00 Surgetica Dinner

Tuesday, June 18, 2019

08:30 Image processing and registration

Session chair: Jean-Louis Dillenseger (FR)

Intraoperative Ultrasound-based Augmented Reality Guidance
Xuan Thao Ha, Philippe Zanne and Florent Nageotte; ICube lab., University of Strasbourg

Investigating the Role of Helical Markers in 3D Catheter Shape Monitoring from 2D Fluoroscopy
Anne En-Tzu Yang and Jérôme Szewczyk; ISIR, Sorbonne Université

Localization of brachyterapy seeds in TRUS images using rigid priors and medial forces
Vincent Jaouen, Julien Bert, Antoine Valeri and Dimitris Visvikis ; LaTIM, UMR 1101, Inserm, Université de Bretagne Occidentale, CHRU Brest

Automatic segmentation of intraoperative ultrasound images of the brain using U-Net
François-Xavier Carton, Jack Noble, Bodil Munkvold, Ingerid Reinertsen and Matthieu Chabanas; Univ Grenoble Alpes, CNRS, Grenoble INP, TIMC-IMAG; Dept of Electrical Engineering and Computer Science, Vanderbilt Univ; Dept of Neuroscience, Norwegian Univ of Science and Technology, Trondheim; Dept of Medical Technology, SINTEF, Trondheim

10:00 Coffee break

10:30 Invited lecture

Chair: Jean-Philippe Verhoye (FR)

Data-driven solutions for deep brain stimulation surgery
Clément Baumgarten; University Hospital Grenoble; University Hospital Rennes

11:15 Navigation and interventional planning

Session chair: Marie-Aude Vitrani (FR)

Real-time Prediction of High-risk Instrument Motion based on Location Information
Yuichiro Sawano, Nobuyoshi Ohtori and Ryoichi Nakamura; Graduate School of Science and Engineering, Chiba University; Department of Otorhinolaryngology, Jikei University School of Medicine, Tokyo; Center for Frontier Medical Engineering, Chiba University; Japan Science and Technology Agency, Saitama

Transcranial robot-assisted Blood-Brain Barrier opening with Focused Ultrasound
Gaelle Thomas, Laurent Barbé, Pauline Agou, Benoît Larrat, Jonathan Vappou and Florent Nageotte ; ICube, UMR 7357, CNRS, Université de Strasbourg; CEA

Accurate Instrument Tracking in Minimally Invasive Surgery
Mario Arico and Guillaume Morel; Sorbonne Université, CNRS, INSERM, ISIR-Agathe

12:15 Closing session

Poster session (Monday, June 17, 15:30)

Statistical shape model of vascular structures with abdominal aortic aneurysm
Claire Dupont, Christelle Boichon-Grivot, Adrien Kaladji, Antoine Lucas, Michel Rochette and Pascal Haigron; Univ Rennes, INSERM, LTSI - UMR 1099; Ansys France

Pelvic parameters measurement with sterEOS: a preliminary reliability study
Morgane Dorniol, Guillaume Dardenne, Aziliz Guezou-Philippe, Hoel Letissier, Christian Lefevre and Eric Stindel; University Hospital, University of Western Brittany, LaTIM - UMR 1101, Brest

Extended field-of-view of the knee bone surface using ultrasound
Maged Nasan, Yannick Morvan, Guillaume Dardenne, Jean Chaoui and Eric Stindel; LaTIM - INSERM UMR 1101, Brest; CHRU Morvan, Brest; IMASCAP, Plouzané

Towards a patient-specific simulation of the balloon angioplasty treatment technique
Bernard Al-Helou, Claire Dupont, Aline Bel-Brunon, Wenfeng Ye, Adrien Kaladji and Pascal Haigron; Univ Rennes, INSERM, LTSI - UMR 1099; Univ Lyon, INSA-Lyon, CNRS UMR5259, LaMCoS; ANSYS

Nervous System Exploration Using Tractography To Enhance Pelvic Surgery
Cécile Muller, Alessandro Delmonte, Pierre Meignan, Quoc Peyrot, Alessio Virzi, Laureline Berteloot, David Grevent, Thomas Blanc, Pietro Gori, Nathalie Boddaert, Isabelle Bloch and Sabine Sarnacki; IMAG2 Laboratory, Imagine Institute, Paris; Université Paris Descarte; Pediatric Surgery and Radiology Departments, Necker Hospital, APHP, Paris; LTCI, Telecom ParisTech, Université Paris-Saclay

Transvaginal Uterine Biopsy: Robot Comanipulation
Nassim Tajeddine, Marie-Aude Vitrani and Rémi Chalard; ISIR UMR CNRS 7222, Sorbonne Université, Univ Paris 06

Surface imaging for patient positioning in radiotherapy
Souha Nazir, Julien Bert, Dimitris Visvikis and Hadi Fayad; LaTIM, UBO, INSERM UMR 1011, Brest; Hamad Medical Corporation OHS, PET/CT center Doha, Qatar

Orientability evaluation of concentric tube robots deployed in natural orifices
Quentin Peyron, Kanty Rabenorosoa, Nicolas Andreff and Pierre Renaud; AS2M department, FEMTO-ST Institute; AVR team, ICube laboratory

Diabetic Retinopathy Detection and Grading From Fundus Image Using Deep Learning Library Tensorflow
Abhijit Jha, Shailesh Kumar, Ajitabh Srivastava, Rajeev Gupta and Basant Kumar; MNNIT Allahabd, Prayagraj

Simulation for preoperative planning, balloon inflation for tibial plateau fracture reduction
Kévin Aubert, Tanguy Vendeuvre, Michel Rochette, Philippe Rigoard and Arnaud Ger-

maneau; Institut Pprime, UPR 3346 CNRS - Université de Poitiers - ISAE-ENSMA; ANSYS France; Spine & Neuromodulation Function Unit. PRISMATICS Lab CHU - Poitiers

Computer Assisted Detection of Good View Frame from USG Video for ONSD Measurement
Aniket Pratik, Maninder Singh, Kokkula Sriraj, Meesala A. Kumar, Rajeev Gupta, Deepak Agrawal and Basant Kumar; MNNIT Allahabd, Prayagraj

Patient's specific computer simulations to assist coronary artery bypass surgery
Agnes Drochon, Amedeo Anselmi, Herve Corbineau and Jean-Philippe Verhoye; Univ Technologie Compiègne, UMR CNRS 7338; Service Chirurgie Cardio-Thoracique, CHU PontChaillou, Rennes

CFD based study of blood stagnation caused by LVAD inflow cannula angulation
Amal Ben Abid, Valery Morgenthaler, Pascal Haigron and Erwan Flecher; Univ Rennes, CHU Rennes, INSERM, LTSI - UMR 1099; ANSYS France

Transesophogeal HIFU cardiac fibrilation therapy guidance by two perpendicular US images
Batoul Dahman and Jean-Louis Dillenseger; Univ Rennes, INSERM, LTSI - UMR 1099

Potential of global vision system for learning laparoscopy surgical skills
Sinara Vijayan, Elio Keddiseh, Bertrand Trilling and Sandrine Voros; Laboratory TIMC-IMAG, GMCAO; Faculty of Medicine, La Tronche

Segmenting Surgical Tasks using Temporal Convolutional Neural Network
Mégane Millan and Catherine Achard; Sorbonne Université - CNRS UMR 7222 - Institut des Systèmes Intelligents et de Robotique

An Experimental Protocol on Attentional Abilities in Classic and Robot-Assisted Laparoscopy
Eleonore Ferrier-Barbut, Vanda Luengo and Marie-Aude Vitrani; Sorbonne Université, CNRS UMR 7222; Institut des Systèmes Intelligents et de Robotique, ISIR

Mixed Reality Experiment for Hemodialysis Treatment
Christophe Lohou, Marc Bouiller and Emilie Gadea-Deschamps; Université Clermont Auvergne, CNRS, SIGMA Clermont, Institut Pascal; Service de Néphrologie-Hémodialyse, Centre Hospitalier Emile Roux, Le Puy-en-Velay; Unité de Recherche Clinique, Centre Hospitalier Emile Roux, Le Puy-en-Velay

Image-based registration for lung nodule localization during VATS
Pablo Alvarez, Simon Rouzé, Matthieu Chabanas, Yohan Payan and Jean-Louis Dillenseger; Univ Rennes, Inserm, LTSI - UMR 1099; Univ. Grenoble Alpes, CNRS, Grenoble-INP, TIMC-IMAG; CHU Rennes, Service of Thoracic and Cardiac Surgery

Additive Manufacturing of a Microbiota Sampling Capsule Based on a Bistable Mechanism

Mouna Ben Salem, Guillaume Aiche, Lennart Rubbert, Thomas Soranzo, Philippe Cinquin, Donald K. Martin, Pierre Renaud and Yassine Haddab; University of Montpellier, LIRMM - UMR 5506; University of Strasbourg, ICube; University of Grenoble Alpes, TIMC-IMAG - UMR 5525

Towards a novel man-machine interface to speed up training on robot-assisted surgery
Gustavo Gil, Julie Walker, Nabil Zemiti, Allison Okamura and Philippe Poignet; LIRMM - CNRS, UMR 5506, Université de Montpellier; Department of Mechanical Engineering, Stanford University, USA

Percutaneous osteoplasty
Julien Garnon, Laurence Meylheux, Bernard Bayle and Afshin Gangi; ICube - University of Strasbourg - UMR 7357 CNRS - INSA Strasbourg

Development of a finite element model of prostate validated by a realistic prostate phantom
Mohamed Dieng, Grégory Chagnon and Sandrine Voros; Univ. Grenoble Alpes, CNRS, Grenoble INP, INSERM, TIMC-IMAG

FEM-based confidence assessment of non-rigid registration
Paul Baksic, Hadrien Courtecuisse, Matthieu Chabanas and Bernard Bayle; University of Strasbourg, CNRS, AVR-Icube; Univ. Grenoble Alpes, CNRS, Grenoble INP, TIMC-IMAG

Tumor heterogeneity estimation from DW-MRI and histology data by linking macro- and micro-information in a quantitative way
Yi Yin, Oliver Sedlaczek, Kai Breuhahn, Irene Vignon-Clementel and Dirk Drasdo; INRIA Paris; Translational Lung Research Center Heidelberg (TLRC), University Hospital of Heidelberg; Thoraxklinik at University of Heidelberg and DKFZ; Institute of Pathology, University Hospital Heidelberg, Germany

Improved prostate cancer radiotherapy planning with decreased dose in a rectal subregion highly predictive for toxicity
Oscar Acosta, Caroline Lafond, Anais Barateau, Baptiste Houede, Axel Largent, Eugenia Mylona, Nicolas Perichon, Nolwenn Delaby, Pascal Haigron and Renaud de Crevoisier; Univ Rennes, INSERM, LTSI - UMR 1099

Experimental test bench for the hemodynamic study of coronary arteries: bifurcation, stent, aneurysm
Manuel Lagache, Ricardo Coppel, Amida Gomez, Gérard Finet and Jacques Ohayon; TIMC-IMAG - Techniques de l'Ingénierie Médicale et de la Complexité - Informatique, Mathématiques et Applications, Grenoble; SYMME - Laboratoire SYstèmes et Matériaux pour la Mecatronique, Chambéry; Département de Cardiologie, Hôpital Cardiovasculaire et Université Claude Bernard, Lyon

Keynote lecture

Ingerid Reinertsen

SINTEF Digital, Dpt. of Health Research, Norway

Image guided surgery - inside and outside the OR

Abstract:

In this talk, I will discuss how the field of "image guided surgery" transforms into "data guided surgery" where images of the patient only represent one source of information among many others. I will illustrate how these developments represent exciting opportunities but also place new demands on the tools and systems that are developed. I will also show some relevant examples from the research group at SINTEF.

Short bio:

Ingerid Reinertsen is a Senior Research scientist at SINTEF Digital, Dept. Health Research, Trondheim Norway. She completed her undergraduate studies at *Institut National des Sciences Appliquees (INSA) de Toulouse*. She received her PhD from McGill University in Montreal in 2007 on ultrasound-based correction of brain shift in neurosurgery. Her research interests lie in the area of computer assisted surgery and intra-operative imaging with a special focus on ultrasound and neurosurgical applications. She works closely with neurosurgeons, radiologists, pathologists and clinical staff and has attended close to 200 neurosurgical procedures. She has served as area chair and program committee member for several editions of MICCAI and IPCAI.

Keynote lecture

Emmanuel Vander Poorten

Dept. of Mechanical Engineering, division PMA, KU Leuven, Belgium

Driving and controlling flexible surgical instruments – new developments and challenges

Abstract:

Minimization of access trauma is a key driver for the development of surgical instruments and other medical devices. As instrument diameters go down mechanisms inherently become more flexible. Also, when locations deep inside the human body are to be reached along tortuous trajectories, flexibility helps keeping trauma low. However controlling flexible instruments imposes some particular challenges whether it is done manual or in a computer-controlled fashion. This talk highlights the differences from operating traditional straight rigid minimal invasive instruments. It provides an overview of some recently developed steerable instruments and gives an overview of important challenges to drive such instruments through a fragile anatomy. Where traditional keyhole surgery is already confronted with long learning curves, partial or shared autonomy seems to be essential to keep control manageable and safe.

Short bio:

Emmanuel B. Vander Poorten graduated in 2000 from the Mechanical Engineering Department in KU Leuven, Belgium. In 2007 he obtained the title of Doctor of Engineering from Kyoto University, Japan. Currently Dr. Vander Poorten is assistant professor at the Faculty of Engineering Technology and the Mechanical Engineering Department of KU Leuven where he is coordinating the Robot-Assisted Surgery (RAS) group of KU Leuven. His research interests include surgical robotics, medical device design, human-robotic interaction, shared control and haptic interfacing. He has been coordinating several international EU-funded projects under FP7 (RADHAR, SCATh and CASCADE on robotic navigation and catheterization) and H2020 (EurEyeCase on robot-assisted vitreoretinal microsurgery) and is Principal Investigator and Scientific Manager for KU Leuven in GIFT-SURG, a major Wellcome Trust-ESPRC funded project on fetal surgery. Dr. Vander Poorten is coordinating ATLAS, a Marie-Curie Training Network on Autonomous IntraLuminAl Surgery. He is also member of the Steering board of ACTUATOR and founding member of CRAS.

Invited lecture

Clément Baumgarten

University Hospital Grenoble

University of Rennes 1, University Hospital Rennes, LTSI – INSERM UMR 1099

Data-driven solutions for deep brain stimulation surgery

Abstract:

Subthalamic deep brain stimulation is a surgical procedure to treat early stages and severe forms of Parkinson' s disease. This surgery is still performed under local anesthesia, so the clinicians can assess the functional effect of the surgery. Moving from awake surgery under local anesthesia to asleep surgery under general anesthesia will require to precisely predict the outcome of deep brain stimulation. This translational work was conducted in the computer lab, the operating room and at the patient's bedside. Precision diagnostic studies have shown superior results to the reference method and was consistent with clinical use. We trained an artificial neural network with prospective clinical data to predict the clinical effect of surgery. This model is an incremental model: each new patient's data trains a new algorithm that becomes more efficient. This pioneering work is an example of the medicine of tomorrow based on new technologies of artificial intelligence. Patient data: at their service, for their health, and benefiting future patients.

Short bio:

Clément Baumgarten is a resident in neurosurgery in the University Hospital of Grenoble. He did his medical school in the University of Rennes where he also received his MS degree in Biomedical Engineering with Pr. Jannin and Pr. Haegelen. He proposed a data-driven solution to predict functional effects of deep brain stimulation surgery. This work was awarded several times particularly in the SPIE Medical Imaging conference in USA and by the National Academy of Surgery in France, with the Computer-Assisted Medical-Surgical Innovation Award (supported by Labex CAMI). He is focusing now in skull base surgery. He is also studying continuous monitoring of emotions in the operating room applied to quality of life at work and surgical outcomes.

Modeling the non-linearities of flexible endoscopes using machine learning

Rafael ALELUIA PORTO, Florent NAGEOTTE and Michel DE MATHELIN

ICube - Laboratoire des sciences de l'ingénieur, de l'informatique et de l'imagerie
300 bd Sbastien Brant - CS 10413 - F-67412 Illkirch, France - Tel : +33 (0)3 68 85 45 54
Contact: r.aleluiaporto@unistra.fr

This work is an extension of the approach presented in [1]. This extension shows how to combine machine learning and kinematic modeling to model the inverse kinematics of flexible systems with coupled joints. The approach has been validated on the STRAS robotic platform [3].

1 Introduction

Flexible endoscopes are versatile tools used in minimally invasive surgeries. They can be used on several kinds of procedures, some of which do not require any incision on the patient. Robotizing such systems, however, is a real challenge due to the mechanical transmission used to control the distal effectors. The antagonistic cables are usually subject to internal friction and tension loss, introducing a hysteresis shape between the actuation and distal tip position [2].

In [1], a new inverse kinematic model was proposed to model hysteresis effects in surgical instruments with a pair of driving tendons by combining classical kinematic modeling with machine learning. This paper is an extension of the above technique applied to the control of flexible endoscopes with two orthogonal pairs of driving tendons. The main contribution is that the joints of the flexible endoscope are coupled, contrary to the ones of the surgical tools.

2 Materials and methods

Our study is focused on flexible endoscopes with two bending planes actuated by antagonistic cables. Each pair of cables, when actuated independently, makes the endoscope bend in the XZ or the YZ plane. The actuation is denoted ΔL_x and ΔL_y, which affect the bending on X (β_x) and bending on Y (β_y) respectively. For this system, the task space can be parameterized by using the radius ρ, the depth d and rotation θ with respect to the frame. These parameters and those of the configuration space can be seen in Fig. 1. Our objective is to determine the motor positions allowing to achieve a reference position $P^* = (x^*, y^*)$ despite the non-linearities introduced by the mechanical transmission.

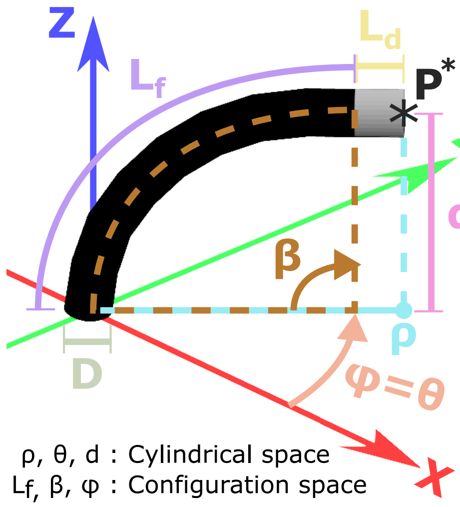

Figure 1: *Depiction of a flexible endoscope and its important modeling parameters.*

The modeling of this kind of flexible system is usually done by assuming that the shape of the instrument while bending describes an arc of a circle of constant curvature [4]. On this basis, we can derive:

$$\rho = \frac{L_f}{\beta}(1 - cos\beta) + L_d sin\beta \tag{1}$$

with L_f being the length of the flexible part and L_d the length of the rigid part located at the tip of the endoscope. Given the orthogonal disposition of the cables, we can find:

$$\theta = atan2(\beta_y, \beta_x) \tag{2}$$

with

$$\beta^2 = \beta_x^2 + \beta_y^2. \tag{3}$$

The relation between the actuation space and the configuration space, assuming no tension loss, is :

$$\Delta L_q = \frac{D}{2}\beta_q \tag{4}$$

with D being the diameter of the endoscope and $q = \{x, y\}$. Given these equations, the inverse kinematic model can be determined by the following steps:

- Write P^* in a cylindrical parameterization with $\rho^* = \sqrt{x^{*2} + y^{*2}}$ and $\theta^* = atan2(y^*, x^*)$;

- Convert the cylindrical representation to the configuration space with β^* being found by numerically inverting (1) and noting that $\varphi^* = \theta^*$;
- Using equations (2) and (3), we can find:
$$\beta_x^* = \frac{\beta^*}{\sqrt{1+tan^2(\varphi^*)}} \quad (5)$$
and
$$\beta_y^* = \sqrt{\beta^{*2} - \beta_x^{*2}}; \quad (6)$$
- Find ΔL_x and ΔL_y with equation (4).

The main issue with this classical modeling is that the antagonistic cables do not perfectly transmit the movement from the proximal to the distal side. Our approach to handle the imperfections of the mechanical transmission is to combine classic kinematic modeling with machine learning in the same spirit as in [1]. The formulated hypothesis are that the flexible part of the endoscope describes the arc of a circle, meaning that equations (1), (2) and (3) are valid, but the cable transmission is subject to hysteresis effects ((4) is invalid).

The distal parameters used to describe the configuration of the tool are β_x and β_y. These parameters can be linked to the motors positions in a decoupled way as shown before.

The first step when using this method is the training stage. It consists of obtaining the training dataset with an external sensor and then training the models linking the configuration space with the actuation space. The models searched are :

- $\Delta L_x = f^{-1}(\beta_x)$ - inverse bending on X model;
- $\Delta L_y = g^{-1}(\beta_y)$ - inverse bending on Y model.

Two datasets of 250 points were used to train both models. Each dataset is composed of forward and backward movements on one of the bending direction performed separately. First ΔL_y is fixed to zero and ΔL_x is changed from -6mm to 6mm with a 0.24mm step (50 points per range span). Then the same trajectory is performed on ΔL_y with ΔL_x fixed to zero. These data are acquired using the setup shown in Fig. 2.

Once the models are trained, they can be used to predict the actuation capable of compensating the nonlinearities. To do so, first we determine the desired bending angles β_x^* and β_y^* using equations (5) and (6). The actuator positions can then be found as:
$$\Delta L_x^* = f^{-1}(\beta_x^*) \text{ and } \Delta L_y^* = g^{-1}(\beta_y^*). \quad (7)$$
It should be noted that the prediction is performed completely in open-loop. For implementing this approach Gaussian Process Regression [5] was used as machine learning algorithm. The input and output data used for learning, noted ξ_i and ξ_o respectively are:
$$\xi_i[k] = (\beta_q[k], d^q[k]) \text{ and } \xi_o[k] = \Delta L_q[k]$$
where $d^q[k]$ is the displacement direction (coded as $+1/-1$) of axis q. The mean $m(\xi_i)$ and covariance function $K(\xi_i, \xi_i')$ used for both regressions are :
$$m(\xi_i) = \frac{2\beta_q}{D}$$
and
$$K(\xi_i, \xi_i') = \sigma_o^2 exp\left(-\frac{(\xi_i - \xi_i')^2}{2l^2}\right) + \sigma_n^2 \delta_{jj'}$$
where σ_o^2 is the output variance, l is the length parameter, σ_n^2 is the noise variance and $\delta_{jj'}$ is the Kronecker's symbol. The mean function comes from the classical IKM shown in equation (4). The hyperparameters of the covariance function $\{\sigma_o, l, \sigma_n\}$ are determined by maximizing the log marginal likelihood [5].

Figure 2: *The experimental setup consists of the STRAS robotic platform and the external measurement system composed of two cameras and Chillitag markers [6].*

3 Results

The proposed approach was evaluated by executing 2D trajectories in open-loop. These trajectories - ellipses defined in the XY-plane with a major and minor axis of 76.5 mm and 49.5 mm respectively - were performed twice to evaluate not only the precision, but also the repeatability of the method. The results are presented on Fig. 3.

A great improvement can be obtained by using our approach. A RMS error of 2.79mm was obtained on this experiment, compared with the 12.75mm achieved using the IKM. Our model generalizes well and is able to compensate the hysteresis effects of the transmission.

This approach could be directly compared to a state-of-the-art, learning-based technique, proposed in [7]. The main difference is that we propose to incorporate kinematic knowledge to make the learning phase more efficient, whereas in [7] it is necessary to cover the whole workspace during training. The RMS errors reported in [7] are comparable to the ones obtained by our proposed approach, but a total of 20,000 points was required to train their model. Additionally, the trajectory used to validate their approach is exactly the same shape as the ones used for training (a circle on the XY-plane that is always performed on the same direction). Using 40 times less points, we can achieve similar precision on trajectories that greatly differ from the training dataset.

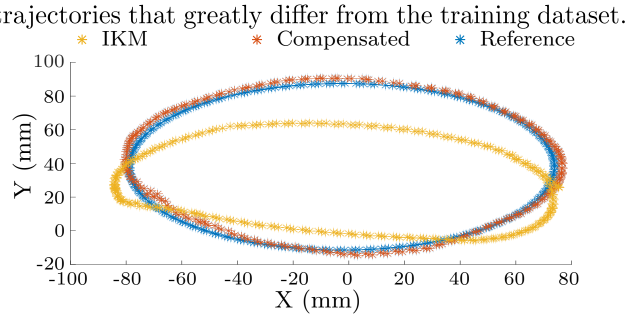

Figure 3: *2D trajectory performed by a flexible endoscope.*

4 Conclusion and discussion

The experiments show the potential of the approach by reducing the open-loop positioning RMS error by more than 4 times. Duration of training can also be considerably reduced compared to other state-of-the-art techniques, which makes the approach more suitable for clinical applications.

References

[1] R. A. Porto, F. Nageotte, P. Zanne and M. de Mathelin. Position control of medical cable-driven flexible instruments by combining machine learning and kinematic analysis, presented at IEEE International Conference on Robotics and Automation (ICRA), 2019, Montreal, Canada, May 2019.

[2] V. Agrawal Varun Agrawal, W. J. Peine and Bin Yao. "Modeling of transmission characteristics across a cable-conduit system" in IEEE Transactions on Robotics, vol. 26, no. 5, 914-924, 2010.

[3] L. Zorn et al. "A Novel Telemanipulated Robotic Assistant for Surgical Endoscopy: Preclinical Application to ESD" in IEEE Transactions on Biomedical Engineering, vol. 65, no. 4, April 2018.

[4] R. J. Webster and B. A. Jones. "Design and kinematic modeling of constant curvature continuum robots: A review" in The International Journal of Robotics Research, vol. 29, no. 13, 1661-1683, 2010.

[5] C. E. Rasmussen, "Gaussian processes in machine learning" in Summer School on Machine Learning, Springer, Berlin, Heidelberg, 2003, 63-71.

[6] Q. Bonnard et al. "Chilitags: Robust Fiducial Markers for Augmented Reality". CHILI, EPFL, Switzerland. http://chili.epfl.ch/software. 2013.

[7] W. Xu, J. Chen, H. Y. K. Lau and H. Ren. "Data-driven methods towards learning the highly nonlinear inverse kinematics of tendon-driven surgical manipulators" in International Journal of Medical Robotics and Computer Assisted Surgery, vol. 13, no. 3, 2017.

5 Acknowledgements

This work was supported by ITMO Cancer in the framework of "Plan Cancer" under the project named ROBOT and by French state funds managed by the ANR within the Investissements d'Avenir program under the ANR-11-LABX-0004 (Labex CAMI). The authors thank Pr. J.Szewczyk from ISIR, Paris for his useful advices.

Kernel selection in statistical femur modeling

Alireza ASVADI [1], Guillaume DARDENNE [1], Aziliz GUEZOU-PHILIPPE [1], Asma SALHI [2], Bhushan BOROTIKAR [1], Jocelyne TROCCAZ [3] and Valérie BURDIN [2]

[1] Univ of Western Brittany, LaTIM INSERM U1101, Brest, France
[2] IMT Atlantique, Mines Telecom Institute, LaTIM INSERM U1101, Brest, France
[3] Univ Grenoble Alpes, CNRS, Grenoble INP, TIMC-IMAG, F-38000 Grenoble, France

We aim to contribute to the development, analysis, and assessment of the statistical femur model when combined with a set of different analytical kernel functions. Reported results demonstrate the superior performance of data-driven femur model (computed from a few femur examples) when combined with an anisotropic kernel. These femur models have great potential for surgery applications.

1 Introduction

The topic of this paper is the construction of the femoral Statistical Shape Model (SSM) from a limited number of data for surgical applications to build a patient-specific femur model and to plan implant placement. Most of the current models are based on deep learning and trained on big data. However, in medical image analysis despite the large anatomical variations in size and shape, sometimes only a few medical data are available. In this context, statistical models have demonstrated to be promising [1, 2]. The main goal of SSMs is to build a flexible shape model using the statistics computed from a set of shape instances. Many variants of SSMs exist in the literature [3]. Among them, the Point Distribution Model (PDM) [4] is the most known. Considering a set of aligned and in correspondence shapes, PDMs model the shapes as a normal distribution of point variations. Gaussian Process Morphable Models (GPMMs) [5] are the generalization of PDMs which model shapes by deformations from a reference shape. GPMMs offer more flexibility in defining covariance (also known as 'kernel') function than in PDMs. This paper describes the impact of using different kernel functions in GPMM-based modeling of the morphological variation of femurs. Performances on a femur dataset are presented.

This work was partly supported by the Investissements d'Avenir programme (Labex CAMI) under reference ANR-11-LABX-0004. Contact: alireza.asvadi@univ-brest.fr

2 Materials and methods

2.1 The Femur Dataset

Our dataset was generated using cadaveric femurs which were scanned at the University Hospital of Brest (CHRU Brest). It consists of a set of 13 femur meshes (about 116k points per mesh) and their corresponding landmarks (6 anatomical landmarks per femur, similar to Albrecht et al. [6]). The dataset was shuffled and partitioned into two groups: 9 meshes as training and 4 as the test set. To perform this study Scalismo framework [7] was used.

2.2 Shape Modeling Pipeline

Figure 1 shows the global femur modeling pipeline. The first step consists in preprocessing to make the meshes in our training dataset rigidly aligned using landmarks and scaled using bounding box information of femurs. Next step is establishing the dense correspondences among the meshes. This step is crucial and involves: Firstly, the rigid registration to build the unbiased reference mesh using IMCP algorithm [8] followed by the screened poisson surface reconstruction algorithm [9]. The reference mesh was decimated to about 5k points. Secondly, the non-rigid registration which involves the construction of the 'deformable femur model' using the unbiased reference mesh with smooth Gaussian deformation assumption. The Gaussian deformation kernel parameters were considered as s:100 and ℓ:100. The 'deformable femur model' was fitted to each of the aligned and scaled meshes using non-rigid ICP algorithm based on Gaussian Process (GP) regression. The fitting Root Mean Square Error (RMSE) in this step was computed as 1.22 ± 0.09 mm. The fits (i.e., the set of fitted 'deformable femur model' to the meshes in the training set) were considered as the 'incorrespondence mesh set'. It consists of the aligned, scaled and incorrespondence mesh data. It was used to

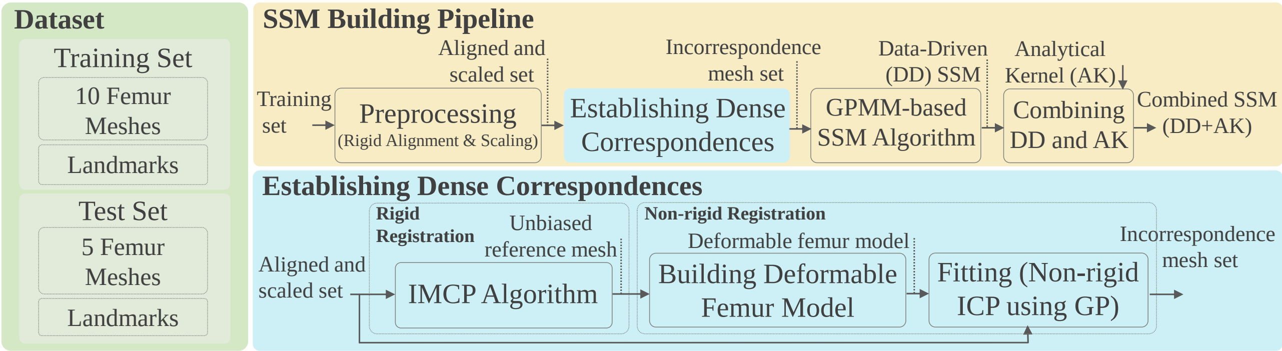

Figure 1: *The shape modeling pipeline.*

Table 1: *Comparison of employed kernel functions.*

Kernel func.	Parameters
Data-driven	Computed from 9 samples
Gaussian	s:50 ℓ:50
Multiscale	s_1:50 ℓ_1:200, s_2:200 ℓ_2:50
Anisotropic	s_x:50 ℓ_x:50, s_y:50 ℓ_y:50, s_z:200 ℓ_z:200

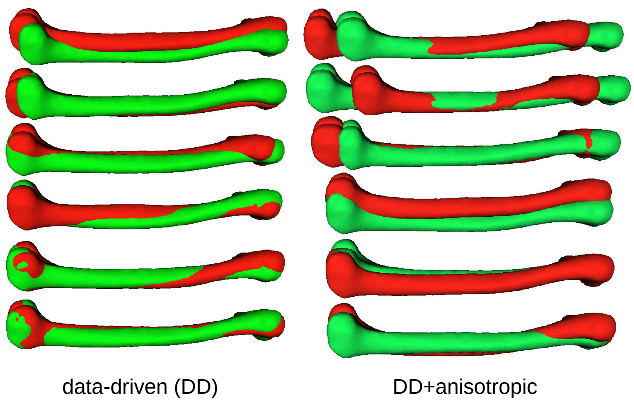

Figure 2: *Six dominant modes of variation of the data-driven model and its combination with the anisotropic kernel. Represented in red and green are the variation of the mean femur by three times standard deviations along eigenmodes.*

build the 'data-driven model' using GPMM-based SSM algorithm [5]. The next step was the combination of 'data-driven model' with the defined analytical kernel functions (see Table 1). The Gaussian kernel was defined by $k(x,x') = s\ e^{-(x-x')^2/\ell^2}$, where s is the scale and l indicates the length-scale (the influence radius of the kernel). The multiscale kernel was constructed by the summation of 2 Gaussians. The anisotropic kernel was defined as having more variation in the length direction of the femur. The kernels were low-ranked using the 10 prominent basis functions.

3 Experiments and results

Experiments were carried out for a comparative study to evaluate the model performance when combined with the specified kernels. The evaluation is performed by fitting the SSMs to mesh data in the test set and then computing RMSE of the fitted femur models to the test set. Figure 2 shows some modes of the data-driven SSM and its combination with the anisotropic kernel. Results for comparing the SSMs can be seen in Fig. 3. The RMSE for the data-driven SSM and its combination with the Gaussian, multiscale and anisotropic kernels were computed as 6.48 ± 4.53, 5.36 ± 2.98, 3.73 ± 1.36 and 3.27 ± 1.00 mm, respectively.

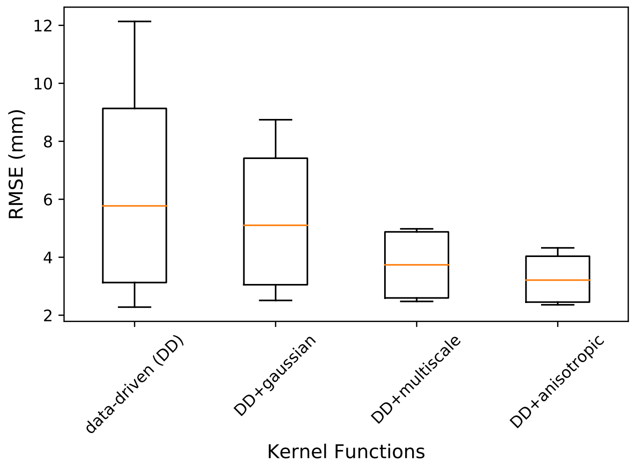

Figure 3: *Evaluation of different kernel functions.*

4 Discussion and conclusion

The current study developed SSMs for femur bone modeling based on GPMMs. Out of different analytical kernels (Gaussian, multiscale and anisotropic kernels) and keeping the 10 most prominent basis functions, it has been found that the combination of our data-driven model with the anisotropic kernel more accurately encodes the patterns of variability of femurs in our dataset. Specifically, we observed that the modes of data-driven SSM when combined with the anisotropic kernel corresponds well with the actual deformation of the femur bone (this can be confirmed by seeing how the dominant modes vary in Figure 2). Exploration of other customized kernels or transferring the knowledge of femur variations from a larger dataset can be considered for future works.

References

[1] Mutsvangwa, Tinashe, et al. (2015). An automated statistical shape model developmental pipeline: application to the human scapula and humerus. *IEEE Transactions on Biomedical Engineering*, 62.4:1098-1107.

[2] Salhi, Asma, et al. (2017). Comparing statistical shape model-based mesh fitting methods: towards patient-specific muscle modeling. *In: Proc. RITS*.

[3] Heimann, Tobias, and Hans-Peter Meinzer. (2009). Statistical shape models for 3D medical image segmentation: a review. *Medical image analysis*, 13.4:543-563.

[4] Cootes, Timothy F., et al. (1992). Training models of shape from sets of examples. *In: Proc. BMVC*, 9-18.

[5] Luthi, Marcel, et al. (2018). Gaussian process morphable models. *IEEE transactions on pattern analysis and machine intelligence*, 40.8:1860-1873.

[6] Albrecht, Thomas, et al. (2013). Posterior shape models. *Medical image analysis*, 17.8:959-973.

[7] Scalismo (2016). scalismo - scalable image analysis and shape modeling. *available online at: http://github.com/unibas-gravis/scalismo*

[8] Jacq, Jean-José, et al. (2008). Performing accurate joint kinematics from 3-D in vivo image sequences through consensus-driven simultaneous registration. *IEEE Transactions on Biomedical Engineering*, 55.5:1620-1633.

[9] Kazhdan, Michael, and Hugues Hoppe. (2013). Screened poisson surface reconstruction. *ACM Transactions on Graphics*, 32.3:29.

PRE-OPERATIVE PLANNING IN ACETABULAR AND PELVIC RING SURGERY: THE FIRST BIOMECHANICAL MODEL

M. Boudissa[1,2] , M.Chabanas[2], H. Oliveri[2] , G. Bahl[2], J. Tonetti[1,2]

1. Orthopedic and Traumatology Surgery Department, Grenoble University Hospitals, La Tronche, 38700, France, mboudissa@chu-grenoble.fr
2. TIMC-IMAG lab, Univ. Grenoble Alpes, CNRS UMR 5525, La Tronche, 38700, France
Tel : +33 6 01 04 68 24
Contact: m.boudissa@chu-grenoble.fr

1 Introduction

The development of imaging modalities and computer technology provides a new approach in acetabular surgery. A full understanding of the fracture, based on CT images and 3D reconstructions, is required to specify the best planning, especially the surgical acces(es). Several preoperative planning tools have been proposed for acetabular fractures but no one exists for pelvic ring fractures [1].

All these preoperative planning tools are geometrical repositioning with their own limitations. Indeed, reducing the fracture in 3D through mouse interactions is difficult, quite non-intuitive and hardly guaranty non-penetration between fragments. An intuitive simulation of the fracture reduction using a mechanical model was developed with promising results regarding acetabular fractures [2]. To our knowledge, it is the first biomechanical model used for virtual planning in acetabular surgery.

The aim of this study was to confirm whether our prototype virtual planning tool using a rigid biomechanical model can predict success or failure in fracture reduction according to the choice of the surgical approach and the surgical strategy in acetabular fracture surgery and to assess its predictability in pelvic ring fractures surgery. To our knowledge, it is the first biomechanical model used for virtual planning in acetabular fracture and pelvic ring fracture surgery.

2 Materials and Methods

2.1 Patients

Between November 2015 and November 2018, 29 patients operated by the first author (M. Boudissa) for acetabular fracture were included. All patients had given their consent for the study. The mean age was 44.8 years +/- 17.8 [18-80]. The mean delay between accident and surgery was 8.7 +/- 5 [4-24]. The fracture patterns were 24 acetabular fractures and 5 pelvic ring fractures.

2.2 Methods

Each patient had a pre-operative high-resolution CT scan. The surgery was performed by anterior ilio-inguinal approach, Stoppa anterior approach or posterior Kocher-Langenbeck approach or both of them according to the fracture patterns. The mean operative time was 139 min. Reduction quality was assessed on post-operative CT scans by an independent observer according to Matta for acetabular surgeries and according to Tornetta et al for pelvic ring surgeries. [3,4]. Data from CT in DICOM format were used. A 3D model of the hip bones, including separated fragments, was first build out of the CT images. Semi-automatic segmentation procedures were performed using the non-commercial software itksnap to perform automatic threshold, region growing with active contours and finally manual refinements [5]. To simulate the surgical procedure a mechanical model of the hip joint bony elements was used, implemented within the non-commercial Artisynth framework [6]. Each bone fragment is considered as an independent rigid body. One of them is usually considered as fixed, e.g. the anterior or posterior column and/or the femoral head. Collisions are handled to ensure non-penetration between elements. The action of a clamp and Schanz screw are simulated in translation and rotation with collisions response. In reality, the soft tissues apply heavy constraints to the bones during their repositioning. A first approximation is to add a strong global damping to the all system. This high resistance ensures the response to collisions and numerical instabilities are very low in comparison to the forces directly applied to the bones. The soft tissue environment i.e the hip capsule, the sacrospinous ligament, the inguinal ligament and the pubic symphysis are modeled.

Surgical approach and surgical strategy according to the operative report were simulated. The simulated reductions and the surgical reductions were compared.

3 Results

29 surgeries were practiced and 29 simulations were performed immediately after the surgery. The reduction sequences according to each surgical access and the surgical tool that were used (clamps, Schanz' screw, femoral traction…) were simulated. In all cases, the biomechanical model had reproduced the surgical behavior and so the surgical reduction. An anatomical reduction was achieved in 19 cases (65,5%), a satisfactory reduction in 4 cases (14%) and an imperfect reduction was achieved in 6 cases (20,5%) and so was the simulation. The biomechanical simulation found similar results using the same surgical strategy.

The mean duration to perform semi-automatic segmentation was 148 min +/- 33.2 [100-180]. The mean duration for acetabular planning surgery was 21 min +/- 5 [12-38].

An example of pelvic ring fracture simulation (fig 1) and acetabular fracture simulation (fig 2) is presented.

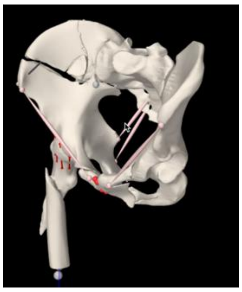

Figure 1: Tile C pelvic ring fracture simulation

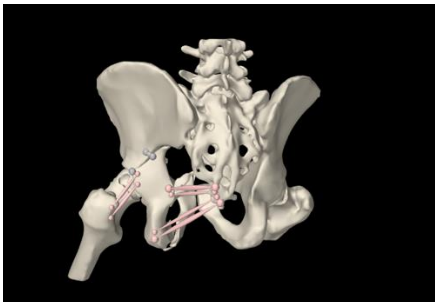

Figure 2: T-type acetabular fracture simulation

4 Conclusion

Our virtual planning tool using a rigid biomechanical model can predict success or failure in fracture reduction according to the surgical approach and the surgical strategy in acetabular fractures surgeries. The results are quite promising for planning in pelvic ring fractures surgeries even if more simulations are needed to validate these preliminary results. It could be an effective planning tool for the surgeon to define which surgical access and in which order to reposition bone fragments. A controlled randomized prospective study is needed to validate our preliminary results.

ACKNOWLEDGMENTS

This work was partly supported by the French ANR within the Investissements d'Avenir program (labex CAMI) under reference ANR-11-LABX-0004.

5 References

[1] Boudissa M, Courvoisier A, Chabanas M, Tonetti J. (2018). Computer assisted surgery in preoperative planning of acetabular fracture surgery: state of the art. Expert Rev Med Devices,15:81-89.

[2] Boudissa M, Oliveri H, Chabanas M, Tonetti J. (2018). Computer-assisted surgery in acetabular fractures: Virtual reduction of acetabular fracture using the first patient-specific biomechanical model simulator. Orthop Traumatol Surg Res, 104:359-362.

[3] Matta JM, Merritt PO. (1988) Displaced acetabular fractures, Clin Orthop Relat Res, 230, 83-97.

[4] Tornetta P, Matta JM. (1996) Outcome of operatively treated unstable posterior pelvic ring disruptions. Clin Orthop Relat Res, (329):186-93.

[5] Yushkevich PA, Piven J, Hazlett HC, Smith RG, Ho S, Gee JC, Gerig G. (2006). User-guided 3D active contour segmentation of anatomical structures: Significantly improved efficiency and reliability, Neuroimage, 31, 1116-28.

[6] Loyd J, Stavness I, Fels S. (2012). ArtiSynth: A fast interactive biomechanical modeling toolkit combining multibody and finite element simulation. Soft Tissue Biomechanical Modeling for Computer Assisted Surgery, pp. 355-394, Springer.

Biomechanical modeling of the lung deflation during minimally-invasive surgery

*Anne Cécile LESAGE, David RICE, Kristy K BROCK, Bastien RIGAUD, Alda TAM and Guillaume CAZOULAT**

The University of Texas MD Anderson Cancer Center, Houston, Texas

Contact: gcazoulat@mdanderson.org

Localization of the tumor during video-assisted thoracoscopic surgery (VATS) relies on visual inspection only. As the lung is deflated during the procedure, only tumors close to the lung surface can be localized, limiting the eligibility for this minimally invasive procedure. In order to enable the localization of tumors deeper in the lung and the use of VATS for these cases, we propose to predict the deflation of the lung during the procedure using a biomechanical model solely based on the pre-operative CT scan. The feasibility was evaluated using CT scans of pneumothorax from three patients.

1 Introduction

In comparison to traditional open thoracotomy, video-assisted thoracoscopic surgery (VATS) for lung tumor resection significantly reduces morbidity and postoperative pain. Unfortunately, because the lung has to be deflated during VATS and the localization of the resection target relies on visual inspection, only patients with tumors located close to the lung surface are usually eligible for this technique without the need for a pre-operative invasive marking of the lung nodule. Previously, anatomical modeling using finite element models has demonstrated accuracy in modeling normal physiological motion of the lung, for example breathing motion, daily anatomical positioning and response to focal therapy [1, 2]. We propose to expand these biomechanical models to predict the deflation of the lung during the resection process, enabling localization of the nodules and potential expansion of the VATS eligibility criteria. In this study, CT scans from three patients whose pneumothorax occurred during or after lung biopsy were retrospectively analyzed.

2 Materials and methods

In this preliminary study before application to VATS, three patients whose pneumothorax occurred during or after lung biopsy were retrospectively analyzed. For each patient, a CT scan showing the deflated lung and a CT scan showing the re-inflated lung after chest tube insertion were collected. The lung was semi-automatically segmented on both images and used to generate 3D surface triangular meshes with faces of mean size 5mm. The surface mesh of the inflated lung was used to define a rigid thoracic cavity and to create a first order initial tetrahedral mesh with a mean element size of 5mm. To generate the biomechanical finite element model of the lung deflation, we adapted the method proposed by Eom et al [3] to predict lung motion over the respiratory cycle. A time explicit finite element solver (Altair RADIOSS) was used to build a biomechanical model with physiological boundary conditions and loading. A realistic contact model of sliding without friction was imposed using a non-linear stiffness penalty method between the pleura mesh nodes (slaves) and the lung surface (master). Physiologically, in the absence of pneumothorax the lung is held in contact with the pleura by a negative intra-pleural pressure. During deflation, the lung experiences gravity and positive pressure. In the model, no pre-constraint was applied to the inflated lung. To ensure numerical stability, only a small positive pressure could be applied on the lung surface mesh gradually over 0.1s of physical time with a maximum 880 Pa final pressure. A gravity field of $9.81 m.s^{-2}$ at t=0s and density of $1.e^{-6} kg/mm^3$ was applied to the model. Elastic and Ogden hyperelastic properties [4] were tested for the lung parenchyma solid mechanics with a Young's modulus of 4kPa and Poisson's ratio of 0.3. The lung deflation with the described boundary conditions was dynamically simulated over 0.2s of physical time and the simulated state showing a lung volume equal to the volume of the

lung on the pneumothorax image was selected as the final result.
To evaluate the accuracy of the model, the overlap between the simulated deflated lung and the ground truth was measured with Dice scores. To evaluate the accuracy in displacing internal tissues, corresponding vessel bifurcation landmarks were identified in the original images to measure target registration errors (TRE).

3 Results

The computation time to simulate deflation was approximately 20 minutes for each case on a cluster with 32 parallel processes. Figure 1 shows the original images of a patient (Patient 1) and the FEM before and after simulation of the deflation with the linear elastic model.

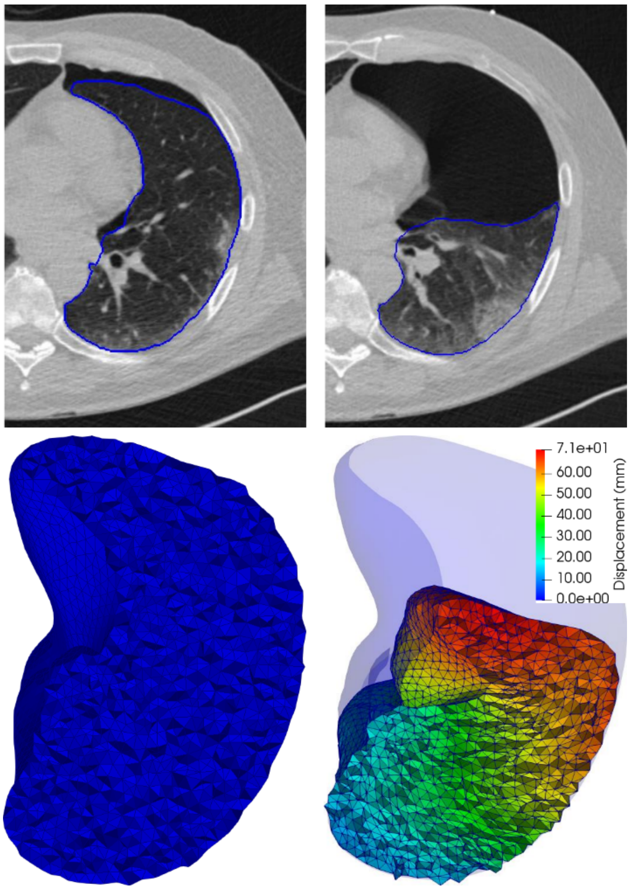

Figure 1: *Top: CT scans showing an inflated (left) and deflated (right) lung (Patient 1). Bottom: Representation of the 3D FEM clipped at the same location.*

The Dice scores for the three patients between the ground truth inflated and deflated lungs were 0.77, 0.74 and 0.85. The Dice score between the simulated deflated lung and ground truth were 0.89, 0.82 and 0.89 for the elastic model and 0.86, 0.77 and 0.90 for the hyperelastic model. The maximum magnitude of the node displacements obtained after simulation were 7.1, 5.6 and 2.1 cm, for the three patients, respectively.
Identifying anatomical correspondences revealed to be very challenging due to the extreme deformation of the tissues. Five landmarks were identified on vessel bifurcations for Patient 1 and 3, while it was possible to identify only two for Patient 2. For Patient 1 and 2, the large displacements in the superior part of the lung made possible the localization of corresponding bifurcations only in the posterior part where the observed displacements remained moderate. Table 1 reports the mean TRE in cm before and after simulation of the deflation for the three patients.

Table 1. Mean (min-max) target registration errors (cm)

	Initial	Elastic	Hyperelastic
Patient 1	1.8 (1.4-2.6)	1.4 (0.7-1.8)	1.1 (0.7-1.5)
Patient 2	2.7 (1.9-3.5)	1.6 (1.5-1.7)	1.4 (1.0-1.8)
Patient 3	2.2 (1.2-3.1)	1.7 (1.1-2.4)	1.1 (0.7-1.8)
Mean	2.2	1.6	1.2

As expected based on previous rheological experiments, modeling the lung with hyperelastic material properties yielded to a better prediction of the internal tissue displacements, allowing to achieve an average accuracy of 1.2 cm. When considering a linear elastic model, an overestimation of the vessel tree collapse could be observed as well as some stability issues in terms of final mesh quality.

4 Conclusion

Finite-element modeling of the lung deflation is challenging because of the large displacements which lead to simulation instability but this study demonstrated the feasibility of such an approach. While both the linear elastic and hyperelastic models provided similar surface matching as indicated by Dice scores of the lung, hyperelasticity was more appropriate to describe the internal deformations. Ongoing investigations to improve the accuracy of the model include parameter optimization and adding the main airway attachment with Dirichlet boundary conditions, the lung lobes, and vessel tree in the model. For further evaluation and adaption of the model to the clinical setup, an acquisition protocol of CT scans from patients undergoing VATS is under preparation. Future research will aim to combine the information from the biomechanical model and intra-procedural video.

Acknowledgement

This research was supported by the University Cancer Foundation via the Institutional Research Grant

program at the University of Texas MD Anderson Cancer Center.

References

[1] A Al-Mayah et al. "Toward efficient biomechanical-based deformable image registration of lungs for image-guided radiotherapy". Physics in Medicine and Biology, vol. 56, no. 15, pp. 4701, 2011.
[2] G Cazoulat et al, "Biomechanical deformable image registration of longitudinal lung CT images using vessel information". Physics in Medicine and Biology, vol. 61, no. 13, pp. 4826–4839, 2016.
[3] J Eom et al. "Predictive modeling of lung motion over the entire respiratory cycle using measured pressure-volume data, 4DCT images, and finite-element analysis". Med. Phys. 2010 Aug;37(8):4389-400.
[4] A Naini, R Patel, and A Samani. "Measurement of Lung Hyperelastic Properties Using Inverse Finite Element Approach". IEEE TBME, 58,:10, Oct 2011.

Situation awareness in the "Virtual Operating Room of Errors": a pilot study

Marie-Stéphanie Bracq[1,2], Marie Le Duff[2], Estelle Michinov[1], Bruno Arnaldi [3], Valérie Gouranton[3], Jeanne Descamps[4], Pierre Jannin[2].

1. Univ Rennes, LP3C (EA 1285), F-35000 Rennes, France
2. Univ Rennes, Inserm, LTSI - UMR 1099, F-35000 Rennes, France
3. Univ Rennes, INSA Rennes, Inria, CNRS, IRISA, F-35000 Rennes, France
4. Ecole d'Infirmier(e)s de Bloc Opératoire – Pôle de formation des professionnels de santé du CHU de Rennes, France

Contact: marie-stephanie.bracq@univ-rennes2.fr

Training healthcare professionals in non-technical skills has revealed a crucial issue for patient safety and quality of care. Simulation offers good opportunities to follow that goal. Technologies for simulation are emerging, among which, virtual reality (VR). Yet, few VR simulators address non-technical skills (NTS)[1]. The "Virtual Operating Room (OR) of errors" scenario aims at training situation awareness in a VR environment.

1 Introduction

Situation awareness is the ability to gather information, recognize and understand information, as well as anticipate its future state [2]. It is a crucial NTS in the OR as it has a direct impact on communication, decision making, leadership and teamwork[3], other key NTS. The OR of Errors is a simulation scenario that is often implemented "in real" with a mock OR in order to sensitize healthcare professionals to quality and safety standards as well as hygiene rules. Our goal in implementing the OR of errors in a VR environment was to extend its pedagogical interest to situation awareness training, in particular for scrub nurses who are responsible for hygiene and security and for whom situation awareness is a major NTS[4].

2 Materials and methods

2.1 Virtual Reality Simulator

Participants are immersed in a virtual operating room, and are not guided during this simulation; they can move and interact freely in the environment. 19 errors were implemented in the scene, and divided into five categories: identity monitoring, hygiene and infective risk, wrong-site surgery, patient safety, and rupture of continuity of care. The VR equipment used for the experimentation was a HTC Vive system. It is composed of a Head Mounted Display and two hand-controllers.

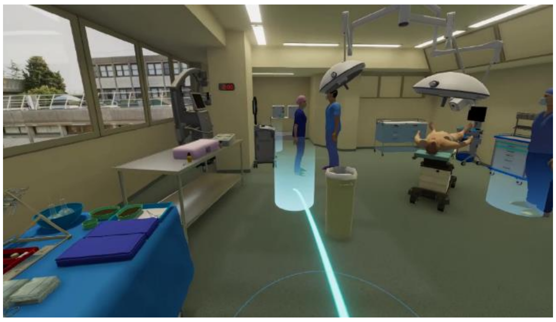

Fig 1. Scenario of the OR of errors

2.2 Participants and setting

The scenario of the "Virtual OR of Errors" was pretested by three second-year students of the Scrub Nurses School of Rennes in December 2018. The simulation session for the pilot study took place on the 22nd and 23rd of January 2019, in the Scrub Nurses School of Rennes. It involved all first year students (n=18). Participations were individual, and organized in parallel by two assessors. A short individual debriefing followed each simulation, and a collective debriefing including scrub nursing teachers took place after all sessions were done. Approval was obtained for the study by the Ethics Committee of the University Hospital of Rennes.

2.3 Tasks

Participants had to make sure that quality standards, safety and hygiene rules were respected in the virtual OR. They had 14 minutes to report any surgical error they would find. Before getting in the virtual environment, participants were invited to read a paper version of the patient file. The case was a craniotomy for Mr. Jean Dupond, born on July 12^{th} 1955, who suffered from a left frontal meningioma (brain tumor).

2.4 Assessment metrics

Data were gathered from self-reported post-simulation questionnaires: situation awareness (SART[5]) and workload (NASA TLX[6]). As this was a pilot study, participants also assessed the simulator for ease of use, immersion, and efficiency on a 5-Point-Likert scale. Detail and number of reported errors were gathered from the application logs.

2.5 Hypotheses

Our main hypotheses are the following:

H1: Participants with a lower number of detected errors (group 1) have a higher level of workload than participants with a higher number of detected errors (group 2).

H2: Participants with a higher number of detected errors (group 2) have a higher level of situation awareness than participants with a lower number of detected errors (group 1).

H3: Participants with a higher number of detected errors (group 2) will evaluate the simulator better for ease of use, immersion and efficiency, than participants with a lower number of detected errors (group 1).

3 Results

Statistical analyses were conducted with JASP [7]. The median number of detected errors was 9. We median-split participants into two groups in order to compare their results with Student's T- tests, after the normality hypothesis was checked: group 1 members detected less than 9 errors (n_1=7), and group 2 members, 9 errors or more (n_2=11). For group 1, mean value for Workload is 56.96 (min=30.83, max=69.17, *SD*=13.04), and for group 2, 44.06 (min=20, max=58.83, *SD*=13.87). Difference between both groups for Workload is significant t (16) =1.967, p=.033, validating H1. For group 1, mean value for Situation Awareness is 12.14 (min=-8, max=25, *SD*=12.18), and for group 2, 22.27 (min=10, max=33, *SD*=7.31). Difference between both groups for Situation Awareness is significant t (16) =-2.22, p=.021, validating H2. For ease of use and efficiency, differences between both groups are not statistically significant. Regarding immersion, mean value for group 1 is 3.32 (min=1.25, max=5, *SD*=1.31), and for group 2, 4.36 (min=3, max=5, *SD*=0.69). Difference between both groups for Immersion is significant t (16) = -2.216, p=.021, partially validating H3.

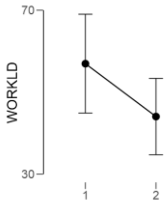

Fig 3. Workload

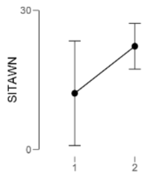

Fig 4. Situation awareness

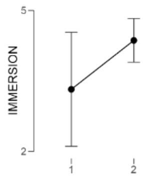

Fig 5. Immersion

4 Discussion and conclusion

In this study, we analyzed the workload and situation awareness of participants immersed in a virtual medical simulation. The results confirmed two of our main hypotheses, that participants with a lower number of detected errors had a higher level of workload, and participants with a higher number of detected errors had a higher level of situation awareness. The latter also felt more immersed in the environment.

Although tested on a small sample, the OR of Errors gives an assessment of Situation Awareness and seems an appropriate tool to train on this NTS, especially after debriefing. Participants were not asked about their previous experience in video games or VR, as the acceptability study of the environment showed us that it had no impact (Bracq et al., *in revision*), but it could have been interesting to make sure this was still valid.

Future studies such as adding errors, expanding and diversifying the population and the specialty of participants will be considered. The challenges of future studies is to test the genericity of the "Virtual OR of Errors".

References

1. Bracq MS, Michinov E, Jannin P. Virtual Reality Simulation in Nontechnical Skills Training for Healthcare Professionals: A Systematic Review. *Simul Healthc*. December 2018. doi:10.1097/SIH.0000000000000347.
2. Flin R, O'Connor P, Crichton M. *Safety at the Sharp End, a Guide to Non-Technical Skills*. Farnham: Ashgate Publishing Limited; 2008.
3. Flin R, Youngson GG, Yule S. *Enhancing Surgical Performance: A Primer in Non-Technical Skills*. CRC Press; 2015.
4. Mitchell L, Flin R, Yule S, Mitchell J, Coutts K, Youngson G. Evaluation of the Scrub Practitioners' List of Intraoperative Non-Technical Skills (SPLINTS) system. *International Journal of Nursing Studies*. 2012;49(2):201-211. doi:10.1016/j.ijnurstu.2011.08.012.
5. Taylor RM. Situation awareness rating technique (SART): the development of a tool for aircrew systems design. In: *Situational Awareness in Aerospace Operations (Chapter 3).* France: Neuilly sur-Seine: NATO-AGARD-CP-478.; 1990.
6. Hart SG, Staveland LE. Development of NASA-TLX (Task Load Index): Results of Empirical and Theoretical Research. In: *Advances in Psychology*. Vol 52. Elsevier; 1988:139-183. doi:10.1016/S0166-4115(08)62386-9.
7. JASP Team. *JASP (Version 0.9)[Computer Software]*.; 2018. https://jasp-stats.org/.

Preliminary evaluation of haptic guidance for pre-positioning a comanipulated needle

Hadrien GURNEL, Maud MARCHAL, Laurent LAUNAY, Luc BEUZIT and Alexandre KRUPA

Univ. Rennes, IRISA, Inria, INSA Rennes, IRT b<>com
Campus de Beaulieu, 35042 Rennes Cedex, France
Contact: maud.marchal@irisa.fr, alexandre.krupa@inria.fr

In minimally-invasive procedures like biopsy, the physician has to insert a needle into the tissues of a patient to reach a target. Currently, this task is mostly performed manually. This can result in a large final positioning error of the tip that might lead to misdiagnosis and inadequate treatment. In this paper, we present 5 haptic guides to assist the clinical gesture of needle insertion. Those guides were evaluated through a preliminary user study involving two physicians, both experts in needle manipulation.

1 Introduction

Percutaneous needle insertion is frequently used for diagnosis or treatment and the outcome of those minimally-invasive procedures depends almost exclusively on the accuracy of the placement of the tip of the needle on an anatomical target. Inaccurate positioning may force the physician to perform the insertion again, thus increasing the duration of the intervention and discomfort for the patient. Currently, needle insertion is mostly performed manually, which is prone to error for several reasons [1]. Among those, the interaction forces between the needle and the tissues [2][3], make it nearly impossible to correct the trajectory of the needle once it is inside soft tissues. Therefore, correct pre-positioning of the needle is essential. To make needle pre-insertion more precise and reliable, one idea is to provide the physician with robotic assistance. In this paper, we propose 5 haptic guides dedicated to comanipulated-needle pre-positioning and inspired from guiding virtual fixtures [4] [5]. They are designed to attract the physician towards the entry point and the correct orientation, while ensuring close proximity with the patient.

2 Methods

We present 5 haptic guides denoted by FTip, TTip, FTTip, FTATip and TEff and illustrated in figure 1. The unassisted reference gesture is denoted by Ref. Each haptic guide produces a 6x1 force-feedback vector, computed either in the needle-tip frame or the end-effector frame of the haptic device. This force vector is computed from the pose error between the current measure of the pose of the needle-tip frame (or the end-effector frame) and the desired pose of the entry-point frame. The latter is centered on the entry point and its z axis corresponds to the desired angle of incidence to reach.

FTip constrains the position of the tip of the needle, to keep it close to the normal of the tissue surface that crosses the entry point. So, the tip can be translated along the normal, but as soon as it deviates from it, a lateral force $\mathbf{f}_{\text{lateral}}$ is generated to pull it back. Translations along the z axis and rotations around the yaw, pitch and roll axes of the tip frame are free. TTip constrains the orientation of the needle to the desired angle of incidence, regardless of the current position of the tip. Thus, it applies a torque $\mathbf{t}_{\text{tip}}$ to the needle, around the yaw and pitch axes of the tip frame. All the translations and the rotation around the roll axis of the needle are free. FTTip combines FTip and TTip, i.e. $\mathbf{f}_{\text{lateral}}$ and $\mathbf{t}_{\text{tip}}$, to constrain both the position and the orientation of the needle. Only translations along the z axis and rotations along the roll axis of the tip frame are free. FTATip adds an attractive force $\mathbf{f}_{\text{attraction}}$ to the force-feedback vector of FTTip. It is computed in the tip frame and oriented towards the entry point. With FTATip, only the rotations around the roll axis of the tip frame are free. TEff ensures the needle always points toward the entry point, by applying a torque $\mathbf{t}_{\text{eff}}$ to the yaw and pitch axes of the end-effector frame of the haptic device.

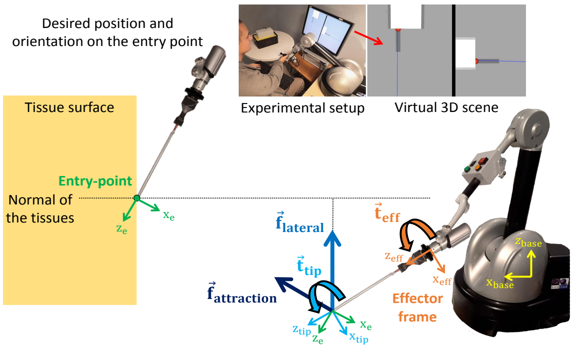

Figure 1: *The five proposed haptic guides and the experimental setup of the preliminary user study. The blue arrows represent the needle-tip frame, as well as forces and a torque expressed in this frame. FTip, TTip, FTTip and FTATip implement one or a combination of those forces and torque. The orange arrows represent the end-effector frame of the haptic device and a torque expressed in this frame, which is implemented by TEff.*

3 Prelimary user study and results

We conducted a preliminary user study to compare the 5 haptic guides and the unassisted reference gesture. It involved an interventional radiologist and an anaesthetist, both experts in needle manipulation. Our evaluation focused on the performance of the physicians for pre-positioning a needle before its insertion into soft tissues, but also on user experience. The task consisted in positioning a needle on a target in 3D space and under a desired orientation. The participants handled an instrumented needle, tracked electro-magnetically by an Aurora^{TM}device, (Northern Digital Inc., Ontario, Canada). The needle was attached to a 6-DOF haptic device (Virtuose^{TM}6D, Haption [6], France) (see Figure 1). A computer screen displayed a simulated version of the real scene. The physicians were asked to place the tip of the needle on a green virtual sphere representing the entry point, and to give the axis of the needle a desired angle of incidence represented by a grey virtual cylinder. The latter was achieved by keeping a blue line, representing the needle, parallel to the grey cylinder displayed on the screen.

Performance-wise, the best positioning accuracy was obtained with TTip for both physicians, with improvements of 54% for the first one and 20.4% for the second one, compared to Ref. However, less obvious results were achieved in terms of orientation accuracy with the guides. Overall, TTip comes out as the best for both physicians with regard to positioning accuracy. The goal of the subjective study is to compare the 5 haptic guides and the unassisted reference gesture from a user-experience point of view. The criteria are the level of assistance, accuracy, ease of use, comfort and usefulness of haptic feedback. The physicians filled a subjective questionnaire after performing the task with the guides or Ref, answering questions within a 7-point Likert scale. At the end of the experiment, they were also asked to choose the approach they preferred and the one they enjoyed the least. The results of the subjective study are presented by the radar charts in figure 2. Those indicate that the methods the physicians preferred are TEff and FTip and that the ones they enjoyed the least are FTTip and Ref.

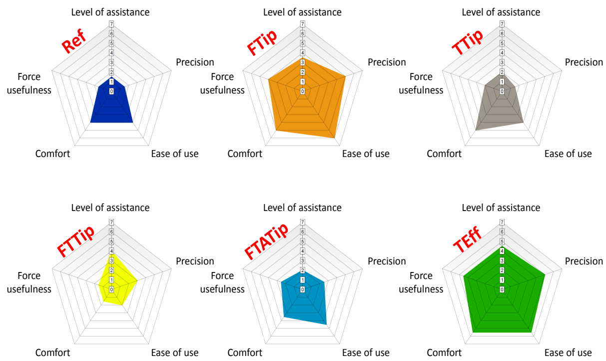

Figure 2: *Radar charts presenting the results of the subjective comparison of the 5 haptic guides and the unassisted reference gesture*

4 Discussion and conclusion

The objective and subjective study showed that the positioning accuracy was enhanced with haptic guidance, with improvements of 54% for the first participant and 20.4% for the second one, compared to Ref. The outcome of the study was less conclusive in terms of orientation accuracy, however. In the questionnaire, both participants stated about TEff, i.e the haptic guide they enjoyed the most, that it was comfortable and precise. The first user noted that it was very helpful at the beginning of the task, for correctly orienting the needle toward the target, and that it did not disturb accurate positioning closer to the target. The other added that it enabled good handling of the needle with a good amount of stiffness, which facilitated accurate positioning. They also enjoyed FTip. On the contrary, they were less satisfied by Ref, FTTip and FTATip. It appears that they preferred to be in control of the final orientation of the needle, while at the same time receiving soft feedback from the haptic device, for comfortable needle positioning.

Those promising results open possibilities for increasing the level of accuracy and reliability of needle pre-positioning and pre-orienting. It also paves the way for the design of efficient haptic guides dedicated to comanipulated needle insertion in soft tissues.

References

[1] N. Abolhassani and R.V. Patel. Deflection of a flexible needle during insertion into soft tissue. In *The 28th IEEE Engineering in Medicine and Biology Society*, pages 3858–3861. IEEE, 2006.

[2] A.M. Okamura, C. Simone, and M.D. O'Leary. Force modeling for needle insertion into soft tissue. *IEEE Transactions on Biomedical Engineering*, 51(10):1707–1716, October 2004.

[3] R. J. Roesthuis, Y. R. J. van Veen, A. Jahya, and S. Misra. Mechanics of needle-tissue interaction. In *IEEE/RSJ International Conference on Intelligent Robots and Systems*, pages 2557–2563, Sep. 2011.

[4] L.B. Rosenberg. *Virtual Fixtures: Perceptual Overlays Enhance Operator Performance in Telepresence Tasks*. PhD thesis, Stanford University, Stanford, CA, USA, 1994. UMI Order No. GAX95-08441.

[5] B.L.; Baena R.F. Bowyer, S.A.; Davies. Active constraints/virtual fixtures: A survey. *IEEE Transactions on Robotics*, 30(1):138–157, 2014.

[6] Haption. *Virtuose^{TM}6D*, 2001.

Analyzing the practice of expert surgeons based on video spatial features

Arthur DERATHE[1,2,3,4], Sandrine VOROS[1,2,3,4,7], Fabian RECHE[1,2,3,4,5], Pierre JANNIN[7,8,9], Alexandre MOREAU-GAUDRY[1,2,3,4,5,6] and Bernard GIBAUD[7,8,9]

CNRS[1], UGA[2], Grenoble INP[3], TIMC-IMAG[4], CHU de Grenoble[5], CIC-IT[6], INSERM[7], Univ Rennes 1[8], LTSI[9]

Faculté de Médecine, Pavillon Taillefer - F-38706 La Tronche Cedex

Tel : +33 (0)4 56 52 00 02

Contact: arthur.derathe@univ-grenoble-alpes.fr

Surgical practice is a complex phenomenon, especially in laparoscopy. We predict an aspect of the surgical quality called 'surgical exposure', as well as the practicing surgeon based on spatial features extracted from the laparoscopic video. We use an algorithm with a linear feature selection, which allows us to closely analyze the most discriminant features. This allows us to observe how spatial features are correlated with the prediction of both the surgical exposure and the practicing surgeon.

1 Context

In Minimal invasive surgery (MIS), patients benefit from overall better post-operative follow-up compared to open surgery [1]. On the other hand, the surgeon's practice is complex and the training specific to MIS is a long process [2]. To complement the classical training process, usually done by mentoring, video-based assessment tools is a domain that has raised interest for many years.

The processing of MIS videos has been an active domain of research for many years. More precisely the analysis of the video's spatial content leads to the extraction of tool detection or trajectory information, and also to some optical flow information [3]. So far, these research projects are still facing technical issues regarding the complexity and the variability of the surgical environment.

Still, the next step of research is already being investigated: the automatic assessment of surgical metrics. A first classical analysis is to discriminate between surgeons with different levels of expertise [4, 5, 6]. In [7] an enhancement was proposed by correlating the levels of expertise with specific parts of the surgical instruments trajectories. Similarly, in [8], level of expertise was described by features describing the movements of surgical tools.

As a more global approach of the spatial content of the video, we propose to consider features describing all objects appearing in the video. Our objective was to study how these features could be used to predict two quality-related factors, namely:

1. the quality of the surgical exposure (*quality*)
2. the surgeon performing the surgery (*surgeon*)

2 Method

2.1 Material

We worked on a cohort of 29 patients treated by laparoscopic Sleeve Gastrectomy (LSG) at the CHU Grenoble Alpes. LSG is a bariatric procedure (surgical treatment of obesity) in which the stomach body is resected, which causes weight loss by restricting the food intake. Two confirmed surgeons performed these surgeries: one is an expert of bariatric surgery and performed 15 surgeries, the other is a confirmed, non-expert surgeon and performed 14 surgeries. We only focused on the video of a critical surgical step called the "Fundus Dissection".

A manual annotation was then performed on the video images. Only specific images were treated. A surgeon selected them based on the quality of surgical exposure that they marked using a binary score ("good" versus "bad"). We segmented the entire images and labeled each object appearing on it. Semantically meaningful features were then extracted for each segmented object (see Table 1).

Feature Name	Count	Description
Barycenter	2	x and y coordinates
Color	3	CIELAB color space
Eigenvalue	1	Ratio between the eigen-values of the two main directions
Eigenvectors	4	x and y components of the two main direction vectors
Perimeter	1	Perimeter count of pixel
Surface	1	Count of pixel covered
Texture	1	Description of the texture [9]

Table 1: *Description of the spatial features extracted for each segmented object*

2.2 Features analysis

The population of features we generated was used as input of a pipeline algorithm in which we mainly performed a dimension reduction (here a Linear Discriminant Analysis LDA) followed by a classification step (Support Vector Machine SVM). The objective was to predict two different responses: the "good" or "bad" *quality*, or the *surgeon* 1 or 2. To tackle as effectively as possible the data bias during the learning process, a cross-validation method was applied (inspired by [10]).

Once we optimized and trained this algorithm, and because the dimension reduction step is linear, we could observe the discriminating power of the input features as processed by the LDA. More precisely, we studied how the input features were combined in the transformation matrix, and also considered the ordering of eigenvectors implied by eigenvalues. Thus, we defined a variance for each feature which describes its discriminating power regarding the two predicted classes. We obtained an ordering of the input features according to their variance.

Experimentally, as we needed to observe the behavior of a sole model, we chose to optimize it only to predict the *quality*. Then, to compare the discriminant power of features for the prediction of both the *quality* and the *surgeon*, we generated an ordering of the features, for each class.

3 Results

We optimized the algorithm to predict the *quality* binary class, and thus got a stable model. We then trained this model to predict the *quality* class and the *surgeon* class. The prediction performances are shown in Fig.1.

Then, for both trained models, we extracted a list of features with their associated variance. We computed for each feature the difference between the variance of the *quality* trained model and the *surgeon* trained model. Thus, We obtained a heat-map showing a variance percentage value for each feature and segmented object (Fig.2). Positive value (red cells) denote features that are more discriminant for characterizing the *quality* than the *surgeon*. Those features showing the highest variances are the main directions of the form for the Liver retractor and the compress, as well as the perimeter of the Liver, and the yellow-blue color component of the Liver retractor. Inversely, negative values (blue cells) denote features that are more discriminant for characterizing the *surgeon* than the *quality*. Those are the green-red color component of the abdominal wall, and the y component of the barycenter for the flat grasper and the Spleen.

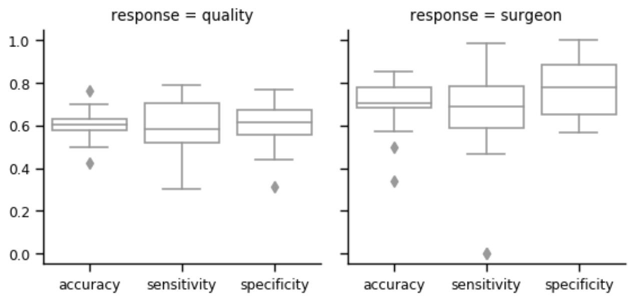

Figure 1: *Model performances for the prediction of the quality or the surgeon*

4 Conclusion

Fig.1 shows that although we optimized our model to predict the *quality*, its training gives better prediction results for *surgeon*. It may seem surprising, but the *quality* class is highly unbalanced in our dataset (85% - 15% ratio) whereas the *surgeon* class is much more balanced. As our study is a proof of concept and because of the linearity constraint necessary for the feature analysis, the performance of our algorithm may still be greatly improved.

It appears clearly that the heat-map in Fig.2 requires deeper analysis: by analyzing the predictive model, we plan to bring these spatial features closer to their clinical meanings.

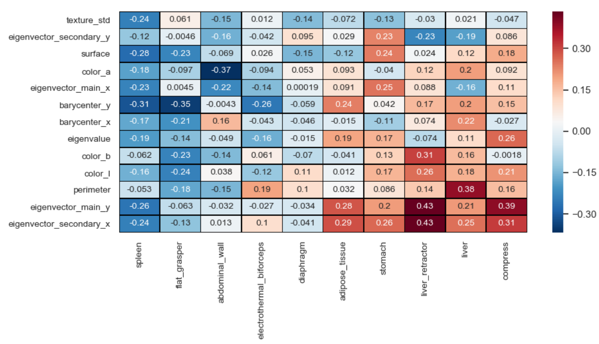

Figure 2: *Heatmap with the visible objects (X axis) and their associated spatial features (Y axis). Each value is the variance percentage difference of the feature between the prediction of the quality and the surgeon*

Acknowledgements
This work was supported by French state funds managed by the ANR within the Investissements d'Avenir programme (Labex CAMI) under reference ANR-11-LABX-0004.

References

[1] Laparoscopic surgery versus open surgery for colon cancer: short-term outcomes of a randomised trial. *The Lancet Oncology*, 6(7):477–484, July 2005. ISSN 1470-2045. doi: 10.1016/S1470-2045(05)70221-7.

[2] Timothy J. Babineau, James Becker, Gary Gibbons, Stephen Sentovich, Donald Hess, Sharon Robertson, and Michael Stone. The Cost of Operative Training for Surgical Residents. *Arch Surg*, 139(4):366–370, April 2004. ISSN 0004-0010. doi: 10.1001/archsurg.139.4.366.

[3] David Bouget, Max Allan, Danail Stoyanov, and Pierre Jannin. Vision-based and marker-less surgical tool detection and tracking: a review of the literature. *Medical Image Analysis*, 35:633–654, January 2017. ISSN 1361-8415. doi: 10.1016/j.media.2016.09.003.

[4] Aneeq Zia, Yachna Sharma, Vinay Bettadapura, Eric L. Sarin, Thomas Ploetz, Mark A. Clements, and Irfan Essa. Automated video-based assessment of surgical skills for training and evaluation in medical schools. *Int J CARS*, 11(9):1623–1636, September 2016. ISSN 1861-6429. doi: 10.1007/s11548-016-1468-2.

[5] Richard J. Gray, Kanav Kahol, Gazi Islam, Marshall Smith, Alyssa Chapital, and John Ferrara. High-Fidelity, Low-Cost, Automated Method to Assess Laparoscopic Skills Objectively. *Journal of Surgical Education*, 69(3):335–339, May 2012. ISSN 1931-7204. doi: 10.1016/j.jsurg.2011.10.014.

[6] Constantinos Loukas. Video content analysis of surgical procedures. *Surg Endosc*, 32(2):553–568, February 2018. ISSN 1432-2218. doi: 10.1007/s00464-017-5878-1.

[7] Hassan Ismail Fawaz, Germain Forestier, Jonathan Weber, Lhassane Idoumghar, and Pierre-Alain Muller. Evaluating surgical skills from kinematic data using convolutional neural networks. *arXiv:1806.02750 [cs]*, 11073:214–221, 2018. arXiv: 1806.02750.

[8] Sandeep Ganni, Sanne M. B. I. Botden, Magdalena Chmarra, Richard H. M. Goossens, and Jack J. Jakimowicz. A software-based tool for video motion tracking in the surgical skills assessment landscape. *Surg Endosc*, 32(6):2994–2999, June 2018. ISSN 1432-2218. doi: 10.1007/s00464-018-6023-5.

[9] Timo Ojala, Matti Pietikinen, and Topi Menp. A Generalized Local Binary Pattern Operator for Multiresolution Gray Scale and Rotation Invariant Texture Classification. In Sameer Singh, Nabeel Murshed, and Walter Kropatsch, editors, *Advances in Pattern Recognition ICAPR 2001*, Lecture Notes in Computer Science, pages 399–408. Springer Berlin Heidelberg, 2001. ISBN 978-3-540-44732-0.

[10] Gavin C. Cawley and Nicola L. C. Talbot. On Over-fitting in Model Selection and Subsequent Selection Bias in Performance Evaluation. *Journal of Machine Learning Research*, 11(Jul):2079–2107, 2010. ISSN ISSN 1533-7928.

Intraoperative Ultrasound-based Augmented Reality Guidance

***Jun Shen*[1,2]*, Nabil Zemiti*[2]*, Christophe Taoum*[3]*, Jean-Louis Dillenseger*[1]*, Philippe Rouanet*[3]*, Philippe Poignet*[2]**

1. Inserm, U1099, Rennes, France; Université de Rennes 1, LTSI, Rennes, France;
2. LIRMM, Université de Montpellier, Montpellier, France
3. Institut du Cancer de Montpellier Val d'Aurelle, Montpellier, France
Contact: jun.shen@etudiant.univ-rennes1.fr

This paper presents an ultrasound-based augmented reality framework for minimally invasive surgery. We achieved high accuracy in each calibration step. The framework was evaluated by localizing a hidden target in a soft tissue phantom.

1 Introduction

Minimally invasive surgery (MIS) such as laparoscopic surgery is done through small incisions. It brings many benefits to patients for instance small incisions, low risk of infection and quick recovery time. Meanwhile, it increases the difficulty for surgeons by reducing surgeons ability of differentiating the lesions and healthy tissues. Augmented reality (AR) system facilitates the surgical procedure by augmenting the endoscopic view with structures that are not visible directly from cameras but are visible in medical imaging data. This allows surgeons to localize tumors and vessels without palpating and tactile feedback.

Some of the MIS are performed under US guidance. The intraoperative US is able to localize and track in real time the target (e.g. a tumor) even in high soft tissues deformation conditions. In 3D conditions, the US images can be used to generate a 3D virtual model of the tumor for AR systems [1][2].

In this paper, we propose an intraoperative US-based AR framework for hidden structures visualization and surgical gesture guidance.

2 Framework Overview

Fig.1 shows the process of implementing an US-based AR framework. A 2D US probe is used and motorized to obtain a 3D US image. The objective of implementing this framework is to extract useful information (e.g. tumor area) from the 3D US image and superimpose it on the 3D endoscopic view, as shown in the visualization flowchart in blue in Fig.1. A mixture of the real and virtual information is presented to the user through a head mounted display (HMD). The key point of the visualization workflow is the registration ${}^{c}T_{us}$ between the 3D US image and the endoscopic camera. To solve it, we propose the following registration flowchart (in red in Fig.1): A tracking system is used as world coordinate system (CS) w and tracks a marker $m1$ (with CS $m1$) fixed on the endoscope and the marker $m2$ (with CS $m2$) fixed on the US probe. The transformation ${}^{m1}T_c$ between the endoscopic camera (with CS c) and the marker m1 is obtained by hand-eye calibration method [3]. The transformation ${}^{m2}T_{us}$ from 3D US image (with CS us) to the marker $m2$ is obtained by US calibration [4]. Finally, the transformation ${}^{c}T_{us}$ is computed by:

$$
{}^{c}T_{us} = ({}^{m1}T_c)^{-1} * ({}^{w}T_{m1})^{-1} *^{w} T_{m2} *^{m2} T_{us} \qquad (1)
$$

where ${}^{b}T_a$ represents the transformation from CS of a to CS of b.

3 Ultrasound Calibration

The goal of US calibration is to find the rigid transformation ${}^{m2}T_{us}$ between the acquired 3D US image and a marker fixed on the probe. In a previous study, we proposed a fast US calibration procedure [4] which greatly simplified the calibration procedure compared to some classical methods [5][6]. The main idea was to use a custom-designed calibration phantom attached to the marker and visible by the US device. In order to adapt this method to our US probe, we designed a calibration phantom as a tube in which the US probe can be inserted. On this tube, we hollow out some circles and squares that are features for US imaging (Fig.2). Marker $m3$ is fixed on the phantom and the

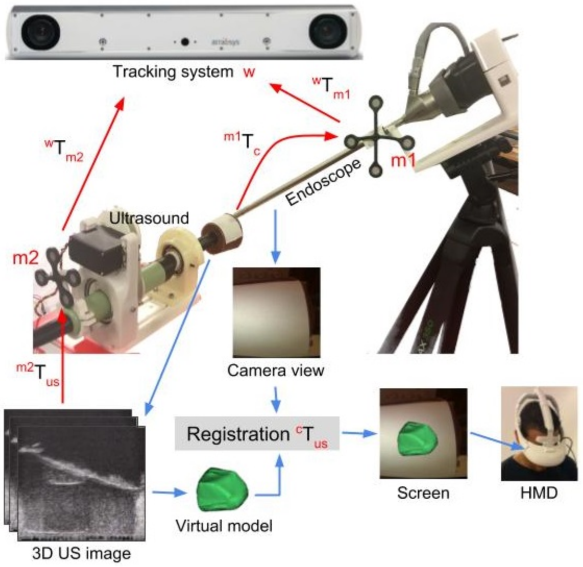

Figure 1: *Framework overview of the augmented reality setup based on a calibrated ultrasound.*

coordinates of the features (circles and squares) in the CS of the marker $m3$ are obtained by computer-aided design (CAD). The calibration process started with mounting the phantom on the US probe and placing the acoustic matching layer of the probe and the phantom into water for US imaging. The transformation $^{m2}\hat{T}_{us}$ is estimated by

$$^{m2}\hat{T}_{us} = (^{w}T_{m2})^{-1}\ ^{w}T_{m3}\ ^{m3}T_{us} \qquad (2)$$

where us, $m2$, $m3$ and w respectively represent the CS of the 3D US image, marker $m2$, marker $m3$ and the tracking system. $^{m3}T_{us}$ is obtained by rigid registration between the US image and the phantom's CAD model, as explained in method [4].

The accuracy of the US calibration was evaluated by point reconstruction tests, as presented in [4]. we acquired the data of the stylus tip at 5 different positions and the root mean square (RMS) error was 0.92 mm.

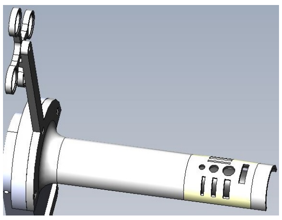

Figure 2: *CAD model of calibration phantom for our US probe.*

4 Endoscope Tracking

Before using the 3D endoscopic camera, it has to be calibrated to find the camera projection matrix. The calibration is achieved by a chessboard-based stereo camera calibration method proposed in [7] which is implemented in OpenCV library [8].

Hand-eye calibration method proposed in [3] is implemented to obtain the transformation $^{m1}T_c$. Fig3 (a) illustrates the data acquisition for applying hand-eye calibration method proposed in [3]. The transformation $^wT_{m1}$, $^wT_{m4}$ and $^cT_{ch}$ in 17 different positions are saved. The data is used in method [3] to estimate the transformation $^{m1}T_c$ and $^{m4}T_{ch}$. The obtained $^{m1}\hat{T}_c$ was evaluated as shown in Fig3 (b): the green circle is the coordinates of a fiducial's contour projected on the endoscopic view by $^{m1}\hat{T}_c$. The distance between the green circle and the fiducial's contour in the endoscopic view was computed. The RMS of distances along 72 radial directions was 0.32 mm for the left camera and 0.44 mm for the right camera.

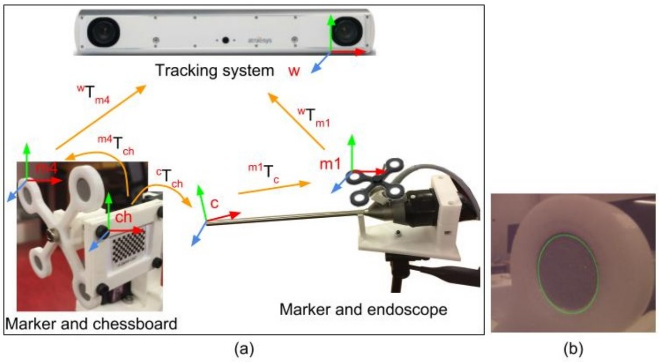

Figure 3: *(a) Hand-eye calibration for 3D endoscopic camera; (b) using obtained $^{m1}\hat{T}_c$ to project the coordinates of a fiducial's contour on the endoscopic view in green color.*

5 Result and Conclusion

The proposed framework was evaluated by localizing a hidden target set inside a soft tissue phantom (Fig.4 (a)). An US imaging was performed on the hollowed silicon phantom and the hidden target was manually segmented on this data to generate the virtual model. Our AR framework presented the virtual information to the user (Fig.4 (b)), then the user cut the phantom according to the augmented view (Fig.4 (c)). We found that the hidden target was well resected from the soft tissue phantom.

In conclusion, we presented an US-based AR guidance system with high accuracy in the design and each calibration step. The framework successfully localized a hidden target from a soft tissue phantom.

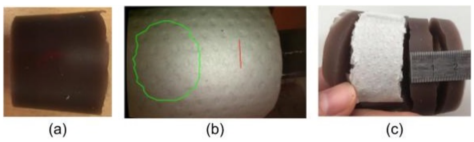

Figure 4: *(a) soft tissue phantom, (b) AR view showing the hidden target (green) and resection margin (red) , (c) scalpel cut following the augmented view.*

Acknowledgement

This work was supported in part by the French ANR within the Investissements d'Avenir Program (Labex CAMI, ANR-11-LABX0004, Labex NUMEV, ANR-10-LABX-20, and the Equipex ROBOTEX, ANR-10-EQPX-44-01) and by the Region Bretagne.

References

[1] Fuchs, H., et al. (1998). Augmented reality visualization for laparoscopic surgery. *International Conference on Medical Image Computing and Computer-Assisted Intervention. Springer Berlin Heidelberg*, 934-943.

[2] Sauer, F., et al. (2001). Augmented reality visualization of ultrasound images: system description, calibration and features. *Augmented Reality. Proceedings. IEEE and ACM International Symposium on. IEEE*, 30-39.

[3] Tsai R. Y. and Lenz R. K. (1998). Real time versatile robotics hand-eye calibration using 3D machine vision. *IEEE International Conference on Robotics and Automation*, 554-561.

[4] Shen, J., et al. (2018). Fast and simple automatic 3D ultrasound probe calibration based on 3D printed phantom and an untracked marker. *40th Annual International Conference of the IEEE Engineering in Medicine and Biology Society (EMBC)*, 878-882.

[5] Lange, T., et al. (2011). Automatic calibration of 3D ultrasound probes. *Bildverarbeitung fr die Medizin. Springer Berlin Heidelberg*, 169-173.

[6] Lasso, A., et al. (2014). PLUS: open-source toolkit for ultrasound-guided intervention systems. *IEEE Transactions on Biomedical Engineering*, 61.10: 2527-2537.

[7] Zhang, Z., et al. (2000). A Flexible New Technique for Camera Calibration. *IEEE Transactions on Pattern Analysis and Machine Intelligence* 22(11):1330-1334.

[8] Bradski, G., et al. (2008). Learning OpenCV: Computer vision with the OpenCV library. *O'Reilly Media, Inc.*

3D landmark detection for augmented reality based otologic procedures

Raabid HUSSAIN, Caroline GUIGOU, Kibrom Berihu GIRUM, Alain LALANDE and Alexis BOZORG GRAYELI
ImViA Laboratory, Université de Bourgogne Franche-Comté, 21000 Dijon, France
Tel : +33 (0)6 95 96 55 40
Contact: raabid.hussain@u-bourgogne.fr

Ear consists of the smallest bones in the human body and does not contain significant amount of distinct landmark points that may be used to register a preoperative CT-scan with the surgical video in an augmented reality framework. Learning based algorithms may be used to help the surgeons to identify landmark points. This paper presents a convolutional neural network approach to landmark detection in preoperative ear CT images and then discusses an augmented reality system that can be used to visualize the cochlear axis on an otologic surgical video.

1 Introduction

Augmented reality (AR) has been widely accepted and applied in different surgical domains like orthopedics, hepatobiliary and pancreatic systems. However, owing to minuscule operative space, limited field of view and complex instrument trajectory, AR has not been widely accepted for otologic procedures. Otologic structures constitute some of the smallest structures in the human body and their handlings require submillimetric precision and expert knowledge of intra and inter anatomic relations as critical nerves and vessels are in close proximity.

Image registration is one of the critical processes in an AR system. In otology, preoperative computed tomography (CT) is particularly helpful as the ear is composed of mostly rigid bony structures. Precise identification of anatomical landmarks for registration is often difficult and time consuming as the points are not well defined. Due to low number of prominent features between preoperative CT reconstructions and endoscopic videos, different studies have used fiducial markers to register the pre and intra-operative images [1, 2].

This study aims at simultaneously determining locations of multiple anatomical landmarks in preoperative CT-scan using a learning based approach. The detected landmarks may then be used to register CT with microscopic images. Typical learning models employ Gaussian heat maps to optimally determine the landmark position [3]. However, since the distance between each landmark is very small, this is not a viable option in this scenario. Moreover, state-of-the-art learning architectures often require manual fine-tuning of meta-parameters which often leads to loss of important information. This study proposes and evaluates the performance of a convolutional neural network (CNN) for middle and inner ear landmark detection without standardizing the meta-parameters and tests them on an AR scenario to infer the cochlear axis.

2 Methodology

2.1 Dataset

We used a dataset of 25 patients (age range: 15-77 years) comprising of 40 ear CTs (17 right and 23 left ears) acquired from different scanners. The pixel resolutions of the acquired CT scans ranged from 0.156x0.156x0.100 mm^3 to 0.292x0.292x0.625 mm^3. The x-y image size was the same for all the images: 512 x 512 while the z image size ranged from 92 to 876. Locations of seven anatomical landmarks were identified in all the scans by an expert surgeon:

round window niche, tip of the incus, umbo and short process of malleus, pyramid, cochlear apex and base.

2.2 Landmark detection

To homogenize the data, the left ear CTs were flipped to resemble the right ear CTs. Due to memory limitations, the surgeon was asked to crop a 200x200x100 region of interest from the original CT data that contained the middle and inner ear contents. The region of interest was passed through a convolutional neural network depicted in Figure 1. All layers had 'elu' activations except the final layer which had linear activation. The output layer had 21 units comprising of x, y and z coordinates of each landmark. The training was carried out for 3500 epochs with a batch size of 5, using Adam optimizer with a learning rate of 0.0005, and mean squared logarithmic error as the loss function. The architecture was implemented on a computer with dedicated GPU (NVIDIA TITAN X, 12 GB RAM processor) using Keras and Tensorflow libraries. The network was trained from scratch and assessed using 5 fold cross validation approach.

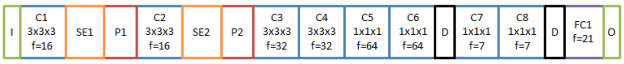

Figure 1: CNN for landmark detection. I=Input layer, C=Convolutional layer, SE=Squeeze and excitation block [4], P=Max pooling layer, FC=Fully-connected layer, D=Dropout with a rate of 0.2, O= Output layer, f=number of filters.

2.3 AR system

An AR system was developed to test the output of the landmark detection step. Cochlear base point was used as a test landmark as it is obscured in microscopic view. Remaining six landmarks were used to register the preoperative CT with the real-time microscopic video. The surgeon was asked to select their corresponding points in the initial microscope image. Fundamental matrix of the microscope camera (determined through the 2D points in microscope image and their respective 3D coordinates in CT image) was used to register the two information, followed by the use of a SURF based feature matching to track the motion of the microscope (similar system as used in [5]). The cochlear axis (defined by cochlear apex and base points) was drawn onto the microscopic video for the surgeon to have more insight about the inner ear. The system was tested on a phantom resin model of the temporal bone with the tympanic membrane removed.

3 Results

The landmark detection on CT-scan yielded an average error of 0.88 ± 0.27 mm (mean absolute distance between position of the detected landmark and its location as indicated by surgeon). Individual errors for each landmark are listed in Table 1.

Table 1: Landmark detection process accuracy. R=Round window niche, I=Incus tip, U=Umbo of malleus, S=Short process of malleus, P=Pyramid tip, A=Cochlear apex, B=Cochlear base

	R	**I**	**U**	**S**	**P**	**A**	**B**
Error (mm)	0.82 ± 0.36	0.71 ± 0.22	0.88 ± 0.26	0.92 ± 0.31	0.89 ± 0.27	0.93 ± 0.16	1.05 ± 0.31

The AR system is displayed in Figure 2. An ENT expert verified that the position of the cochlear axis was indeed in close proximity to where the axis was expected. The system maintained correspondence throughout the experimental time of 2 minutes.

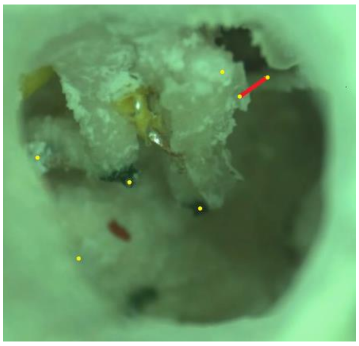

Figure 2: Augmented reality display. The cochlear axis is shown with a red line and the landmark points are represented by yellow dots.

4 Conclusion

This paper presented a CNN based otologic landmark detection and its potential application in AR based surgery. The AR system showed promising results, compatible with otologic requirements, but also highlighted the need for extending the system to 3D for better visualization and ergonomics.

5 Acknowledgements

The authors would like to thank Oticon Medical, France for their financial support and NVIDIA for donating the TITAN X processor under their GPU grant program.

6 References

[1] Liu,W.P., Azizian, M., Sorger, J., Taylor, R.H., Reilly, B.K., Cleary, K. and Preciado, D. (2009). Cadaveric feasibility study of da vinci si–assisted cochlear implant with augmented visual navigation for otologic surgery. *JAMA Otolaryngol. Head Neck Surg.*, 140(3):208-214.

[2] Hussain, R., Lalande, A., Marroquin, R., Girum, K.B., Guigou, C. and Bozorg-Grayeli, A. (2018). Real-Time Augmented Reality for Ear Surgery. *International Conference on Medical Image Computing and Computer Assisted Intervention*, 324-331.

[3] Payer, C., Štern, D., Bischof, H. and Urschler, M. (2016). Regressing heatmaps for multiple landmark localization using CNNs. International Conference on Medical Image Computing and Computer-Assisted Intervention, 230-238.

[4] Hu, J., Shen, L., and Sun, G. (2018). Squeeze-and-excitation networks. *IEEE conference on computer vision and pattern recognition*, 7132-7141.

[5] Marroquin, R., Lalande, A., Hussain, R., Guigou, C. and Bozorg-Grayeli, A. (2018). Augmented reality of the middle ear combining otoendoscopy and temporal bone computed tomography. *Otol. Neurotol.*, 39(8):931-939.

Fusion of X-Ray and patient specific model to assist cardiac resynchronisation therapy

Nicolas COURTIAL, Antoine SIMON, Sophie BRUGE, Mathieu LEDERLIN, Erwan DONAL, Christophe LECLERCQ, Mireille GARREAU

Univ Rennes, CHU Rennes, Inserm, LTSI – UMR 1099, F-35000 Rennes, France
Contact: nicolas.courtial@univ-rennes1.fr

Cardiac Resynchronisation Therapy is widely used to treat heart electromechanical asynchrony. Depending on studies, the rate of success of this procedure is 60-70%. The left ventricle probes position is considered to be a key point to improve this ratio. This work aims to fuse a patient specific multimodal model and the X-Ray sequences acquired during the procedure to assist this probe implantation. We focused here on the projection matrix between the 3D model and the 2D X-Ray sequences. The presented method has been tested retrospectively on 5 patients.

1 Introduction

Cardiac resynchronisation therapy (CRT) is a therapy aiming to cure symptoms of drug resistant cardiac contraction asynchrony. Introduced in the early 1990's in France, it consists into placing three stimulation probes: on the right atria (RA) and the right ventricle (RV) epicardium, and one on the left ventricle (LV) epicardium through the coronary veins. It is now a therapy widely used[1]. However, 30-40% of the patients are non responders. Three main leads are explored to improve this rate: the patient selection, the stimulator programming, and the probes position.

It has been shown that the LV probe position against LV's tissular and mechanical properties has a great impact on CRT success[2]. Our team conducted works to exploit multimodality during planning step for selecting the best LV pacing site[3, 4]. However, intra-operative complications can lead to a change of strategy, due to difficult site access for example. This is why, bringing these planning informations to the CRT's procedure room is of major interest.

Propositions have been made to fuse X-Ray images and planning descriptors [5, 6]. We propose here an automatic X-Ray and patient specific multimodal model fusion, relying on anatomical informations. Computed tomography (CT), as the highest spatially resolved modality, is used to define this anatomical reference. Methods are presented in section 2, evaluation in section 3, and conclusion and perspectives in section 4.

2 Methods

The model, obtained from CT, contains left heart cavity segmented using the convolutional neural network in [7], and coronary veins, defined by tubes of chosen diameter along manually defined control points.

The workflow is presented on figure 1. Heart's dynamic is assessed by tracking the RV and RA probes on X-Ray sequences (2.1). Using veins segmentation centrelines on X-Ray injection sequence (2.2), the projection matrix is initialized (2.3). On other X-Ray sequences, the drift is compensated (2.4). Finally, the integration in the clinical environment is presented in 2.5.

2.1 Probes Tracking

RA and RV probes are implanted before LV's. They are tracked on X-Ray sequences for two purposes: heart's dynamic assessment, and for drift compensation. The tracking is performed using an adaboost classifier[8], trained on cropped probes' haar wavelets. Heart's dynamic is estimated by the two probes relative distance: the local minima are considered to be telesystoles, and local maxima to be telediastoles.

2.2 Veins Segmentation

A median filter followed by a CLAHE filter is applied on input frames as a pre processing. Then the top-hat proposed in [9] is applied to magnify veins. Pixel values inferior to a threshold T, modifiable online, are kept.

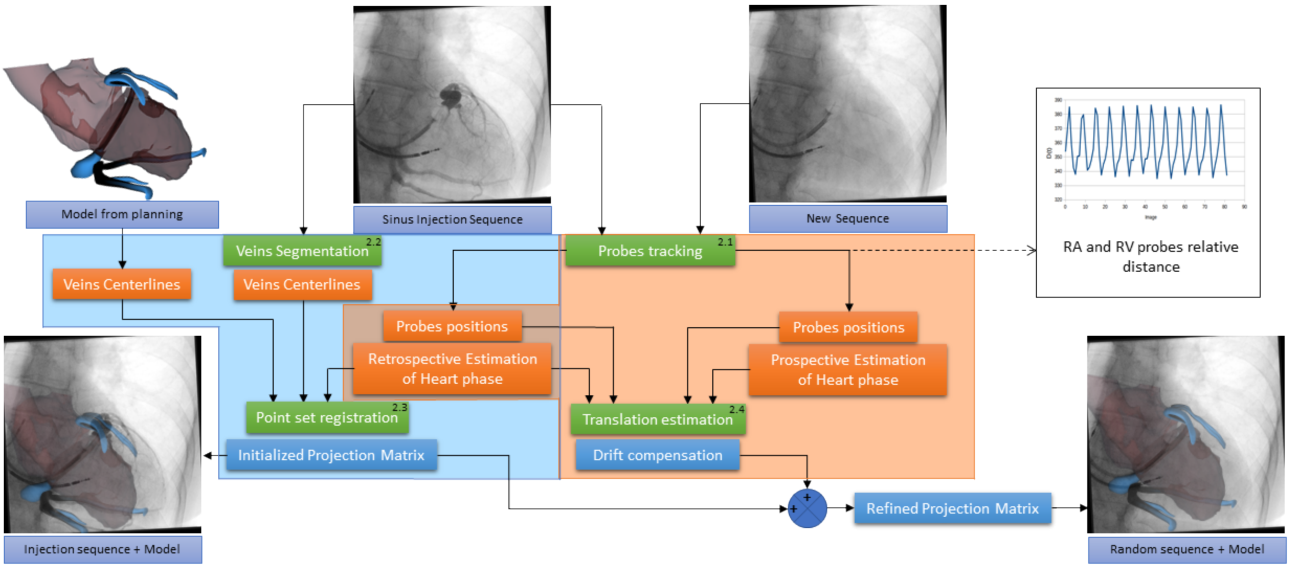

Figure 1: *Workflow presentation*

Morphological opening and closing are then applied to clean the resulting structures. Connected regions counting more than 400 pixels correspond to the detected veins. The result is then skeletonized, providing veins centrelines.

2.3 Projection Matrix Initialisation

The CT is segmented at a specific cardiac phase. The X-Ray image chosen for the registration is the one, thanks to the probes tracking, coming from a phase close to the CT one, with the largest skeleton. The projection matrix is considered to be:

$$P_{tot} = P_{C-Arm} \circ Trans_{Mod \to Room}$$

where P_{C-Arm} is the X-Ray acquisition projection, and $Trans_{Mod \to Room}$ is the rigid transform between the model and the room referential. P_{C-Arm} is deduced from the C-Arm position informations, such as cranial/caudal orientations, available in DICOM tags group 0018. Many methods have been proposed for 3D/2D registration[10]. Here, we rely on the veins centrelines, in a point set registration, using an iterative closest point method[11], the sum squared difference as a metric, and the Levenberg-Marquardt algorithm to solve the minimization problem. The transform is initialized by aligning the 3D barycentre projection on the 2D barycentre.

2.4 Drift compensation

The drift is considered to be translation only. The probes positions on the current frame are aligned with the probes coming from the injection sequence at the same phase. The phase estimation requiring at least 3 frames, this compensation is performed from the fourth frame of the sequence only.

2.5 Implementation

The C-Arm devices in CHU Pontchaillou Rennes don't have any video output, preventing the clinician from having live X-Ray sequences augmented with the model. To solve this issue, a video splitter adaptor has been installed on the computer dedicated to the C-Arm, and the doubled output connected to an acquisition card. It's then connected to a laptop set on a mobile cart, running our software. It is operated by an engineer. However, grabbing the frames only means we can't access DICOM fields required forP_{C-Arm} estimation. So these geometrical parameters are manually entered into our system.

3 Evaluation

A simulated environment has been developed, replacing the C-arm by a computer reading sequences coming from previous CRT procedures. Its video output is connected to the laptop, as in 2.5. First, the injection sequence is read, initializing the 2D/3D rigid registration between the model and the X-Ray images. The other sequences are then read. At this stage, the results are assessed visually, drift compensation by overlaying the reference sequence image on the current frame. In all 5 test cases, results are satisfying in terms of precision, meaning the possible paths trough veins can be differentiated.

4 Conclusion

This work validates on test cases the proposed tool. It shows the feasibility of such approach, and its compatibility in terms of procedure's constraints, regarding clinical time and interactions. We aim now to use this software prospectivelyand to evaluate its impact on procedure in terms of efficacy and patients outcomes.

References

[1] Jaffe et al., (2014), "Cardiac resynchronization therapy: history, present status, and future directions.," *The Ochsner journal*, vol. 14, no. 4, pp. 596–607.

[2] Bilchick et al., (2014), "Impact of mechanical activation, scar, and electrical timing on cardiac resynchronization therapy response and clinical outcomes," *Journal of the American College of Cardiology*, vol. 63, no. 16, pp. 1657–1666.

[3] Tavard et al., (2014), "Multimodal registration and data fusion for cardiac resynchronization therapy optimization," *IEEE Transactions on Medical Imaging*, vol. 33, no. 6, pp. 1363–1372.

[4] Betancur et al., (2016), "Synchronization and Registration of Cine Magnetic Resonance and Dynamic Computed Tomography Images of the Heart," *IEEE Journal of Biomedical and Health Informatics*, vol. 20, no. 5, pp. 1369–1376.

[5] Ma et al., (2012), "An integrated platform for image-guided cardiac resynchronization therapy," *Physics in Medicine and Biology*, vol. 57, pp. 2953–2968.

[6] Leyva et al., (2011), "Cardiac resynchronization therapy guided by late gadolinium-enhancement cardiovascular magnetic resonance," *Journal of Cardiovascular Magnetic Resonance*, vol. 13, no. 1, pp. 29.

[7] Dormer et al., (2018), "Heart Chamber Segmentation from CT Using Convolutional Neural Networks," *Proc.SPIE*, vol. 10578, pp. 10578 – 10578 – 6.

[8] Schapire Freund, (1996), "Game theory, on-line prediction and boosting," *Proceedings ofthe Ninth Annual Conference on Computational Learning Theory*, pp. 325–332.

[9] Bai et al., (2012), "Image enhancement using multi scale image features extracted by top-hat transform," *Optics & Laser Technology*, vol. 44, no. 2, pp. 328–336.

[10] Markelj et al., (2012), "A review of 3D/2D registration methods for image-guided interventions," *Medical Image Analysis*, vol. 16, no. 3, pp. 642–661.

[11] Bellekens et al., (2014), "A Survey of Rigid 3D Pointcloud Registration Algorithms," *AMBIENT 2014, The Fourth International Conference on Ambient Computing, Applications, Services and Technologies*, pp. 8–13.

X-ray free breach detection in robot-assisted spine surgery with real-time conductivity sensing

Jimmy DA SILVA(1,2)*, Florian RICHER*(2)*, Valentin KERSPERN*(1)*, Thibault CHANDANSON*(1) *and Guillaume MOREL*(2)

[1]*SpineGuard,* [2]*Institut des Systèmes Intelligents et de Robotique (ISIR)*
Contact: jimmy.dasilva@spineguard.com

Robot-assisted spine surgery still requires the use of fluoroscopy or CT scans for safety purposes during pedicle screws insertion. This paper reports a proof of concept verified by *in vivo* experiments showing that a robotic arm holding a local conductivity sensor during vertebrae drilling can avoid vertebral breach without radiologic technologies.

1 Introduction

Many spine surgical procedures require the surgeon to insert screws in vertebral pedicles for spinal fusion. Misplacement of these screws can induce many complications due to their proximity to critical neural or vascular elements (spinal cord, nerves, aorta) [1].

Free handed placement has resulted in relatively high inaccuracy, and thus a high percentage of surgeries leading to further complications. To try to improve precision of this surgery, new medical robots and tools emerged from the market in the last few years to assist surgeons [2], such as SpineAssist [3] from Mazor, ROSA [4] from Zimmer Biomet, iSYS 1 [5] from Interventional Systems.

These solutions mostly rely on CT or fluoroscopy scans to be taken at specific moments of the procedure for verification. But nothing alerts the surgeon in real-time of a bad insertion.

This paper reports a proof of concept, verified by *in vivo* experiments, showing that a robotic arm holding an electrical conductivity sensor during vertebrae drilling can avoid vertebral breach, thus improve the safety of the patient.

2 Material and methods

The experimental setup is a combination of the DSG® technology developed by SpineGuard, a 7 DOFs robot arm WAM® sold by Barrett Technology, and a motor.

2.1 Dynamic Surgical Guidance® (DSG)

The DSG® technology [6, 7] is a bipolar sensor that pulses current flow at the tip of its probe. With this tool, the surgeon can differentiate between soft and hard tissue thanks to its local electrical conductivity sensor and be alerted prior to an imminent cortical breach during pedicle preparation.

The PediGuard®, and its DSG® technology, informs the surgical team in real time of the incoming tissue type. This is achieved by changes in the pitch and cadence of an audio signal and a flashing LED light.

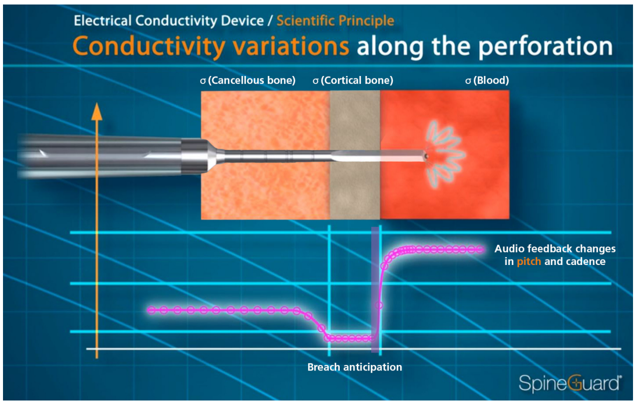

Figure 1: *DSG technology principle*

During our experiments, the conductivity signal measured at the tip of the drill bit is transferred wirelessly to the robot controller and then processed to detect the different bone phases: spongious (soft) bone, cortical (hard) bone, blood (breach).

The processing algorithm of the signal $s(t)$ is the following: At all time, the global signal's minimum s_{min} is saved. **Cortical:** A cortical bone is detected when $s(t)$ gets below a configuration variable s_1. **Breach anticipation:** A breach alert is sent when, in a cortical phase, $s(t) > s_2 = s_{min} + \Delta s$.

2.2 Robotic assistant

At the beginning of the procedure, the surgeon can put the arm in a gravity compensation mode while pressing on a pedal to correct the entry point and the drilling axis. A simple click on a GUI starts the drilling algorithm at a constant speed v_{des} shown in Fig.2

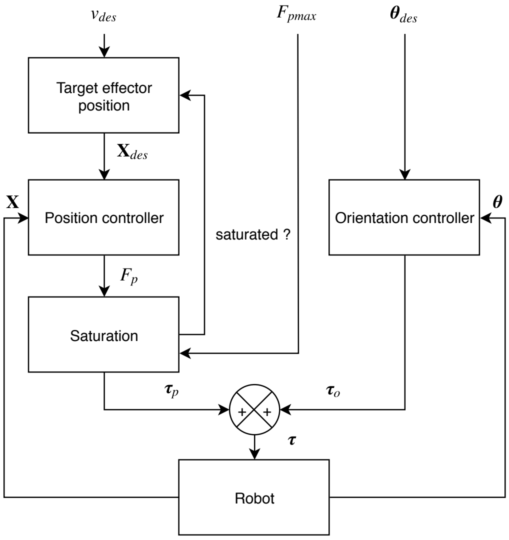

Figure 2: *Control scheme*

When the drilling starts, an orientation controller and a position controller are initialized with the initial orientation $\boldsymbol{\theta}_{ini}$ and position $\mathbf{X}_{ini}$. At all time the desired orientation $\boldsymbol{\theta}_{des}$ equals $\boldsymbol{\theta}_{ini}$ to keep the same tool axis $\mathbf{z}_{ini}$. The desired position $\mathbf{X}_{des}$ is just incrementally increased with the speed variable $\mathbf{X}_{des} = \mathbf{X}_{des} + v_{des} * \Delta t * \mathbf{z}_{ini}$, where Δt is the control period. But if the resulting control force norm $||\mathbf{F}_p||$ reaches saturation F_{pmax}, then $\mathbf{X}_{des} = \mathbf{X}_{des}$.

The desired orientation and position are controlled with two independent PD controllers with the corresponding gains (K_{po}, K_{do}) and (K_{pp}, K_{dp}).

3 Experimental results

To validate the above experimental setup, *in vivo* experiments have been performed on pigs with veterinary surgeons.

The DSG instrument was attached to a motor rotating at 300 rpm, positioned along the 7^{th} axis of the WAM. The practician was asked to move the robot arm so that the drill bit could perforate the spinous process of the vertebra, then click on the GUI to start the drilling.

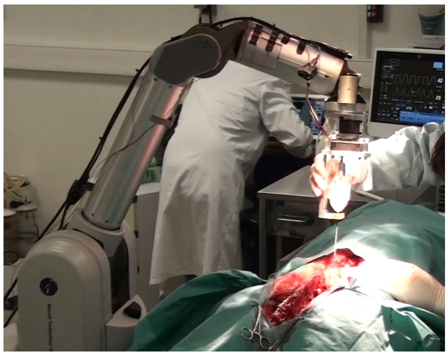

Figure 3: *Experimental setup*

The curve of the DSG signal in Fig.4 shows the expected signature: high signal at the entrance, then stabilization in the spongious phase, decrease in the cortical bone around s_1, followed by a fast rise stopped to s_2.

The force and position curves clearly show oscillations corresponding to the pig's breathing.

The current setup permitted to stop the drilling right before breaching out.

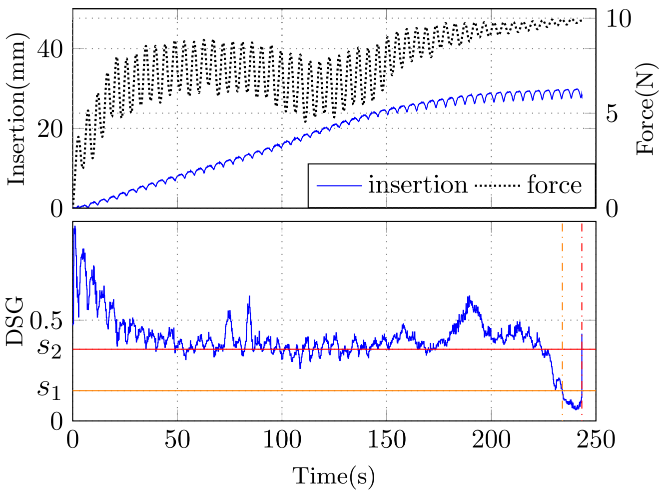

Figure 4: *Robot and DSG signals during an experiment*
$K_{po} = 18, K_{do} = 0.087,\ K_{pp} = 5000, K_{dp} = 60$
$\Delta t = 2ms,\ v_{des} = 0.2mm.s^{-1},\ s1 = 0.15,\ \Delta s = 0.3$

4 Conclusion

An innovative system for radiation-free breach anticipation during spine surgery has been presented. It uses a measurement of the local conductivity to determine if a breach out of the bone is imminent.

The *in vivo* experiments were successfully performed but further improvements can be considered to increase robustness and accuracy. For instance, the values of variables s_1 and Δs might not work on every specimens. A better signal processing algorithm needs to be defined to eliminate the tuning of these parameters and allow the recognition of a conductivity change pattern.

The DSG technology could be used in many bone surgeries as a safety sensor to reduce the use of x-rays.

References

[1] J. E. Lonstein, F. Denis, J. H. Perra, M. R. Pinto, M. D. Smith, and R. B. Winter, "Complications associated with pedicle screws," *JBJS*, vol. 81, no. 11, pp. 1519–1528, 1999.

[2] F. Shweikeh, J. P. Amadio, M. Arnell, Z. R. Barnard, T. T. Kim, J. P. Johnson, and D. Drazin, "Robotics and the spine: a review of current and ongoing applications," *Neurosurgical focus*, vol. 36, no. 3, p. E10, 2014.

[3] A. Bertelsen, J. Melo, E. Sánchez, and D. Borro, "A review of surgical robots for spinal interventions," *The International Journal of Medical Robotics and Computer Assisted Surgery*, vol. 9, no. 4, pp. 407–422, 2013.

[4] M. Lefranc and J. Peltier, "Evaluation of the rosa™ spine robot for minimally invasive surgical procedures," *Expert review of medical devices*, vol. 13, no. 10, pp. 899–906, 2016.

[5] J. Kettenbach, L. Kara, G. Toporek, M. Fuerst, and G. Kronreif, "A robotic needle-positioning and guidance system for ct-guided puncture: Ex vivo results," *Minimally invasive therapy & allied technologies*, vol. 23, no. 5, pp. 271–278, 2014.

[6] C. Bolger, M. O. Kelleher, L. McEvoy, M. Brayda-Bruno, A. Kaelin, J.-Y. Lazennec, J.-C. Le Huec, C. Logroscino, P. Mata, P. Moreta, *et al.*, "Electrical conductivity measurement: a new technique to detect iatrogenic initial pedicle perforation," *European Spine Journal*, vol. 16, no. 11, pp. 1919–1924, 2007.

[7] O. Suess and M. Schomacher, "Control of Pedicle Screw Placement with an Electrical Conductivity Measurement Device: Initial Evaluation in the Thoracic and Lumbar Spine," *Advances in Medicine*, 2016.

Toward a design method for tensegrity-based medical robots

Jérémy BEGEY[1,2], Marc VEDRINES[1], Nicolas ANDREFF[2], Pierre RENAUD[1]

[1]ICube, University of Strasbourg, CNRS, INSA Strasbourg
IRCAD, 1 Place de l'Hôpital, 67091 Strasbourg, France - Tel : +33 (0)3 88 11 91 03
[2]Femto-ST, University of Franche-Comté, CNRS
Contact: jeremy.begey@etu.unistra.fr

Medical robots must offer high level of safety for human-robot interaction. Tensegrity-based robots can interestingly provide compliance for that purpose. Their design remains however challenging, without specific design methods. In this paper, a design approach for tensegrity-based robots is introduced with illustration in the context of medical applications requiring a remote center of motion.

1 Introduction

Medical robot safety can be ensured by restricting its workspace to the medical need, with for instance remote center of motion (RCM) property to respect insertion of surgical tools in the human body. Robot-patient contacts are at the same time needed, so safety of these interactions must be in addition addressed. Force-controlled manipulators [1] and use of compliant actuators [2] have been often considered for this reason. Obtaining a large workspace with significant load as sometimes needed [3, 4] is however difficult. One promising way to solve this issue is to rely on tensegrity mechanisms, as suggested in [5].

Tensegrities are self-stressed structures composed of compressed elements, *i.e.* bars, linked by a network of tensile elements, *e.g.* cables or springs. In addition to their high resistance, these structures are deployable and large workspaces with respect to their size can then be obtained. When actuated, tensegrities are called tensegrity mechanisms. If elastic elements are used [6], these mechanisms can be compliant. Finally, thanks to the obtained compliance and the self-stress property, adaptable stiffness can be achieved.

The design of tensegrity-based medical robots is still an open issue, without any formalized design method to elaborate the robot architecture. In the following, an approach for the design is thus presented and its use is illustrated with an example.

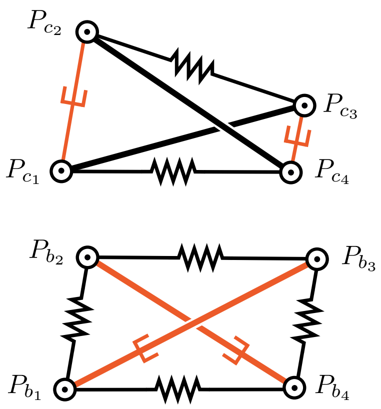

Figure 1: *Illustrations of the cable-actuated SC (top) and the bar-actuated SC (bottom) with the actuated elements in orange.*

2 A design approach for tensegrity-based robots

2.1 Principle

In [7] and [8], design methods are proposed and rely on the assembly of tensegrity modules to create complex passive structures. In [9], a method is proposed to optimize the position and the number of actuators and sensors in a tensegrity mechanism for a given control law, but the selection of the actuation mode is not discussed. Contrarily to conventional mechanisms (*e.g.* serial or parallel), there is then no method, grounded in sound mathematical theory, for designing complex tensegrity mechanisms taking into account the specifity of incorporating actuators in the tensegrity structure. However, some simple mechanisms are now well-known, such as the Snelson Cross (SC) [10], analyzed in the literature. The SC is a X-shaped mechanism which is composed of two bars and four tensile elements. In [11], it was considered as a basic module to design more complex architectures. It was also shown in the literature that the choice of actuation mode and mechanical parameters of the tensile elements can significantly modify the behavior and the performances of a SC. As a first attempt to exhibit a methodology, and by analogy with serial kinematics, where a robot is built by assembling elementary joints, we propose to rely on these observations about SC to build a robot by assembly of several simple SC. In particular, we suggest to use two different SC for this initial work. One is a cable-actuated SC, represented in Fig. 1, top. The position and the orientation of $P_{c_2}P_{c_3}$ with respect to $P_{c_1}P_{c_4}$ can then be adjusted. The other one is a bar-actuated SC, in Fig. 1, bottom. Due to the internal static equilibrium obtained in such SC, $P_{b_2}P_{b_3}$ is constrained to be parallel to $P_{b_1}P_{b_4}$ in the whole workspace. With these 2 SC, it is then possible to design a specific manipulator by assembling multiple SC of the two types in a serial or a parallel way. This is illustrated in the next paragraph.

2.2 Illustration

RCM property is often a desired kinematic property of medical robots. To get the property, a 3-DOF planar manipulator is proposed and represented in Fig. 2. The RCM is ensured by the control of 2 SC, one cable-actuated and the other one bar-actuated. The red SC is cable-actuated with articular coordinates ρ_{c_1} and ρ_{c_2} to control the orientation θ of the end-effector which is a platform mounted on nodes A_4 and B_4. The orange one is bar-actuated with articular coordinates ρ_{b_1} and ρ_{b_2} and it provides 2-DOF motions in the plane for the control of the point G position. For the red SC, a modification of orientation leads to a modification of the end-effector position. The two tensegrity mechanisms have then to be controlled altogether to obtain a RCM. Decoupling the control of both actuated SC allows to perform other motions. For instance, the bar-actuated SC can be used to carry out a positioning task. All non-actuated tensile members are linear springs so the mechanism also offers compliance for patient safety.

The provided architecture allows for planar motions. Spatial trajectories can then be quite easily achieved by mounting the mechanism for instance on a prismatic joint which axis is perpendicular to the mechanism, or by adding another SC.

3 Results and discussion

Verification of the mechanism behavior was performed using a case study of RCM manipulation around the head of a subject as required in transcranial magnetic stimulation [3]. The desired radius R of the RCM is set to 200 mm. The following parameters are then used: $\rho_{b_1}, \rho_{b_2} \in [100, 250]$ mm as the range of actuation of the bars, $\rho_{c_1}, \rho_{c_2} \in [50, 200]$ mm as the actuation range of the cables and $L = 200$ mm the length of the bars linking A_3 to B_4 and A_4 to B_3. The linear springs linking nodes A_1 to A_2 and B_1 to B_2 have a free length of 30 mm, a maximum total length of 200 mm and a stiffness K while all the other ones present a free length of 15 mm, a maximum total length of 100 mm and a stiffness $2K$. The y coordinates of nodes A_1 and B_1 are null while those of nodes A_2 and A_3 and nodes B_2 and B_3 are considered equal.

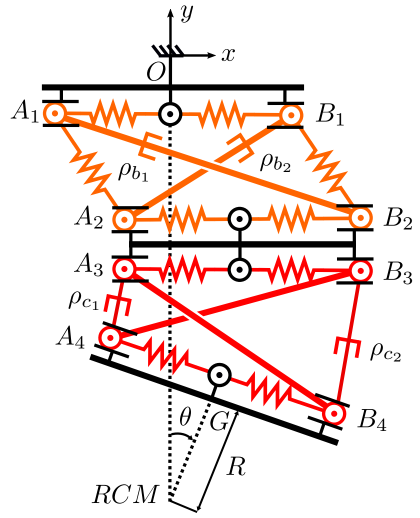

Figure 2: *Proposed 3-DoF planar manipulator composed of two tensegrity mechanisms, the first one being bar-actuated (orange) and the second one being cable-actuated (red).*

Using a numerical analysis, the workspace of the manipulator is computed. This workspace is defined as the set of all reachable end-effector poses ensuring stability and tensioned cables and springs. Selecting the appropriate set of end-effector poses, a RCM is successfully obtained with an angular range of approximately $\pm 23°$ for the desired radius of 200 ± 0.1 mm. Thus, the manipulator can perform the desired motions. Moreover, thanks to modifications of the actuator and spring strokes, the workspace can be easily enlarged if larger movements are needed, or shrunk if boundaries must be ensured for safety reasons.

Next step will be to consider load capability and to evaluate mechanism compliance for the control of such type of robots when human-robot interactions are needed.

Acknowledgement

This work is part of Multiflag projet (ANR-16-CE33-0019) funded by the French National Research Agency (ANR) and supported by Investissements d'Avenir program (Labex CAMI & Equipex ROBOTEX) under references ANR-11-LABX-0004, ANR-10-EQPX-44.

References

[1] L. Villani and J. D. Schutter, "Force Control," in *Springer Handbook of Robotics*. Springer, Berlin, Heidelberg, 2008, pp. 161–185.

[2] R. V. Ham, T. G. Sugar, B. Vanderborght, K. W. Hollander, and D. Lefeber, "Compliant actuator

designs," *IEEE Robotics Automation Magazine*, vol. 16, no. 3, pp. 81–94, Sep. 2009.

[3] L. Zorn, P. Renaud, B. Bayle, L. Goffin, C. Lebosse, M. de Mathelin, and J. Foucher, "Design and Evaluation of a Robotic System for Transcranial Magnetic Stimulation," *IEEE Transactions on Biomedical Engineering*, vol. 59, no. 3, pp. 805–815, Mar. 2012.

[4] F. Carpi and C. Pappone, "Stereotaxis Niobe magnetic navigation system for endocardial catheter ablation and gastrointestinal capsule endoscopy," *Expert Review of Medical Devices*, vol. 6, no. 5, pp. 487–498, Sep. 2009.

[5] Q. Boehler, M. Vedrines, S. Abdelaziz, P. Poignet, and P. Renaud, "Toward an MR-compatible needle holder with adaptive compliance using an active tensegrity mechanism," in *Surgetica: Computer-Assisted Medical Interventions. Scientific problems, tools and clinical applications.*, Dec. 2014.

[6] M. Arsenault, "Développement et analyse de mécanismes de tenségrité." Ph.D. dissertation, Université Laval, 2006.

[7] B. Bickel, S. Mani, B. Thomaszewski, and S. Coros, "Modular Design of Complex Tensegrity Structures," US Patent US20 160 012 156A1, Jan., 2016.

[8] L. Rhode-Barbarigos, H. Jain, P. Kripakaran, and I. F. C. Smith, "Design of tensegrity structures using parametric analysis and stochastic search," *Engineering with Computers*, vol. 26, no. 2, pp. 193–203, Apr. 2010.

[9] F. Li and R. E. Skelton, "Sensor/actuator selection for tensegrity structures," in *Proceedings of the 45th IEEE Conference on Decision and Control*, Dec. 2006, pp. 2332–2337.

[10] K. Snelson, "Continuous tension, discontinuous compression structures," US Patent 3 169 611, 1965.

[11] M. Arsenault and C. M. Gosselin, "Kinematic and static analysis of a planar modular 2-DoF tensegrity mechanism," in *Proceedings 2006 IEEE International Conference on Robotics and Automation, 2006.*, May 2006, pp. 4193–4198.

Bright pill: ingestible biorobot using light to control therapeutic molecule release produced by embarked bacteria

Thomas Soranzo[1], Guillaume Aiche[2], Clément Caffaratti[1], Don K. Martin[1], Philippe Cinquin[1] and Yassine Haddab[2]

[1]University Grenoble Alpes, TIMC-IMAG - UMR 5525, F-38000 Grenoble, France
- Tel : +33 (0)4 76 63 75 58
[2]University of Montpellier, LIRMM - UMR 5506 161 Rue Ada, F-34000 Montpellier, France
- Tel : +33 (0)4 67 41 85 85

Contacts : Thomas.soranzo@univ-grenoble-alpes.fr, Yassine.haddab@lirmm.fr

The Gastro Intestinal Tract (GIT) is a major organ of the human body. It is used as the primary pathway for drug delivery. Therapeutic molecules are ingested, *per os* (by mouth), and depending on their formulation are absorbed in the mouth, the stomach or intestine. The GIT is also the source of many diseases such as metabolic, neurological, cardiovascular and Inflammatory Bowel Diseases (IBD). IBD are characterized by the inflammation of the wall of a part of the digestive tract, linked to a hyperactivity of the digestive immune system. Approximately 1.6 million Americans [1] and 1.8 million Europeans [2] currently have IBD and this number is growing. Existing treatments are limited in efficacy and new alternatives are needed. Here we present the development of a novel therapeutic tool, a biorobot, able to produce and deliver therapeutic molecules for IBD treatment in a controlled manner.

1 – Therapeutic concept

Many environmental factors contribute to IBD pathogenesis (Diet, microbiota…). It results in a decrease of the mucosal layer and an increase in gut permeability. Microorganisms are thus able to penetrate the gut epithelia and trigger a dysregulated immune response that corresponds to inflammation. IBD patients are subject to severe abdominal pain, frequent and sometimes bloody diarrhea and damage to the anal region (fissures, abscesses). Current treatments are disabling, present side effects or lose their efficiency. IL-10 is a natural immunomodulator that decreases inflammation and is thus a promising drug. However, its formulation is difficult and trials to use this molecule have failed. We propose to use gut commensal bacteria (E. coli) to produce and secrete IL-10 directly in the gut. A similar solution has had already been proposed with promising results [3]. We propose to contain the genetically modified organism within a robotic pill with semipermeable walls and regulate therapeutic molecule release using light and a light sensing based control loop (Figure 1).

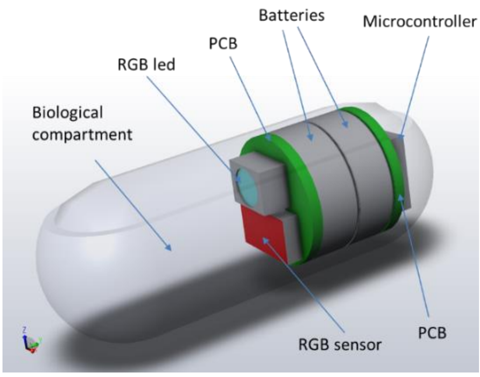

Figure 1: Biorobotic pill concept

2 - Biorobotic pill development

2.1 Biological component

To produce the IL-10 molecule, we introduced the genetic material of IL-10 with a secretion tag into E. coli in order for the bacteria to export the molecule and deliver it into the gut lumen. To control genetic regulation of the bacteria we opted for a combination of genetic and optical methods (Optogenetic)[4]. Shinning blue light on bacteria enables the production and secretion of IL-10. Blue light activation and intensity will be modulated by the robotic part of the pill. To observe the level of production we coupled IL-10 expression with a red fluorescent protein (mRFP1 or mCherry). The robot equipped with the proper sensor will then be able to evaluate production and regulate blue light intensity using a control loop. Using blue light, we were able to induce mRFP1 production which was measured by fluorescence (Figure 2).

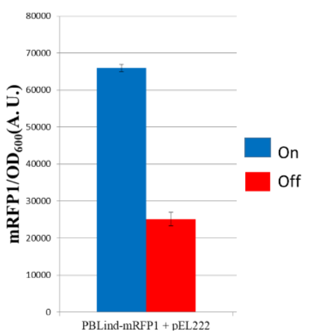

Figure 2: Fluorescence production controlled by blue light

2.2 Robotic design

The regulation system integrates an RGB-C color sensor, a microcontroller and an RGB Led as actuator. The fluorescent phenomenon is based on the shift between the excitation energy and a lower restitution energy due to quantum phenomena (Stokes shift). Thus, fluorescent response wavelength is higher than the wavelength of emission.

2.3 Fluorescence sensor concept

Conventional fluorescence spectrophotometers are able to emit at a single wavelength and detect a different single wavelength (in a fluorescence response spectrum) thanks to monochromators. To detect this color shift, we propose a simpler approach using a simple RGB-C digital color sensor. The principle is based on the detection of a color shift that is not emitted by the source (e.g. Led) but produced by fluorescence only.

2.4 Experimental setup

In order to experiment this concept, we used Nile Red (NR) as red fluorescent sample at different concentrations in ethanol 96% (mimicking IL-10 and mRFP1 coexpression at different durations of exposure to blue light), placed in a 96-well plate. A RGB led (Cree CLY6D-FKC) was placed below a sample well, and a color sensor (Adafruit TCS 34725) was placed above, facing the led. First experiments were performed using only ethanol 96% as reference, a set Nile Red concentration and a twice more concentrated sample. The well plate was then moved manually, using visual landmarks, and clamped to avoid vibrations during measurement. To compensate manual positioning errors each sample was duplicated.
According to NR sample fluorescence spectrum, led and color sensor spectral responsivity, we chose to

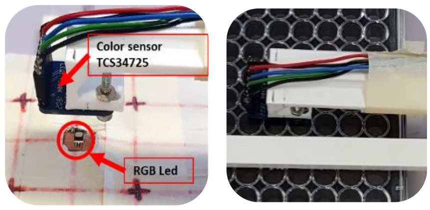

Figure 3: Parts of experimental setup. RGB-C color and RGB led mounted. Well plate set for measurement

use the green led as a source. A part of the green light is absorbed by the sample and another part is re-emitted as red light.
As green light emission was caught by both R,G, B and Clear (unfiltered) cells of the sensor, we could define a reference reading for the R,G,B channels and evaluate the fluorescence produced by NR only. After normalizing the results using the amount of light received on the Clear channel, each filtered component was expressed as a ratio of the clear value. Although evolution is subtle, we were nevertheless able to measure a slight positive evolution consistent with NR increase in concentration.

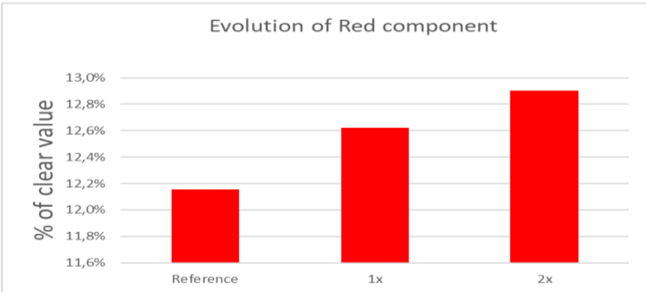

Figure 4: Evolution of red component sensed from green light Nile Red sample excitation

3 – Conclusion and perspectives

Here presented the ongoing development of a novel smart pill. Recent efforts on smart pills [5-7] have underlined the benefit that such devices can offer. To our knowledge only the MIT have associated a robotic capsule and a living organism [8] for diagnostic purposes. Compared to this later device, our work aims to establish a dialogue between the robotic and the biologic component of the pill enabling a complete autonomy of therapeutic molecule release following a set prescription.
Further investigations are ongoing to better identify fluorescence from the absorption phenomenon, better control IL-10 expression and increase yields.

4 – References

[1]http://www.crohnscolitisfoundation.org/assets/pdfs/updatedibdfactbook.pdf

[2] https://www.cregg.org/_MICI/2.html

[3] Huyghebaert N, Vermeire A, Neirynck S, Steidler L, Remaut E, Paul J. Development of an enteric-coated formulation containing freeze-dried , viable recombinant Lactococcus lactis for the ileal mucosal delivery of human interleukin-10. 2005;60:349-359. doi:10.1016/j.ejpb.2005.02.012

[4] Jayaraman P, Devarajan K, Chua TK, Zhang H, Gunawan E, Poh CL. Blue light-mediated transcriptional activation and repression of gene expression in bacteria. Nucleic Acids Res. 2016;44(14):6994-7005. doi:10.1093/nar/gkw548

[5] Söderlind E, Abrahamsson B, Erlandsson F, Wanke C, Iordanov V, Von Corswant C. Validation of the IntelliCap® system as a tool to evaluate extended release profiles in human GI tract using metoprolol as model drug. J Control Release. 2015;217:300-307. doi:10.1016/j.jconrel.2015.09.024

[6] Abramson A, Caffarel-Salvador E, Khang M, et al. An ingestible self-orienting system for oral delivery of macromolecules. Science. 2019;363(6427):611-615. doi:10.1126/science.aau2277

[7] Kong YL, Zou X, Mccandler CA, et al. 3D-Printed Gastric Resident Electronics. Adv Mater. 2019;1800490(1800490):1-11. doi:10.1002/admt.201800490

[8] Mimee M, Nadeau P, Hayward A, et al. An ingestible bacterial-electronic system to monitor gastrointestinal health. Synth Biol. 2018;918(May):915-918.

5 – Acknowledgements

We would like to thank the TheREx team for hosting our biology experiments in their lab and the Dr. Legouellec for the discussions on synthetic biology.

Robust tracking of tissues for flexible endoscopy

Xuan Thao HA, Philippe ZANNE and Florent NAGEOTTE
ICube, UMR 7357, Univ. of Strasbourg, CNRS, Strasbourg, France
Tel : +33 (0)3 88 11 91 29
Contact: Nageotte@unistra.fr

A method is presented for robustly tracking a patch of tissues in endoscopic images and estimate the position of a target. Experiments show that the algorithm is able to track targets in challenging conditions including occlusion of the patch and provide good accuracy.

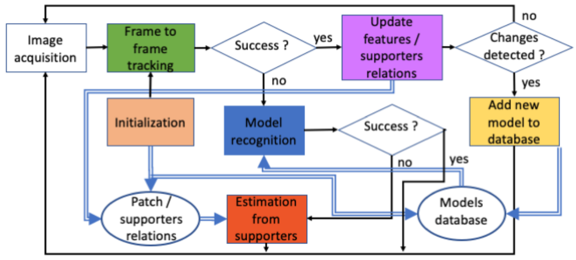

Figure 1: *Overview of the tracking algorithm*

1 Introduction

Tracking patches of tissues in images from flexible endoscopes can be interesting for analyzing motions, for guiding gestures or even for realizing automatic tasks with medical robots [1]. However, images from flexible endoscopes are challenging because of their low quality and resolution. The medical environment involves tissues deformations, large changes of point of view, occlusions and even the target going out of the field of view. For avoiding failure or interruption of robotic tasks such as physiological motion rejection, image tracking should be able to provide consistent positions and scales of the patch in all these cases.

In this work we have developed a tracking algorithm able to handle all the previously mentioned issues. We present the basic of the approach and we report quantitative results in laboratory experiments.

2 Methods

We propose a tracking technique inspired by [2] adapted and completed for flexible endoscopy. The overview of the proposed algorithm is shown in Fig. 1. Here we briefly describe the main steps of the algorithm.

2.1 Initialization

The user initiates the tracking by defining a patch by drawing a contour in the image. and clicking a target (a point of interest).

Several information are extracted from the initial definition of the patch. Histograms of colors of the patch and the environment are computed in the Hue - Saturation color space (HS). in order to estimate the probability of a pixel to belong to the patch given its color. Features to be tracked (GFTT [3]) are extracted from the patch. SURF features [4] are computed from both the patch and the whole image. The SURF features from the patch are put in relation (positions and orientation) with the contours and the target defined by the user and stored as a model in a database. The relative positions of SURF features outside the patch and inside the patch are stored for supporters estimation (see later).

2.2 Tracking methods

Frame to frame tracking (FFT): GFTT features are recursively tracked using the Kanade-Lucas-Tomasi algorithm (KLT). If KLT succeeds, SURF features inside the estimated contour are matched with the current model of the database and all features are used to obtain the new position and scale of the patch. This allows tracking small rigid motions, but this approach is subject to drifts and does not allow to handle large changes of orientations and deformations.

Model recognition (MR): If FFT tracking fails because of detected inconsistencies (see 2.3), a patch recognition process is carried out. SURF are extracted from a search region and matched with SURF features from all the models in the database. The model with the highest number of matched points is selected and becomes the current model. New GFTT features are extracted for subsequent FFT tracking. This process allows dealing with larger displacements as well as deformations.

Estimation from supporters (ES): FFT and MR cannot provide positions when the patch is occluded or outside of the image field of view. For handling these cases, supporting features are used as proposed in [5]. SURF features from the visible part of the image are extracted, matched with the existing supporters list and then used to predict the position of the patch in the image (or outside of the image) on the basis of their previous relative positions.

2.3 Adaptation to changes

For avoiding drifting effects, the quality of tracked GFTT features is checked using affine consistency checks. SURF features matching is followed by a Hough transform in the 4D (position x-y / rotation / scale) space allowing to remove outliers [6]. However, this prevents tracking changes of appearance and deformation. Therefore, a mechanism is used to register new models in the database during tracking. When FFT succeeds but some SURF features inside the patch contour cannot be matched with the model, the SURF features are included in a new model, which is added to the model database. In order to avoid registering features belonging to occluding areas, the color of the window around each feature is analyzed and features with low probability of belonging to the tracked patch are excluded from the new model.

2.4 Target position reconstruction

It can happen that no salient features lie in the neighborhood of the target. Moreover, in the context of surgical procedures deformations should also be handled in order to obtain the contours of the patch and the target with good accuracy. For this purpose we rely on an interpolation scheme based on multi-level B-splines [7]. The input of this process are the matched keypoints with their displacements between the model and the current image. Multi-level B-splines interpolation provides as output the estimated displacement of points of the contours and the target.

3 Experiments and results

The software was developed in C++ with Microsoft Visual Studio and OpenCV, with OpenMP and CUDA library. The program was run under Windows 7 Operating system on a machine with CPU Intel Core i7-5820K (6 cores) and GPU NVIDIA Quadro K620.

In order to assess the accuracy of the algorithm a printed image from an endoscopic procedure was attached to a motorized pan-tilt platform and was moved in all directions during 4min and 30s in front of a gastroscope (images: 25 fps, 640 x 480 pixels). To obtain

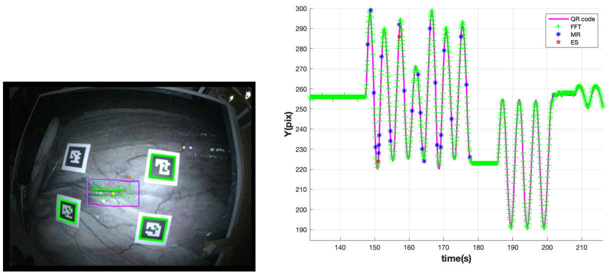

Figure 2: *Tracking of a moving patch with GT provided by QR codes*

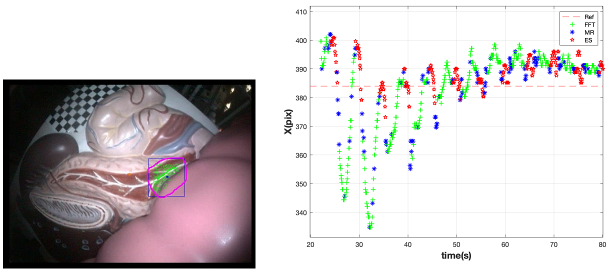

Figure 3: *Tracking of a moving target during a visual servoing task with occlusions*

ground truth, QR codes were printed onto the image and tracked [8] (QR codes were excluded from the tracking algorithm). The patch was approximately 160 × 80 pixels (see Fig. 2) and the target was at the center of the patch. The mean computation times were 54ms, 73ms and 68ms for FFT, MR and ES respectively, allowing to process one frame over two 98% of the time. Ground truth was obtained for 68% of the processed frames, (less robust than the proposed algorithm). FFT was used 3349 times, MR 96 times and ES 7 times in cases where the patch was not recognized, providing accuracies (mean - max error in pixels) of $1.5 - 10$, $1.7 - 6$, $3.4 - 4.7$ respectively. Fig. 2 shows tracking results during fast motions of the environment. ES was triggered a few times due to incorrect matching of the visible features with the model. However, this did not prevent correct continuous tracking.

Another experiment was carried out during the visual servoing of a robotic endoscope onto a target on a fake organ. The video is 1min40s long and features important occlusions. Qualitative results are shown on Fig. 3. FFT, MR and ES were used for 55%, 23% and 22% of the frames respectively. The evolution of the target appears smooth without visible outliers and it was possible to use the obtained information for a 3DOFs visual servoing of the robotic endoscope.

4 Conclusion

Quantitative results obtained on the laboratory setup are very promising. The algorithm was also tested on *in vivo* images acquired during endoluminal surgery and proved capable of tracking targets during long sequences.

References

[1] Ott, L., Nageotte, F., Zanne, P., de Mathelin, M. (2011) Robotic Assistance to flexible endoscopy by physiological motion tracking. *IEEE Transactions on Robotics*, pages 346–359, Volume 27, no.2

[2] Penza, V., Du, X., Stoyanov, D., Forgione, A., Mattos, L. and de Momi, E. (2017). Long Term Safety Area Tracking (LT-SAT) with online failure detection and recovery for robotic minimally invasive surgery. *Medical Image Analysis, 45, pp. 13-23*

[3] Shi, J., Tomasi, C., (1994). Good Features to track. *IEEE CVPR* pp. 593-600.

[4] Bay, H., Tuytelaars, T., Van Gool, L., (2006). SURF: speeded up robust features. *ECCV*. Springer, pp. 404-417.

[5] Grabner, H., Matas, J. and Van Gool, L. (2010). Tracking the invisible: Learning where the object might be. *IEEE Computer Vision and Pattern Recognition* pp. 1285-1292.

[6] Seib, V., Kusenbach, M., Thierfelder, S., Paulus, D., (2012). Object recognition using hough-transform clustering of surf features. *International Workshops on Electrical and Computer Engineering*

[7] Lee, S., Wolberg, G. and Shin S.Y. (2002). Scattered data interpolation with multilevel B-splines. *IEEE Transactions on Visualization and Computer Graphic*, vol.3, no. 3, pp.228-244.

[8] Q. Bonnard et al. (2013) Chilitags: Robust Fiducial Markers for Augmented Reality. http://chili.epfl.ch/software.

5 Acknowledgements

This work was supported by ITMO Cancer in the framework of "Plan Cancer" under the project named ROBOT and by French state funds managed by the ANR within the Investissements d'Avenir program under the ANR-11-LABX-0004 (Labex CAMI).

Investigating the Role of Helical Markers in 3D Catheter Shape Monitoring from 2D Fluoroscopy

Anne En-Tzu YANG and Jérôme SZEWCZYK
Institut des Systèmes Intelligents et de Robotique, Sorbonne Université
CC 173 - 4 Place Jussieu, 75005 Paris, FR - Tel : +33 (0)1 44 27 51 41
Contact: yang@isir.upmc.fr

This work provides preliminary results indicating that helical markers and neural networks can enable efficient monitoring of the 3D shape and orientation of an active catheter from isolated 2D fluoroscopic images.

1 Introduction

Accurate performance of minimally invasive surgeries (MIS) requires intra-operative feedback. For active catheters, particularly, it is necessary to track beyond the tip and include an extended longitudinal section so as to avoid tissue damages by unintended operations of active components along the length.

The present study aims to obtain shape and orientation of active catheters with fluoroscopy, which has been a standard protocol for catheter monitoring[1]. To overcome the limitations of 2D while avoiding the additional computational and financial costs of bi-plane imaging[2], radiopaque markers are introduced.

Publications have shown that band markers aid tip orientation tracking[3] and that helical markers aid curvature sensing[4]. This work trains a shallow neural network (NN) to reconstruct the full-length 3D configuration of an active catheter[5] from projections of designed markers. The system can potentially be generalized beyond fluoroscopy for ultrasound[6][7] or magnetic resonance imaging (MRI)[8].

2 Methods

2.1 Experimental setup and variables

A catheter prototype was made from a torque coil (Fig.1). To assist with tracking, compression springs were attached as radiopaque helices surrounding the coil. An additional copper wire looped around one end of the coil to serve as a reference for base point. Images of the prototype in various shapes and orientations were acquired by Siemens' radiology system, Artis Zeego.

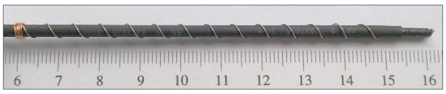

Figure 1: *A prototype of catheter and helical markers (the scale bar is in cm).*

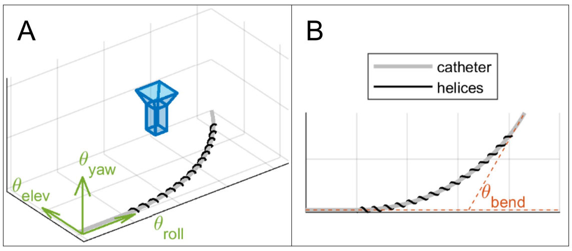

Figure 2: *(A) Three variables for orientation with respect to imaging plane (in blue) and (B) one for shape.*

The orientation of a catheter can be defined by three variables– yaw, roll, and pitch (Fig. 2A). The shape of an active catheter can be approximated by a global bending angle measured between the base and the tip (Fig. 2B). This study focused on two of the variables:

Roll angle θ_{roll} is the angle about the unbent catheter's length. θ_{roll} varied between 0° and 75° in 188 increments automatically by the 20sDR-H 30 protocol on Artis Zeego.

Bending angle θ_{bend} is the difference between angles in the distal and proximal segments. In this work, the catheter was manually deflected into five different θ_{bend}.

There were, therefore, a total of 940 configurations. Note that the variations of yaw and pitch are also crucial and have been part of the work in progress (see 3.2).

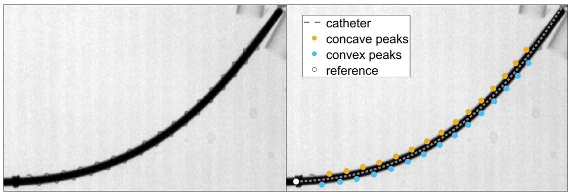

Figure 3: *An example of 2D image (left) and the image overlaid with extracted peaks, catheter shape, and reference point (right).*

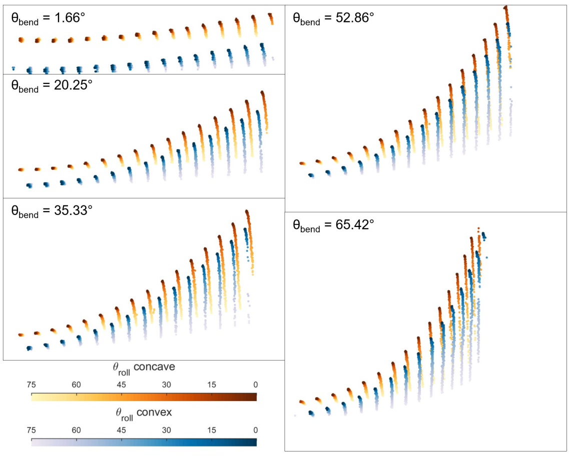

Figure 4: *The 2D trajectories of helical peaks in different roll (θ_{roll}) and bending (θ_{bend}) angles. All subplots share the same horizontal axis limit.*

2.2 Image analysis

All images were post-processed in MATLAB™. Fig. 3 shows an example frame before and after processing. The projected shape of the catheter was approximated as a 3^{rd}-order polynomial. Helical peaks were identified by two methods. The first method found regions of connected pixels and retained those in proper sizes. In each region, the pixel furthest away from the catheter was labeled as a peak. Nevertheless, due to θ_{bend} and projection perspective, not all peaks displayed as closed areas to be identifiable with the first method. The second method, based on the Qhull algorithm[9], searched for points which formed the greatest convex hull around the catheter. After eliminating overlaps and falsely identified peaks by thresholding inter-peak and peak-to-catheter distances, the trajectories of peaks over θ_{roll} are shown in each subplot in Fig. 4 for each θ_{bend}.

3 Results

3.1 Neural network prediction

Each catheter configuration yielded about two dozens of x- and y- of helical peaks. The information of each set of peaks was consolidated into single variables. To uniquely recognize the two catheter configuration variables (θ_{bend} and θ_{roll}), it is expected that a minimum of two predictors are needed.

A two-layer feedforward network was trained with a

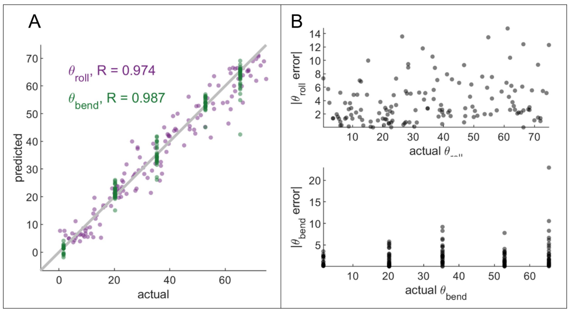

Figure 5: *(A) The correlation of θ_{roll} and θ_{bend} between neural network output (predicted) and ground truth (actual). (B) The absolute errors of θ_{roll} (top) and θ_{bend} (bottom) predictions.*

nonlinear least square fitting algorithm[10]. All data were divided randomly into training (70%), validating (15%), and testing (15%) sets. Different predictors were tested in a number of sessions. The two predictors resulting in the best shape recognition were– d_0 (longitudinal distance between the most proximal marker and the reference point) and $\overline{d_{i1}} - \overline{d_{i2}}$ (difference between concave and convex average inter-peak distances).

The correlations between predicted and actual θ_{bend} and θ_{roll} of the testing set ($n = 141$) are depicted in Fig. 5A. The errors of both variables are plotted in Fig. 5B. Almost all errors are under 15°, and neither of the errors seem to display any trends of variation.

3.2 Discussions

A significant contribution of the present work is the recognition of large θ_{bend} at large θ_{roll} (e.g. bright markers in the fifth subplot in Fig. 4), an ambiguity primarily introduced by θ_{roll}. The markers does not interfere with the incision in cases where the markers are covered with an external layer[5]. It is also worth noting that the present study attempted a framework without regard to the perturbation of the table and the calibration of the projection perspective.

Several aspects still need to be addressed. Improved image quality and processing may resolve the small portion of missing or erroneous peaks in the current results. Moreover, simulation covering a broader variety of possible configurations is expected to robustize neural network performance. Presently, θ_{bend} variation was limited to five distinct values.

As mentioned in 2.1, future work is ongoing to expand the model to include θ_{yaw} and θ_{pitch} variations. Separate simulations supported the validity of θ_{pitch} recognition with the addition of one predictor– coefficient of variation of inter-peak distances. As for θ_{yaw}, parallel to the imaging plane, it is expected to be correlated with the overall x-y slopes.

In summary, to achieve efficient shape and orientation identification of a 3D catheter with single-plane fluoroscopy, the present work demonstrated the potential of neural network and helical markers.

*The authors thank Dr. Pascal Haigron and Mr.

Miguel Castro for their assistance with image acquisition at Centre Hospitalier Universitaire de Rennes. This work was supported by French state funds managed by the ANR within the Investissements d'Avenir programme (Labex CAMI) under reference ANR-11-LABX-0004.

References

[1] C. E. Metz and L. E. Fencil, "Determination of three-dimensional structure in biplane radiography without prior knowledge of the relationship between the two views: Theory," Med. Phys., vol. 16, no. 1, pp. 45–51, 1989.

[2] S. A. M. Baert, E. B. van de Kraats, T. van Walsum, M. A. Viergever, and W. J. Niessen, "Three-dimensional guide-wire reconstruction from biplane image sequences for integrated display in 3-D vasculature," IEEE Transactions on Medical Imaging, vol. 22, no. 10, pp. 1252–1258, Oct. 2003.

[3] S. Hwang and D. Lee, "3D Pose Estimation of Catheter Band Markers based on Single-Plane Fluoroscopy," in 2018 15th International Conference on Ubiquitous Robots (UR), 2018, pp. 723–728.

[4] R. Xu, A. Yurkewich, and R. V. Patel, "Curvature, Torsion, and Force Sensing in Continuum Robots Using Helically Wrapped FBG Sensors," IEEE Robotics and Automation Letters, vol. 1, no. 2, pp. 1052–1059, Jul. 2016.

[5] T. Couture and J. Szewczyk, "Design and Experimental Validation of an Active Catheter for Endovascular Navigation," *Journal of Medical Devices*, vol. 12, no. 1, pp. 011003-011003–12, Nov. 2017.

[6] J. Stoll, H. Ren, and P. E. Dupont, "Passive Markers for Tracking Surgical Instruments in Real-Time 3-D Ultrasound Imaging," IEEE Transactions on Medical Imaging, vol. 31, no. 3, pp. 563–575, Mar. 2012.

[7] J. Guo, C. Shi, and H. Ren, "Ultrasound-Assisted Guidance With Force Cues for Intravascular Interventions," IEEE Transactions on Automation Science and Engineering, vol. 16, no. 1, pp. 253–260, Jan. 2019.

[8] S. Zuehlsdorff et al., "MR coil design for simultaneous tip tracking and curvature delineation of a catheter," Magn. Reson. Med., vol. 52, no. 1, pp. 214–218, Jul. 2004.

[9] C. B. Barber, D. P. Dobkin, D. P. Dobkin, and H. Huhdanpaa, "The Quickhull Algorithm for Convex Hulls," ACM Trans. Math. Softw., vol. 22, no. 4, pp. 469–483, Dec. 1996.

[10] M. T. Hagan and M. B. Menhaj, "Training feed-forward networks with the Marquardt algorithm," IEEE Transactions on Neural Networks, vol. 5, no. 6, pp. 989–993, Nov. 1994.

Localization of brachytherapy seeds in TRUS images using rigid priors and medial forces

Vincent JAOUEN, Julien BERT, Antoine VALERI and Dimitris VISVIKIS
LaTiM-UMR 1101, Inserm, Brest University Hospital, University of Western Britanny, 29200 Brest, France
Contact: vincent.jaouen@inserm.fr

We propose a new semi-automatic strategy for the localization of brachytherapy seeds with transrectal ultrasound imaging. We formulate the problem as a rigid surface-to-image registration, where a geometric model is embedded in an external force field pointing towards the last implanted seed. Considering the seed shape as a prior, we alleviate the need for *a posteriori* filtering among candidate shapes. Robustness to noise is enforced by constraining the model to rigid body motion and by privileging image intensity over higher order information. We present encouraging preliminary results on noisy synthetic images. More advanced validation on physical phantoms and clinical images is ongoing.

1 Introduction

Low-dose rate brachytherapy (LDR-B), one of the key treatment for prostate cancer, consists in inserting radioactive implants through the perineum directly into the prostate. The procedure is generally supervised under transrectal ultrasound (TRUS) guidance [1]. For every seed, potential errors may occur between expected and actual insertion site, advocating the recommendation for dynamic dose recalculation, where the configuration of the remaining seeds would ideally be updated using real time localization feedback [2]. In this context, one of the major difficulties of LDR-B lies in accurately localizing seeds directly from TRUS, a challenging task due to the inherent limitations of this modality [3][4][5].

In this paper, we propose a proof of concept for a seed localization technique based on evolving geometric models. We embed a seed-like cylindrical model in an image-derived force field and constrain its evolution to rigid-body deformation, i.e. we only allow translations and rotations. The force field is computed so that it is oriented towards the medial axis of the nearest seed, providing fast and robust convergence towards the desired target. We successfully validate this concept on synthetic images. Validation on ultrasound imaging using physical phantoms and clinical data is ongoing.

This work was partly supported by the French ANR within the Investissements dAvenir program (Labex CAMI) under reference ANR-11-LABX-0004 (Integrated project CAPRI)

2 Method

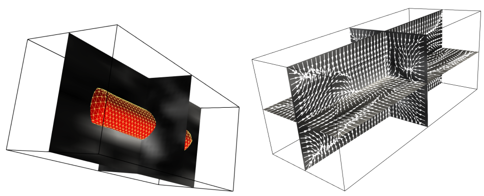

Figure 1: *Search space I_i, initial model S^0 and orthogonal projections of the medial vector field $\mathcal{F}_i$ (see text) for a real clinical case. Vectors are mostly oriented towards the medial axis of the seed.*

The proposed localization workflow is as follows: 1) after each seed s_i is implanted, a cuboidal search space is defined in the vicinity of an initial position marked by the operator, reducing the image to a cropped region I_i (Fig. 1). 2) Then, a triangulated surface model S^t, where t is an artificial time variable, is rigidly evolved under an external force field $\mathcal{F}_i$ associated with s_i, until it reaches steady state around the actual seed location. 3) The seed position is finally communicated to the treatment planning system to recalculate the dose plan accordingly.

One of our main contribution lies in the expression of the vector field $\mathcal{F}_i$ associated with seed s_i. We exploit a side property of external edge fields for deformable models such as Vector Field Convolution fields [6, 7] or gradient vector flow [8]: their ability to point towards the medial axis of objects if the intensity image itself is substituted for the edge map [9]. Rigid motion towards the medial axis can then be used to perform object segmentation, alleviating the need for higher order information (e.g. gradient or Hessian) typically employed in active contours frameworks [10, 11]. Such high order information would be unreliable in TRUS imaging due to excessive noise levels.

A Medial Vector Field [12] guiding the surface model is expressed as:

$$\mathcal{F}_i = I_i * \mathcal{K}, \tag{1}$$

where $*$ represents the convolution operation and:

$$\mathcal{K}(\mathbf{x}) = [K_x(x,y,z), K_y(x,y,z), K_z(x,y,z)] \tag{2}$$

is a vector field kernel (VFK), a vector kernel whose vectors point towards its center with decreasing magnitude [6]. To evolve the seed model, we first compute the motion of the set of free surface vertices $\mathcal{V}_j$ of S^t embedded in the vector field $\mathcal{F}_i$:

$$\mathbf{V}^t = \mathbf{V}^{t-1} + \gamma\mathbf{F}, \tag{3}$$

where $\gamma < 1$ is a small artificial time step, $\mathbf{V}^t$ is the coordinate matrix of vertices $\mathcal{V}_j$ and $\mathbf{F}$ is the force matrix corresponding to values of $\mathcal{F}_i$ interpolated at $\mathcal{V}_j$. We then look for the rotation matrix $\mathbf{R}$ and the translation vector $\mathbf{T}$ closest to $\mathbf{V}^t - \mathbf{V}^{t-1}$ in the $\mathcal{L}_2$ sense:

$$\underset{\mathbf{R}^t,\mathbf{T}^t}{\arg\min} \frac{1}{N_v} \sum_{k=1}^{N_v} ||\mathbf{R}^t \cdot \mathbf{V}_k^{t-1} + \mathbf{T}^t - \mathbf{V}_k^t||^2. \tag{4}$$

The solution of which is provided by singular value decomposition [13]. The rigid evolution of from S^{t-1} to S^t is then expressed as:

$$\mathbf{V}_{\mathcal{R}}^t = \mathbf{V}^{t-1}[\mathbf{R}^t]^T + \mathbf{1}[\mathbf{T}^t]^T \tag{5}$$

where $\mathbf{1}$ is a vector composed only of ones.

The vertices coordinates $\mathcal{V}_j$ of $\mathcal{S}$ are then updated according to (5), and steps (3) to (5) are repeated until the surface converges to the location of seed s_i. The algorithm stops when the maximum displacement between two steps is less than a threshold value ϵ. These steps are performed after each implantation in almost real time, providing estimations of the orientation and localization of the last seed.

3 Results

We are currently at an early stage of the validation. As a proof of concept, we generated a synthetic 3D image showing pseudo seeds (PS) with different orientations, that we corrupted with heavy noise and Gaussian blur (Fig. 1). For each PS, we performed 50 initializations of the model by uniformly drawing initial coordinates in a $25 \times 25 \times 5$ voxels neighborhood window (red square, Fig. 1). Distance (in voxels) between true and estimated barycenters and angular error between the PS and the surface model (obtained through principal component analysis) were used as quantitative metrics [4], and are shown in Fig. 3. Results are encouraging given the low signal-to-noise ratio of the image, with errors of a few voxels and orientation estimations generally less than ten degrees off, with rare failure cases. A physical phantom for ultrasound is also currently studied for which preliminary, unquantified results are presented in Fig. 4. Results on real TRUS images using expert consensus are also considered for a thorough validation of the approach.

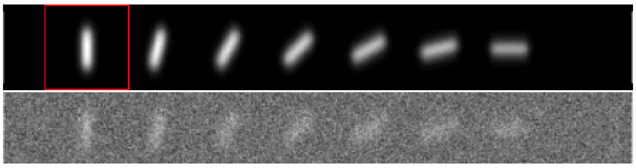

Figure 2: *Axial slice of a synthetic 3D image showing seven seed-like patterns with various orientations. Top: clean image. Bottom: noisy image.*

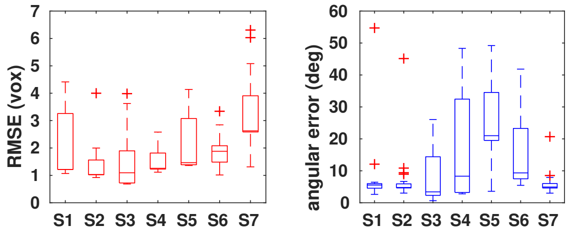

Figure 3: *Barycenter distance and angular error for the 7 pseudo seeds using multiple initializations*

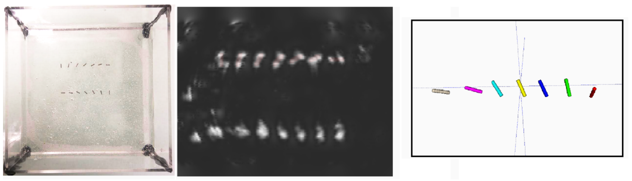

Figure 4: *Left: physical seed phantom. Middle: US image. Right: preliminary unquantified localization results corresponding to the bottom row.*

4 Conclusion

We have presented a proof of concept for a fast semi-automatic seed localization method using rigid geometric models, where the seed shape is incorporated as a prior. Early results on synthetic images support the potential interest of the approach for real time, intraoperative seed localization for dynamic dose estimation.

References

[1] S. Nag, D. Beyer, J. Friedland, P. Grimm, and R. Nath, "American Brachytherapy Society (ABS) recommendations for transperineal permanent brachytherapy of prostate cancer," *International Journal of Radiation Oncology* Biology* Physics*, vol. 44, no. 4, pp. 789–799, 1999.

[2] A. Polo, C. Salembier, J. Venselaar, P. Hoskin, P. group of the GEC ESTRO, *et al.*, "Review of intraoperative imaging and planning techniques in permanent seed prostate brachytherapy," *Radiotherapy and Oncology*, vol. 94, no. 1, pp. 12–23, 2010.

[3] B. H. Han, K. Wallner, G. Merrick, W. Butler, S. Sutlief, and J. Sylvester, "Prostate brachytherapy seed identification on post-implant TRUS images," *Medical physics*, vol. 30, no. 5, pp. 898–900, 2003.

[4] Z. Wei, L. Gardi, D. B. Downey, and A. Fenster, "Automated localization of implanted seeds in 3D TRUS images used for prostate brachytherapy," *Medical physics*, vol. 33, no. 7Part1, pp. 2404–2417, 2006.

[5] X. Wen, S. E. Salcudean, and P. D. Lawrence, "Detection of brachytherapy seeds using 3-D transrectal ultrasound," *IEEE Transactions on Biomedical Engineering*, vol. 57, no. 10, pp. 2467–2477, 2010.

[6] B. Li and S. T. Acton, "Active contour external force using vector field convolution for image segmentation," *IEEE Transactions on Image Processing*, vol. 16, no. 8, pp. 2096–2106, 2007.

[7] V. Jaouen, J. Bert, N. Boussion, H. Fayad, M. Hatt, and D. Visvikis, "Image enhancement with PDEs and nonconservative advection flow fields," *IEEE Transactions on Image Processing*, vol. DOI: 10.1109/TIP.2018.2881838, 2018.

[8] C. Xu, J. L. Prince, *et al.*, "Snakes, shapes, and gradient vector flow," *IEEE Transactions on Image Processing*, vol. 7, no. 3, pp. 359–369, 1998.

[9] S. Mukherjee and S. T. Acton, "Vector field convolution medialness applied to neuron tracing," in *2013 IEEE International Conference on Image Processing*, pp. 665–669, IEEE, 2013.

[10] B. Li, S. A. Millington, D. D. Anderson, and S. T. Acton, "Registration of surfaces to 3D images using rigid body surfaces," in *2006 Fortieth Asilomar Conference on Signals, Systems and Computers*, pp. 416–420, IEEE, 2006.

[11] V. Jaouen, P. Gonzalez, S. Stute, D. Guilloteau, S. Chalon, I. Buvat, and C. Tauber, "Variational segmentation of vector-valued images with gradient vector flow," *IEEE Transactions on Image Processing*, vol. 23, no. 11, pp. 4773–4785, 2014.

[12] V. Jaouen, J. Bert, I. Hamdan, A. Valéri, U. Schick, N. Boussion, and D. Visvikis, "Purely edge-based prostate segmentation in 3D TRUS images using deformable models," in *Surgetica 2017*, 2017.

[13] K. S. Arun, T. S. Huang, and S. D. Blostein, "Least-squares fitting of two 3-D point sets," *IEEE Transactions on Pattern Analysis and Machine Intelligence*, no. 5, pp. 698–700, 1987.

Automatic segmentation of intraoperative ultrasound images of the brain using U-Net

François-Xavier Carton[1,2], Jack H. Noble[2], Bodil K. R. Munkvold[3], Ingerid Reinertsen[4] and Matthieu Chabanas[1,2]

[1] Univ Grenoble Alpes, CNRS, Grenoble INP, TIMC-IMAG, F-38000 Grenoble, France
[2] Dept of Electrical Engineering and Computer Science, Vanderbilt Univ, Nashville, USA
[3] Dept of Neuroscience, Norwegian Univ of Science and Technology, Trondheim, Norway
[4] Dept of Medical Technology, SINTEF, Trondheim, Norway
Contact: francois-xavier.carton@univ-grenoble-alpes.fr

The brain is significantly deformed during neurosurgery, in particular because of the removal of tumor tissue. To allow accurate navigation during surgery, one method is to register preoperative MR with intraoperative ultrasound images. The resection cavity need to be segmented to take the tissue removal into account in the registration model. Manually segmenting this cavity is error-prone and time consuming and cannot be performed in the operating room. In this work, we present an automatic segmentation method of the resection cavity.

1 Context

The brain is significantly deformed during neurosurgery, because of several causes including tissue resection. Thus, preoperative images do not match the actual configuration of the brain in the operating room and cannot be used as is for navigation during the surgery. As intraoperative images have poorer quality than preoperative MR (pMR) images, several methods [1–3] have been developed to register the pMR with intraoperative data. Segmenting intraoperative ultrasound (iUS) images of the brain has several uses.

To take the tissue resection into account in registration models, the resection cavity needs to be segmented so that the corresponding nodes can be removed from the model. Our current method [1] do not take the tissue resection into account. To implement it, a method to segment the resection cavity in iUS images is needed [4]. By registering and overlaying the pMR on the iUS, surgeons can ensure the resection is complete.

It is also useful to segment other structures in iUS images, such as the ventricles and sulci, to use as features for the registration [5]. Currently our method uses blood vessels as features to guide the registration, but the results could be improved by using other structures in addition to the blood vessels.

Also, segmenting the tumors could help surgeons to analyze iUS images. We are evaluating the segmentation method on these regions of interest.

As segmenting ultrasound images is extremely time consuming and error-prone, an automatic method is preferred. In this paper, we present a method to automatically segment iUS images and focus on the segmentation of the resection cavity.

2 Methods

Data We used the iUS volumes from the RESECT database [6]. We manually segmented the ground truth for the resection cavity on the volumes where the cavity was visible (during and after resection volumes). We evaluated the inter-rater variability (with two observers) and intra-rater variability (with one of the observer) on 10 volumes. We also tested our method to segment the tumor on the before-resection volumes, using the segmentations from Munkvold et al. [7] as the ground truth.

Segmentation network The segmentation neural network we used is based on U-Net [8]. It is a 2D network, so the 3D volumes are processed slice by slice. To give more context to the network, we changed the network's input to a group of several adjacent slices (using multiple input channels) and the output to the segmentation of the middle slice. We evaluated and compared networks with different numbers of input slices $c_i \in \{1, 3, 7\}$.

Training We split the volumes into a training set (27 volumes) and a test set (10 volumes). Because the

Case	2 after	4 after	8 after	17 during	19 after
Middle slice	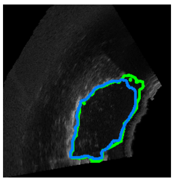	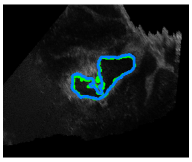	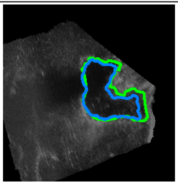	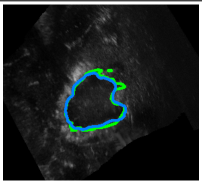	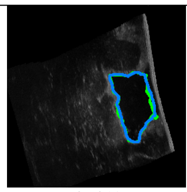
Dice	0.90	0.83	0.68	0.93	0.95
Case	19 during	21 after	24 after	25 during	26 during
Middle slice	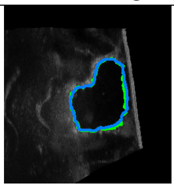	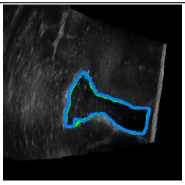	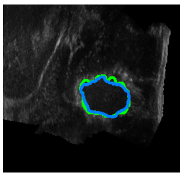	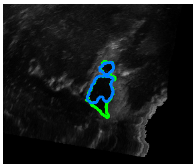	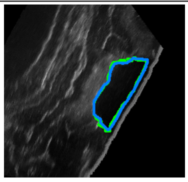
Dice	0.96	0.96	0.76	0.76	0.87

Figure 1: *Segmentation of the resection cavity in iUS (per case results; green: ground truth, blue: prediction)*

size of the volumes was bigger than the network input size, we cropped the volumes around the cavity (for the training phase). We used a loss function based on the Dice score: $\text{loss}(y_{true}, y_{pred}) = 1 - \text{Dice}(y_{true}, y_{pred})$.

Testing The test volumes also had to be reduced to the network's input size, we tested three methods:

1. downsampling: the input volume is downsampled, the prediction is upsampled to the original size;
2. sliding window: patches are extracted from original volume, and the prediction patches are combined using the average value on each voxel;
3. region of interest (ROI): a ROI is estimated using the output of the downsampling method, then the network is evaluated on the ROI (original scale).

Post-processing The predicted volumes were thresholded to obtain a binary mask. Then, a largest connected component filter was applied to remove the disconnected noise components around the cavity.

3 Results

Our best method (ROI sampling, number of slices $c_i = 1$) had a mean Dice score 0.86 over the ten test cases and is overall successful. Figure 1 shows an example slice with the segmentation result for each test case. The segmentations obtained with the automatic method were comparable to the manual segmentations. Figure 2 compares the Dice scores obtained with the best method with the intra-rater and inter-rater variability. The automatic method performed almost as well as the inter-rater variability, especially when the predicted volumes are compared to observer 2's segmentations. It should be noted that the case that had the lowest Dice score compared to observer 1 is also the case where the inter-rater variability is the highest and had a score of 0.78 compared to observer 2's segmentation.

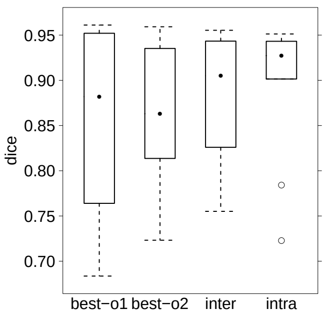

Each box-plot represents the Dice scores over the 10 test cases. The Dice scores were computed between:

- best-o1: best method and observer 1's segmentations
- best-o2: best method and observer 2's segmentations
- inter: observer 1 and observer 2's segmentations
- intra: observer 1 first and second segmentations

Figure 2: *Resection cavity Dice scores (10 cases)*

The sliding window and ROI method had similar results and performed better than the downsampling method. Using 7 slices of context did not improve the results (especially after post-processing), it is probably not enough context to make significant improvements.

We also tested our method on tumor segmentation and found that the results were not as good as with the resection cavity. On four test cases, the mean Dice score was 0.68. We found that for the segmentation of the tumor, adding more slices of context slightly improved the results: the Dice scores ranged from 0.53 to 0.89 with $c_i = 1$ and from 0.65 to 0.88 with $c_i = 9$. As more context seems to be needed to improve the results, we are evaluating a 3D version of the network and have obtained promising results.

4 Conclusions

We developed an automatic method to segment the resection cavity in iUS images. In future work, we will use it with our registration model [1] to take the tissue resection into account. We will also evaluate the method on other structures in iUS images, to be used as features for the registration process. We are evaluating a 3D version of the network to segment tumor tissue, to help surgeons in analysing iUS images.

Acknowledgments

This work was partly supported by the French National Research Agency (ANR) through the framework *Investissements d'Avenir* (ANR-11-LABX-0004, ANR-15-IDEX-02).

References

[1] Fanny Morin, Hadrien Courtecuisse, Ingerid Reinertsen, Florian Le Lann, Olivier Palombi, Yohan Payan, and Matthieu Chabanas. Brain-shift compensation using intraoperative ultrasound and constraint-based biomechanical simulation. *Medical Image Analysis*, 40:133 – 153, 2017.

[2] Marek Bucki, Olivier Palombi, Mathieu Bailet, and Yohan Payan. *Doppler Ultrasound Driven Biomechanical Model of the Brain for Intraoperative Brain-Shift Compensation: A Proof of Concept in Clinical Conditions*, pages 135–165. Springer Berlin Heidelberg, Berlin, Heidelberg, 2012.

[3] Xiaoyao Fan, David W Roberts, Jonathan D Olson, Songbai Ji, Timothy J Schaewe, David A Simon, and Keith D Paulsen. Image updating for brain shift compensation during resection. *Operative Neurosurgery*, 14(4):402–411, 2018.

[4] François-Xavier Carton, Jack H. Noble, and Matthieu Chabanas. Automatic segmentation of brain tumor resections in intraoperative ultrasound images. To appear in *Proceedings of SPIE*, 10951(104), 2019.

[5] Jennifer Nitsch, Jan Klein, Jan Hendrik Moltz, Dorothea Miller, Ulrich Sure, Ron Kikinis, and Hans Meine. Neural-network-based automatic segmentation of cerebral ultrasound images for improving image-guided neurosurgery. To appear in *Proceedings of SPIE*, 10951(45), 2019.

[6] Yiming Xiao, Maryse Fortin, Geirmund Unsgård, Hassan Rivaz, and Ingerid Reinertsen. Retrospective evaluation of cerebral tumors (resect): A clinical database of preoperative mri and intra-operative ultrasound in low-grade glioma surgeries. *Medical Physics*, 44(7):3875–3882, 2017.

[7] Bodil Karoline Ravn Munkvold, Hans Kristian Bø, Asgeir Store Jakola, Ingerid Reinertsen, Erik Magnus Berntsen, Geirmund Unsgård, Sverre Helge Torp, and Ole Solheim. Tumor volume assessment in low-grade gliomas: A comparison of preoperative magnetic resonance imaging to coregistered intraoperative 3-dimensional ultrasound recordings. *Neurosurgery*, 83(2):288–296, 2018.

[8] Olaf Ronneberger, Philipp Fischer, and Thomas Brox. U-net: Convolutional networks for biomedical image segmentation. In *Medical Image Computing and Computer-Assisted Intervention – MICCAI 2015*, pages 234–241. Springer International Publishing, 2015.

Real-time Prediction of High-risk Instrument Motion based on Location Information

Yuichiro SAWANO [1], Nobuyoshi OHTORI [2] and Ryoichi NAKAMURA [3,4]

1. Graduate School of Science and Engineering, Chiba University, Chiba, Japan.
2. Department of Otorhinolaryngology, Jikei University School of Medicine, Tokyo, Japan.
3. Department of Biodesign Institute of Biomaterials and Bioengineering, Tokyo Medical and Dental University, Tokyo, Japan.
4. Japan Science and Technology Agency, Saitama, Japan.

Contact: sawano@chiba-u.jp

In endoscopic sinus surgery, any incorrect movement of a surgical instrument can lead to a serious accident. We aim to devise a method of detecting high-risk operations by predicting the motion of surgical instruments in real-time. We were able to attain a 77.7% alert rate as the surgeon was working. Alerts were issued 4.1 ± 4.9 s prior to the motion of the instrument. This made the surgeon aware of the high-risk nature of an upcoming operation.

1 Introduction

Endoscopic sinus surgery (ESS) is a general surgical procedure that is commonly used for treating sinusitis due to its being minimally invasive. Although this procedure greatly improves a patient's quality of life (QOL), the surgeon is required to be highly skilled. A contributing factor is that the procedure is performed by a solo surgeon, and any incorrect movement of a surgical instrument can lead to serious accidents given that the procedure is performed in a lumen adjacent to the brain and eyes. To improve the safety of this procedure, navigation systems have been introduced. However, because the risk of accidents remains large, further risk avoidance systems should be implemented. Therefore, we focused on the location information for the surgical instruments as provided by the navigation system. In a previous study [1], the motion and locational relationship of the surgical instruments were quantified by analyzing the navigation log data after the surgery. We aimed to develop a system capable of analyzing the quantitative location data of the surgical instruments in real-time and thus promote the avoidance of risks presented by the surgical instruments. In the present study, to detect high-risk motion, we developed a means of predicting the motion of the surgical instruments in real-time using time-series data analysis.

2 Materials and Methods

Based on the results of a study of otolaryngologists, we focused on those motions that presented a high degree of risk, which we defined as a distance of more than 15 mm from the center of the endoscopic view to the tip of the microdebrider. Any further displacement of the microdebrider would increase the risk of damage to important organs in that they would move away from the center of the endoscopic view. The time-series data recorded by the navigation system with which we observed the target revealed an increasing trend in the distance between the microdebrider and the tip of the endoscope. Several methods are available for analyzing trends in time-series data. We adopted a method that was capable of predicting, in real-time, future trends by analyzing two moving-average lines of the time-series data. This method, called the exponential moving average (EMA) crossover method, is commonly used in financial engineering [2]. In the present study, we used it to identify an upward trend. The exponential moving average that we used is defined by Eq. 1 [3]:

$$\text{Smoothing} \qquad S_t = \alpha \cdot y_t + (1 - \alpha) \cdot S_{t-1} \qquad (1)$$

where y_t denotes an observation at time t and α is the smoothing parameter. To estimate a future value of time-series data, prediction using the Holt exponential smoothing method was performed. When using this method, the future value is predicted from the level and trend components of the time-series data [4]. The Holt exponential smoothing method is defined by Eq. 2 [4]:

$$\begin{array}{ll} \text{Forecast} & F_{t+h} = S_t + h \cdot b_t \\ \text{Level} & S_t = \alpha \cdot y_t + (1-\alpha) \cdot (S_{t-1} + b_{t-1}) \\ \text{Trend} & b_t = \beta \cdot (S_t - S_{t-1}) + (1-\beta) \cdot b_{t-1} \end{array} \quad (2)$$

where F_{t+h} is a forecast value at time $t+h$, S_t is an estimate of the level, b_t is an estimate of the trend, α is the smoothing parameter for the level, and β is the smoothing parameter for the trend. In the present study, we analyzed the upward trend by applying the exponential moving average (EMA) crossover method and issued an alert at the timing at which the predicted value output by the Holt exponential smoothing method is 15 mm or more while the trend is increasing.

To verify the efficacy of our method, we applied it to the time-series data for the relative distance between the microdebrider and the endoscope, using it to predict the placement of the surgical instruments a few seconds in the future, and investigated whether the target operation could be predicted. In addition, we measured the time that would have to elapse between our method predicting a high-risk operation and the displacement exceeding 15 mm. Each parameter used in the EMA crossover method was manually set with exponential smoothing line parameters of 0.09 and 0.01, while parameters α and β of the Holt exponential smoothing method were set to 0.9 and 0.05. We applied the method to the ESS navigation log data for ten otolaryngologists practicing at The Jikei University Hospital, Tokyo.

3 Results

Figure 1 shows when our system issued alerts upon its predicting the occurrence of a high-risk operation. The black lines correspond to the observed data, while the red and blue lines indicate the EMA (α = 0.09 and 0.01, respectively). The blue dotted line indicates the values predicted by Holt exponential smoothing after 3 s (h = 9). In addition, the yellow star indicates the timing at which an alert is issued while the red star indicates when a displacement of 15 mm is exceeded.

We found that an alert was issued for 77.7% of those operations that would result in the displacement between the microdebrider and endoscope reaching or exceeding 15 mm. After alerting by our method, 59.2% of the distance values were 15 mm or more. Alerts could be issued 4.1 ± 4.9 s in advance. This provided the surgeon with a sufficiently advanced warning of a high-risk operation.

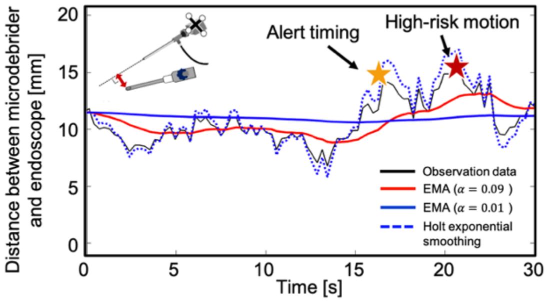

Figure 1: Issue of alerts

4 Discussion

Those cases in which the prediction and issue of an alert failed predominantly featured movements causing the distance to instantaneously increase to 15 mm or more. If an alert could be issued for these operations, although the system sensitivity would improve, the specificity would decrease. When many alerts are output, that is, when the system sensitivity is high, it might be difficult to perform the operation. Rather, it would be necessary to adapt and examine our system during the operation. The greatest merit of this method is that teaching data is not necessary. Estimation based on statistical and probabilistic models is also used as a state transition estimation method using time-series. In these methods, it is necessary to create a model from teaching data. However, artificial behavior in surgical operations is believed to make it difficult to create a database with a high level of reliability because of the large differences in techniques of surgeons and the anatomical factors of patients. Thus, our method would be particularly useful in that it can predict surgical operations in real-time regardless of individual differences.

5 Conclusion

We have devised a means of identifying high-risk operations in ESS by analyzing navigation log data and issuing alerts, thus enhancing the safety of surgeries by reducing the workload of the surgeon. By adding an EMA crossover method, we created a new intraoperative annotation system that did not require teaching data and which had an excellent real-time response. A verification of the system revealed the possibility of providing a surgeon with a warning of a high-risk operation, sufficiently far in advance.

Acknowledgments: This research was partly supported by JST PRESTO JPMJPR16D9 and JSPS KAKENHI grant number 17K11366.

6 References

[1] Sugino T, Nakamura R, Kuboki A, Honda O, Yamamoto M, Ohtori N. (2017). Quantitative Analysis of a Camera Operation for Endoscopic Sinus Surgery Using a Navigation Information Clinical Study, *Journal of Japan Society of Computer Aided Surgery*, 19(1):17–26.

[2] El-Khodary I.A. (2009). A Decision Support System for Technical Analysis of Financial Markets Based on the Moving Average Crossover. *World Applied Sciences Journal*, 6(11):1457-1472.

[3] Brown R.G. (1962). Smoothing, forecasting and prediction of discrete time series. Prentice-Hall, Englewood Cliffs, NJ.

[4] Hyndman, R.J., and Athanasopoulos, G. (2018). Forecasting: principles and practice, 2nd Edition, OTexts: Melbourne, Australia.

Transcranial robot-assisted Blood-Brain Barrier opening with Focused Ultrasound

Gaelle THOMAS, Laurent BARBÉ, Pauline AGOU, Benoît LARRAT, Jonathan VAPPOU and Florent NAGEOTTE

ICube, UMR 7357, CNRS, Université de Strasbourg, 1 place de l'hôpital 67091 Strasbourg
CEA / DRF / Joliot / Neurospin, Université Paris Saclay, 91191 Gif sur Yvette
Contact: gaelle.thomas@unistra.fr Tel : +33 (0)3 88 11 91 57

Disrupting the Blood-Brain Barrier (BBB) is a major challenge for localized drug delivery to treat brain tumors or neurodegenerative diseases. 3BOPUS is a project that aims at using Focused Ultrasound under robotic guidance to perform controlled and reversible BBB opening. This paper describes a method to compute the accessible brain targets space regarding specific design choices.

1 Clinical context

Almost 99% of the drugs that are injected into the blood will never deliver their effects to the brain cells because of the BBB [1]. The BBB is a biological frontier constituted of extremely selective protein junctions that avoid contamination by molecules coming from the blood. Techniques to provide a temporary, localized and reversible BBB disruption have been studied [2] but most of today's solutions are either very invasive or not effective enough for the risk taken.
Breakthroughs in acoustic sciences have provided extensive knowledge of the interactions between Focused Ultrasound (FUS) and biological tissues [3], and, since the 1990's, many studies have been conducted to propose applications for BBB opening [4, 5, 6]. This technique relies on acoustic cavitation effects of microbubbles.
Firstly studied *in vitro* and then on various animal models, cavitation effects for BBB disruption are now better understood and controlled [7]. Although very promising, the results cannot be used yet in routine treatments for human patients. Several clinical trials are currently being conducted, but the tested devices are still either invasive [8], or not optimal for the BBB opening application [9].
Robotic assistance is increasingly used for medical devices in various healthcare fields such as surgery, diagnosis, or imaging. It can relieve the medical staff of most tedious tasks, while providing speed and accuracy improvements. In this context, the Blood-Brain Barrier OPening with UltraSound (3BOPUS) project aims at developing a robotized solution for BBB opening with FUS. By automatizing the positioning of the FUS generator, also called transducer, thanks to pre-acquired brain images, the BBB opening would be safe, precise and patient-specific.

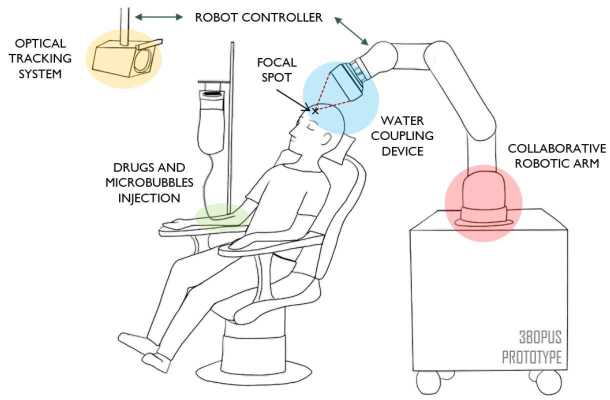

Figure 1: *The main elements of the 3BOPUS project*

The device is composed of a transducer mounted on a collaborative robotic arm able to position the focal spot on a brain target, with the feedback of an optical tracking system (Figure 1). The visual control loop ensures automatized repositioning in case of parasite motions of the patient. Microbubbles are injected to enhance the cavitation phenomenon, whose effects are measured with Passive Cavitation Detectors (PCD).
The work presented in this article focuses on the robotic part of the project and more especially the results of a preliminary workspace study.

2 Brain targetability

The objectives of this preliminary study is to quantify the brain space that is accessible to a transducer mounted on a robotic arm. Some assumptions were made, notably regarding the scene items (patient anatomy, water container) and the chosen devices (robot, transducer). Acoustic and kinematic constraints were defined and the percentage of targetable brain space for the chosen conditions was assessed.

2.1 Simulation conditions

Anonymized real head images were processed in order to get a simple 3D model with a discretized scalp surface and an homogeneous brain point cloud. The water coupling system and the transducer were simulated as simple 3D cylindrical shapes. The chosen manipulator is the collaborative robot UR5 (Universal Robot), with 6 Degrees of Freedom. The simulations were run with MATLAB codes interfaced with the V-REP simulator (Coppelia Robotics).

2.2 Definition of acoustic constraints

For one given brain target, there is an infinite number of possible transducer configurations (position, orientation, focal length of the transducer) around the skull to reach it. Not all of them are valid, and acoustic constraints were defined to sort them out. A transducer configuration is kept if: (a) its main axis lies within a cone centered on the scalp normal direction, (b) the distance to the target lies within the focal length range of the transducer, and (c) the active face of the transducer is above the water limit (Figure 2). These constraints are used to guarantee a good ultrasound focal beam quality, in spite of the irregular and badly known skull acoustic properties. The output of this computation is a list of valid transducer configurations for each target of the brain point cloud.

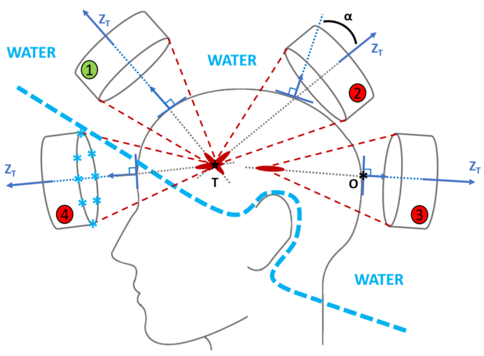

Figure 2: *(1) Valid transducer configuration. (2) α too high (>20°). (3) Distance OT not within the focal length range. (4) Transducer not immersed.*

2.3 Definition of kinematic constraints

The set of valid transducer configurations are then sent to the robot controller. Because of the constrained environment and the workspace of the UR5, not all of these configurations can be reached by the robot. The kinematic constraints consist in checking, for each target, for each transducer configuration, its kinematic feasibility. The solution is kept if: (a) no collision or self-collision is detected within the 3D scene, (b) the Position Inverse Kinematic can be solved within the joints ranges of the UR5, and (c) no part of the robot is in contact with water. The output of this phase is a percentage of targets that are accessible with the robot.

3 First results

By respecting the defined acoustic constraints, the available brain space is reduced to 82.2 % of its initial size (1339 over 1629 targets have at least one valid transducer configuration). The regions that were filtered out are the cerebral trunk and the peripheral areas, mainly because they are respectively too deep or too close to the scalp surface (Figure 3).

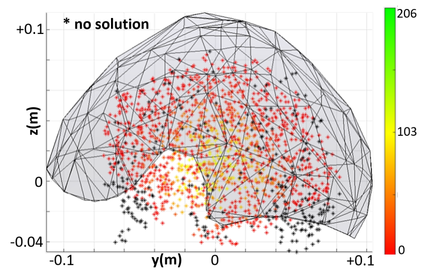

Figure 3: *Number of solutions per target respecting the acoustic constraints (17.8 % with no solution).*

95.4 % of the 82.2 % are reachable by the robot, assuming that it can have three distinct poses around the patient (60 cm front/right/left). This means that, when covering all the targets of the initial brain area, 78.4 % are accessible with the transducer mounted on the UR5 arm, and with the patient head within a virtual water container.

4 Conclusion and perspectives

The results presented in this study correspond to particular simulation conditions, and they depend strongly on the size and the position of the scene elements, on transducer parameters and thresholds chosen for the constraints. Despite such limitations, this supporting work is essential to the 3BOPUS project. 78.4 % is considered as acceptable by neurooncologists for BBB opening in brain tumors. The tools developed during this work will be used to solve the inverse problem, consisting in finding the best acoustic and kinematic configurations for a given target.

References

[1] Pardridge, W. (2005). The blood-brain barrier: Bottleneck in brain drug development. *NeuroRx*, 2:3–14.

[2] Dove, A. (2008). Breaching the barrier. *Nature Biotechnology*, 26:1213–1215.

[3] Nyborg, W. (2001). Biological effects of ultrasound: Development of safety guidelines. Part II: General review. *Ultrasound in Medicine and Biology*, 27:301–333.

[4] Sheikov, N., McDannold, N., Vykhodtseva, N., Jolesz, F. and Hynynen, K. (2004). Cellular mechanisms of the blood-brain barrier opening induced by ultrasound in presence of microbubbles. *Ultrasound in Medicine and Biology*, 30:979–989.

[5] Marty, B., Larrat, B., Van Landeghem, M., Robic, C., Robert, P. Port, M., Le Bihan, D. Pernot, M., Tanter, M., Lethimonnier, F. and Mériaux, S. (2012). Dynamic study of blood-brain barrier closure after its disruption using ultrasound: A quantitative analysis. *Journal of Cerebral Blood Flow and Metabolism*, 32:1948–1958.

[6] Hynynen, K., McDannold, N., Sheikov, N., Jolesz, F., and Vykhodtseva, N. (2005). Local and reversible blood-brain barrier disruption by noninvasive focused ultrasound at frequencies suitable for trans-skull sonications. *NeuroImage*, 24:12–20.

[7] Ohl, S.W., Klaseboer, E., and Khoo, B.C. (2015). Bubbles with shock waves and ultrasound: a review. *Interface Focus*, 5:3–14.

[8] Carpentier, A., Canney, M., Vignot, A., Reina, V., Beccaria, K., Horodyckid, C., Karachi, C., Leclercq, D., Lafon, C., Chapelon, J.-Y., Capelle, L., Cornu, P., Sanson, M., Hoang-Xuan, K., Delattre, J.-Y., and Idbaih, A. (2016). Clinical trial of blood-brain barrier disruption by pulsed ultrasound. *Science Translational Medicine*, 8:343–343.

[9] ExAblate Neuro - Insightec, Israel https://clinicaltrials.gov/ct2/show/NCT03739905 Consulted: 28th of February 2019.

5 Acknowledgements

This project is part of the 3BOPUS project funded by a grant from the Healthcare technologies call of the French Agence Nationale de la Recherche.

Accurate Instrument Tracking in Minimally Invasive Surgery

Mario ARICÒ and Guillaume MOREL
Sorbonne Université, CNRS, INSERM, ISIR-Agathe, Paris, France.
Tel : +33 (0)7 82 23 95 29
Contact: {mario.arico, guillaume.morel}@sorbonne-universite.fr

Navigation systems deploy pointers to estimate the position of anatomical structures. However, in laparoscopy, the tool length induces large reconstruction errors of the tip position. We propose to increase the accuracy of a standard navigation system by integrating a vision-based module that tracks the tool on endoscopic images.

1 Introduction

Minimally Invasive Surgery (MIS) has proven beneficial for the clinical recuperation of the patients. However, surgeons have to adapt their dexterity to the loss of direct vision and distorted hand-eye coordination induced by the fixed entry point [1]. The drawbacks of MIS can be mitigated thanks to navigation systems based on Image-Guided Surgery (IGS) and Augmented Reality (AR) [2]. Both IGS and AR rely on the accurate estimation of the intra-operative tip position. Standard surgical navigation [5] is based on a surgical pointer tracked by an optical localizer that measures the pose of a Dynamic Reference Frame (DRF) with an accuracy below 0.2mm. In MIS, standard systems fail to provide an accurate estimate of the instrumen tip [2], [8] due to the large reconstruction errors induced by the tool length that separates the tip from the DRF. In this paper we propose to improve the degraded accuracy of a standard navigation system by integrating a vision-based module that independently tracks the tip on the image and compares the results. The mismatch between the current image of the tip and its pose issued from optical measures is used to correct the instrument calibration to visually matching results.

2 System Calibration

In MIS, surgeons rely on endoscopic images to locate the anatomical structures. Therefore, using the instrument as a 3D pointer for intra-operative navigation requires the accurate estimation of the tip position in the image plane. Both the instrument and the endoscope are equipped with Dynamic Reference Frames (DRF), RF_{in} and RF_{end}. Although the external localizer provides the pose of these local frames (Sec. 3), a pre-operative calibration is required to compute the end-effector position on the image plane. Pivoting methods [9] are used to calibrate the instrument tip ${}^{in}\mathbf{p}$ in the local DRF. The endoscope calibration is a two-phase process requiring the estimation of the intrinsic parameters K and the extrinsic parameters E. The intrinsic matrix K are usually estimated via a calibration chessboard [10]. Extrinsics are estimated by solving a hand-eye calibration system in the form $AX = XB$ [6].

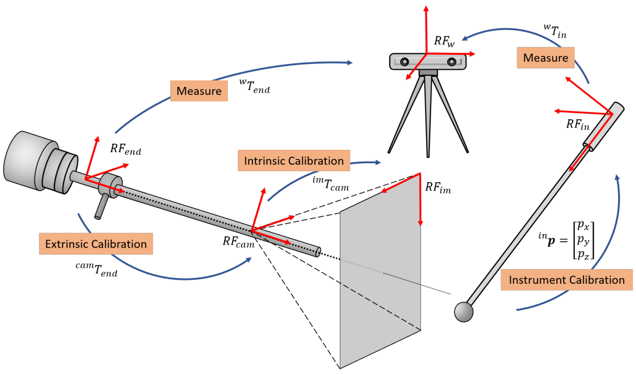

Figure 1: *Scheme of the surgical set-up.*

3 Instrument Tracking

Instrument tracking for MIS can be achieved in two ways: external localizers and image-based techniques. External localizers represent the State-if-the-Art for surgical navigation [2]: the instrument and the camera are equipped with a DRFs(RF_i) that are directly measured by the system. However, despite the sub-millimetic accuracy, the length of the tools degrades the recon-

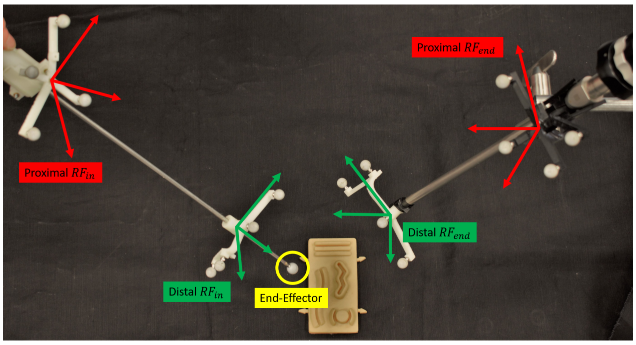

Figure 2: *Experimental Set-up.*

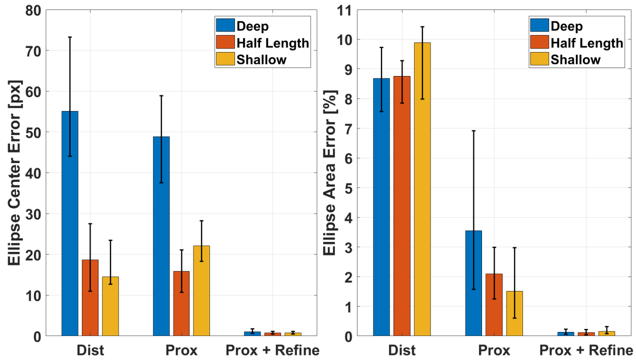

Figure 3: *In-plane error (Left Image) and off-plane error (Right Image).*

struction of the tip position [7]. In vision-based tracking, the tip position is extracted from the endoscopic images [3]: image features (i.e., color, gradient, texture, shape, etc.) are used to discriminate the instrument against the background. However, at present the optimal selection of the feature vector remains challenging, due to changes in the lighting conditions, low robustness to noise, occlusions and deformations. Moreover, the selection of the optimal dimensionality is a trade-off between discriminative power and computational cost.

4 Hybrid Tracking

In this paper, a hybrid tracking solution for a surgical pointer is proposed. The method is based on the use of a State-of-the-Art external localizer for high-frequency tracking of the instrument tip. The reconstruction errors induced by the instrument length are compensated in real-time by integrating an independent, image-based tracker that computes the instrument position directly from the images. The error ε between the two estimates is used to locally maximize the accuracy by refining the pre-operative calibration ${}^{in}\mathbf{p}$ of the tool:

$$\arg\min_{{}^{in}\mathbf{p}} ||\varepsilon||^2 \tag{1}$$

The definition of the error depends on the tip geometry. In our scenario, the instrument tip is equipped with a spherical marker that can be easily tracked by the optical localizer and extracted from images through threshold operations. The spherical geometry of the marker is included in the projective model of the camera (the image of a sphere is an ellipse) [4].

5 Experimental Results

The experimental set-up (Fig. 2) for hybrid tracking consists of: the optical tracker Atracsys ftk500 (Atracsys LLC), (335Hz sampling frequency, accuracy in the interval $[0.09 - 0.15]mm$ RMS); a fullHD monocular endoscope (25Hz); an instrument with a passive optical marker at the end-effector. Both the endoscope and the tool are equipped a couple of DRFs: proximal DRFs, fixed at the handle level to mimic the real surgical conditions; distal DRFs, fixed close to the end-effectors to quantify the effect of the tool lengths on the performance (Fig. 2). To test the hybrid tracker, the endoscope is fixed onto a rigid support and a screen is used for visual feedback. Nine experimental conditions are tested: three different insertion levels (deep, half-length, shallow insertions) cross-tested with three tracking approaches (standard tracking based on distal DRFs, standard tracking based on proximal DRFs, refined tracking based on proximal DRFs). The user uses the instrument to aim at 3D points in space. A set of 20 samples per condition are sampled. In Fig. 3 are shown the results. The in-plane error (Fig. 3, left) represents the Euclidean distance between the ellipse centres, issued by the optical and vision-based trackers. For both standard tracking approaches, the in-plane median error is around 50px for the deep configurations, while it remains confined in the interval $15 - 25$px in the half-length and shallow configurations. By applying the refinement algorithm (10Hz), the performance dramatically improves across the three conditions as the offset in reduced below 5px. The off-plane error (Fig. 3, right) represents the depth precision and is estimated as percentage difference between the areas of the ellipses. Also in this case, the refinement algorithm provides optimal results, reducing the median error below 0.5%.

6 Conclusions

In this paper, a hybrid technique for precise and robust instrument tip tracking for MIS is presented. It enhances the accuracy of an optical tracker by integrating an independent, image-based tracker to refine the pre-operative instrument calibration and provide visually matched reconstructions on the image frame. Results of the hybrid tracking algorithm have been reported in a simplified set-up, where the instrument tip is easily detectable on the image as an elliptic region. Future tests in a realistic clinical scenario will make use of realistic MIS tools by integrating marker-less techniques and integrating their 3D geometry into the optimization system.

References

[1] Adrien Bartoli, Toby Collins, Nicolas Bourdel, and Michel Canis. Computer assisted minimally invasive surgery: Is medical computer vision the answer to improving laparosurgery? *Medical hypotheses*, 79(6):858–863, 2012.

[2] Sylvain Bernhardt, Stéphane A Nicolau, Luc Soler, and Christophe Doignon. The status of augmented reality in laparoscopic surgery as of 2016. *Medical image analysis*, 37:66–90, 2017.

[3] David Bouget, Max Allan, Danail Stoyanov, and Pierre Jannin. Vision-based and marker-less surgical tool detection and tracking: a review of the literature. *Medical image analysis*, 35:633–654, 2017.

[4] François Chaumette. *La relation vision-commande: théorie et application à des tâches robotiques*. PhD thesis, 1990.

[5] Andreas F Mavrogenis, Olga D Savvidou, George Mimidis, John Papanastasiou, Dimitrios Koulalis, Nikolaos Demertzis, and Panayiotis J Papagelopoulos. Computer-assisted navigation in orthopedic surgery. *Orthopedics*, 36(8):631–642, 2013.

[6] Mili Shah, Roger D Eastman, and Tsai Hong. An overview of robot-sensor calibration methods for evaluation of perception systems. In *Proceedings of the Workshop on Performance Metrics for Intelligent Systems*, pages 15–20. ACM, 2012.

[7] Gwenllian Fflur Tawy and Philip Rowe. Is the instrumented-pointer method of calibrating anatomical landmarks in 3d motion analysis reliable? *Journal of biomechanics*, 53:205–209, 2017.

[8] Jay B West and Calvin R Maurer. Designing optically tracked instruments for image-guided surgery. *IEEE transactions on medical imaging*, 23(5):533–545, 2004.

[9] Ziv Yaniv. Which pivot calibration? In *Medical Imaging 2015: Image-Guided Procedures, Robotic Interventions, and Modeling*, volume 9415, page 941527. International Society for Optics and Photonics, 2015.

[10] Zhengyou Zhang. A flexible new technique for camera calibration. *IEEE Transactions on pattern analysis and machine intelligence*, 22, 2000.

Statistical shape model of vascular structures with abdominal aortic aneurysm

Claire DUPONT[1], Christelle BOICHON-GRIVOT[2], Adrien KALADJI[1], Antoine LUCAS[1], Michel ROCHETTE[2] and Pascal HAIGRON[1]

[1]Univ Rennes, CHU Rennes, INSERM, LTSI – UMR 1099, F-35000 Rennes, France

[2]ANSYS France, F-69100 Villeurbanne, France

Contact: claire.dupont@univ-rennes1.fr

This work presents a statistical shape model built from a large dataset of aortoiliac anatomies with abdominal aortic aneurysm (AAA).

1 Introduction

The computers spread stimulated the development of methods to analyze large amount of data. Statistical shape modeling (SSM) is used to represent a set of shapes described by a distribution of points to capture the morphological variability in a population of interest.

Popularized by [1] for model-based automated image segmentation [2], there is an increasing of interest for this approach to improve knowledge in biomedical field or to be integrated in decision support process [3]. It is used, for example, to understand shape variation in a population [4,5], to create new patients for simulation [6,7,8] or to develop atlas to design implant [9].

SSM techniques were used to study the thoracic aorta morphology of healthy subjects [10, 11]. In the context of aortic pathologies, endovascular treatments represent a significant part of the therapeutic arsenal. They consist in introducing medical devices through tortuous iliac arteries to reach the lesions (e.g. AAA, aortic valve) [12]. The optimization of such endovascular techniques raises issues related to the analysis of pathological populations. However, in the case of AAA treatment, the tortuosity of aortoiliac arteries, which can be represented by centrelines (*CL*), results in a large morphological variability.

The objective of this work is to develop a SSM of aortoiliac anatomies with AAA. The method is presented in section 2. The results with the analysis of modes required to describe this type of anatomy are presented in Section 3.

2 Methodology

2.1 Input data

For each patient of the learning dataset, the preoperative CT-scan is imported into Endosize® software (Therenva, France) used in clinical routine to extract the vascular geometry. The point P_R is positioned manually in the lumen center on the slice below the lowest renal artery. The points P_{LI} and P_{RI} are selected at the center of each femoral common artery on the slice before the bifurcation with superficial femoral artery. These points delimit the vascular structure of interest. The position of the point P_{Bif} at iliac bifurcation is also defined. The *CL* is extracted from the vascular geometry by means of Vascular Modeling ToolKit (VMTK) [13].

In order to consider isotopological *CL*s, each branch of the vascular structures, i.e. abdominal aorta, left and right iliac arteries, is discretized with 80 points. All the *CL*s are aligned *(Fig.1a)*: a translation is applied so that P_{Bif} is at the center of the coordinate system (O, $\vec{x}$, $\vec{y}$, $\vec{z}$) and a rotation of center O around $\vec{z}$-axis is applied so that P_{IR} is in the plane $y = 0$. No other rotation is applied to keep $\vec{z}$-axis unchanged since it refers to the patient craniocaudal axis.

2.2 Statistical shape model

For a patient *i*, *CL* is represented by the vector L_i. Its number of components is 3 times the number of points used to discretize the *CL*, i.e. 720. The vectors L_i are used to construct the matrix *P* whose columns number equals to the number of patients in the learning dataset. Using the singular value decomposition (SVD) technique, the matrix *P* can be written as:

$$[L_1 \quad \dots \quad L_m] = P_m = M_m S_m V_m^T \qquad (1)$$

where the columns of M and V are respectively the left and right unit singular vectors and S_m the diagonal matrix composed of the *m* singular values σ_i of *P* listed in descending order. As the main information is contained in the first singular values, the matrix *P* can be approximated by *r* modes. The issue is to determine the minimum number of modes to capture anatomical variability. For a patient *i* of the learning dataset, the approximated $\hat{L}_i$ is expressed as the following linear combination:

$$\hat{L}_i = \sum_{k=1}^{r} M_k \alpha_k \quad \text{with} \quad \alpha_k = S_k V_k^T \qquad (2)$$

The mean *CL* of the learning dataset is then given by the 1st mode:

$$CL_{\text{mean}} = mean(\alpha_1)\ M_1 \qquad (3)$$

The range of CL deformation induced by the mode *i* is delimited by CL_{max} and CL_{min}:

$$\begin{cases} CL_{\max}(i) &= CL_{\text{mean}} + \max(\alpha_i)\, M_i \\ CL_{\min}(i) &= CL_{\text{mean}} + \min(\alpha_i)\, M_i \end{cases} \qquad (4)$$

2.3 Result analysis

The relative projection error ε_{in} due to the approximation with *r* modes is obtained by projecting the *CL* of the patients in the learning dataset considering a basis of *r* modes. ε_{in} is directly calculated from the singular values:

$$\varepsilon_{in}(r) = \sqrt{\frac{\sum_{k=r+1}^{m} \sigma_k^2}{\sum_{k=1}^{m} \sigma_k^2}} \qquad (4)$$

In order to evaluate the performance of the SSM, a leave-on-out approach was used. The removed *CL* L_i is approximated by $\hat{L}_i$ in the basis of *r* modes (for different values of *r*). For a dataset composed of *m* *CL*, the relative projection error ε_{out} is given by:

$$\varepsilon_{out}(r) = \sqrt{\frac{\sum_{i=1}^{m} \left\| L_i - \hat{L}_i(r) \right\|_2^2}{\sum_{i=1}^{m} \| L_i \|_2^2}} \qquad (5)$$

3 Results and Discussion

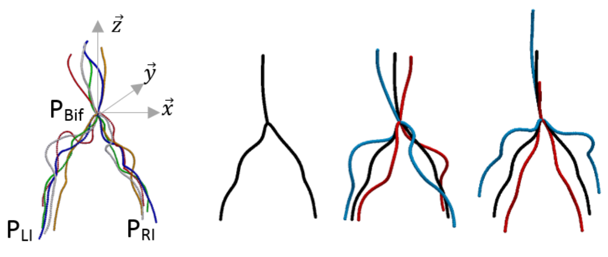

a) Learning dataset *b)* Mode 1 *c)* Mode 2 *d)* Mode 3

Fig. 1: a) Representation of some CLs of the learning dataset and b), c), d) reconstruction of CLs from the first three modes (CL_{mean}, CL_{max}, CL_{min}).

Preoperative CTs showing the vascular segments of interest of 556 patients who underwent endovascular AAA repair at the University Hospital of Rennes (France) between 2007 and 2017 were used to constitute the learning dataset (Fig.1a).

An illustration of the *CL*s reconstructed from the first three modes (Eq. 3, 4) is given in Fig. 1b,1c, 1d. The mode 2 corresponds to a complex deformation of the iliac arteries and an inclination of the abdominal aorta. The mode 3 influences the iliac tortuosity and the distance between P_{Bif} and the boundary points (P_R, P_{LI}, P_{RI}). Even if the definition of the boundary points is a source of inaccuracy, it is assumed to be negligible compared to the length of the vascular segments.

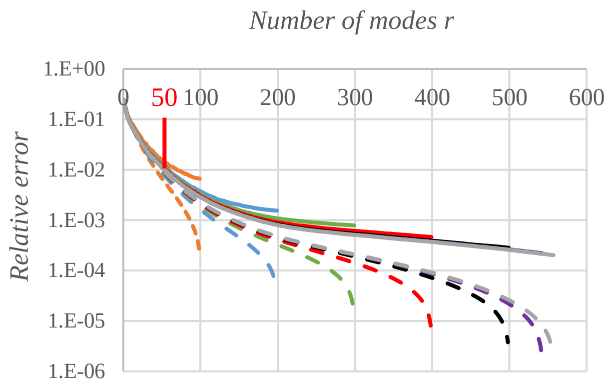

Fig. 2: Evolution of ε_{in} (dot line) and ε_{out} (closed line) according to r. For each curve, the maximum number of modes equals the number of patients in the learning dataset.

When the number of patients increases in the learning dataset, ε_{out} decreases and converges (Fig. 2). A large learning dataset is thus necessary to construct the SSM.

ε_{out} and ε_{in} are coincident for 50 modes. The relative error is then of about 1%. A CL external to the learning datasets can thus be estimated accurately.

These results show that a relatively high number of modes must be considered to accurately represent the human variability of aortoiliac anatomies with abdominal aortic aneurysm.

4 Conclusion

This study dealt with statistical shape modeling of tortuous and pathological vascular structures by considering a large dataset. We showed that it is possible to accurately represent the centerlines of aortoiliac structures of patients with AAA, provided that the numbers of modes and cases in the learning dataset are sufficient.

5 Acknowledgement

This work was partially supported by the French National Research Agency (ANR) in the framework of the Investissement d'Avenir Program through Labex CAMI (ANR-11- LABX-0004).

6 References

[1] Cootes, T.F., Taylor, C.J., Cooper, D.H., Graham, J. (1995) Active shape models—their training and application. *Comput. Vis. Image Underst*. 61, 38–59.

[2] Heimann, T., Meinzer, H.-P. (2009) Statistical shape models for 3D medical image segmentation: a review. *Med. Image Anal.* 13, 543–563.

[3] Rigaud, B., Simon, A., Gobeli, M., Leseur, J., Duverge, L., Williaume, D., Castelli, J., Lafond, C., Acosta, O., Haigron, P., De Crevoisier, R. (2018) Statistical shape model to generate a planning library for cervical adaptive radiotherapy. *IEEE Trans Med Imaging*. 33:1-11.

[4] Keustermans, W., Huysmans, T., Danckaers, F., Zarowski, A., Schmelzer, B., Sijbers, J., Dirckx, J.J.J. (2018) High quality statistical shape modelling of the human nasal cavity and applications. *R. Soc. open sci.* 5: 181558.

[5] Gaffney, B.M.M., Hillen T.J., Nepple J.J., Clohisy J.C., Harris, M.D. (2019) Statistical Shape Modeling of Femur Shape Variability in Female Patients with Hip Dysplasia. *J. Orthop Res.*

[6] Mousavi, S.R., Khalaji, I., Naini, A.S., Raahemifar, K., Samani A. (2012) Statistical finite element method for real-time tissue mechanics analysis. *Comp Methods Biomech Biomed Engin*, 15(6):595-608

[7] Scarton, A., Sawacha, Z., Cobelli, C., Li X. (2016) Towards the generation of a parametric foot model using principal component analysis: A pilot study. *Med Eng Phys*, 38(6):547-559.

[8] Bonarettia, S., Seiler, C., Boichon, C., Reyesa, M., Büchler, P. (2014) Image-based vs. mesh-based statistical appearance models of the human femur: Implications for finite element simulations. *Med Eng Phys*, 36:1626-1635.

[9] Wu, K., Daruwalla, Z.J., Wong, K.L., Murphy, D., Ren, H. (2015) Development and selection of Asian-specific humeral implants based on statistical atlas: toward planning minimally invasive surgery. *Int J Comput Assist Radiol Surg*, 10(8):1333-45.

[10] Wörz, S., von Tengg-Kobligk, Rohr, K. (2015) 3D statistical models of the aorta and the supra-aortic branches. *2015 IEEE 12th ISBI.*

[11] Casciaro, M., Craiem, D., Chironi, G., Graf, S., Macron, L., Mousseaux, E., Simon, A., Armentano, R. (2013) Identifying the Principal Modes of Variation in Human. *J. Thorac. Imaging*, 29(4):224-232.

[12] Thompson, M. M., Morgan, R. A., Matsumura, J. S., Sapoval, M., Loftus, I. M. (2007) Endovascular Intervention for Vascular Disease: Principles and Practice. *CRC Press.*

[13] Antiga, L., Piccinelli, M., Botti, L., Ene-Iordache, B., Remuzzi, A. and Steinman, D. A. (2008) An image-based modeling framework for patient-specific computational hemodynamics. *Med. Biol. Eng. Comput.*, 46 (11): 1097–1112.

Pelvic parameters measurement with sterEOS: a preliminary reliability study

Morgane DORNIOL, Guillaume DARDENNE, Aziliz GUEZOU-PHILIPPE, Hoel LETISSIER, Christian LEFEVRE and Eric STINDEL

University Hospital, University of Western Brittany, LaTIM - UMR 1101, 29200 Brest, France

Contact: Aziliz.GuezouPhilippe@univ-brest.fr

The goal of this preliminary study was to assess the reliability of the 3D pelvic parameters measurement by sterEOS. Two observers made measurements three times on pre and postoperative EOS images coming from ten patients. Intra- and inter-observer precision have been evaluated with intraclass coefficient (ICC). High intra- and inter-observer precision (ICC>0.8) was obtained for some parameters such as the femur length or the pelvic version, while others, such as the acetabulum anteversion or the anterior pelvic plane inclination had a low intra- and inter-observer precision, on both pre and postoperatives EOS images. Our results are partially consistent with the literature and further studies are needed to evaluate the impact of the observer experience on the reliability of those measurements.

1 Introduction

The orientation of the acetabular cup remains a major challenge in total hip arthroplasty (THA)[1]. New tools are continuously developed to allow orthopaedic surgeons to measure clinical parameters and assist them in their task [2, 3].EOS Imaging® developed a low-dose bi-planar radiography system and a planning software, sterEOS. It allows to measure on EOS images, several three dimensional (3D) pelvic parameters useful in THA: the acetabulum inclination and anteversion, the femoral head diameter, the offset, the femoral neck length, the CCD angle, the femur torsion, the pelvic incidence, the sacral slope, the pelvic version, the pelvic obliquity, the pelvis axial rotation and the anterior pelvic plane (APP) inclination. 3D parameters are automatically calculated after defining manually various anatomical landmarks (Fig.1). The goal of this study was to assess the reliability of these measurements, evaluating (1) the learning effect and (2) the precision of the measurements.

2 Methods

Two observers, a novice and an intermediate user, respectively an engineer and an orthopaedic surgeon, carried out measurements on pre and postoperative EOS images coming from ten patients in standing position. There were 5 males and 5 females and the mean age was 67.5±5.0 years old. Both observers made three times the measurements on the 20 images.

Learning effect has been assessed by recording the time required for the analysis of one radiograph in each session. Times in the first and last sessions were compared using the Wilcoxon and t tests for paired values [4].

Intraclass coefficient (ICC), their p-value and their 95% confidence interval (CI) have been calculated for each parameter to assess the intra-observer and inter-observer precision (with irr library in R version 3.5.3) based on a mean-rating, absolute agreement, two-ways mixed model [5].

3 Results

A learning effect has been observed for both observers. The intermediate and novice users reduced their measurement time between the first and the last sessions, from 14.2±8.3min to 5.1±1.8min and from 14.5±4.0min to 10.0±2.0min respectively, on preoperative EOS images. For both observers, this time reduction was statistically significant in terms of mean (t test p-value<0.02) and median (Wilcoxon test p-value<0.02).

Preoperative pelvic parameters	Intra-rater: engineer ICC	CI	Intra-rater: surgeon ICC	CI	Inter-rater ICC	CI
Acetabulum inclination	0.84***	0.54-0.96	0.39 .	-1.1-0.84	0.40 .	-0.26-0.72
Acetabulum anteversion	0.78**	0.36-0.94	0.67*	0.05-0.91	0.71***	0.40-0.86
Femoral head diameter	0.98***	0.93-0.99	0.97***	0.92-0.99	0.90***	0.75-0.96
Offset	0.99***	0.96-1.00	0.92***	0.79-0.98	0.90***	0.78-0.95
Femoral neck length	0.99***	0.98-1.00	0.95***	0.86-0.99	0.93***	0.84-0.96
CCD angle	0.91***	0.75-0.98	0.81**	0.45-0.95	0.80***	0.57-0.90
Femur torsion	0.75**	0.27-0.93	0.87***	0.62-0.96	0.69**	0.35-0.85
Femur length	0.99***	0.99-1.00	1.00***	1.00-1.00	1.00***	0.99-1.00
Pelvic incidence	0.98***	0.95-1.00	0.99***	0.96-1.00	0.96***	0.92-0.98
Sacral slope	0.97***	0.92-0.99	0.98***	0.93-0.99	0.94***	0.87-0.97
Pelvic version	0.99***	0.97-1.00	0.99***	0.98-1.00	0.98***	0.96-0.99
Pelvic obliquity	1.00***	0.99-1.00	0.99***	0.95-1.00	0.99***	0.96-0.99
Pelvis axial rotation	-0.43 .	-5.3-0.66	0.45 .	-0.66-0.85	0.61**	0.17-0.82
APP inclination	0.87***	0.63-0.97	0.77**	0.32-0.94	0.76***	0.50-0.88

Table 1: *Intraclass coefficient (ICC) and confidence interval (CI) for intra and inter-rater agreement, for every parameter measurement on preoperative EOS images (ICC p-value is (.)>0.05, (*)<0.05, (**)<0.01, (***)<0.001)*

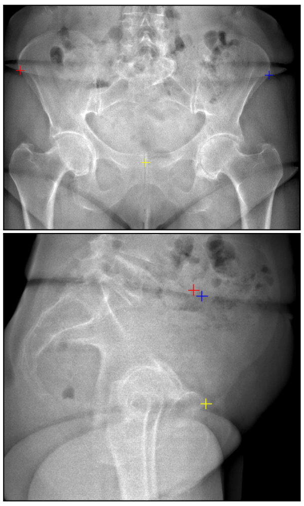

Figure 1: *Example of EOS images: the anterior posterior iliac spines (red, blue) and pubic symphysis (yellow) are defined by the user.*

All agreement results for preoperative parameters, are reported in Table 1.

Regarding the intra-observer precision on preoperative images, ICC greater than 0.8 with a small confidence interval was obtained for the femoral head diameter, the offset, the femoral neck length, the femur length, the pelvic incidence, the sacral slope, the pelvic version and the pelvic obliquity. ICC lower than 0.8 or with a large confidence interval was obtained for the acetabulum inclination, the acetabulum anteversion, the CCD angle, the femur torsion, the pelvis axial rotation and the APP inclination.

Regarding the inter-observer precision on preoperative images, we obtained good to excellent agreement for the femoral head diameter, the offset, the femoral neck length, the CCD angle, the femur length, the pelvic incidence, the sacral slope, the pelvic version and the pelvic obliquity. The agreement was poorer for the acetabulum inclination and anteversion, the femur torsion, the pelvis axial rotation and the APP inclination.

Similar results were found on postoperative EOS images. Intra-observer agreement was high (ICC>0.8) with small CI for the offset, the CCD angle, the femur length, the pelvic incidence, the sacral slope, the pelvic version and the pelvic obliquity. Intra-observer agreement was lower (ICC<0.8) or with big CI for the cup inclination, the cup anteversion, the stem torsion, the pelvic axial rotation and the APP inclination. Inter-observer agreement was high (ICC>0.8) for the offset, the CCD angle, the stem torsion, the femur length, the pelvic incidence, the sacral slope, the pelvic version, the pelvic obliquity and the pelvic axial rotation; and lower (ICC<0.8) for the cup inclination, the cup anteversion and the APP inclination.

4 Conclusion

We first observed a learning effect regarding the sterEOS software since the measurements time significantly decreased between the first and the last session. We also obtained a high intra and inter-observer precision regarding the femoral head diameter, the femur length, the pelvic version and pelvic obliquity. However, the agreement between and among observers was lower for the acetabulum inclination and anteversion, the CCD angle, the femur torsion, the pelvis axial rotation and the APP inclination.

These results are partially consistent with the litterature. Demzik *et al.* performed measurements on 25 postoperative images of patients [6]. The three involved physicians followed a training session before performing measurements. They obtained good inter- and intra-observer agreement with an ICC higher than 0.75 for all measurements. Thelen *et al.* analyzed the acetabular anteversion and inclination only, on 30 good quality EOS images from asymptotic volunteers [7]. Measurements were performed by two physicians and they obtained a good inter- and intra- agreement (ICC>0.8).

Those differences may be partly explained by the users' expertise level (novice and intermediate) and by the quality of images in our dataset. Further studies are therefore needed to evaluate the impact of the observer experience on the reliability of those measurements.

References

[1] Lewinnek, G.E., Lewis, J.L., Tarr, R., Compere, C.L., Zimmerman, J.R. (1978) Dislocations after total hip-replacement arthroplasties. *The Journal of Bone & Joint Surgery*, 60(2):217–220.

[2] Dardenne, G., Dusseau, S., Hamitouche, C., Lefèvre, C., Stindel, E. (2009). Toward a Dynamic Approach of THA Planning Based on Ultrasound. *Clinical Orthopaedics and Related Research*, 467(4):901–908.

[3] Rivière, C., Lazic, S., Villet, L., Wiart, Y., Allwood, S., Cobb, J. (2018) Kinematic alignment technique for total hip and knee arthroplasty *EFORT Open Reviews*, 3:98–105.

[4] Rietveld, T., van Hout, R. (2017) The paired t test and beyond: Recommendations for testing the central tendencies of two paired samples in research on speech, language and hearing pathology. *Journal of Communication Disorders*, 69:44–57.

[5] Koo, T.K. and Li, M.Y. (2016) A Guideline of Selecting and Reporting Intraclass Correlation Coefficients for Reliability Research *Journal of Chiropractic Medicine*, 15(2):155-163.

[6] Demzik, A., Alvi, H., Delagrammaticas, D., Martell, J., Beal, M., Manning, D.(2016). Inter-Rater and Intra-Rater Repeatability and Reliability of EOS 3-Dimensional Imaging Analysis Software. *The Journal of Arthroplasty*, 31(5):1091–1095.

[7] Thelen, T., Thelen, P., Demezon, H., Aunoble, S., Le Huec, J.-C. (2017) Normative 3D acetabular orientation measurements by the low-dose EOS imaging system in 102 asymptomatic subjects in standing position: Analyses by side, gender, pelvic incidence and reproducibility. *Orthopaedics & Traumatology: Surgery & Research*, 103(2):209–215.

Extended field-of-view of the knee bone surface using ultrasound

M. Nasan, Y. Morvan, G. Dardenne, J. Chaoui and E. Stindel
LaTIM, CHRU Brest, IMASCAP
Contact: nasan@univ-brest.fr

Since the invention of the Patient Specific Instruments (PSIs), they became the modern way to assist the surgeon in performing femur and tibia resection in Total Knee Arthroplasty (TKA). However, enable to have an accurate PSI, an accurate reconstruction of the surface of the knee bones is crucial. In this work, we introduce a new solution to build an extended field-of-view of the bones of the knee joint using ultrasound. Two registration methods are proposed using only a motorized ultrasound transducer: (1) a dense voxel-based method, and (2) a sparse point-based registration method. The preliminary qualitative results performed in vitro show that from a set of consecutive ultrasound volumes, an extended field-of-view can be reconstructed using only ultrasound images without any external trackers.

1 Methods

In this work, we investigated two different approaches to perform the registration of two consecutive ultrasound volumes: (1) a dense voxel-based registration method and (2) a sparse point-based registration method. The aim is to find the geometrical transformation which aligns every two volumes to compensate the absence of navigation data of the ultrasound transducer. In dense voxel-based, we need to pre-process the data before the alignment. Then, we perform a rigid 3D-3D voxel-based registration using Mutual Information of each pair of consecutive volumes. Sparse point-based registration is a different approach to find the best geometric transformation of two consecutive poses. Only a set of 3D points located on the surface of the bone is taken into account instead of the entire ultrasound volume. Therefore, in order to build a point set that represents the bone surface out of a stack of frames, we extract the Oriented FAST and rotated BRIEF (ORB) [1] features which represent the bone surface. Finally, we perform the so-called Coherent Point Drift (CPD) [2] point matching approach to find the best alignment of every two consecutive point sets.

2 Results

The preliminary qualitative results performed in vitro show that from a set of consecutive ultrasound volumes we can construct an extended field-of-view using only ultrasound images without any tracking markers as shown in Figure 1 and Figure 2.

Figure 1: *An aligned pair of ultrasound volumes using the dense voxel-based approach*

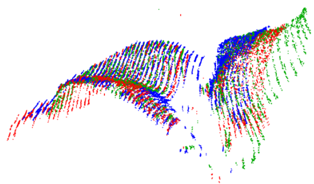

Figure 2: *Alignment of three ultrasound volumes of knee joint bones using the point-based approach*

3 Conclusion

Future work will focus on an in-vitro quantitative evaluation of the reconstruction and an in-vivo evaluation of the bone surface reconstruction.

SURGETICA 2019

Computer-assisted medical interventions

June 17-18
Rennes, France

Extended field-of-view of the knee bone surface using ultrasound

Maged Nasan[1,2,3], Yannick Morvan[3], Guillaume Dardenne[2,4], Jean Chaoui[3] and Eric Stindel[1,4]

([1] University of Western Brittany, [2] LaTIM, [4] Brest University Hospital Center) Brest, France [3] IMASCAP, Plouzané, France

I INTRODUCTION

Total Knee Arthroplasty (TKA) aims at replacing the damaged knee by a prosthesis to restore its functionality. A good long-term post-operative result is directly linked to the correct placement of the implant.
To design what is so-called Patient-Specific Instrumentations (PSIs), a personalized 3D model of the knee is required.

PSIs are disposable components designed using a planning software allowing surgeons to properly perform bone resections

3D model of patient's knee is essential for a proper implants placement

II CONTEXT

A AVAILABLE SOLUTION

Patient-Specific Instrumentation

PSIs are widely employed in orthopedics to improve the accuracy of bone resection [1]. Designing these PSIs requires a planning software and either:

- Magnetic Resonance Imaging (MRI)
- Computed Tomography (CT) scan

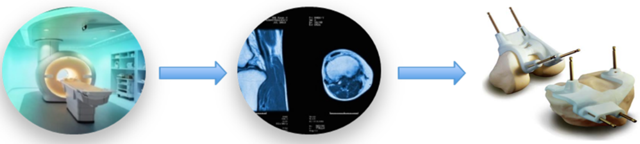

Scanning the patient — **Creation a 3D knee model** — **Printing 3D PSIs**

Invasive CT or costly MRI required

Ultrasound is an alternative, but:

- Noise
- Limited field of view
- Low signal to noise ratio
- Lack of navigation data

III MATERIALS AND METHODS

A MATERIALS

We have: Small volumes, each volume represents an anatomical region

- Ultrasonix SonixTablet
- 4DEC9-5/10 Transducer
- Porta SDK
- Propello
- Water tank
- Sow bone

SonixTablet — **Ultrasound transducer**

B METHODS

We want to Construct the whole ultrasound volume from smaller volumes [2]
How? 3D alignment of every two consecutive ultrasound volumes

3D-3D alignment methods

- Dense voxel-based
- Sparse point-based

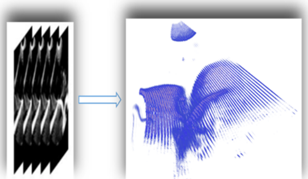

Scan-conversion

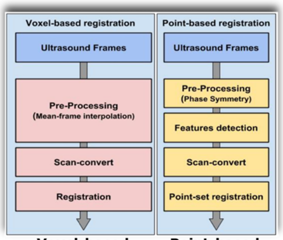

Voxel-based — **Point-based**

B1 DENSE VOXEL-BASED ALIGNMENT

Pre-processing

Why? To avoid zero-correspondence voxels when computing similarity measure and fill gaps

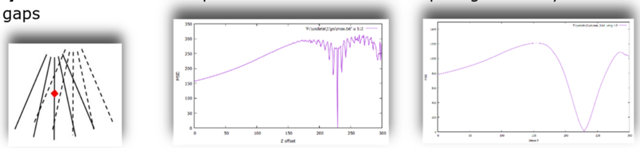

Zero-correspondence — **Mean Squared Displacement (Before pre-processing)** — **Mean Squared Displacement (After pre-processing)**

How? Insert an average-frame between every two frames

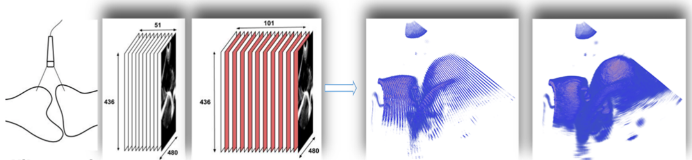

Ultrasound scan — **frame set** — **Interpolation** — **Ultrasound volume** — **Interpolated volume**

3D-3D alignment

How?
- Find mutual information of two ultrasound volumes for each displacement
- Find the displacement where the mutual information is maximal
- 6 DoF (translation and rotation)

B2 SPARSE POINT-BASED ALIGNMENT

Pre-processing

Why? To construct a point set that represents the bone surface in a volume

How?
- Find symmetry phase components [3] in a 2D ultrasound frame [4]
- Bony feature detection
- Scan-conversion

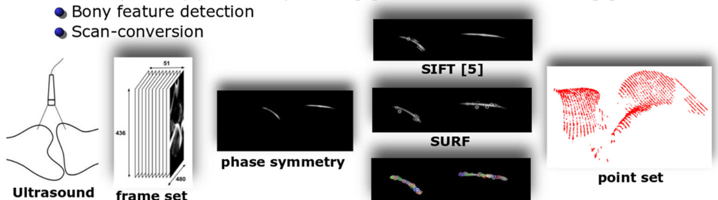

Ultrasound scan — **frame set** — **phase symmetry** — **SIFT [5]** — **SURF** — **ORB [6]** — **point set**

3D-3D alignment

How?
- Assign correspondences to recover the transformation mapping a point set A to another B
- Align 3 point sets having a shared region
- Find 6 DoF (translation and rotation) geometric transformation using Coherent Point Drift (CPD) [7]

IV RESULTS

Dense voxel-based alignment

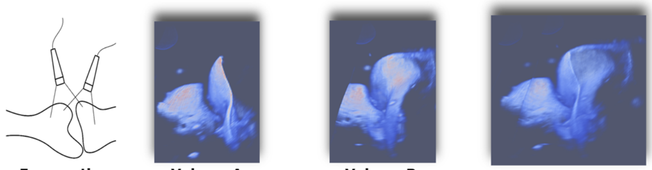

Free motion — **Volume A** — **Volume B** — **Volumes A and B aligned**

Sparse point-based alignment

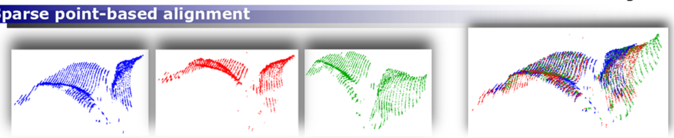

Point set A — **Point set B** — **Point set C** — **Alignment of A, B, and C**

V DISCUSSION AND CONCLUSION

Dense voxel-based approach
- Several similarity measures were tested (Mean Squares and Normalized Correlation)
- Interpolation is crucial to avoid local minima in the alignment process
- Mutual Information similarity measure is more robust against noise in ultrasound

Sparse point-based approach
- Bone surface detection using ORB features is faster than SIFT and SURF
- Fewer false positives when using ORB features
- CPD is more robust against noise than Iterative Closest Point (ICP)
- Faster in term of calculation compared to voxel-based method
- Absence of soft-tissue information

[1] Mattei, L. (2016). Patient specific instrumentation in total knee arthroplasty: a state of the art. In the Annals of translational medicine 4.7.
[2] Poon, Tony C. (2006). Three-dimensional extended field-of-view ultrasound. In The Ultrasound in medicine & biology 32.3: 357-369.
[3] Kovesi, Peter. "Symmetry and asymmetry from local phase.", 1997.
[4] Hacihaliloglu, I. (2008). Bone Segmentation and Fracture Detection in Ultrasound Using 3D Local Phase Features. In International Conference on Medical Image Computing and Computer-Assisted Intervention.
[5] Lowe, David G. "Distinctive image features from scale-invariant keypoints." International journal of computer vision 60.2 (2004): 91-110.
[6] Rublee, E. (2011) ORB: An efficient alternative to SIFT or SURF. In Computer Vision (ICCV), 2011 IEEE international conference on. IEEE.
[7] Myronenko, A. (2010). Point set registration: Coherent point drift. In IEEE transactions on pattern analysis and machine intelligence 32.12: 2262-2275.

Contact: nasan@univ-brest.fr

UBO Université de Bretagne Occidentale — Inserm La science pour la santé From science to health — LaTIM — imascap Surgeons to surgeons solutions — CHRU BREST CENTRE HOSPITALIER RÉGIONAL UNIVERSITAIRE

References

[1] Rublee, E., Rabaud, V., Konolige, K. and Bradski, G. (2011). ORB: An efficient alternative to SIFT or SURF. 2564-2571.

[2] Myronenko, A. and Song, X. (2010). Point set registration: Coherent point drift. *IEEE transactions on pattern analysis and machine intelligence*, 32(12):2262-2275.

Towards a patient-specific simulation of the balloon angioplasty treatment technique

***Bernard AL-HELOU*[1]*, Claire DUPONT*[1]*, Aline BEL-BRUNON*[2]*, Wenfeng YE*[3]*, Adrien KALADJI*[1]*, Pascal HAIGRON*[1]**

[1] Univ Rennes, CHU Rennes, INSERM, LTSI – UMR 1099, F-35000 Rennes, France
[2] Univ Lyon, INSA-Lyon, CNRS UMR5259, LaMCoS, F-69621 Lyon, France
[3] ANSYS, Villeurbanne F-69100, France
Contact: bernard.helou@etudiant.univ-rennes1.fr

This work addresses the issue of patient specific (PS) simulation of balloon angioplasty (BA). As a further step towards an ideal BA simulation scenario, this study focuses on two main issues: material modeling using plastic constitutive law to imitate the plaque permanent deformation and segmentation of the CT images to extract PS 3D geometry of the stenosed artery.

1 Introduction

Percutaneous Transluminal Angioplasty (PTA) is a minimally invasive treatment which consists of inserting and inflating a balloon in a stenosed artery aiming to restore its original lumen. Stents are usually used to maintain the arterial lumen reached by PTA; however, their use is questioned due to restenosis issues. Therefore, the issue of anticipating treatment outcome, in particular residual deformations after PTA remains open.

Several studies have developed computational models for PTA, mainly using finite elements methods (FEM) [1], either towards balloon design or treatment planning. Some FE studies related to the atherosclerotic plaque have considered 2D plaques biomechanical responses under different loadings [2,3] but it has been shown that plaque behavior is more accurately simulated with 3D models [4,5]. Few other studies considered 3D stress distributions within the plaques to analyze their sensitivity to geometrical and material composition changes [6-11].

Most studies modeled the plaque using an isotropic or anisotropic hyper-elastic constitutive law. A recent study shows that considering permanent deformations (using plastic model) should further be investigated in the aim of planning a PTA with FE simulations [12]. In addition to the constitutive law, one other main issue influencing PTA outcomes is the PS material properties assigned to the plaque. It is a challenge to experimentally characterize the plaque behavior *in-vivo*. The alternative is to deduce this mechanical behavior from the PS pre-operative images [1], as idealized geometries studies demonstrated that mechanical stresses are sensitive to small changes in plaque geometry and material properties [10,13].

Several imaging methods exist to model PS geometries of stenosed arteries such as histology, magnetic resonance imaging (MRI), computed tomography (CT) and intravascular ultrasounds (IVUS). Yet they all have limitations [1]: histology and high-resolution MRI can provide detailed description of the plaque but cannot be carried out *in vivo* [2,10]. Clinically used MRI can furnish detailed 3D description of soft plaques (though less spatially resolved) *in vivo* [3] but most protocols do not include it [14]. IVUS allows for 3D reconstruction of the *in vivo* artery, but presents risks on patients' safety and does not help differentiating plaque components. Finally CT technique can provide a 3D representation of stenosed vessel *in vivo*, especially by its ability in identifying calcifications, but with incapacities in distinguishing between other components such as fibrous and lipid-rich plaques. Up to our knowledge, studies that used CT as input images for geometrical PS BA simulations only extracted the stenosed lumen [11]. As CT is the only imaging technique used in BA protocols, we chose to focus on this acquisition method to build our PTA model. A complete workflow for PS simulation of PTA from CT images is under development. Here we focus on two essential steps of this workflow: 1. simulating residual deformations in the plaque after PTA using a plastic model; 2. extracting PS plaque composition and geometry from CT images using a segmentation approach.

2 Material and Methods

2.1 FE simulation

The workflow for a general FE simulation of PTA in an idealized stenosed arterial geometry has been studied. A cylindrical artery of 30 mm in length [8], 1 mm in thickness and stenosed by a non-symmetric calcified plaque of 60 % at its center was modeled as seen in Fig. 1a. Both the artery and the plaque were meshed using tetrahedral elements with connected meshes between the two parts (Fig. 1a). The artery at its two extremities was fixed in both translational and rotational motions. The Neo-Hookean hyper-elastic model was used for the arterial material with parameters from [15]. An isotropic bi-linear plastic model was considered for the calcified plaque. Young modulus for this plaque type was obtained from [16]. A displacement driven cylindrical balloon, mimicking the behavior of a non-compliant stiff balloon was modeled inside the stenosed artery. The 15 mm in length balloon (of shell elements) was inflated until reaching the healthy arterial wall diameter by permanently deforming the plaque and then deflated progressively. This non-linear numerical analysis including large deformations and contacts was solved using ANSYS implicit solver.

2.2 Patient-specific plaque geometry segmentation

CT angiography images of a highly calcified abdominal aortic stenosis were processed using 3D slicer and ITK-snap software. After selecting the desired region of interest and removing secondary branches, the lumen was extracted using the active contour method. Then the calcified plaque was segmented based on its high density. A subtract Boolean operation was then performed obtaining the un-calcified (lipid) plaque from what remains after removing the segmented lumen and calcified parts. Finally a growing operation was applied to the regions segmented previously in order to create the arterial wall (which cannot be clearly seen from the CT images).

3 Results

Fig. 1 shows the stenosed arterial behavior during and after BA treatment technique simulated in idealized geometry. Radial lumen gain is achieved along the plaque length after balloon deflation (Fig. 1c). In addition permanent longitudinal deformation is observed highlighting the importance of considering the 3D analysis in such studies.

In order to consider later a PS geometry in the simulation, CT scans are segmented as presented in Figs. 2 (a and b). Fig. 2 shows a coronal cross section of the CT scans. The 3D geometry is then generated from the segmentation label-map after some smoothing iterations (Fig. 2c).

By mapping material properties based on CT densities, this geometric model could be used to attain a complete PTA simulation workflow.

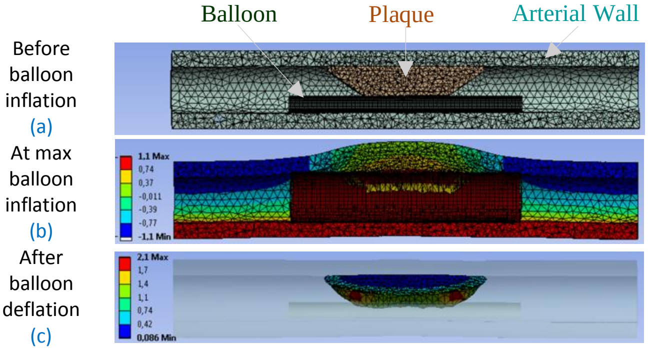

Fig 1: Stenosed artery behavior before, during (radial deformations in mm) & after (Equiv. plastic strains) BA.

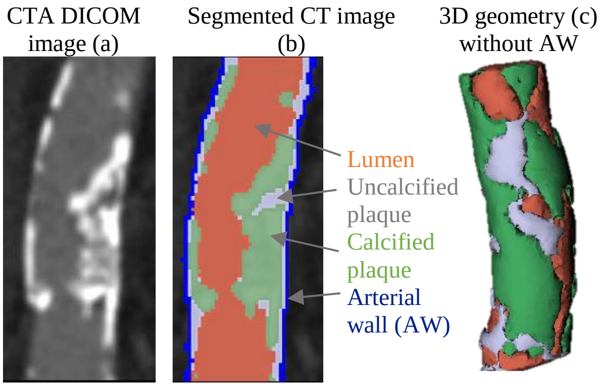

Fig. 2: From CT scans to 3D model of stenosed artery with highly calcified plaque. Lumen is labeled in orange, calcified plaque in green, un-calcified plaque in grey and arterial wall (AW) in blue.

4 Conclusion

This study describes the first steps towards a PS simulation of BA treatment: PS geometry segmentation of different plaque components and FE computation of residual deformations in a generic stenosed artery. After combining both, evaluation of plastic material model contribution in mimicking plaque behaviors will be performed using post-operative CT-scans.

5 Acknowledgements

This work was partially supported by the Bretagne region and by the National Research Agency (ANR) in the framework of Investissement d'Avenir Program through Labex (ANR-11-LABX-0004).
We thank Dr Antoine Lucas from University Hospital of Rennes for his help in understanding the clinical issues related to balloon angioplasty.

6 References

[1] Holzapfel, G. A., Mulvihill, J. J., Cunnane, E. M., & Walsh, M. T. (2014). Computational approaches for analyzing the mechanics of atherosclerotic plaques: A review. *Journal of Biomechanics*, 47(4): 859–869.

[2] Li, Z. Y., Howarth, S., Trivedi, R. A., U-King-Im, J. M., Graves, M. J., Brown, A., … Gillard, J. H. (2006). Stress analysis of carotid plaque rupture based on in vivo high resolution MRI. *Journal of Biomechanics*, 39(14): 2611–2622.

[3] Sadat, U., Li, Z. Y., Young, V. E., Graves, M. J., Boyle, J. R., Warburton, E. A., … Gillard, J. H. (2010). Finite element analysis of vulnerable atherosclerotic plaques: A comparison of mechanical stresses within carotid plaques of acute and recently symptomatic patients with carotid artery disease. *Journal of Neurology, Neurosurgery and Psychiatry*, 81(3), 286–289.

[4] Tang, D., Yang, C., Kobayashi, S., Ku, D.N. (2004). Effect of a lipid pool on stress/strain distributions in stenotic arteries: 3-D fluid–structure interactions (FSI) models. *Journal of Biomechanical Engineering*, 126, 363–370.

[5] Nieuwstadt, H. A., Akyildiz, A. C., Speelman, L., Virmani, R., van der Lugt, A., van der Steen, A. F. W., … Gijsen, F. J. H. (2013). The influence of axial image resolution on atherosclerotic plaque stress computations. *Journal of Biomechanics*, 46(4), 689–695.

[6] Liang, D. K., Yang, D. Z., Qi, M., & Wang, W. Q. (2005). Finite element analysis of the implantation of a balloon-expandable stent in a stenosed artery. *International Journal of Cardiology*, 104(3), 314–318.

[7] Timmins, L. H., Meyer, C. A., Moreno, M. R., & Moore, J. E. (2008). Effects of Stent Design and Atherosclerotic Plaque Composition on Arterial Wall Biomechanics. *Journal of Endovascular Therapy*, 15(6), 643–654.

[8] Karimi, A., Navidbakhsh, M., Faghihi, S., Shojaei, A., & Hassani, K. (2013). A finite element investigation on plaque vulnerability in realistic healthy and atherosclerotic human coronary arteries. Proceedings of the Institution of Mechanical Engineers, Part H: *Journal of Engineering in Medicine*, 227(2), 148–161.

[9] Kiousis, D. E., Rubinigg, S. F., Auer, M., & Holzapfel, G. A. (2009). A Methodology to Analyze Changes in Lipid Core and Calcification onto Fibrous Cap Vulnerability: The Human Atherosclerotic Carotid Bifurcation as an Illustratory Example. *Journal of Biomechanical Engineering*, 131(12), 121002.

[10] Holzapfel, G. A., Stadler, M., & Schulze-Bauer, C. A. J. (2002). A Layer-Specific Three-Dimensional Model for the Simulation of Balloon Angioplasty using Magnetic Resonance Imaging and Mechanical Testing. *Annals of Biomedical Engineering*, 30(6), 753–767.

[11] Auricchio, F., Conti, M., De Beule, M., De Santis, G., & Verhegghe, B. (2011). Carotid artery stenting simulation: From patient-specific images to finite element analysis. *Medical Engineering and Physics*, 33(3), 281–289.

[12] Conway,C., McGarry, J.P., Edelman , E.R.,& McHugh, P.E. (2017). Numerical Simulation of Stent Angioplasty with Predilation: An Investigation into Lesion Constitutive Representation and Calcification Influence. *Annals of biomedical engineering*, 45, 2244-2252.

[13] Akyildiz, A.C., Speelman, L., van Brummelen, H., Gutiérrez, M.A., Virmani, R., van der Lugt, A., van der Steen, A.F., Wentzel, J.J., & Gijsen, F.J., (2011). Effects of intima stiffness and plaque morphology on peak cap stress. *Biomedical Eng Online* 10, 25

[14] Nieuwstadt, H.A., Geraedts, T.R., Truijman, M.T.B., Kooi, M.E., vanderLugt, A., van der Steen, A.F.W., Wentzel, J.J., Breeuwer, M., Gijsen, F.J.H., (2013). Numerical simulations of carotid MRI quantify the accuracy in measuring atherosclerotic plaque components in vivo. *Magn. Reson. Med*. 72, 188-201

[15] Paini, A., Boutouyrie, P., Calvet, D., Zidi, M., Agabiti-Rosei, E., & Laurent, S. (2007). Multiaxial mechanical characteristics of carotid plaque: Analysis by multiarray echotracking system. *Stroke*, 38(1), 117–123.

[16] Maher, E., Creane, A., Sultan, S., Hynes, N., Lally, C., & Kelly, D. J. (2009). Tensile and compressive properties of fresh human carotid atherosclerotic plaques. *Journal of Biomechanics*, *42*(16), 2760–2767

Nervous System Exploration Using Tractography To Enhance Pelvic Surgery

***Cécile Olivia MULLER**, Alessandro DELMONTE*, Pierre MEIGNAN, Quoc PEYROT, Alessio VIRZI, Laureline BERTELOOT, David GREVENT, Thomas BLANC, Pietro GORI, Nathalie BODDAERT, Isabelle BLOCH, Sabine SARNACKI**

IMAG2 Laboratory, Imagine Institute, Paris, France
Université Paris Descartes, Paris, France
Pediatric Surgery and Radiology Departments, Necker Hospital, APHP, Paris, France
LTCI, Télécom ParisTech, Université Paris-Saclay, Paris, France
Contact: sabine.sarnacki@aphp.fr

Pelvic surgery raises the challenge of preservation of nerves that handle urinary, genital and digestive functions, especially in situations where these structures may be modified by tumors or malformations. Recent works on 3D nerve visualization, that rely on cadavers dissections [1, 3] or intra-operative use of probes detecting myelin-binding fluorophores [5], do not provide pre- or post-operative analysis of the pelvic nervous anatomy. Magnetic resonance neurography as in [12] requires a slice by slice manual segmentation of the nerves. Diffusion MRI, associated with tractography algorithms, is currently the only technique allowing for in-vivo exploration of the nervous network [2] with no need for manual nerve segmentation. In contrast to brain imaging that motivated a lot of work, only few studies focus on peripheral nerves visualization [9, 10, 14]. In this paper, we propose a method for pelvic tractography analysis based on patient-specific organ segmentation. It is demonstrated with promising results on a healthy adult subject.

1 Anatomy of the Pelvic Nervous Network

The pelvis region is a complex 3D structure gathering urinary, genital and digestive systems (see e.g. [8]). These systems are both irrigated and innervated by an intricate network of vessels and nerves, enclosed by a tight bony and muscular cage (Fig. 1). Somatic functions of pelvic organs are ensured by a ramified nervous network, originating from the spine and issuing from L4-L5 vertebral canals and S1-S4 sacral holes. Autonomous functions are ensured by the presacral sympathetic/parasympathetic networks originating from neural crest migration. Being directly involved in both conscious and unconscious motricity and sensitivity of organs and skin, the main nerve bundles to be preserved during surgical operations are the sacral plexus, pudendal plexus, pudendal nerve, and inferior hypogastric plexus.

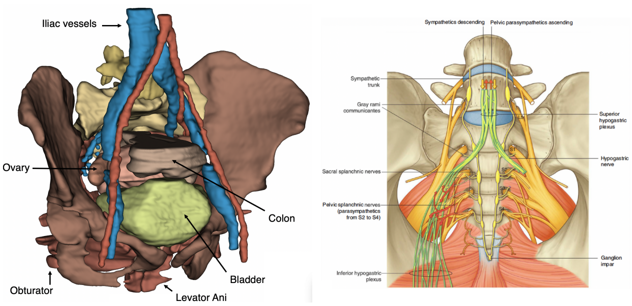

Figure 1: *Left: Pelvis 3D model for an adult healthy female subject. Right: Pelvic somatic and autonomous nerves [8].*

2 Methods

The complexity of the nervous network anatomy makes it difficult both to observe using standard CT and MRI sequences, and to analyze, thus limiting the de-

*A. Delmonte and C. Muller contributed equally to this work.

velopment of nerve preservation techniques in pelvic surgery. The proposed method relies on a combination of anatomical and diffusion MRI sequences, segmentation of anatomical structures, and recognition of the nerves from tractography based on their spatial arrangement.

2.1 Data Preparation

The data used to illustrate the method are MRI images of an adult healthy female subject. A volumetric T2w image (with a voxel size of $0.625 \times 1 \times 0.625\, mm^3$) was used for the organ segmentation. A DWI image was acquired with 50 directions, $b = 1000$, voxel size of $2.5 \times 2.5 \times 3.5\, mm^3$, and a tractogram was computed using a diffusion tensor based algorithm, with the software MRTrix3 [13]. To avoid inherent limitations of ROI based pelvic tractography (e.g. lack of reliable seeds positioning due to noise issues) [10] limiting tractograms accuracy, we selected seeds sparsely in a whole-body mask. The parameters were set as follows: seeds condition $FA > 0.15$, termination condition $FA < 0.01$, fibers length $= 50 - 800mm$. The final whole-body tractogram was composed by one million fibers.

2.2 Organ Segmentation

Pelvic organs segmentation (Fig. 1) was manually performed by an expert surgeon on the T2w image within the 3DSlicer [11] environment. The segmented regions were: pelvic bones (hips and sacrum) and muscles (piriformis, coccygeal, obturator and levator ani), bladder with the ureters, genital system (vagina, uterus and ovaries), colon and rectum, iliac vein and arteries. In order to provide additional spatial references to the tractography segmentation algorithm, specific regions of interest for nerves (sacral canal, sacral holes and ischial spine) were subsequently identified in the image.

2.3 Tractogram Processing and Nerve Recognition

Due to the huge amount of false positives encountered in whole-body tractograms, we introduce a filtering algorithm that exploits spatial relations between nerve bundles and segmented anatomical structures. The core of the contribution is the recognition of each nerve bundle based on directional, path, connectivity and orientation information. For instance, S4 is described as "crossing **SacralHoleS4** *and* crossing **SacrumCanal**". Similar descriptions have been developed for all nerve bundles of interest. Translating these descriptions, expressed in natural language, into operational algorithms requires modeling each spatial relation. An approach based on simple relations between bounding boxes of organs, as proposed in [15] for brain white matter, is not sufficiently accurate given the complexity of the pelvic structures. Therefore, we propose to rely on the previous segmentation, and on fuzzy definitions of spatial relations [4], similarly to [6, 7]. For instance, a directional relation with respect to a given structure is modeled as a cone originating from this structure and oriented in the desired direction, and a fiber in this cone satisfies the directional relation to the structure. A recognized bundle is then a set of fibers satisfying the description.

3 Results

Sacral Plexus (from L5 to S4), Pudendal Plexus (P) and Inferior Hypogastric Plexus (IHP) are represented in Fig. 2 along with relevant structures. Optimal concordant anatomical results were obtained for the sacral plexus, including sacral root S4. The pudendal nerve, originating from the pudendal plexus, was not viewed in its entirety until the pubic junction. The inferior hypogastric plexus is a thin but rich nervous network which was not completely represented either. The use of higher resolution diffusion images could further improve the results.

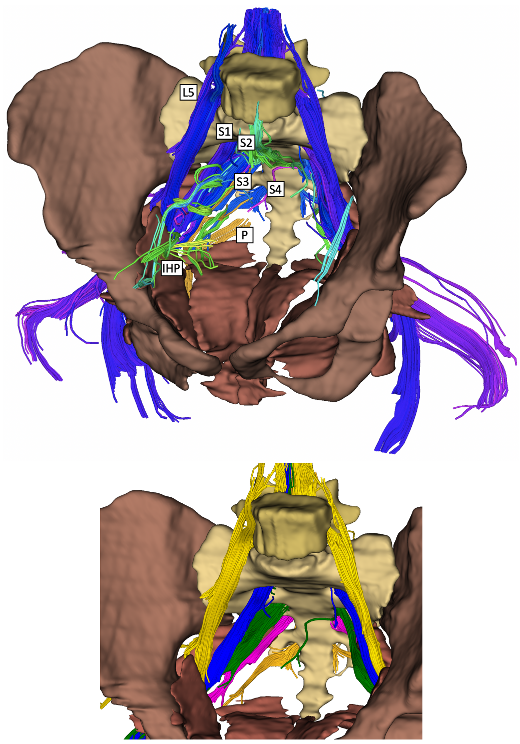

Figure 2: *Top: Sacral (Blue), Pudendal (Orange) and Hypogastric (Green) plexuses obtained with the proposed method. Bottom: Sacral Plexus detail.*

4 Conclusion

This preliminary study demonstrates the feasibility to visualize both somatic and autonomous pelvic nervous network using in-vivo tractography techniques. We are currently evaluating applications for surgical planning and post-operative follow-up in pediatric cases of pelvic malformations and tumors.

References

[1] V. Balaya, F. Guimiot, J. F. Uhl, C. Ngo, M. Delomenie, H. Bonsang-Kitzis, M. Gosset, M. Mimouni, A. S. Bats, V. Delmas, R. Douard, and F. Lécuru. Three-Dimensional Modelization of the Female Human Inferior Hypogastric Plexus: Implications for Nerve-Sparing Radical Hysterectomy. *Gynecologic and Obstetric Investigation*, 2018.

[2] P. J. Basser, S. Pajevic, C. Pierpaoli, J. Duda, and A. Aldroubi. In vivo fiber tractography using DT-MRI data. *Magnetic Resonance in Medicine*, 44(4):625–632, 2000.

[3] M. M. Bertrand, F. Macri, R. Mazars, S. Droupy, J. P. Beregi, and M. Prudhomme. MRI-based 3D pelvic autonomous innervation: a first step towards image-guided pelvic surgery. *European Radiology*, 24(8):1989–1997, 2014.

[4] I. Bloch. Fuzzy Spatial Relationships for Image Processing and Interpretation: A Review. *Image and Vision Computing*, 23(2):89–110, 2005.

[5] V. E. Cotero, S. Y. Kimm, T. M. Siclovan, R. Zhang, E. M. Kim, K. Matsumoto, T. Gondo, P. T. Scardino, S. Yazdanfar, V. P. Laudone, and C. A. Tan Hehir. Improved Intraoperative Visualization of Nerves Through a Myelin-Binding Fluorophore and Dual-Mode Laparoscopic Imaging. *PloS One*, 10(6):1–18, 2015.

[6] A. Delmonte, I. Bloch, D. Hasboun, C. Mercier, J. Pallud, and P. Gori. Segmentation of White Matter Tractograms Using Fuzzy Spatial Relations. In *Organization for Human Brain Mapping (OHBM)*, Singapore, 2018.

[7] A. Delmonte, C. Mercier, J. Pallud, I. Bloch, and P. Gori. White matter multi-resolution segmentation using fuzzy set theory. In *IEEE International Symposium on Biomedical Imaging (ISBI)*, Venice, Italy, 2019.

[8] R. L. Drake, W. Vogl, A. Mitchell, and H. Gray. *Gray's Anatomy for Students*. Churchill Livingstone/Elsevier, Philadelphia, 41st edition, 2015.

[9] D. S. Finley, B. M. Ellingson, S. Natarajan, T. M. Zaw, S. S. Raman, P. Schulam, R. E. Reiter, and D. Margolis. Diffusion Tensor Magnetic Resonance Tractography of the Prostate: Feasibility for Mapping Periprostatic Fibers. *Urology*, 80(1):219–223, 2012.

[10] W. Haakma, J. Hendrikse, L. Uhrenholt, A. Leemans, L. Warner Thorup Boel, M. Pedersen, and M. Froeling. Multicenter reproducibility study of diffusion MRI and fiber tractography of the lumbosacral nerves: DTI of the Lumbosacral Nerves. *Journal of Magnetic Resonance Imaging*, 48(4):951–963, 2018.

[11] R. Kikinis, S. D. Pieper, and K. G. Vosburgh. 3D Slicer: A Platform for Subject-Specific Image Analysis, Visualization, and Clinical Support. *Intraoperative Imaging and Image-Guided Therapy*, 3(19):277–289, 2014.

[12] P. Li, P. Liu, C. Chen, H. Duan, W. Qiao, and O. H. Ognami. The 3D reconstructions of female pelvic autonomic nerves and their related organs based on MRI: a first step towards neuronavigation during nerve-sparing radical hysterectomy. *European Radiology*, 28(11):4561–4569, 2018.

[13] J. D. Tournier, F. Calamante, and A. Connelly. MRtrix: Diffusion tractography in crossing fiber regions. *International Journal of Imaging Systems and Technology*, 22(1):53–66, 2012.

[14] P. K. N. van der Jagt, P. Dik, M. Froeling, T. C. Kwee, R. A. J. Nievelstein, B. ten Haken, and A. Leemans. Architectural configuration and microstructural properties of the sacral plexus: a diffusion tensor MRI and fiber tractography study. *NeuroImage*, 62(3):1792–1799, 2012.

[15] D. Wassermann, N. Makris, Y. Rathi, M. Shenton, R. Kikinis, M. Kubicki, and C. F. Westin. On describing human white matter anatomy: the white matter query language. In *International Conference on Medical Image Computing and Computer-Assisted Intervention (MICCAI)*, volume LNCS 8149, pages 647–654, 2013.

Transvaginal Uterine Biopsy: Robot Comanipulation

Nassim TAJEDDINE, Marie-Aude VITRANI and Rémi CHALARD
Sorbonne Universite, CNRS UMR 7222, INSERM U1150, ISIR
ISIR, 4 Place Jussieu, CC173, 75005 Paris
Contact: nassim.tajeddine@etu.upmc.fr

Uterine laparoscopy in sarcoma ablation risks the spread of cancer cells in the abdominal cavity because of the Laparoscopic Power Morcellator (LPM). To adapt the ablation procedure, transvaginal uterine biopsy has been proposed in pre-operative diagnosis. Based on a robot assisted transrectal prostate biopsy, this paper studies the adaptability of the robot to the transvaginal uterine biopsy procedure in order to enhance the precision of the surgeon's movements.

1 Introduction

Every year, 6000 new cases of uterine cancer occur in France [1]. Uterine cancer can be suspected via invasive and non invasive tests: pelvic or transvaginal ultrasound and hysteroscopy to observe the potential cancerous area [2]. The usual method is to remove the suspect lesion using laparoscopy with the Laparoscopic Power Morcellator (LPM) and examine it postoperatively. The major issue with that method is that, if the patient suffers from uterine cancer, the spread of cancer cells in the abdominal cavity is possible, resulting in the possible expansion of cancer to other organs [3]. Indeed, LPMs are used to fragment tissues to allow surgical specimens to be removed through small incisions. To adapt the ablation procedure (laparoscopy vs open surgery) and minimize the risk of expanding cancer cells, the kind of tissue to be removed should be known preoperatively. Based on this consideration, a new cancer detection procedure by using transvaginal uterine biopsy is presented in [4]. That procedure would be performed during routine transvaginal clinical examination and would thus require less preparation than surgery. To locate and reach the suspect regions on the uterus, high precision and stabilization of the clinician's movements are required. Robot-assisted ultrasound-guided biopsies have shown that degree of precision in robot assisted transrectal prostate biopsy described in [5]. This paper presents the adaptability of the robot used for transrectal prostate biopsy to transvaginal uterine biopsy.

2 Anatomical description

The uterus is described in [6]. It is a hollow pear-shaped organ located in the pelvic cavity between the rectum and the bladder and is generally anteflexed and anteverted over the bladder. The basal extremity of the uterus, namely the cervix, is located in the vagina (see Fig.1). The vagina is an elastic muscular canal. Its average dimensions are 9.4cm in length [7].

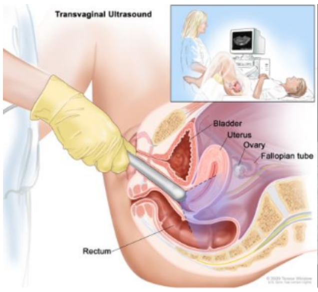

Fig.1: Transvaginal echography with patient anatomy.

It is important to note that the anatomy of the uterus and vagina has strong inter-individual variability. Moreover, the patients undergoing the diagnosis procedures might suffer from uterine cancer, resulting in more variations of the shape, weight and position of these organs. Based on [4], the uterine biopsy procedure should be similar to the gynecological physical exam. The patient is lying down on a gynecological table, her legs are suspended on stirrups. The diagnosis test is described as follows: the ultrasound probe is inserted into the vagina up to the cervix as shown in fig.2. The probe has a small mobility described by the our referent surgeon as a 2 cm square limited by the cervix and the vaginal wall. This area of movement has also been highlighted in other works [8]. The probe can still be moved in many orientations limited by the anatomy of the vagina.

3 Results: Workspace simulation

To test the adaptability of the robot used for transrectal prostate biopsy to transvaginal uterine biopsy, both the workspace of the robot and the estimated workspace of the physician's movements have been modeled and compared. The robot is presented in [5], it is an anthropomorphic arm with 3 active DoFs and a free-wrist presented in fig.2 and tab.1.

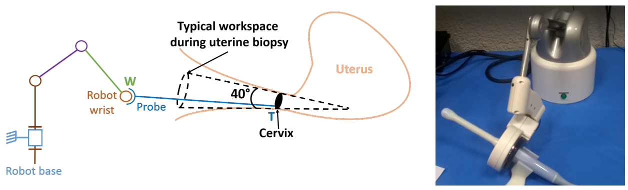

Fig.2: Apollo Robot [5] and its kinematic model.

Table 1: DH parameters of the Apollo robot

i	α_i	a_i	θ_{i+1}	d_{i+1}
0	0	0	θ_1	0
1	$\pi/2$	0	θ_2	0
2	0	25	θ_3	0
3	$-\pi/2$	0	θ_4	-30
4	$-\pi/4$	0	θ_5	0
5	$-\pi/2$	0	θ_6	0

Mechanical constraint: $\theta_2 + \theta_3 < 90°$.

The possible movements of the probe and the anatomical limitations described previously have been modeled using Matlab environment and shown in fig.3.

It is hypothesized that the tip of the probe is located between the cervix and the vaginal wall. They both make up the limits of an area in which the physician can move the tip of the probe and change its orientation with a 20° angle. It is also hypothesized the patient's organs are of average dimensions and positioning, inter-individual anatomical variability has not yet been taken into account.

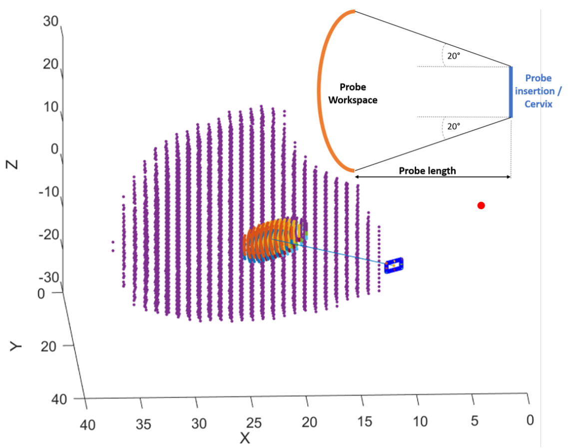

Fig.3: Possible positions of the probe and its orientations within the cropped workspace of Apollo & sketch of the probe workspace

In fig.3, the possible movements of the tip of the ultrasound probe between the vaginal wall and the cervix described in Section.2 are shown by the 2 cm blue square. The ultrasound probe is modeled by the blue line. The red dot is the origin of the system located in the robot basis. The insertion area and the probe length are known so, as it is highlighted on the 2-D scheme in fig.3, it is possible to model the possible movements of the end of the probe held by the physician during the clinical exam by the arcs as shown in fig.3.

Thanks to the simulation, it appears that all the surgeon's possible movements during a uterine biopsy session are compatible with the robot workspace (see fig.3). However, during the clinical routine, the patient can be considered as fixed so the surgeon workspace is fixed also. Moreover, the reference position of the robot impacts the robot workspace. Taking into account these two considerations, the position of the robot in the clinical routine appears as a main issue.

4 Application to clinical routine

Based on previous studies, the optimal position of the robot basis is next to the right of the patient's insertion point (1 in fig.4a) but it is not possible in uterine biopsy due to the leg of the patient being an obstacle to the axis of the robot. With current kinematic parameters and to allow all the physician's movements, the best position of the robot basis is beside the patient, under her legs laterally to the vulva (2 in fig.4a). However, as shown in fig.4a, this position is also impossible due to the stirrups. The surgeon partner suggested to position the robot directly between the legs of the patient central and lower to the vulva (3 in fig.4a). That position would not allow the physician's full movements with current kinematic parameters (see fig.4b). Lengthening the a_2 and d_4 parameters respectively to 35 cm and 40 cm as well as increasing the mechanic constraint $\theta_2 + \theta_3 < 90°$ to 135° would make that positioning possible (see fig.4c).

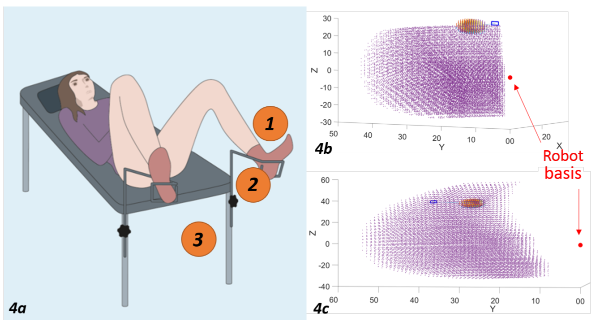

Fig.4: Positions of the robot in relation to the patient during a physical examination [9], modified.

5 Conclusion

Adaptability of the Apollo robot from transrectal prostate biopsy to transvaginal uterine biopsy is possible despite anatomical differences. Positioning of the robot during physical examination is still being studied and is dependant on potential kinematic modifications of the robot.

References

[1] Sancho-Garnier, H. (2013). Epidémiologie des cancers gynécologiques: utérus, ovaire, vulve, vagin. *Cancers gynécologiques pelviens. Elsevier Masson, Paris*, 85–99.

[2] American Cancer Society.https://www.cancer.org/

[3] Fda 2014: Laparoscopic power morcellation during uterine surgery for fibroids, 2014.

[4] Fazel, A. , Vitrani, M.-A., Gaudrard, E. and Baumann, M. (2016) Robotic Biopsy of the Uterus Standardized Technique (ROBUST): A New Technique for Uterine Biopsy Prior to Minimally Invasive Surgery. *Journal of Minimally Invasive Gynecology. Elsevier*, 23(7):227-228.

[5] Poquet, C. , Mozer, P. , Morel, G. and Vitrani, M.-A. (2013) A novel comanipulation device for assisting needle placement in ultrasound guided prostate biopsies *2013 IEEE/RSJ International Conference on Intelligent Robots and Systems*, 4084–4091.

[6] Bouton, J.-M., Dehnez, M. Ebou, F., Hainaut, F., Michelin, J., and Mac Aleese, J. (1990) Pratique de lchographie en gyncologie et obsttrique.

[7] Tan, J. S., Lukacz, E. S., Menefee, S. A., Luber, K. M., Albo, M. E., and Nager, C. W. (2006). Determinants of vaginal length. *American journal of obstetrics and gynecology*, 195(6):1846-1850.

[8] De Smet, J., Deprest, J., Vander Poorten, E. (2019). In-vivo Force Sensing during Laparoscopic Sacrocolpopexy Vaginal Vault Manipulation. *Journal of Medical Robotics Research*

[9] https://www.ameli.fr

Surface imaging for patient positioning in radiotherapy

Souha NAZIR, Julien Bert, Dimitris VISVIKIS and Hadi FAYAD

LaTIM, UBO, INSERM UMR 1011, 29200 Brest, France
Hamad Medical Corporation OHS, PET/CT center Doha, Qatar
Tel : +33 (0)6 23 36 67 73
Contact: souha.nazir@univ-brest.fr

One of the main concerns in external beam radiation therapy is the daily patient positioning. The positioning accuracy is crucial for optimal dose delivery providing a maximum absorbed dose in the tumor than in the surrounding healthy tissues. Clinical techniques expose the patient to extra radiation dose. In this paper, we propose a noninvasive technique, based on surface imaging, that estimates the patient's 6 degrees of freedom (DOF) position using the Iterative Closest Point (ICP) registration algorithm. This technique allows an accurate patient positioning with a real time monitoring of intra-fraction motion.

1 Introduction

In external beam radiation therapy, accurate patient positioning emphasizes patient safety, optimizes treatment set-up, and improves clinical efficiency.
The patients are routinely positioned based on the skin marks and the conventional laser-alignment system. This technique is associated to reliable methods of daily radiographs images that are used to ensure accurate positioning providing good visualization of internal anatomical structures (bones, soft tissue) [1]. However, these ionizing techniques expose patients to additional radiation dose [2], and do not provide real time information such as respiratory, cardiac or gastrointestinal motion that may cause the movement of the target.
Alternative techniques such as AlignRT (VisionRT) [3] and Sentinel from C-RAD [4] have been recently introduced. These techniques are optical systems that reconstruct a 3D surface based on the structured light approach. Though, these systems provide noninvasive tools for patient positioning, their frame rate is limited, thus do not allow for real time positioning. Furthermore, these techniques are not able to accurately reconstruct low reflective surfaces such as hair or clothes [5]. Another optical imaging system, Catalyst from C-RAD [6], has been developed allowing for real time positioning. However, this system yields deficient performance [7].

In the last few years, new technologies based on depth imaging have been developed presenting a potential challenge for traditional 3D imaging methods [8]. For instance, time of flight (TOF) technology used in various depth imaging cameras has showed higher frame rate allowing for real time acquisitions.

In this paper, we investigate the position detection accuracy of SR4000 and Kinect V2 depth cameras. This is a primary step to find a reliable patient positioning system that could be used for as alternative to the existing clinical techniques.

2 Materials and methods

A TOF camera is a depth sensor that provides 3D surface information at 30 frames per second. It measures the distance from the camera to each object in the scene based on the time of flight principle. This principle consists of finding the phase delay between the emitted and reflected infrared (IR) waves following the equation below:

$$D = \frac{c}{2}\frac{\Delta\varphi}{2\pi f} \qquad (1)$$

Where c is the speed of light, $\Delta\varphi$ is the phase delay between signals and f is the camera modulation frequency.

In this study, two surface imaging systems (SR4000 and Kinect V2) were used for patient monitoring. The cameras were mounted on the ceiling of the radiotherapy treatment room, at the CHRU Brest, at a distance of 1.34 m from the isocenter.

The couch 6 DOF motions were calculated using a surface registration method based on ICP algorithm [9]. Patients were routinely positioned using conventional clinical techniques. A simultaneous surface scan by our imaging system was performed. The surfaces acquired before and after patient positioning were analyzed and registered in order to calculate the couch 6DOF movements. A rigid registration is performed using ICP algorithm that aims to find the transformation (rotation matrix R and translation matrix T) between two surfaces allowing the best match between them. Thus, for each point of the source surface Y, ICP finds the closest point in the reference surface X by minimizing the distance E between the corresponding surfaces in the least square sense.

$$E(R,T) = \frac{1}{N}\sum_{i=1}^{N}\|X_i - RY_i - T\|^2 \qquad (2)$$

To evaluate the position detection accuracy, the initial patient position (acquired before the clinical radiographs) is registered to the final patient position acquired after the clinical images positioning procedure. The patient respiratory signal was extracted in order to register the surfaces at the same respiratory phase. This allows to reduce errors due to breathing movements.

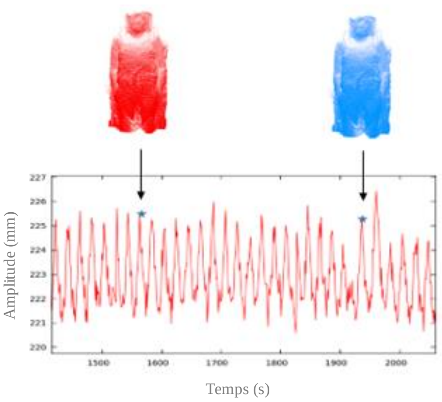

Figure 1: Surface registration at a same respiratory phase between the reference surface in blue (final clinical position) and the target surface in red (initial position before clinical radiographs).

The displacements matrix obtained after surface registration defines the motion that should be applied to the treatment couch in order to place the patient in its final position (clinical position). This 6DOF motion was compared to the real couch displacements, obtained by the clinical positioning procedure, by calculating the mean set-up error and its standard deviation.

3 Results

We analyzed the patient positioning of 140 fractions for 40 patients admitted in the CHRU Brest, having thoracic, abdominal, or pelvic tumor locations. The mean set-up error obtained after surface registration is shown in table 1.

Table 1: Mean set-up error (in mm) between the calculated and the real displacements.

	Lung	ORL	Pelvis
SR4000	4.8±0,9	5.1±0.8	4.9±0.6
Kinect V2	1.6±0.5	1.7±0.7	1.7±0.9

We can notice a large difference between the results obtained by the two acquisition systems (total average errors 1.7 ± 0.7 mm Vs 4.8 ± 0.7 mm for Kinect V2 and SR4000 respectively). The results obtained with SR4000 system are consistent to those obtained in [10].

4 Conclusion

In this paper, we have investigated noninvasive surface imaging systems for daily patient positioning that optimize treatment outcomes and reduce the radiation dose. The proposed systems have the advantage of tracking respiratory and intra-fractional movements in real time. These systems were tested on clinical data. The Kinect V2 surface imaging sensor has shown better performance and an accuracy that is clinically acceptable compared with SR4000 and other commercialized systems.

5 References

[1] L. A. Dawson and M. B. Sharpe, "Image-guided radiotherapy: rationale, benefits, and limitations," *Lancet Oncol.*, vol. 7, no. 10, pp. 848–858, 2006.

[2] P. Alaei and E. Spezi, "Imaging dose from cone beam computed tomography in radiation therapy," *Phys.*

Medica Eur. J. Med. Phys., vol. 31, no. 7, pp. 647–658, 2015.

[3] P. J. Schöffel, W. Harms, G. Sroka-Perez, W. Schlegel, and C. P. Karger, "Accuracy of a commercial optical 3D surface imaging system for realignment of patients for radiotherapy of the thorax," *Phys. Med. Biol.*, vol. 52, no. 13, p. 3949, 2007.

[4] S. Pallotta, L. Marrazzo, M. Ceroti, P. Silli, and M. Bucciolini, "A phantom evaluation of Sentinel™, a commercial laser/camera surface imaging system for patient setup verification in radiotherapy," *Med. Phys.*, vol. 39, no. 2, pp. 706–712, 2012.

[5] T. Willoughby *et al.*, "Quality assurance for nonradiographic radiotherapy localization and positioning systems: report of Task Group 147," *Med. Phys.*, vol. 39, no. 4, pp. 1728–1747, 2012.

[6] F. Stieler, F. Wenz, M. Shi, and F. Lohr, "A novel surface imaging system for patient positioning and surveillance during radiotherapy," *Strahlenther. Onkol.*, vol. 189, no. 11, pp. 938–944, 2013.

[7] F. Walter, P. Freislederer, C. Belka, C. Heinz, M. Söhn, and F. Roeder, "Evaluation of daily patient positioning for radiotherapy with a commercial 3D surface-imaging system (Catalyst™)," *Radiat. Oncol.*, vol. 11, no. 1, p. 154, 2016.

[8] M. Laukkanen, "Performance Evaluation of Time-of-Flight Depth Cameras," 2015.

[9] P. J. Besl and N. D. McKay, "Method for registration of 3-D shapes," in *Sensor Fusion IV: Control Paradigms and Data Structures*, 1992, vol. 1611, pp. 586–607.

[10] M. Gilles *et al.*, "Patient positioning in radiotherapy based on surface imaging using time of flight cameras," *Med. Phys.*, vol. 43, no. 8Part1, pp. 4833–4841, 2016.

Orientability evaluation of concentric tube robots deployed in natural orifices

[1,2]***Quentin PEYRON***, [2]***Kanty RABENOROSOA***, [2]***Nicolas ANDREFF***, [1]***Pierre RENAUD***
[1]*ICube, UDS-CNRS-INSA, 300 bd Sébastien Brant - Illkirch, France.*
[2]*FEMTO-ST Institute, UBFC-CNRS, Besancon, France.*
Contact: quentin.peyron@femto-st.fr

Assessment of concentric tube robot orientability is considered in this work. A numerical method is proposed to estimate the robot capability to be oriented around a fixed point of interest, typically a surgical site in natural orifices.

1 Introduction

Concentric tube robot (CTR) is a promising class of continuum robot for medical interventions [1] which require to operate through natural orifices, such as trans-nasal skull base surgery [2], middle-ear surgery [3] and trans-urethral surgery [4]. During these applications, the access to the surgical site is difficult due to the narrowness of the natural orifices. In addition, capability to orient the surgical tool at the surgical site is of importance.

CTR consists in a telescopic assembly of pre-curved tubes. The elastic interaction between the tubes creates distributed forces and torques which deform the robot backbone. The rotation and translation of the tubes allow then to control the shape of the robot during its deployment through natural orifices, as well as its tip pose during the operation. The capability of CTR to orient their tip while maintaining the same tip position at the surgical site, that is referred as orientability in [5], is of interest and actually limited in the above-mentioned applications. Orientability is indeed not yet a criterion for CTR tube selection, and it is even today still difficult to assess. This work is dedicated to the development of a numerical evaluation of CTR orientability.

2 Orientability

Orientability analysis of continuum robot is a very recent topic, and only one evaluation method exists which is described in [7, 5]. In these works, the studied robots have more than 3 degree of freedom (DoF), which allows to control their tip position at the surgical site position, denoted here $\boldsymbol{p_E}$, and to vary their tip orientation. When transposed to CTR, the evaluation method consists in computing all the possible configurations of the robot for given ranges of rotation and translation of the tubes. The specified actuation ranges are randomly discretized, and the forward kinematic model (FKM) of the CTR has to be solved for each possible combination of actuation input. This provides a discrete set of robot configurations and robot tip poses. The different tip orientations of the robot at the surgical site can then be determined following two approaches. The workspace volume of the robot can be discretized in terms of Cartesian coordinates, forming a cluster of voxels with given dimensions which represents each possible surgical site [5], or a spherical voxel can be defined as centered on the surgical site [7]. The robot configurations which tip position lies in the targeted voxel are finally gathered, giving a set of tip orientations.

This discretization-based method allows to assess the orientability of the robot in all of its workspace. However, it does not seem adapted to the medical constraints when only a very small volume around $\boldsymbol{p_E}$ is admissible. In particular, it is difficult with the current method to compute the local orientability of the robot, since it uses a FKM which does not allow to target one specific tip position. Moreover, the CTR may experience large shape variations during tip orientation, which are difficult to capture with standard numerical methods due to the FKM non-linearity.

We propose then a new numerical method to evaluate the local orientability of CTR. It is based on an inverse kinematic model which allows to constrain the robot tip position at the surgical site. The different orientations are then computed by applying to this model the numerical framework described in [9], which is robust to non-linear behaviors.

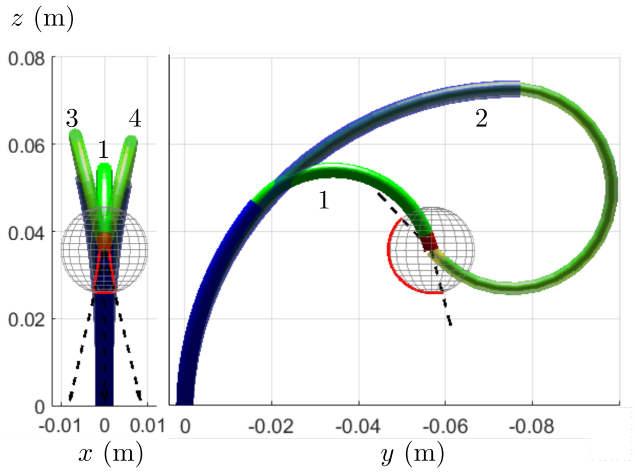

Figure 1: *Configurations of CTR sharing the same tip position, tip tangent in dotted line.*

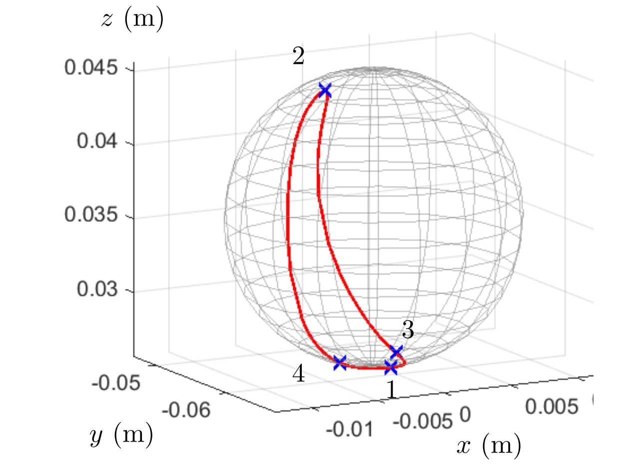

Figure 2: *Service sphere representing the evolution of the tip orientation. The 4 configurations of Fig 1 are marked with blue crosses.*

3 Method

We consider an inverse kinematic model (IKM) of a CTR composed of n tubes, which provides the robot configuration and the $2n$ actuation inputs as a function of the required robot tip position $\boldsymbol{p_E}$. We build such a model by considering first of all a FKM composed of the equations presented in [9], which computes the robot configuration in terms of torsion angle of the tubes according to the actuation inputs, and the equations in [6] which computes the robot tip position $\boldsymbol{p}$ and orientation $\boldsymbol{a}$ represented with Euler angles. Euler angles provide a minimal and intuitive representation of the tip orientation, without leading to any geometrical singularity in the case studies considered so far. Following the approach in [9] for the numerical analysis of CTR, the robot is then discretized along its backbone in a finite number of nodes, transforming the FKM into a set of non-linear equations:

$$\boldsymbol{G}(\boldsymbol{X}, \boldsymbol{u}) = \boldsymbol{0} \tag{1}$$

where $\boldsymbol{X} = \begin{bmatrix} \boldsymbol{Y^T} & \boldsymbol{p^T} & \boldsymbol{a^T} \end{bmatrix}$ is the state vector to compute, with $\boldsymbol{Y}$ a vector of states containing the torsion angles and the position and the orientation of the nodes, and $\boldsymbol{u} = \begin{bmatrix} u_1 & u_2 & \dots & u_{2n} \end{bmatrix}$ the actuation inputs set by the user.

Following the approach in [8], the IKM is finally built by considering that a subset of actuation inputs is used to set the tip pose at $\boldsymbol{p_E}$. This task requires three DoF, that we consider to be parametrized by three of the available actuation inputs, denoted generally u_1, u_2 and u_3. The IKM is then written:

$$\boldsymbol{G}(\boldsymbol{X}^\star, \boldsymbol{u}^\star) = \boldsymbol{0} \tag{2}$$

where $\boldsymbol{X}^\star = \begin{bmatrix} \boldsymbol{Y^T} & \boldsymbol{a^T} & u_1 & u_2 & u_3 \end{bmatrix}$ is the new state vector to determine, and $\boldsymbol{u}^\star = \begin{bmatrix} u_4 & \dots & u_{2n} & \boldsymbol{p_E^T} \end{bmatrix}$ is the vector of parameters set by the user.

The different possible orientations of the robot tip at $\boldsymbol{p_E}$ can be obtained by varying one by one the free actuation inputs and by solving the IKM for each resulting value. This last task is challenging since the CTR kinematics may exhibit non-linear behavior, difficult to predict. Therefore, we perform it with the numerical framework described in [9], which captures efficiently the intricate kinematics of CTR when one actuation input is varied.

4 Results for a two-tube CTR

The method developed above is used to evaluate the local orientability of a CTR composed of two tubes made in NiTi alloy, represented in Fig 1. The pre-curvature of the inner and outer tubes equals respectively 43.5 m^{-1} and 7.2 m^{-1}. Their outer and inner diameters are respectively $(0.65, 0.41)$ mm and $(1.07, 0.77)$ mm. The two tubes can be both rotated and translated, giving a 4-DoF continuum robot. The position of interest $\boldsymbol{p_E}$ is determined by solving the FKM with an initial set of actuation inputs and by picking the robot tip position. The initial configuration is labeled 1 on Fig 1. We choose then to use the translation of the two tubes and the rotation of the inner tube to constrain the tip position at $\boldsymbol{p_E}$. The rotation of the outer tube is varied in order to sweep the possible tip orientations. Our method finds successfully the different configurations of the robot which lead to the same tip position. The robot shapes obtained during the continuation process which provides the most different tip orientations are represented in two planes on Fig. 1.

The resulting orientations are also represented on a service sphere centered at $\boldsymbol{p_E}$ like in [5]. The robot tip tangent intersects with the sphere, creating a point on the sphere surface. The tip orientations obtained with successive variations of the outer tube rotation give then a succession of points, that can be represented as a curve on the sphere surface. The resulting service sphere is represented on Fig. 2. It provides information about the tip orientation ranges at $\boldsymbol{p_E}$, which equals 151.3 degrees around the $\boldsymbol{x}$-axis.

Acknowledgement

This work was supported by the French National Agency for Research within the Biomedical Innovation program (NEMRO ANR-14-CE17-0013), the Investissements d'Avenir (Robotex ANR-10-EQPX-44, Labex CAMI ANR-11-LABX-0004), the EIPHI Graduate School (contract ANR-17-EURE-0002) and Aviesan France Life Imaging infrastructure.

References

[1] Burgner-Kahrs, J. and Rucker, D. C. and Choset, H. (2015). Continuum Robots for Medical Applications: A Survey. *IEEE Transactions on Robotics*, 31:1261–1280.

[2] Burgner, J. and Rucker, D. C. and Gilbert, H. B. and Swaney, P. J. and Russel, P. T. and Weaver, K.D. and Webster, R.J. (2014). A Telerobotic System for Transnasal Surgery. *IEEE/ASME Transactions on Mechatronics*, 19:996–1006.

[3] Granna, B. and Rau, T. S. and Nguyen, T. and Lenarz, T. and Majdani, O. and Burgner-Kahrs, J. (2018). Toward automated cochlear implant insertion using tubular manipulators. *Medical Imaging 2016: Image-Guided Procedures, Robotic Interventions, and Modeling*, 9786:9786F.

[4] Hendrick, R. J. and Mitchell, C. R. and Herell, S. D. and Webster, R. J. (2015). Hand-held transendoscopic robotic manipulators: A transurethral laser prostate surgery case study. *The International journal of robotics research*, 34:1559-1572.

[5] Wu, L. and Crawford, R. and Roberts, J. (2017). Dexterity Analysis of Three 6-DOF Continuum Robots Combining Concentric Tube Mechanisms and Cable-Driven Mechanisms. *IEEE Robotics and Automation Letters*, 2:514–521.

[6] Cao, D.Q. and Tucker, R. W. (2008). Nonlinear dynamics of elastic rods using the Cosserat theory: Modelling and simulation *International Journal of Solids and Structures*, 45:460–477.

[7] Chickhaoui, M. T. and Rabenorosoa, K. and Andreff, N. (2016). Kinematics and performance analysis of a novel concentric tube robotic structure with embedded soft micro-actuation. *Elsevier, Mechanism and Machine Theory*, 104:234–254.

[8] Black, C. B. and Till, J. and Rucker, D. C. (2018). Parallel Continuum Robots: Modeling, Analysis, and Actuation-Based Force Sensing. *IEEE Transactions on Robotics*, 34:29–47

[9] Peyron, Q. and Rabenorosoa, K. and Renaud, P. and Andreff, N. (2019). A numerical framework for the stability and cardinality analysis of concentric tube robots: Introduction and application to the follow-the-leader deployment. *Elsevier, Mechanism and Machine Theory*, 132:176–192.

Diabetic Retinopathy Detection and Grading From Fundus Image Using Deep Learning Library Tensorflow

Abhijit Jha, Shailesh Kumar, Ajitabh Srivastava, Rajeev Gupta and Basant Kumar

Motilal Nehru National Institute of Technology Allahabad, Prayagraj, U. P. India, 211004
Contact: shailesh@mnnit.ac.in

This paper presents a computerized, preliminary diabetic retinopathy detection and grading method from colour fundus image using Convolutional Neural Network (CNN). The proposed algorithm uses Tensorflow machine learning framework for the implementation of CNN model. Retinal fundus image is fed as input to the CNN model, which firstly analyses the image and learns the attributes of an eye with the early symptoms (microaneurysms and hemorrhages) of diabetic retinopathy. The methodology followed in this paper is to pass the digital colour fundus image of healthy as well as diabetic retinopathy eye through the CNN model. The output of the CNN model is fused with the inception V3 model and then finally classifies the result either as diseased or not diseased. We have used a Convolutional Neural Network having 6 hidden layers. The result of the algorithm is compared with ophthalmologist opinion, which certify the accuracy of proposed algorithm.

1 Introduction

Diabetic mellitus has become one of the primary challenge to our population around the world. The number of diabetic patients will ascend to 592 million by 2035 as per estimation of International Diabetes Federation [1]. Diabetic retinopathy (DR) is common cause of diabetic mellitus which cause severe vision loss and even blindness in the patient [2], [3]. Everyone with type 1 or type 2 diabetes is at risk for DR diabetic retinopathy. Early treatment of DR can help to reduce the risk factor of vision loss of patient [4].

Deep learning techniques, particularly the convolutional neural networks (CNNs), have achieved phenomenal success in image identification [5], [6]. CNN is a kind of neural network in which number of hidden layers varies from five to ten or more. CNN has powerful ability in learning and improving with training. For DR detection, training CNN-based classifiers for DR lesions lacks large explained sets of these lesions [7], [8]. This demands the use of pre-trained models such as Inception V3, ResNet, VGG and ImageNet to reduce the computation complexity, time and huge training data set requirements.

This paper presents an automated early DR detection and grading scheme from retinal fundus image a framework involving using CNN and Inception V3 and ANN for classification.

2 Proposed Algorithm For Detection And Grading Of Retinal Fundus Image

In this section, we will describe our deep learning method for DR detection. Detection model is shown in Fig. 1. In this paper, Diabetic retinopathy detection and grading is accomplished using CNN with Tensorflow library. We use transfer learning, a pre-trained model namely Inception V3, which is developed by Google Inc. Transfer learning, is a type of machine learning in which we utilize the

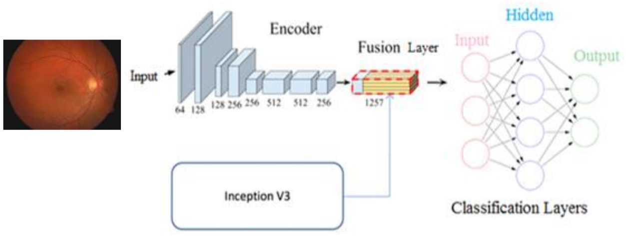

Fig 1. The framework for DR detection using CNN and Inception V3 (ANN based classification)

ability of a pre-trained machine for our purpose, which is trained for classification of other objects. This classifier has been trained over 1.2 million objects. Finally, we fuse the features extracted by this model into our model for which we used auto-encoder technique. Since we don't have to train the feature extraction part (which is the most complex part of the model), we can train the model with less computational resources and training time, thereby increasing the efficiency and reducing the cost of the training process.

Methodology

The block diagram in Fig. 1 presents the exact flow of our algorithm. The steps followed in its implementation are as follows:

- Fundus image is passed through Inception V3 in parallel as it is passed through the encoder.
- Fusion by repeating the result.
- The combined result is fed into a neural network based classifier.
- As output, we get the probability of a fundus image being diseased or healthy.

3 Results

The results of CNN classifier model is shown in GPU in Fig. 2 and Fig. 3. First image is disease image and second is healthy respectively. The fundus images for which the algorithm outputs a probability value for diseased greater than 0.65 are classified as diseased. In addition, the fundus images, which output a probability of diseased, value less than 0.25 have been classified as healthy. Rest of the images, which lie in between these two classes, have been classified as ambivalent or ambiguous. The upper threshold is setting by firstly taking the average of probability values of DR images and then slightly lessen for reducing the chance of False Negative. Lower threshold is setting by taking the average probability values of healthy image. The graph of probability- based threshold calculating is shown in Fig. 4.

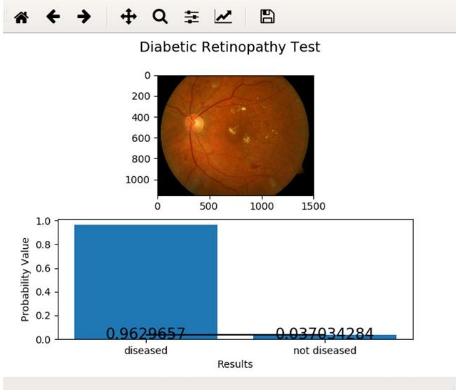

Fig. 2 Output of diseased fundus image along with probability values

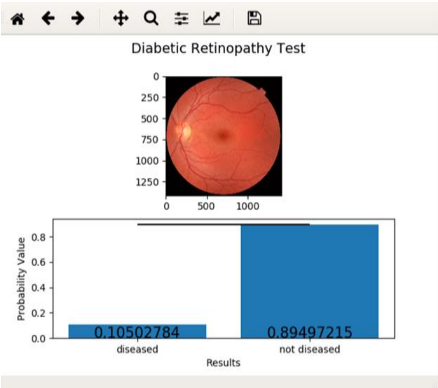

Fig. 3 Output of healthy fundus image along with probability values

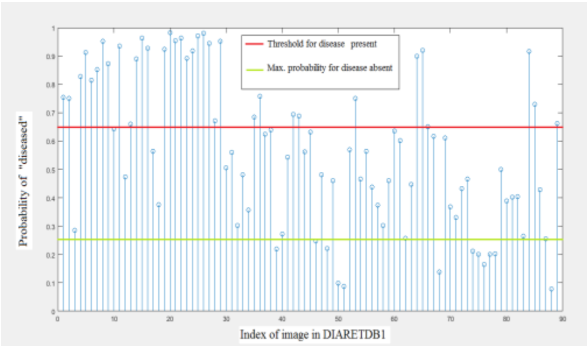

Fig. 4. Plot of probability of disease presence against image index

By comparing the output of the algorithm against the ground truth images and results, the following observations were made regarding the performance of the algorithm. The number of TP, TN, FP, and FN are thirty-four, nine, one and four respectively. For, sensitivity and specificity calculation we have consider first and third class of the classification algorithm and they are calculated as 98.68 % and 69.2% respectively. The accuracy of the classification algorithm was obtained to be 94.38%.

4 References

[1] L. Zhou, Y. Zhao, J. Yang, Q. Yu, and X. Xu, "Deep multiple instance learning for automatic detection of diabetic retinopathy in retinal images," *IET Image Process.*, vol. 12, no. 4, pp. 563–571, 2018.

[2] S. S. Rahim, C. Jayne, V. Palade, and J. Shuttleworth, "Automatic detection of microaneurysms in colour fundus images for diabetic retinopathy screening," *Neural Comput. Appl.*, vol. 27, no. 5, pp. 1149–1164, 2016.

[3] R. A. Welikala *et al.*, "Automated detection of proliferative diabetic retinopathy using a modified line operator and dual classification," *Comput. Methods Programs Biomed.*, vol. 114, no. 3, pp. 247–261, 2014.

[4] B. Kumar, Shailesh and Kumar, "Diabetic Retinopathy Detection by Extracting Area and Number of Microaneurysm from Colour Fundus Image," *2018 5th Int. Conf. Signal Process. Integr. Networks*, pp. 359–364, 2018

[5] G. Quellec *et al.*, "A multiple-instance learning framework for diabetic retinopathy screening," vol. 16, pp. 1228–1240, 2012.

[6] R. Venkatesan, P. S. Chandakkar, and B. Li, "Simpler non-parametric methods provide as good or better results to multiple-instance learning .," pp. 2605–2613.

[7] A. Krizhevsky, I. Sutskever, and G. E. Hinton, "ImageNet Classification with Deep Convolutional Neural Networks," *Adv. Neural Inf. Process. Syst.*, pp. 1–9, 2012.

[9] V. Gulshan *et al.*, "Development and validation of a deep learning algorithm for detection of diabetic retinopathy in retinal fundus photographs," *JAMA - J. Am. Med. Assoc.*, vol. 316, no. 22, pp. 2402–2410, 2016.

Simulation for preoperative planning, balloon inflation for tibial plateau fracture reduction

Kévin AUBERT (1,2), Tanguy VENDEUVRE (1,3), Michel ROCHETTE (2), Philippe RIGOARD (1,3), Arnaud GERMANEAU (1)

1. Institut Pprime, UPR 3346 CNRS – Université de Poitiers – ISAE-ENSMA, France
2. ANSYS FRANCE, Villeurbanne, France
3. Spine & Neuromodulation Function Unit. PRISMATICS Lab CHU – Poitiers, France
Contact : kevin.aubert@univ-poitiers.fr

1 Introduction

In 2013, Vendeuvre et al [1] developed a novel method for tibial plateau fracture treatment using minimally invasive techniques named Tuberoplasty *(Figure 1)*. This allowed the surgeons to reduce the fracture with the inflation of a surgical balloon usually used in Kyphoplasty — vertebrae compression fracture reduction —.
Tuberoplasty gesture phases are : positioning of the surgical plate, positioning and the inflation of the surgical balloon, balloon removing, injection of surgical cement and then tightening of the surgical plate with screws.
Preoperative planning is a key step in surgery gestures. Computer assisted surgery has the potential to facilitate this task by the simulation of the per-operative tasks — during the surgery —. A considerable amount of study exists on the biomechanical behavior after a balloon kyphoplasty surgery — with cement injection —, however the kinematics during the balloon inflation remains unknows.

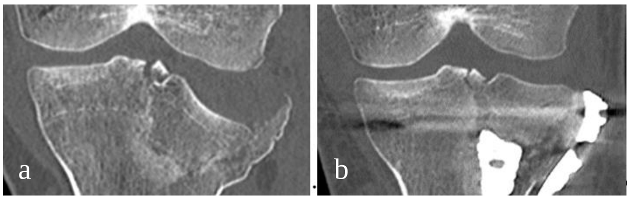

Figure 1: Coronal plane of : a) The preoperative image; b) The postoperative image.

This work aims to develop a patient specific Finite Element (FE) simulation of balloon inflation in tibial plateau fracture model according to the Tuberoplasty [1]. From the preoperative CT-Scan 3D image to the FE simulation result, the workflow consists of : semi-automatic segmentation, geometry simplification, balloon equivalent inclusion, definition of boundary conditions, simulation and result evaluation.

2 Materials & Methods

2.1 Segmentation

The image treatment and segmentation were performed using 3D Slicer software (v4.6.2)[2]. First, a better visualization was obtained with a python extension which includes ITK and VTK functions: Cast Image Filter (IF), Curvature Anisotropic Diffusion IF and Gradient Magnitude Recursive Gaussian IF.
Then, in some of the coronal, sagittal and axial planes of the filtered 3D image, we distinguished four geometries: depressed fragment, separate fragment, healthy tibia, femur, others. This data served as seeds for the fast-growing algorithm implemented in the FastGrowCut extension which produces a 3D labelmap (whole segmentation procedure ≃ thirty minutes). The segmented fragments were smoothed and converted to 3D geometries as .STL file. The postoperative CT scan image enables the surgical plate segmentation with retro-engineering methods.

2.2 Geometric model

After importing the .STL geometries to the ANSYS SpaceClaim software, we reduced the number of faces and the interpenetration caused by the geometry smoothing during the segmentation *(Figure 2)*.

The displacement of a half cylinder modeled the balloon expansion. It produced linear contacts that correspond to the idealization of the contacts between the depressed fragment and the external surface of the balloon. The half cylinder has the same dimension as the balloon longitudinal dimension.

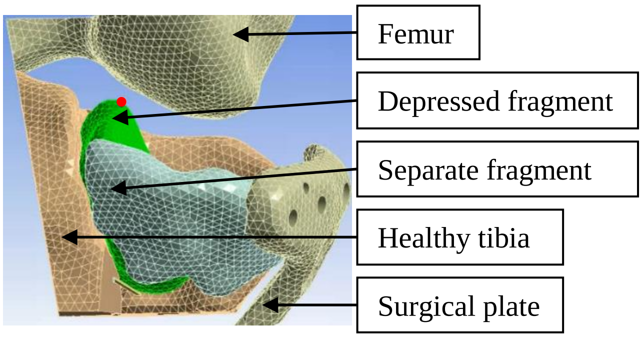

Figure 2: The geometries of the model before simulation. (One visible inspection point in red)

2.3 Mesh & Boundary conditions

We used ANSYS 19.1 Mechanical software to control the meshing, the boundary conditions and to run the simulations. We choose a rigid solid simulation, so only the external surfaces of the geometries were meshed with 28150 triangular and quadrilateral elements.
The simulation was composed of 3 steps:
(1) We performed the surgical plate adaptation to the geometries. The surgical plate was placed close to the geometries, and was pressed to fit the geometries of the model. At this step only the surgical plate was mobile.
(2) The balloon emplacement was identified from the postoperative image in which the resulting balloon cavity filled by PMMA is visible. (Figure 1b) The inflation of the balloon was simulated by the displacement of the half cylinder. The simulation was performed until a displacement of 11 mm of the half cylinder. It corresponds to the maximum balloon diameter — radial inflation —. This often results in too much displacement of the depressed fragment – which going out of the geometries –. At this step, the surgical plate and the healthy tibia were fixed. Three springs of $5\ N.m$ with $1\ N$ preload linked the separate fragment and the healthy tibia. It represents soft tissues that limits rigid solid movements. A 5 N force on the separate fragment models the clamping forceps effort. All the contacts were frictionless.
(3) Scilab software was used to calculate the displacement that minimizes the error at the inspection points. The inspection points were localized on the depressed fragment (Figure 3). The reference was the inspection point localized in the postoperative image. Anatomical points were used to define the transformation matrix between the preoperative local coordinate system and the postoperative local coordinate system.

3 Results & Discussion

For a given position, this work allows us to evaluate the optimal balloon inflation to minimize the fragment position error. We found that the minimum position error is $3.31 \pm 0.61mm$ regarding to the postoperative reference. According to the surgeon protocol, the maximum acceptable error is 5mm [3]. It is obtained with a displacement of the half cylinder of 9.1mm, this corresponds to 82,7% of the maximal radial balloon inflation *(Figure 3).* These results were helpful for fragment kinematic understanding by the surgeon. We assume that, for now, the segmentation process is too time consuming for a real clinical setup.

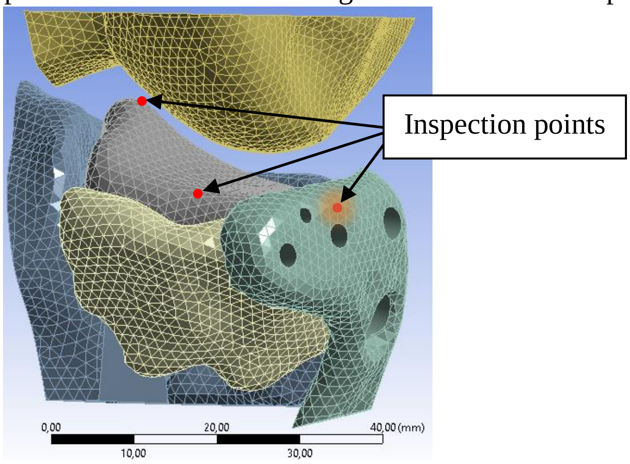

Figure 3: The model geometries after the simulations.

The main limitations of this work are the high simplification of the balloon behavior, the frictionless contact and the rigid body assumption. However, another model can be envisaged with a hyperelastic material to simulate balloon behavior, with flexible solids and with frictional contacts. Then, the balloon inflation could be controlled by its internal volume using a mass flow rate. Another limitation is the validation of the model. This could be investigated by using experimental methods to measure displacements fields of fragments during balloon inflation.
In conclusion, preliminary results provided by this study are interesting to analyze kinematics behavior of bone fragments for a real case of tibial plateau fracture in order to optimize the surgery gesture.

4 Acknowledgements

The authors would like to thank ANSYS SAS France.

5 References

[1] Vendeuvre, T. et al. (2013). Tuberoplasty : Minimally invasive osteosynthesis technique for tibial plateau fractures. Orthopaedics & Traumatology: Surgery & Research, 99: S267-S272.

[2] Fedorov et al. (2012). 3D Slicer as an image computing platform for the Quantitative Imaging Network. Magnetic Resonance Imaging, 30: 1323-1341.

[3] Yu et al. (2009). Functional and radiological evaluations of high-energy tibial plateau fractures treated with double-buttress plate fixation. European Journal of Medical Research, 14: 200

Computer Assisted Detection of Good View Frame from USG Video for ONSD Measurement

Aniket PRATIK[1], Maninder SINGH[1], Kokkula SRIRAJ[1], Meesala A. KUMAR[1], Rajeev GUPTA[1], Deepak AGRAWAL[2]and Basant KUMAR[1]

Motilal Nehru National Institute of Technology Allahabad, Prayagraj, INDIA[1]
All India Institute of Medical Sciences, New Delhi, INDIA[2]
Tel: + 91-9452196139
Contact: singhbasant@mnnit.ac.in

This paper aims to automatically detect diagnostically relevant 'good view frame' containing Optic Nerve, from an Ocular Ultrasonography/Ultrasound (USG) video file using Deep Neural Network object detection model. Accurate measurement of ONSD from USG video requires high level of expertise and experience. The proposed computer assisted automated module for the detection of appropriate frame containing optic nerve, has been developed using Faster Region based Convolutional Neural Network (R-CNN) model with TensorFlow framework. Performance of the developed module has been analyzed considering various evaluation parameters such as average precision, average recall, F1- score and accuracy.

1 Introduction

The diameter of the optic nerve along with its sheath is an important diagnostic parameter for detection and therapeutic planning of several diseases and trauma cases. A strong correlation between Optic Nerve Sheath Diameter (ONSD) and intra-cranial pressure (ICP) has been established to a large extent in many reported research papers [1] [2]. ONSD is viewed as a critical diagnostic parameter for the detection of elevated ICP, which is a life-threatening syndrome; elevated ICP requires immediate medical intervention. ONSD can be measured using imaging modalities such as Computed tomography (CT), magnetic resonance imaging (MRI) and A-scan/ B-scan ultrasonography [3]. Ocular ultrasound imaging does not use harmful radiations and it has many other advantages in terms of equipment portability, patient bed side availability, and rapid performance [4]. However, acquisition of the diagnostically significant 'good view frame' for the accurate measurement of ONSD is very challenging; this requires highly trained and experienced radiologist/medical expert. Therefore, a computer assisted module for automatic detection of the 'good view' frame from the acquired USG video file for ONSD measurement would be very helpful. A Deep Learning based scheme has been presented in this paper for the automatic detection of the appropriate USG frame which contains optic nerve. The proposed module removes the dependency on trained/ experienced human resource for proper acquisition of the USG frame, thus increases the efficiency and accuracy of the diagnostic assessment.

2 Method

In our approach, the obtained USG frames have been divided into two classes which are defined as 'Good View' class and 'Side View' class for the detection of Optic nerve. The USG frame for two classes is the labelled class, where ONSD is marked manually by the medical expert. Mean score value is given to each frame of an ocular USG video; the frame having mean score greater than the threshold is labelled as Good View class. For training purpose, the architecture used at the conceptual level is Faster-RCNN, which is composed of three neural networks i.e. Feature Network, Region Proposal Network (RPN), and Detection Network [5]. The image classification network uses a well-known pre-trained Inception v2 model (developed by Google INC) for training. The targeted object detection method uses Region Proposal Network (RPN). RPN is the backbone of Faster RCNN, which is used to generate a number of bounding boxes around the map corresponding to the targeted Region of Interests (ROIs), which is optic nerve [6] [7]. Selective search algorithm is used to propose about 2000 object boundaries to extract region proposals [8]. Further, Faster RCNN uses SoftMax classifier on top of Region Proposal Network to detect the objects. The detection network generates the final class within the bounding box. To test our object detection classifier for various ONSD ultrasound video files, the classifier outputs the type of the object and its score belonging to that particular class Figure1 represents the steps used for training and object detection.

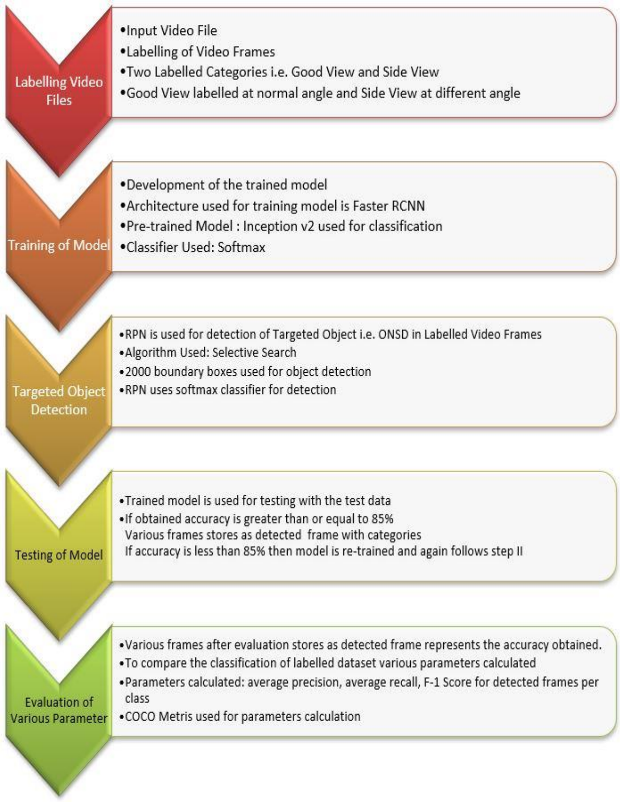

Figure1. Various steps involved in detection of 'Good View' USG frames

3 Results

The ocular ultrasound video files of various patients have been obtained from the Trauma Centre of All India Institute of Medical Sciences (AIIMS), New Delhi, INDIA. The ocular USG frames of 105 patients have been collected. Out of the total 105 USG frames of several patients, 74 frames have been used as training data and 31 frames have been used as testing data. Accuracy of the defined class of frames has been evaluated considering the COCO Metrics in Deep Learning approach [9]. The evaluation parameters used are- 'average precision' (used to rank our classification model), the 'average recall' (also called as sensitivity or true positive rate). In our case, the average precision and average recall for the 100 detections per class is 0.506 and 0.716 respectively. To identify whether the class distribution is balanced or unbalanced and to analyze the reliability of object detection, F-1 score is calculated. The obtained F1-score is 0.69 and the accuracy obtained for detection of ONSD is almost 95-99%. This accuracy obtained by considering the GOOD VIEW frames only. Figure 2 and Figure 3 show the 'Good View' USG frame containing ONSD along with the accuracy percentage of each frame. The obtained values of F-score and accuracy indicate that results are satisfying. However, it is better to have F-score value close to one, to achieve more precise and accurate 'Good View' USG frame for ONSD measurement.

Figure2. Good view ONSD image automatically detected in frame

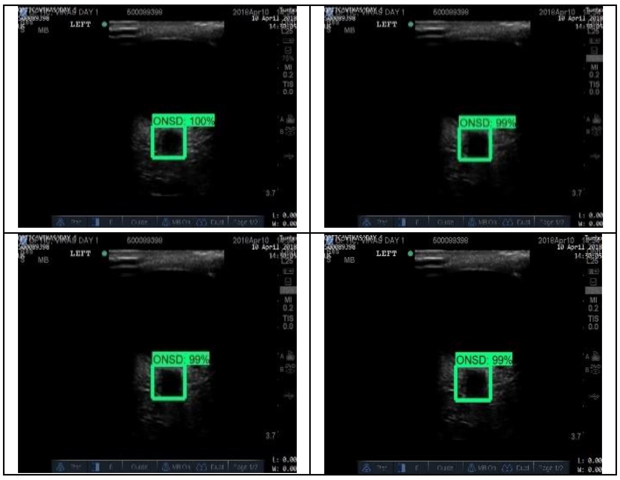

Figure3. Various frames of detected Good View

4 References

[1] Kimberly, Heidi Harbison, Sachita Shah, Keith Marill, and Vicki Noble. "Correlation of optic nerve sheath diameter with direct measurement of intracranial pressure." Academic Emergency Medicine 15, no. 2 (2008): 201-204.

[2] Siddhartha Shankar Sahoo, Deepak Agrawal. Correlation of optic nerve sheath diameter with intracranial pressure monitoring in patients with severe traumatic brain injury. The Indian journal of neurotrauma. 2013; 10:9-12.

[3] Shirodkar, Chetan G et al. “Optic nerve sheath diameter as a marker for evaluation and prognostication of intracranial pressure in Indian patients: An observational study” Indian journal of critical care medicine: peer-reviewed, official publication of Indian Society of Critical Care Medicine vol. 18,11 (2014): 728-34.

[4] Sangani SV, Parikh S. Can sonographic measurement of optic nerve sheath diameter be used to detect raised intracranial pressure in patients with tuberculous meningitis? A prospective observational study. Indian J Radiol Imaging 2015; 25:173-6.

[5] K. He, X. Zhang, S. Ren, and J.Sun, “Faster RCNN: Towards Real-Time Object Detection with Region Proposal Networks”, in IEEE Transactions on Pattern Analysis and Machine Intelligence, vol. 39, no. 6, 2017.

[6] R. Girshick, J. Donahue, T. Darrell, and J. Malik, “Rich feature hierarchies for accurate object detection and semantic segmentation,” in Proc. IEEE Conf. Comput. Vis. Pattern Recognit., 2014, pp. 580–587.

[7] R. Girshick, “Fast R-CNN,” in Proc. IEEE Int. Conf. Comput. Vis., 2015, pp. 1440–1448.

[8] J. R. Uijlings, K. E. van de Sande, T. Gevers, and A. W. Smeulders, “Selective search for object recognition,” Int. J. Comput. Vis., vol. 104, no. 2, pp. 154–171, Sep. 2013.

[9] Tsung-Yi Lin, Michael Maire, Serge Belongie, LubomirBourdev, Ross Girshick, James Hays, Pietro Perona, Deva Ramanan, C. Lawrence Zitnick, Piotr Dollar, “Microsoft COCO: Common Objects in Context,” Computer Vision and Pattern Recognition, arXiv:1405.0312v3, 2015

Patient's specific computer simulations to assist coronary artery bypass surgery

Agnès DROCHON[1], Amédéo ANSELMI[2], Hervé CORBINEAU[2] and Jean-Philippe VERHOYE[2]

[1]Univ Technologie Compiègne, UMR CNRS 7338, 60200 Compiègne, France

[2] Service Chirurgie Cardio-Thoracique, CHU PontChaillou, 35000 Rennes, France

Tel : +33 (0)2 99 28 24 90

Contact: agnes.drochon@utc.fr

We present here a simulating tool developed to compute pressure and flow rate values everywhere in the coronary network. The patients included in the study (n = 22) have very severe stenoses or even thromboses on the main coronary arteries. The model is based on the electric-hydraulic analogy, and the simulations are performed with MatLab-Simulink. Collateral pathways and bypass grafts may be included in order to see their influence on blood delivery to ischemic territories. The results obtained for the 22 patients already studied constitute a data-bank of typical cases to which the surgeons can refer. It is hoped that this can help their surgical decision for the next patients because the simulations provide some data that cannot be clinically measured.

1 Clinical context

Bypass grafting is commonly performed to obtain myocardial reperfusion distal to critical coronary stenoses or thromboses. However, the success of the intervention depends on many factors: quality of the grafts and of the anastomoses, status of the distal territory and peripheral resistances, existence of competitive flows (flow in native artery or collateral flow),… Some of these factors (peripheral resistances, collateral flows, …) are difficult to quantify precisely before the intervention. An accurate model of the coronary circulation is thus helpful for calculating the unknown quantities of interest.

The patients studied here have severe coronary disease: they have stenoses of the left main coronary artery (LMCA), left anterior descending artery (LAD) and left circumflex branch (LCx), and chronic occlusion of the right coronary artery (RCA). In this clinical situation, some collateral circulation may have developed since years to deliver blood to the ischemic right territory. Is it then necessary to revascularize the RCA? Would the strategy with only two grafts (on the left branches LAD and LCx) be the best? Will the hydrodynamic configuration after grafting favour new occlusions in the future for the patient? Will blood delivery be adequate? The model is expected to bring some answers to these questions.

2 The 0D-model

The electrical model is presented in details in [1-3]. The main arteries and the grafts are represented by a resistance, an inductance and a compliance. The value of these parameters are taken from the literature. The collateral pathways (small vessels) are represented by resistances only (R_{col}). At the end of each branch (LAD, LCx, RCA), the capillaries are represented by resistances also (R_{LADc}, R_{LCxc}, R_{RCAc}). The values of these resistances are deduced from measurements for each patient, obtained during the surgical procedure [4]. The input of the model is the aortic pressure of the patient ($P_{ao}(t)$). All the results (pressures or flow rates in any place of the network) are function of time, but mean values over several cardiac cycles may be calculated. Some of the calculated values (for example, the flows in the grafts or the pressure distal to the RCA thrombosis) can be compared to the measured clinical values. This provides an estimation of the simulations' validity.

3 Example with one Patient

The detailed results for the 22 patients are currently under publication. Informations given by the model are illustrated here with one patient of the group.

This person had previously some myocardial infarction, but no stent on any coronary artery and no diabetes. His LVEF (Left Ventricular Ejection Fraction) is 55%. The area reduction is 0% on LMCA , 99% on LAD, 100% (total obstruction) on LCx and RCA (A very severe three vessel disease). The values obtained for the resistances (R_{LADc} = 87.8 mmHg.s/ml, R_{LCxc} = 70.3 mmHg.s/ml, R_{RCAc} = 94 mmHg.s/ml , R_{col} = 480 mmHg.s/ml) are in the same range as the mean of the group (reference values given in [2]).

The simulations indicate a total amount of collateral flow around 14ml/min in the pathological situation (no graft at all) and 18.5 ml/min with the two left grafts (on LAD and on LCx). This amount of blood is delivered to the right ischemic territory, and the improvement due to the presence of the left grafts is modest. When the right graft is present, the collateral flows become rather null, or even negative. This is due to the inversion of the pressure gradient between the two extremities of the collateral pathway, and has been also found by other authors in the literature.

The simulations also show that when the left grafts are operating, the flow in the corresponding native artery decreases significantly, and this can promote progression of the disease in this artery.

In the pathological case (no graft), the flow in LAD is 0.8 ml/min ; in LCx, it is 0.01 ml/min ; in RCA, it is 18.7 ml/min. With the right graft only, these quantities become respectively 0.6 ml/min, 0 ml/min, and 50 ml/min. With the left grafts only, the values are : 41.5 ml/min, 50.1 ml/min and 11.8 ml/min ; and with three grafts (complete revascularization) : 47.5 ml/min, 58.3 ml/min and 49.5 ml/min. For this patient, the best surgical strategy was obviously to do three grafts : the sum of the flows in the three branches is improved with the grafts : it is 19.5 ml/min without any graft, 50.5 ml/min with the right graft only, 103.5 ml/min with the two left grafts only, and 155 ml/min with the three grafts. However, one can notice that even the complete revascularization does not allow to recover a normal level of heart perfusion.

The pressure drop due to each stenosis can also be obtained from the simulations. If P_M is the pressure distal to the LMCA stenosis, P_1 distal to the LAD stenosis, and P_3, the pressure distal to LCx stenosis, the ratios P_M/P_{ao}, P_1/P_M and P_3/P_M can be computed. For the patient presented here, without any graft, the values of these ratios are respectively : 0.99, 0.24, and 0.22. These ratios are similar to the classical FFR Index, except that the values have not been obtained under maximal vasodilation and that the patient presents multiple and ramified stenoses. With the three grafts, the values of P_1/P_M and P_3/P_M are very much improved (resp. 0.93 and 0.92).

4 References

[1] Maasrani, M., Verhoye, J.P., Corbineau, H. and Drochon, A. (2008). Analog electrical model of the coronary circulation in case of multiple revascularizations. *Annals of Biomed. Engin.*, 36:1163-1174.

[2] Maasrani, M., Abouliatim, I., Harmouche, M., Verhoye, J.Ph., Corbineau, H. and Drochon, A. (2011). Patients' specific simulations of coronary fluxes in case of three-vessel disease. *Jour. Biomed .Science and Engineering*, 4:34-45.

[3] Harmouche, M., Anselmi, A., Maasrani, M., Mariano, Ch., Corbineau, H., Verhoye, J. Ph. and Drochon, A. (2014). Coronary three vessel disease: hydrodynamic simulations including the time-dependence of the microvascular resistances. *Advances in Biomech and Applic.*, 1(4):279-292.

[4] Verhoye, J.Ph., De Latour, B., Drochon, A., and Corbineau, H. (2005). Collateral flow reserve and right coronary occlusion: evaluation during off-pump revascularization. *Interactive Cardiovascular Thoracic Surgery* 4:23-26.

CFD based study of blood stagnation caused by LVAD inflow cannula angulation

Amal BEN ABID[1], Valery MORGENTHALER[2], Pascal HAIGRON[1] and Erwan FLECHER[1]
1 Univ Rennes, CHU Rennes, INSERM, LTSI – UMR 1099, F-35000 Rennes, France
2 ANSYS, Villeurbanne F-69100, France
Contact: amal.ben-abid@univ-rennes1.fr

The purpose of this study is to assess whether computational fluid dynamics (CFD) can be an effective tool for analyzing the influence of input cannula orientation on thrombus formation when implanting a left ventricular assist device (LVAD). Blood stagnation was investigated by looking into velocity and virtual dye concentration.

1 Introduction

Left Ventricular Assistant Device (LVAD) which is used as a substitute for heart transplant shortage has known rapid advancement. Nevertheless, it may present serious side effects. An issue raised by LVAD implantation is related to intrathoracic congestion. Once the LVAD is implanted, depending on the intrathoracic space, the chest wall may be difficult to close. This may be prevented by preoperative virtual positioning of the device [1]. Nevertheless, morphology based virtual positioning can result in angular deviation of the inflow cannula. One of the consequences of the inflow cannula angulation may be thrombus formation. Computational Fluid Dynamics (CFD) might be used to anticipate blood stagnation. Recent research [2-4] has focused on the correlation between the angular orientation of the LVAD cannula and blood stagnation. However, they presented preliminary results that raise questions about the efficiency of CFD method. Until now, presented results, obtained on a limited number or limited range of angular configurations, do not seem sufficiently demonstrative. The present study investigates the ability of CFD to establish the link between cannula angulation and blood stagnation.

2 Methods

2.1 Model description

Three-dimensional models, as used in some of the previously reported work [2-4], imply a high computation time, which is likely to limit the number of experiments. Therefore, we opted to use a generic two dimensional model in order to study the ability of CFD computation to investigate blood stagnation. This 2D model consisted in a left ventricular (LV) fluid domain, a rigid LV wall with no slip condition, a zero pressure inlet mitral valve and a mass flow outlet cannula. The LV wall was modeled (figure 1) as a prolate ellipsoid with long axis of 113mm, a short axis of 65mm. The mitral valve was modeled as a 28 mm line flattening the ellipsoid. The cannula was modeled with 18mm diameter and 20mm depth. Five different configurations for cannula angulation (0°, 10°, 20°, 30° and 40°) were simulated for two flow rates : 5 L/min which is a flow rate typically used for patients and 3L/min to investigate the consequences of a reduced flow rate on the stagnation zones.

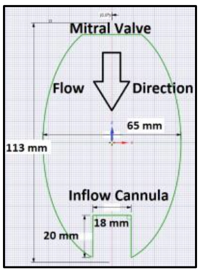

Figure 1: Model 2D Representation.

2.2 Computational Model

Geometries were created using ANSYS AIM 19.0 and meshed using ANSYS Meshing r19 tools. The meshing size interval was set between 0.5 mm and 2 mm and the fluid computation was launched in ANSYS FLUENT r19 using a time step of

0.01second. The blood was considered Newtonian fluid [5] with laminar flow.

2.3 Output and Analysis

Stagnation was analyzed using flow velocity and virtual ink originally described in [6]. The ink was defined as a scalar. The simulation consisted of three phases (Figure 2). An initialization phase aimed to fill the ventricle with blood, a filling phase aimed to fill the ventricle with the ink by dyeing the blood entering from the Mitral Valve till its concentration reaches 1 (No units) and a clearance phase aimed to wash the ink out of the ventricle in order to identify stagnation zones. Washing blood was made by stopping the dyeing of blood in order to define the quantity and the location of the ink concentration (dyed blood) remaining after a defined period of time. The simulation time of the two first phases changed depending on the configuration (cannula angulation), whereas, the simulation time of the last phase was set to 12s for all configurations.

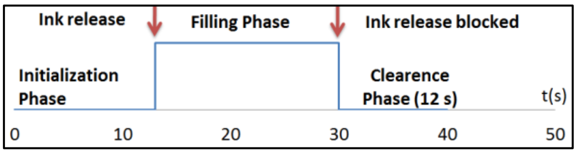

Figure 2: Phases of dyed Blood technique.

3 Results

Figure 3 shows the velocity magnitude within the left ventricle for two different flow rates. The velocity magnitude for both flow rates follows the same pattern. One can observe that the velocity is high at the center of the ventricle and low (represented in dark blue in the figure) within the apex and close to left ventricle wall, especially underneath the mitral valve, for all configurations. Those regions seen in dark blue on the figure, may be considered as potential stagnation regions which is consistent with previous studies [3], [4]. Figure 4 shows the ink concentration within the left ventricle after 12 seconds of clearance for two different flow rates. For the 5L/min flow rate, the remaining ink concentration does not exceed 50% of the original concentration. The apical configuration (0°) shows a better clearance with 14% of ink concentration left in the ventricle. For the 3L/min flow rate, starting from 20° configuration the ink concentration is above 50% of the original concentration. For all cases, the remaining ink concentration is located at the apical region and the more the cannula angulation is important the more the ink stagnation is important. These preliminary results seem coherent with the implantation procedure usually adopted that tends to align the inflow cannula with the apical ventricular axis.

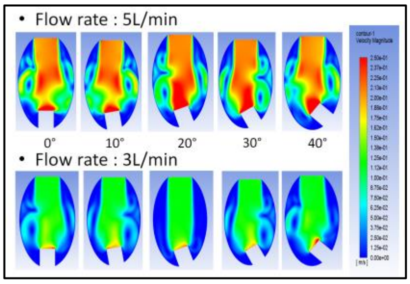

Figure 3: Velocity magnitude: [0-0.25] m/s

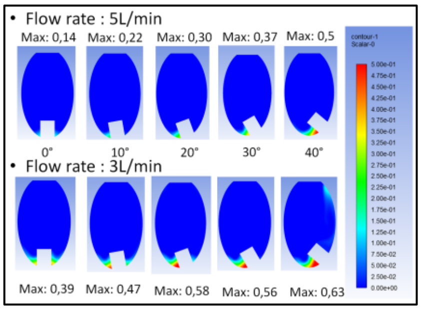

Figure 4: Ink concentration: [0-0.5]

4 Conclusion

The contribution of this paper is to investigate the influence of a wide range of cannula angulation on blood stagnation in case of LVAD implantation using CFD computation. The investigated parameters were the velocity magnitude and the concentration of a virtual ink injected in the left ventricle. The results showed blood stagnation located at the ventricular apex for all configurations, and a markedly faster blood clearing for the apical configuration. Our results are confirmed by the surgical practice that tends to align the inflow cannula with the mitral valve. Blood stagnation being a complex phenomenon, CFD tool may be a way to investigate mechanical factors of blood stagnation even though it does not take account of chemical and biological interactions between different blood components. Further work is still required to devise an advanced marker for anticipating coagulation risk at the surgical planning stage and to address issues related to the consideration of patient-specific 3D model, aortic and mitral valves function or heart motion that may influence blood flow.

5 Acknowledgements

This work was partially supported by the French National Research Agency (ANR) in the framework of the Investissement d'Avenir Program through Labex CAMI (ANR-11- LABX-0004).

6 References

[1] S. Collin, A. Anselmi, J. P. Verhoye, P. Haigron, and E. Flecher, "Virtual positioning of ventricular assist device for implantation planning," *Irbm*, vol. 36, no. 6, pp. 317–323, 2015.

[2] S. Collin, "Preoperative planning and simulation for artificial heart implantation surgery," Université de Rennes, 2018.

[3] A. R. Prisco, A. Aliseda, J. A. Beckman, N. A. Mokadam, C. Mahr, and G. J. M. Garcia, "Impact of LVAD Implantation Site on Ventricular Blood Stagnation," *ASAIO J.*, vol. 63, no. 4, pp. 392–400, 2017.

[4] Venkat Keshav Chivukula, Jennifer A. Beckman, Anthony R. Prisco, Todd Dardas, Shin Lin, Jason W. Smith, Nahush A. Mokadam, Alberto Aliseda, Claudius Mahr, "Left Ventricular Assist Device Inflow Cannula Angle and Thrombosis Risk," *Circ. Hear. Fail.*, vol. 11, no. 4, pp. 1–9, 2018.

[5] S. E. Razavi and R. Sahebjam, "Numerical simulation of the blood flow behavior in the circle of Willis," *BioImpacts*, vol. 4, no. 2, pp. 89–94, 2014.

[6] V. L. Rayz, L. Boussel, L. Ge, J. R. Leach, A. J. Martin, M. T. Lawton, C. McCulloch and D. Saloner, "Flow Residence Time and Regions of Intraluminal Thrombus Deposition in Intracranial Aneurysms," *Ann. Biomed. Eng.*, vol. 38, no. 10, pp. 3058–3069, 2010.

Transesophogeal HIFU cardiac fibrilation therapy guidance by two perpendicular US images

Batoul DAHMAN, Jean-Louis DILLENSEGER

Univ Rennes, INSERM, LTSI – UMR 1099, F-35000 Rennes, France
Tel : +33 (0)2 23 23 62 20
Contact: batoul.dahman@univ-rennes1.fr

1 Introduction

During the last years, cardiac patients with arrhythmia (or irregular heart beat) have been treated using ablatiion therapies such as Radio Frequency (RF). High-intensity focused ultrasound (HIFU) energy can be used to create thermal lesions in deep tissues without damaging the tissues in the propagation path. Transesophogeal HIFU cardiac fibrillation therapy is a mini-invasive treatment that places the HIFU transducer close to the ablation zone by navigating inside the esophagus, the probe navigation and transducer positioning is carry out using an embedded ultrasound (US) imaging system [1].

As any mini-invasive procedure, first a therapy planning (the ablation path) is defined on high-resolution anatomical preoperative 3D imaging (CT/MRI). The goal of this work is to propose a therapy guidance system by the registration of the intraoperative 2D-US images to the preoperative volume.

In a previous study, the registration of one 2D US image perpendicular to the esophagus axis to the preoperative 3D-CT was proposed with the hypothesis of some strong anatomical constraints [2].

A new HIFU probe with 2 perpendicular 2D US imaging planes is now under study. We propose to integrate the information of these new imaging planes in the registration scheme to relieve the anatomical constraints and gain localization accuracy.

2 Two 2D-US/3D-CT image-based Registration

As input we have a 3D-CT and two perpendicular US images acquired on the HIFU probe. Because the US imaging tool is ECG gated, we consider only the US images at the same cardiac phase as the CT and so only a 3D rigid transform with six degrees of freedom has to be estimated. We have also an initial rough estimation of the pose of the probe inside the 3D-CT (e.g. estimated by the method described in [2]). From this initial pose, we performed the following two 2D/3D (two perpendicular slices/volume) image-based registration approach to refine the estimation of the transesophageal probe pose. This approach is characterized by:
1) Slice extraction :
For a specific probe pose, the 3D transform allows us to define the US imaging referential system $(\vec{O}_i, \vec{x}_i, \vec{y}_i, \vec{z}_i)$, in which the 2 perpendicular planes, x_i– y_i and y_i– z_i represent the US perpendicular slices. The CT volume is then sampled along these 2 planes to provide the information in the same spatial context (same size and spatial location) as the US images;
2) similarity metric :
We used Mutual Information to compare the information of the US images and the corresponding information extracted from the CT data. The global similarity will be the sum of the similarity measures between the two sets of slices;
3) Optimizer :
We used gradient descent to estimate the pose which maximize the global similarity.

3 Results

A feasibility study has been conducted on a patient with fibrillation CT dataset, obtained from Louis Pradel University Hospital in Lyon, France. Because the HIFU probe with the 2 perpendicular US imaging planes is still under development. We validate our method on simulated US data. For this, we defined an initial pose (the ground truth-GT) inside the CT volume. From this pose we extracted two perpendicular slices from the CT and simulated the corresponding US slices with the method described in [3]. Then, we randomly produced 55 initial poses in a range of ± 5 mm on translation and ± 5° in rotation around the GT pose and performed the registration. The accuracy of the registration is estimated through (1) transformation parameter estimation errors; and, (2) Target Registration Error (TRE).

3.1 Transformation estimation error

The transformation parameter errors are the differences for each 6 parameters of the transformation between the estimated pose of each trial and GT. Figure 1 shows the boxplot of these errors in (a) translation expressed in mm, and (b) rotation expressed in degree. We can see the median errors are less than 0.7 mm for translation and 0.9 degree for rotation.

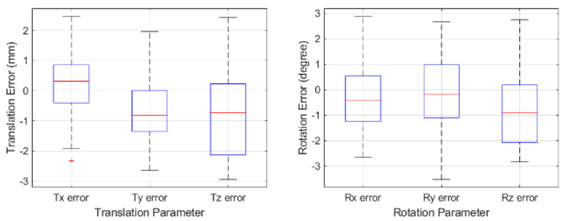

(a) (b)

Figure1: Boxplot corresponding to the estimation error. (a) in terms of translation parameters. (b) in terms of rotation parameters.

3.2 Target Registration Error (TRE)

The validation can be done by estimating registration errors on some specific feature points. To quantify the error, we defined eight specific feature points (or landmarks) Pj in the two 2D-US fixed images, and we used the two transformations matrices T_{Est} and T_{GT} to project these points in the 3D-CT volume.

$$TRE(P_j) = \|T_{GT}\, P_j - T_{Est}\, P_j\|$$

Figure 2 shows the boxplot of the TREs for all the 8 fiducial points. Quantitative results show a mean TRE of 1.76 mm for the overall set of fiducial points.

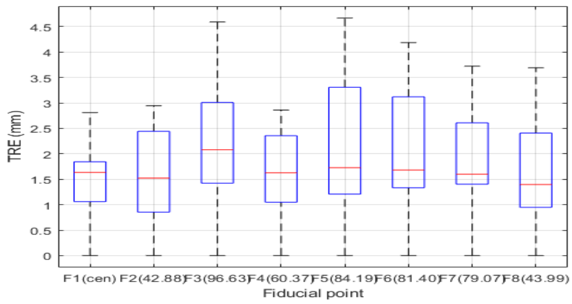

Figure2: Box plots of the Target Registration Error (TRE). The boxplots are ordered from left to right according to the distance of the fiducial points to Oi.

3.3 Visual validation

Figure 3 shows the simulated US images (a and c) and their superimposition to the estimated corresponding reformated CT slice (b and d) The visual examination of these two figures shows a good alignment.

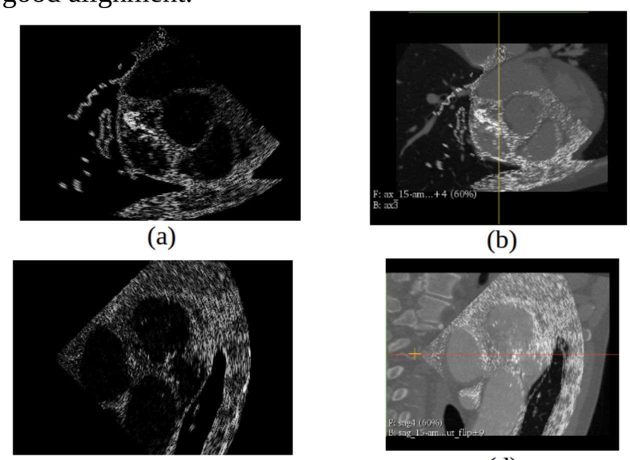

(a) (b) (c) (d)

Figure3: Visualization result (a) image_US1, (b) resulted CT_slice 1, (c) image_US2, (d) resulted CT_slice 2.

4 Conclusion

We performed rigid registration of two 2D planar echocardiography images with a cardiac CT volume. Results indicate promising accuracy of the proposed technique. Our future work aims at include phantom and real-patients data to evaluate the contribution of the registration scheme for the therapy guidance.

5 References

[1] F. Bessiére et al., "Ultrasound-Guided Transesophageal High-Intensity Focused Ultrasound Cardiac Ablation in a Beating Heart: A Pilot Feasibility Study in Pigs," Ultrasound Med. Biol., 42(8), pp. 1848–1861, 2016.

[2] Z. Sandoval et al., "Transesophageal 2D Ultrasound to 3D Computed Tomography registration for the guidance of a cardiac arrhythmia therapy," Phys. Med. Biol., 63(15), p. 155007, 2018.

[3] J.-L. Dillenseger et al., "Fast simulation of ultrasound images from a CT volume," Comput. Biol. Med., 39(2):180–186, 2009.

acknowledgments

This work was part of the CHORUS (ANR- 17-CE19-0017) project which have been supported by the French National Research Agency (ANR).

Potential of global vision system for learning laparoscopy surgical skills

Sinara VIJAYAN, Elio KEDDISEH, Bertrand TRILLING and Sandrine VOROS
Laboratory TIMC-IMAG, GMCAO, Pavillon Taillefer, Faculty of Medicine, La Tronche, France
Tel : +(+33) 4 56 52 00 09
Contact: Sandrine.Voros@univ-grenoble-alpes.fr

1 Introduction

Laparoscopy has been around for almost 40 years now and has become the gold standard for many different organ procedures especially digestive and gynecological procedures [1]. Even though the challenges are more with these procedures, the advantages for the patient with regard to the surgical outcome made it the preferred procedure. The limited field of view (typically 70^o compared to 160^o for humans) still continues to be a challenge for the surgeons to perform the surgical task quickly with precision. Technology has been used to help improve laparoscopy using better imaging methods, surgical techniques and instruments. Training the surgical residents well also has a key role in improving the outcome for laparoscopy. The learning curve is quite steep, as they have to perform a lot more surgeries than open procedures to understand the challenges and how to cope with them. Unlike with open surgeries, the technical skills needed for laparoscopy are distinct. The lack of tactile feedback and impaired depth perception due to limited field of view combined with long instruments create fulcrum effect and amplify tremor. Increasing the field of view using enhanced laparoscopy with distributed vision systems has been explored in the last few years [2-4]. The global vision system developed in our lab [2] increases the field of view by using two additional mini-cameras placed at the same orientation as that of the endoscope, but close to the abdominal wall. These cameras are encased inside an enhanced trocar attachment which when passed through the trocar can be deployed to be suspended. In this study, we look at how we can use the global vision system to help surgical residents improve their skills over multiple sessions.

2 Methods

2.1 Laparoscopic test-bench

A test bench using a curved plexiglass sheet (1) placed on a metallic frame (3) was built (refer Fig 1 for the numbered annotations). The curvature was simulating the inflated abdomen during laparoscopy. The exercise board (2) was placed inside the test bench as shown in Fig 1. Three holes were introduced, two to insert the tools and one for the endoscope. Rubber patches (4) were fixed to the tool trocars on the sides to enable flexibility needed when working with the tools. We fixed an endoscope (5) with a corresponding endoscope holder (6) in the central hole in order to target the scenario where a surgeon is working with a zoomed in endoscope to prevent the effect of any additional factors. The GVS system prototype was attached to the surface of the plexiglass sheet. Two mini-cameras were placed inside the GVS prototype taped to the plexiglass sheet and a third mini-camera was attached to a tool passing through the central trocar which was to act as the endoscope. All the three cameras were attached to three Raspberry Pis for us to be able to automate the recording of videos from each of the cameras.

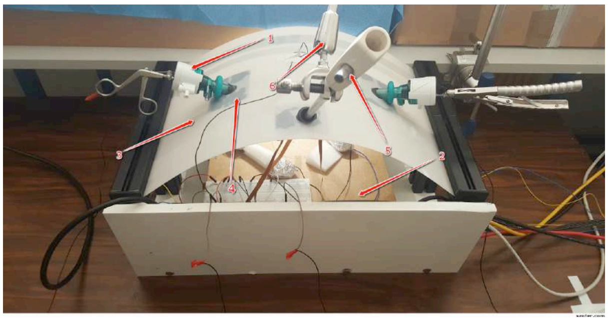

Figure 1 Close view of the test bench with annotations

The feed from the three cameras were displayed on to three monitors (Fig 2).

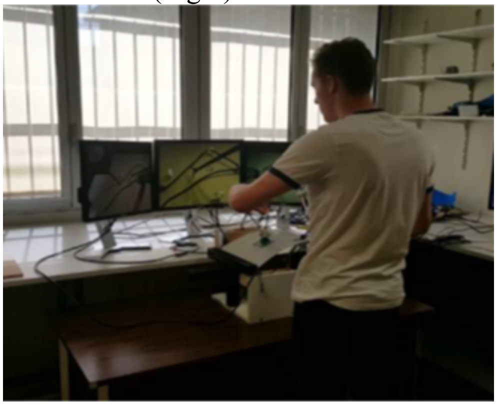

Figure 2 Experimental setup with displays

2.2 *Experimental protocol*

We pooled a population of 20 medical students to (level similar to junior surgery residents) perform exercises mimicking the skills needed for the actual surgical tasks on the test bench and divided them into two groups. One group performed the exercises with the GVS and the other without the GVS. However, since the learning curve can require several hundreds of trials [5], we studied the progression of time performance over five sessions. Four exercises were performed twice after a 3-day interval between each session. These exercises were designed to study the skill progression of the trainees in the two groups, which were to be performed over the five sessions. The participants were asked to start the first session with a training exercise before performing the first exercise. In the subsequent sessions they were asked to repeat the task performed in the previous session before moving on to a slightly more complex exercise than the previous one in the current session. This way we, were able to study the skill progression by computing the difference in performing the same exercise after a short interval between the sessions (3 days). The exercises designed for the purpose of this study had an increasing difficulty, which were inspired from typical training exercises used during laparoscopy courses. They are listed below:

1. Training session: The participants were asked to place thumb-tracks in designated positions on the exercise board. The main objective of this training exercise was to get familiar is getting familiar with the instruments and the setup. Each participant performed this exercise once during Session 1 for 5 minutes.
2. Thread transfer: Having a starting and ending point, the participant had to transfer the thread through four pegs following a given trajectory. This exercise aimed to improve motor skills. (exercise during sessions 1 and 2).
3. Elastic placement: Five screws were bolted onto an exercise board, participants had to expand the elastics with their instruments and position them onto two of the screws as required per elastic color. (exercise during sessions 2 and 3)
4. Paper clip untangle: Participants had to untangle four paper clips placed on the exercise board. This exercise requires motor skills and problem solving skills (exercise during sessions 3 and 4).
5. Paper folding: Participants had to fold a square piece of paper twice so they make a perfect triangle. Main objectives of this exercise are fine instrument control and tissue (here paper) handling (exercise during sessions 4 and 5).

3 Results

The mean time to perform each exercise on each session per group and compared the differences between the sessions and calculated the mean improvement. (Table 1)

Table 1: Mean time to perform exercises in each session (seconds)

Mean time diff. between sessions	S2-Ex1-S1-Ex1	S3-Ex2-S2-Ex2	S4-Ex3-S3-Ex3	S5-Ex4-S4-Ex4
Endosocope	130.8	11.5	-30.4	-47.2
GVS	72.7	50.3	-1.9	112.1

The group that used the endoscope view alone had an improvement rate of 2.25% while the other group had an improvement rate of 21.76%.

4 Conclusion

The global vision system improved the performance of novices while performing complex tasks by at least 10 times compared to when using the endoscope alone. The global vision system clearly would be an useful aid for novices getting into surgical practice.

5 Acknowledgements

This work was partially supported by the French state funds managed by the ANR within the DEPORRA2 project under reference ANR-14-CE17-0009-01 and Investissements d'Avenir programme (Labex CAMI) under reference ANR-11-LABX-0004

6 References

[1]Reynolds W. The first laparoscopic cholecystectomy. JSLS 2001;589-94

[2] Tamadazte B, Fiard G, Long J-A, Cinquin P, Voros S (2013) Enhanced vision system for laparoscopic surgery. Conf Proc IEEE Eng Med Biol Soc 2013:5702–5705.

[3] Kim J-J, Watras A, Liu H, Zeng Z, Greenberg J, Heise C, Hu Y, Jiang H (2018) Large-Field-of-View Visualization Utilizing Multiple Miniaturized Cameras for Laparoscopic Surgery. Micromachines 9:431

[4] Sumi Y, Egi H, Hattori M, Suzuki T, Tokunaga M, Adachi T, Sawada H, Mukai S, Kurita Y, Ohdan H (2019) A prospective study of the safety and usefulness of a new miniature wide-angle camera: the “BirdView camera system.” Surgical Endoscopy 33:199–205

[5] Kim HG, Park JH, Jeong SH, Lee YJ, Ha WS, Choi SK, Hong SC, Jung EJ, Ju YT, Jeong CY, et al. Totally laparoscopic distal gastrectomy after learning curve completion: comparison with laparoscopy-assisted distal gastrectomy. J Gastric Cancer. 2013; 13:26–33

Segmenting Surgical Tasks using Temporal Convolutional Neural Network

Mégane MILLAN and Catherine ACHARD
Sorbonne Université - CNRS UMR 7222 - Institut des Systèmes Intelligents et de Robotique
Tel : +33 (0)1 44 27 62 09
Contact: name@isir.upmc.fr

Automatic tasks segmentation is a necessary step towards robots integration in our daily life, whether in Operating Room (OR) or someone's living-room. In this article, we propose to use deep learning, and more specifically 1D Convolutional to automatically segment surgical tasks. With this kind of approach, features are learned in an end-to-end manner from raw kinematic data.
We tested our method on the recently released JIGSAWS dataset and obtain better results compared to other state-of-the-art methods with a global accuracy of 82%, in a Leave-One-User-Out setup.

1 Introduction

Surgical interventions are complex tasks, composed of multiple gestures and actions to be performed with great precision. Thus,to help surgeons during long interventions, robots are introduced in the Operating Room (OR). Robots must therefore understand the scene they are in and adapt their behavior accordingly. Hence, they must be able to interpret gestures performed by surgeons at all times, which implies tasks segmentation and sub-gestures recognition.

For this purpose, works from [1] use statistical models, such as Hidden Markov Model (HMM) or Conditional Random Fields (CRF). These methods model a task with discrete states. Afterwards, segmentation is done by assigning a state to each timestep.

More recently, a wide variety of neural network architectures has emerged. In [2], DiPietro et *al.* use recurrent neural networks (RNN) to recognize surgical sub-gestures. Actually RNN deals with time-series and have the capacity to capture long-term dependencies. Lea et *al.* [5] propose a temporal convolutional neural network (CNN) with an encoder-decoder-based architecture, which has the property to encode a sequence into a high-level representation. This architecture is similar to one used on 2D images to predict human pose estimation from RGB images [8].

In the present paper, we propose an approach based on the combination of [8] and [5] to segment surgical tasks into sub-gestures.

2 Methodology

To segment time-series, the neural network architecture takes as input a multi-dimensional time-series X with size $\mathbb{R}^{M\times T}$, M being the dimension of the time-series and T its length, and predicts the output Y with size $\{0,1\}^{N\times T}$, N being the number of possible sub-gestures.

Inspired by the hourglass architecture [8], by the temporal encoder-decoder (ED-TCN) [5] and by the skip connections proposed in [4] or in the U-Net network [9], we introduce the ED-TCN with skip connections.

As we can see in Figure 1, the idea is to keep the temporal encoder-decoder architecture, while adding skip connections between the encoder and decoder parts. If an identity mapping is optimal, it would be easier to fit it than trying to do it using stacks of nonlinear layers. Adding skip connections allows the network to learn this identity mapping. Thus, the network can stop decreasing the temporal resolution if it seems relevant. Moreover, during training, gradient will flow through the network following 2 paths, reducing the risk of "vanishing gradient".

The encoder is composed of L blocks, a block being a sequence of a 1D-convolutional layer, a pooling layer and a channel-wise normalization. All pooling layers

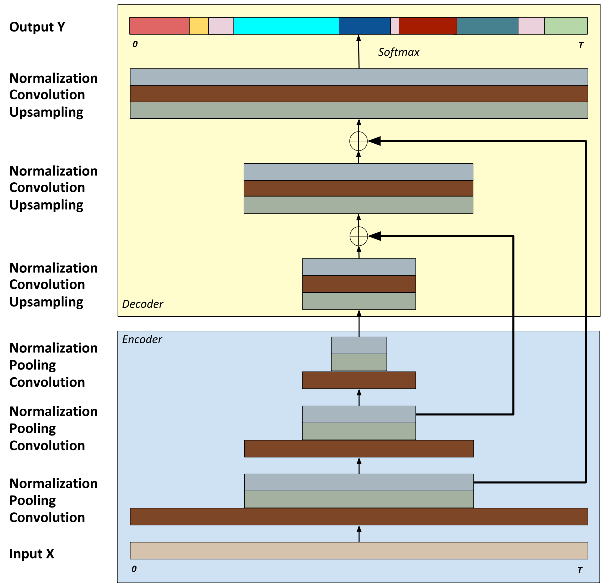

Figure 1: *The ED-TCN with skip connections represented in bold*

half their input length. Moreover, all convolutional layers are composed of filters with the same temporal length d in order to capture information at different temporal scales.

3 Results

Dataset In order to compare our method with previous existing ones, tests are performed on the publicly available JHU-ISI Gesture and Skill Assessment Working Set (JIGSAWS) [3]. We decided to only use kinematic data to compare our results with state-of-the-art methods. Tests were performed in a Leave-One-User-Out setup.

Implementation details The network is composed of $L = 3$ blocks and each block has $F = (32, 64, 96)$ convolutional filters as described in [7]. We performed many tests to find the best number of filters for each layer, and best results were achieved with the number of filters from [5]. For training, we used cross-entropy as a loss function and the ADAM algorithm to optimize parameters. Moreover, the network is trained for 150 epochs and we use a batch size of 5. Batch size and epochs were found empirically.

Results To choose the best parameters for our application, we performed multiple tests on filter length and kinematics dimensions used as input. We tried different lengths d ranging from 10 to 50 samples. Filter duration is the same for all convolutional layers as explained in 2. As we can see in Table 1, the best results are obtained

Filter length	ED-TCN-Skip
10	80.46
20	81.09
30	**82.07**
40	81.73
50	80.13
Features	ED-TCN-Skip
All	77.76
Slave	78.95
PVG	**82.07**

Table 1: *Average segmentation accuracy according to features input and to filter length*

with a filter length d of 30 samples. As proposed in [6], we tried different subsets of dimensions : all kinematics (from master and slave manipulators), kinematics from the slave manipulators, and position P, velocity V and Gripper Angle G, from the slave manipulators(PVG). As presented in Table 1, using PVG as input shows optimum results.

Once we obtained the optimal parameters, we compared our results with state-of-the-art methods [1], [2], [7]. As displayed in Table 2, our method outperforms state of the art by 3%.

4 Conclusion

In this paper, we introduced a new neural network architecture to segment surgical tasks that outperforms state-of-the-art results by 3%.

In future works, we would like to extend this method to video data of real surgery, which are easier to obtain and fit better with real life applications.

Another goal would be to use segmentation results to implement an architecture which predicts surgical skills. The final system would be able to score automatically surgical trainees during their curricula.

	SUTURING	NEEDLE PASSING	KNOT TYING	AVERAGE
GMM-HMM (1)	73.95	64.13	72.47	70.18
KSVD-HMM (1)	73.45	62.78	74.89	70.37
SC-CRF (1)	81.74	74.77	78.95	78.49
LSTM (2)	80.5	**N/A**	**N/A**	**N/A**
BiLSTM (2)	83.3	**N/A**	**N/A**	**N/A**
ED-TCN (7)	**N/A**	**N/A**	**N/A**	79.6
Ours	**83.9**	**78.08**	**84.28**	**82.07**

Table 2 : *Sub-gesture segmentation accuracy of our method and those proposed in [1], [2], [7]. Best results are displayed in blue.*

References

[1] N. Ahmidi, L. Tao, S. Sefati, Y. Gao, C. Lea, B. B. Haro, L. Zappella, S. Khudanpur, R. Vidal, and G. D. Hager. A Dataset and Benchmarks for Segmentation and Recognition of Gestures in Robotic Surgery. *IEEE Transactions on Biomedical Engineering*, 64(9):2025–2041, Sept. 2017.

[2] R. DiPietro, C. Lea, A. Malpani, N. Ahmidi, S. Vedula, G. I. Lee, M. Lee, and G. Hager. Recognizing Surgical Activities with Recurrent Neural Networks. In *Medical Image Computing and Computer-Assisted Intervention MICCAI 2016*, volume 9900, pages 551–558. 2016.

[3] Y. Gao, S. S. Vedula, C. E. Reiley, N. Ahmidi, B. Varadarajan, H. C. Lin, L. Tao, L. Zappella, B. Bejar, D. D. Yuh, C. C. G. Chen, R. Vidal, S. Khudanpur, and G. D. Hager. JHU-ISI Gesture and Skill Assessment Working Set (JIGSAWS): A Surgical Activity Dataset for Human Motion Modeling. *Modeling and Monitoring of Computer Assisted Interventions (M2CAI) MICCAI Workshop*, page 10, 2014.

[4] K. He, X. Zhang, S. Ren, and J. Sun. Deep residual learning for image recognition. *IEEE Conference on Computer Vision and Pattern Recognition (CVPR)*, 2016.

[5] C. Lea, M. Flynn, R. Vidal, A. Reiter, and G. Hager. Temporal Convolutional Networks for Action Segmentation and Detection. pages 1003–1012, July 2017.

[6] C. Lea, G. Hager, and R. Vidal. An Improved Model for Segmentation and Recognition of Fine-Grained Activities with Application to Surgical Training Tasks. pages 1123–1129. IEEE, Jan. 2015.

[7] C. Lea, R. Vidal, A. Reiter, and G. Hager. Temporal Convolutional Networks: A Unified Approach to Action Segmentation. In *Computer Vision ECCV 2016 Workshops*, volume 9915, pages 47–54. Springer International Publishing, 2016.

[8] A. Newell, K. Yang, and J. Deng. Stacked Hourglass Networks for Human Pose Estimation. *computer vision - ECCV 2016*, Mar. 2016.

[9] O. Ronneberger, P. Fischer, and T. Brox. U-net: Convolutional networks for biomedical image segmentation. In *Bildverarbeitung für die Medizin*, 2017.

An Experimental Protocol on Attentional Abilities in Classic and Robot-Assisted Laparoscopy

Eléonore Ferrier-Barbut, Vanda Luengo and Marie-Aude Vitrani
Sorbonne Université, CNRS UMR 7222
Institut des Systèmes Intelligents et de Robotique, ISIR, F-75005 Paris, France
Contact: marie-aude.vitrani@sorbonne-universite.fr

Main goal of robot-assisted laparoscopic surgery is to alleviate surgeons workload and increase their performances. Their impact on the process of learning by residents in medicine is underestimated. Our research project deals with this issue.

1 Purpose

Studies demonstrate that Robot-Assisted Laparoscopic Surgery (RALS) improves dexterity [1] and performance [2]. These studies justify for increasing robots number in operating rooms, forcing residents in medicine to train in both Classic Laparoscopic Surgery (CLS) and RALS. However, they include already expert surgeons and relate observed performance rather than acquired skills. The role of these RALS in long term education of residents in medicine and the transfer of skills with CLS is not well known [3]. Our research project aims at filling this gap.

In this article, we present an experimental protocol which has no experimental results yet, aiming to analyze the impacts of learning in RALS on development of attentional abilities in CLS. We intend to test it on both a telemanipulated and a comanipulated robot. The research question is the following: does learning RALS, with a telemanipulated or comanipulated assistance deteriorate or improve development of eye-hand coordination skills in CLS?

2 Learning in Each Technique

CLS and RALS can be considered similar as they share a large range of skills to be mastered by the apprentice surgeon. Practiced with or without robot, laparoscopic surgery requires knowledge in anatomy, procedures, complications. It requires dexterity, good proprioception, leadership, capacity for anticipation, for formulating action plans, for being aware of the situation, an ability to make decisions [4], among other skills. However, some of these skills are applied very differently in one technique and the other. Dexterity is the most compelling example because in the case of RALS making it easier to master tends to be the first goal. Learning to perform RALS means learning new motor skills which may deteriorate those learnt in CLS. To investigate this, conventional metrics such as time to perform the exercise or traveled distance with the instruments, emphasized as incomplete to analyze improvements in laparoscopic surgery in several studies [5, 6] should be completed with other more dynamic metrics.

3 Material and Methods

We study acquisition of eye-hand coordination skills related to laparoscopic surgery, depending on the form of RALS used for learning. We intend to measure participants off task skills which could bias the results. Study takes place in three steps: one in CLS for measuring participants base level (cf fig.1a), one learning session either in CLS, in RALS with a comanipulated robot (cf fig.1b), or in RALS with a telemanipulated robot (cf fig.1c) depending on the participants group, and one last step for measuring their level after the learning session. Measures taken during first and third step are used to compare differences before and after learning for each group separately.

3.1 Measuring tools

- **Eye-hand coordination**: The 3D trajectory of the tip of the two instruments, videos of the exercises and gaze pattern of the participants on the screen are recorded. Directly linked to the distribution of attention, eye gaze data uncovers the process of learning rather than underpinning improvements in performance [7], while gestures data permits to study motor skills acquisition.

- **Off-task Skills**: Before the learning session, we measure their off-task skills such as video-games, sports, music instruments expertise etc, all of which could bias the results.

3.2 Apparatus

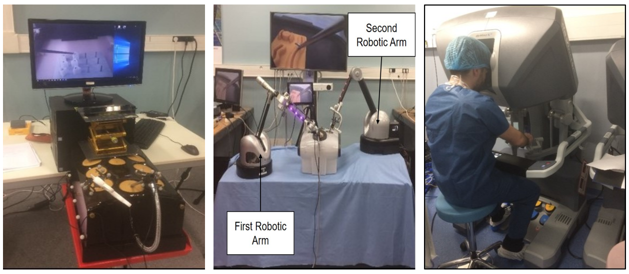

(a) *Classic* **(b)** *Achille* **(c)** *da Vinci*

Telemanipulated Robotic Assistance: System used is the da Vinci. In the case of the da Vinci, the surgeon sits at a console physically separated from the instruments. All technical specifications and differences compared to CLS can be found in Broeders *et al.* article [8]. For this experiment, exercises from the robot's simulator are used.
Comanipulated Robotic Assistance: System used is Achille. Its configuration is the same as the CLS one. It is made of two robotic arms, one for assistance in manipulating the endoscope and the second one in manipulating one of the instruments the surgeon is operating with. Both the arms have a "blocking" function, the second robotic arm has an additional "viscosity" function.

3.3 Tasks

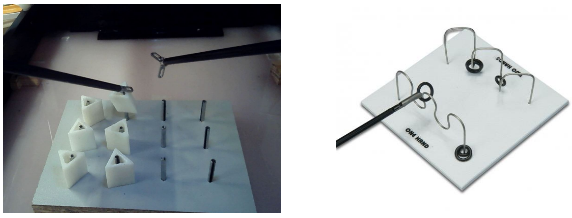

(a) *Peg Transfer* **(b)** *Wire Chaser*

First Step: Completion of three laparoscopic surgery exercises, carried out on a pelvitrainer while measures are taken. Inside it are inserted two laparoscopic graspers and an endoscope. On top is displayed a screen showing in 2D the inside of the pelvitrainer. (1) *"Peg Transfer Dominant"*: subjects have to grab pegs with the instrument held in their dominant hand, transfer it in the instrument held in the other hand, drop them on a target. They had to do as many as they could within four minutes (cf fig.2a). (2) *"Peg Transfer Non Dominant"*: subjects have to transfer the peg from instrument held in non dominant hand to instrument held in dominant hand, in a specified time of four minutes. (3) *"Wire Chaser"*: subjects have to move three rings of decreasing diameter, one by one on a rail. Both hands are used and need to change after each curve of the rail (cf fig.2b).
Second Step: One hour learning session, consisting of exercises of increasing difficulty. Depending on the group participants were in, learning session is performed on a telemanipulated RALS, comanipulated RALS or in CLS. The exercises performed with each technique are slightly different, but develop the same motor skills.
Third Step: At least one week after the learning session, completion of the same exercises as those performed during the first session, in the same conditions. Same measures as during the first step are taken.

4 Hypothetical results

Assuming that our assumptions are confirmed, we should obtain the following results:

- We hypothesize that eye-hand coordination skills will be more developed in group of participants who learned on Achille compared to groups who learned on da Vinci or without robot. This should result in a better capacity to anticipate gesture with gaze which means a greater number of fixations on the aimed target during target-reaching exercises for group Achille compared to group CLS or da Vinci, a smaller number of saccades during moments of transferring and of dropping the object and longer fixation duration.

- We hypothesize that motor skills should be more developed in group of participants who learned on Achille. This should result in a smaller number of movements with each instrument while performing the three exercises for group who learned on Achille compared to two other groups and a smaller path length at the tip of both instruments.

5 Conclusions

The role of robot assistance for motor learning still needs to be better understood. The goal of the study is to give an insight into the part RALS plays in training for surgery: making it less cognitively and physically demanding while not adding more complexity to the task when switching back to without robot condition. However, this study focuses on the development of eye-hand coordination skills which is only one part of the skills needed to practice surgery. One could think of an experiment closer to a realistic surgical put at test not only eye-hand coordination skills but also knowledge in anatomy, procedure, complications and the role of robots for helping to train in these skills as well.

References

[1] Moorthy, K., Munz, Y., Dosis, A., Hernandez, J., Martin, S., Bello, F., ... Darzi, A. (2004). Dexterity enhancement with robotic surgery. Surgical Endoscopy and Other Interventional Techniques, 18(5), 790-795.

[2] Blavier, A., Gaudissart, Q., Cadiere, G. B., Nyssen, A. S. (2007). Perceptual and instrumental impacts of robotic laparoscopy on surgical performance. Surgical endoscopy, 21(10), 1875-1882.

[3] Prasad, S. M., Maniar, H. S., Soper, N. J., Damiano Jr, R. J., Klingensmith, M. E. (2002). The effect of robotic assistance on learning curves for basic laparoscopic skills. The American journal of surgery, 183(6), 702-707.

[4] Darzi, A., Mackay, S. (2001). Assessment of surgical competence. BMJ Quality Safety, 10(suppl 2), ii64-ii69.

[5] Narazaki, K., Oleynikov, D., Stergiou, N. (2006). Robotic surgery training and performance. Surgical Endoscopy and Other Interventional Techniques, 20(1), 96-103.

[6] Smith, C. D., Farrell, T. M., McNatt, S. S., & Metreveli, R. E. (2001). Assessing laparoscopic manipulative skills. The American journal of surgery, 181(6), 547-550.

[7] Sailer, U., Flanagan, J. R., Johansson, R. S. (2005). Eyehand coordination during learning of a novel visuomotor task. Journal of Neuroscience, 25(39), 8833-8842.

[8] Ivo A.M.J. Broeders, Jelle Ruurda, (2001) "Robotics revolutionizing surgery: the Intuitive Surgical Da Vinci system", Industrial Robot: An International Journal, Vol. 28 Issue: 5, pp.387-392 10.1108/EUM0000000005845

Mixed Reality Experiment for Hemodialysis Treatment

Christophe LOHOU[1], Marc BOUILLER[2] and Emilie GADEA-DESCHAMPS[3]
[1]Université Clermont Auvergne, CNRS, SIGMA Clermont, Institut Pascal, F-63000 Clermont-Ferrand, France
[2]Service de Néphrologie-Hémodialyse, Centre Hospitalier Emile Roux, 12 boulevard Docteur Chantemesse, F-43000 Le Puy-en-Velay, France
[3]Unité de Recherche Clinique, Centre Hospitalier Emile Roux, 12 boulevard Docteur Chantemesse, F-43000 Le Puy-en-Velay, France
Tel : +33 (0)4 71 09 90 87
Contact: christophe.lohou@uca.fr

The recent advent of Microsoft HoloLens headsets allows us to design innovative software applications in order to assist clinicians/nurses in their care/treatment. In this study, we present first results of needle positioning assistance for future hemodialysis sessions.

1 Context

1.1 Medical problem

Figure 1: (left) fistula [1], (right) puncture [2]

We are interested in patients with kidney failure. One treatment is to set up hemodialysis sessions: an arteriovenous fistula is first realized (Figure 1 left), then after several months, it is possible to filter blood. Two needles are positioned inside the fistula (Figure 1 right) for “dirty” blood ejection and filtered blood arrival after its travel through a dialyser. Several puncture techniques have been proposed (on the same injection site or not) [3].

We would like to record data about needle position and orientation at each dialysis session to propose a clinical study about the influence of the choice of the injection sites with regard to the pain felt or risks (thrombosis, aneurysm) incurred by patients.

Figure 2: HoloLens headset and user view [4]

1.2 Mixed reality

Microsoft HoloLens headsets [5] were recently released in France (December 2016). Such a headset uses different sensors. It is a self-contained computer with Wi-Fi connectivity. These helmets have a semi-transparent visor on which 3D objects (called *holograms*) are projected; they can thus be superimposed on the user’s environment. A user can interact with these objects through headset-recognized gestures if the software has intended it (for example: aiming at an object to select it, then pinching the fingers and moving the hand to move this object), Figure 2. The helmet also scans the environment and holograms can interact with it (for example, they may fall from an actual table).

In order to design applications running on this type of headset, frameworks for the development of interactive 3D graphics applications can be used. Until recently, only Unity framework [6] was able to develop applications that could be rather easily deployed inside such a hardware (nevertheless with Unity Editor and C# programming language skills).

In order to design an application, it is necessary to plan the digital content (3D objects) to be displayed, the possible interactions of the user with the environment and with these 3D objects. The content (3D models) must be designed, then it must be integrated inside Unity, managed into a scene; the selected interactions must be implemented (C# scripts under Unity, with the Mixed Reality Toolkit MRTK library [7]).

2 Our software

We have then developped the following sequel of steps for our application : (step1) two-part arm modeling to propose a joint at elbow, and patient’s fistula modeling (Blender software [8]), Figure 3 ; (step2) export to Unity and positioning of the two arms parts inside two bounding boxes (one box rotated relative to the other for the elbow joint), Figure 4; (step3) alignment of the two needles on the fistula (color code: blue for blood to be cleaned, red for filtered blood, green for current needle which is aligned), to register them and to display the corresponding parameters values of position and rotation transforms (positioning, Figure 5 left; orientation, Figure 5 right). The transforms parameters for a set of needles into Unity can be recorded, then the application is deployed with these new data into the headset, in order to visualize this set of needles correctly positioned and oriented.

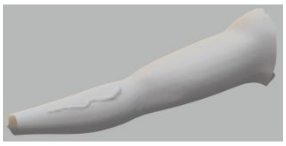

Figure 3: 3D model of the arm-fistula pair

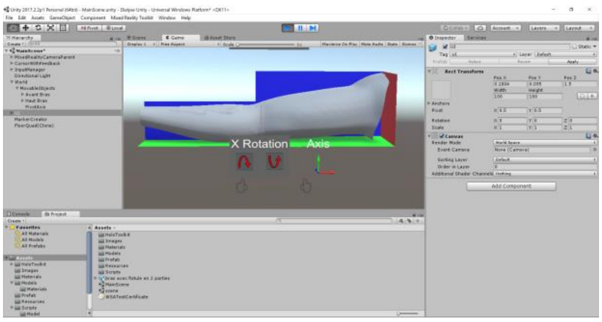

Figure 4: Unity Editor view and import of the 3D model of arm

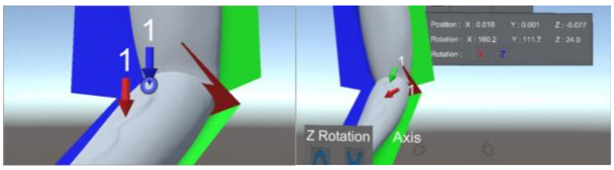

Figure 5: (left) needles positioning, (right) needles orientation and data display

3 Results

We propose two user cases for future hemodialysis sessions. The first case: a nurse places the needles onto the patient’s arm and a healthcare assistant, wearing the headset, interactively registers the virtual 3D arm on the real arm (Figure 6, left), then positions and rotates two virtual 3D needles that need to be interactively and manually registered onto the real ones; then the healthcare assistant can record the position and orientation information of the needles to display them for a next dialysis session. The second case: a nurse determines how s.he wishes to perform the puncture before a dialysis session onto the 3D arm model inside Unity Editor, then deploys the application with this new information into the headset; then a healthcare assistant, wearing the headset, assists the nurse to align two real needles onto the two virtual ones during the dialysis session.
In both cases, both the needles and virtual arms transparency must be adjusted to visualize the real needles. A minimum distance between the headset and the display of 3D objects (*near clipping plane*) must also be taken into account. Positions and orientations of the needles at each session could also be displayed for the current session according to the chosen puncture technique (Figure 6, right).

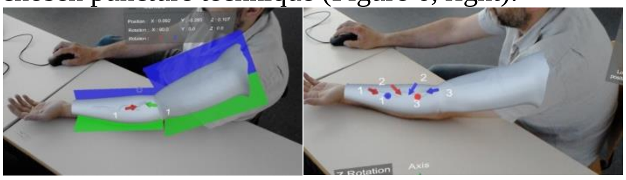

Figure 6 : (left) interactive registration of arm and positioning-orientation of needles, (right) visualization of three successive sets of needles

4 Future works

Several experiments with HoloLens headsets in a medical context have already been proposed (for ex. [4, 9]). In this paper, we propose an interactive and manual registration of 3D model to assist nurses to better position their needles in order to reduce risks incurred by patients. We could replace the 3D model of the arm with the segmentation result of a CT-scan of the patient. It would also be possible to set up a data communication system to save data between the headset and a PC, in order to avoid deploying the application for each new needles dataset. Finally, using markers tracked by the headset (with the Vuforia library [10]) would lead to a better registration of data.

Acknowledgements: Arthur Jacquin, DUT Informatique Graphique student, IUT Le Puy-en-Velay, for the software design ; Owen Kévin Appadoo and Hugo Rositi, assistant professors, DUT Métiers du Multimédia et de l'Internet, IUT Le Puy-en-Velay, for photos. Funding PEPS CNRS INSIS « Sciences de l'Ingénierie pour la Santé pour accompagner des projets translationnels », 2017, AVACM project.

5 References

[1] Article hémodialyse. Polyclinique Courlancy Bezannes, France. https://www.chirurgievasculaire.info/hemo-dialyse/

[2] Article Accès vasculaires (hémodialyses). Service de néphrologie du CHR de Liège (Citadelle), Belgique. http://www.nephro-liege-chr.be/index.php?Option=techniques&Module=acces_vasculaire

[3] M. M. van Loom, T. Goovaerts, A. G. H. Kessels, F. M. van der Sande, J. H. M. Tordoir. Buttonhole needling of haemodialysis arteriovenous fistulae results in less complications and interventions compared to the rope-ladder technique. *Nephrology Dialysis Transplantation*, 2010; 25(1):225-30

[4] H. Rositi, O.K. Appadoo, S. Valarier, M.-C. Ombret, E. Gadea-Deschamps, C. Barret-Grimault, C. Lohou. Presentation of a mixed reality software using HoloLens helmet, for an educational nutrition session. In preparation.

[5] Microsoft HoloLens. https://www.microsoft.com/en-gb/hololens

[6] Unity framework. https://unity3d.com/

[7] Mixed Reality Toolkit. https://github.com/Microsoft/MixedRealityToolkit-Unity

[8] Blender modeler. https://www.blender.org/

[9] https://www.sciencesetavenir.fr/sante/premiere-mondiale-une-operation-en-realite-augmentee_117099

[10] C. Barret-Grimault, M.-C. Ombret, O.K. Appadoo, H. Rositi, S. Valarier, E. Privat, I. Benmabrouk, V. Rousset, S. Verret, C. Lohou, E. Gadea. Innovons en Education Thérapeutique grâce au casque HoloLens en chirurgie bariatrique! 7ème Congrès de la Société d'Education Thérapeutique Européenne, mai 2019, Toulouse, France.

[11] Vuforia library. https://www.vuforia.com/

Image-based registration for lung nodule localization during VATS

Pablo ALVAREZ [1,2], Simon ROUZÉ [3], Matthieu CHABANAS [2], Yohan PAYAN [2] and Jean-Louis DILLENSEGER [1]

[1] Univ Rennes, Inserm, LTSI - UMR 1099, F-35000 Rennes, France
[2] Univ. Grenoble Alpes, CNRS, Grenoble-INP, TIMC-IMAG, Grenoble, France
[3] CHU Rennes, Service of Thoracic and Cardiac Surgery, Rennes, France
Contact: pablo.alvarez@etudiant.univ-rennes1.fr

Lung nodule localization during Video-Assisted Thoracoscopic Surgery (VATS) is a challenging task for small, low-density nodules. Current preoperative localization techniques are still sub-optimal in some cases. In this work, we studied the use and the limitations of an image-based nonrigid registration approach for nodule localization during VATS. Average target registration errors were of 5.67 mm, meaning an error reduction of 84.36 %.

1 Introduction

In clinical practice, early stage lung cancer nodules can be prescribed for resection through Video-Assisted Thoracoscopic Surgery (VATS). Because of their typically reduced size and density, these nodules might be difficult to find during surgery, especially under large lung deformations. This is caused by a pneumothorax (*i.e.* the abnormal presence of air inside the thoracic cage) resulting from the insertion of the surgical ports. To account for this problem, preoperative nodule localization procedures are typically used. These procedures consist mainly on the placement of hook-wires, dyes or microcoils in the nodule [1]. However, studies have found these localization techniques to still be sub-optimal [2].

Consequently, there is a growing interest toward the development of intraoperative lung localization procedures. Previous studies have proposed the use of intraoperative imaging for nodule localization [3, 4]. In addition, image processing techniques can be used in combination with intraoperative imaging for nodule localization. For instance, Uneri *et al.* used intraoperative Cone Beam CT (CBCT) and a hybrid shape-intensity nonrigid registration approach for nodule localization on an animal study [5].

In this preliminary work, we propose to use intraoperative CBCT imaging and nonrigid image registration for lung nodule localization during VATS. Our approach was inspired by Wu *et al.* [6], who proposed an algorithm that takes into account sliding effects for registering images of breathing lungs. To the best of our knowledge, this is the first study on human data using intraoperative imaging and nonrigid image registration for nodule localization.

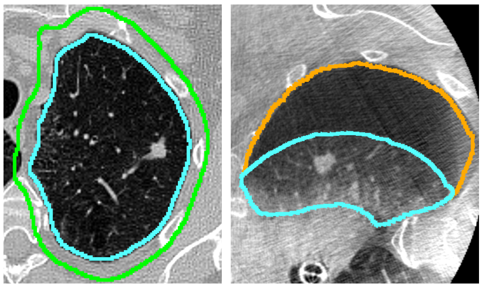

Figure 1: *Left: preoperative CT with the segmentation of the lung (cyan) and its extension (green). Right: intraoperative CBCT with the segmentations of the lung (cyan) and thoracic cage (orange). The pneumothorax is the space between the deflated lung and the thoracic cavity.*

2 Materials and Methods

2.1 Clinical data

This study used two tomographic images issued from a single clinical case of a VATS intervention performed at Rennes University Hospital. The first image, a preoperative CT, was taken following the current clinical protocol (Fig. 1 left). The second image, an intraoperative CBCT, was taken after the patient's lung was deflated as a result of the pneumothorax (Fig. 1 right). Both images were acquired under the patient's informed consent and the local ethics committee approval.

2.2 Segmentation

Three anatomical structures were manually segmented: the lung in the CT and CBCT images and the thoracic cavity in the CBCT image. The binary masks were post-processed using morphological dilatation to extend the boundaries (Fig. 1 left, green contours).

2.3 Nodule localization approach

Our approach consists of two steps: a rigid registration for initial alignment followed by a nonrigid image registration to account for pneumothorax deformation. Both processes were implemented using Elastix [7].

2.3.1 Rigid registration

We used the thoracic cavity as a reference for aligning the preoperative CT and intraoperative CBCT images. We performed rigid image registration using the Mutual Information (MI) similarity metric. The MI computation was filtered to the regions contained in the extended masks of the thoracic cavity. We used discrete probability distributions of a very low resolution for the computation of the MI (*i.e.* the number of bins was only 8). In this way, the strong gradients corresponding to the borders of the thoracic cavity and the main airway branches are more likely to drive the registration process than the weak gradients at the interior of the mismatching thoracic cavities. This is important given that the thoracic cavities contain mismatching lungs.

2.3.2 Nonrigid registration

Before nonrigid registration, we performed an intensity assignment procedure. The intensity values of the voxels outside the segmented lungs were assigned with a constant intensity value, while those at the inside were left unchanged. This constant value (-1500 HU) lies outside the range of values inside the lung. A nonrigid registration process was then performed using these intensity-modified images and the extended masks of the lung parenchyma. We accounted for large deformations using a multi-resolution Free Form Deformation (FFD) strategy, with a total of 4 resolutions. At each iteration, the resolution was doubled and the transformation obtained was carried through consecutive iterations. We used B-Splines as the transformation model with two intensity-based similarity metrics: Mutual Information (MI) and Normalized Cross Correlation (NCC). The B-Spline grid size was allowed to change with image resolution, reaching 16 mm in the last iteration.

3 Results and Discussion

To compute Target Registration Errors (TRE), 27 paired anatomical landmarks were manually placed by an expert thoracic surgeon on the nodule and the bifurcations of airways and vessels. After rigid registration, the mean TRE was 43.72 mm (±9.99 mm).

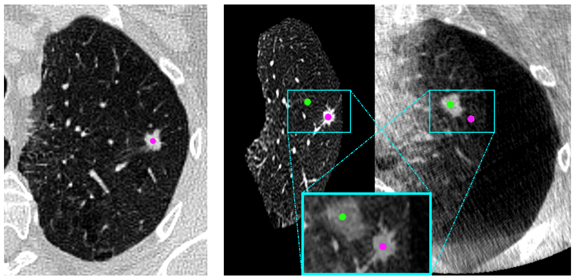

Figure 2: *Result of nonrigid registration with NCC. From left to rigth: preoperative CT, deformed CT and CBCT. Colored circles indicate the paired landmarks on the nodule. The image in the window is a closeup of the superposition of the result.*

Nonrigid registration with MI resulted in TREs of 80 mm (±20.39 mm), which are worse than after rigid registration. This bad performance may be explained by the fact that the MI similarity metric does not necessarily penalize mismatches of intensity, which makes it is less costly to move the CT-lung voxels out of the CBCT-mask than to move them inside.

However, nonrigid registration with NCC reduced the TREs to 5.57 mm (±3.35 mm), which corresponds to an error reduction of 84.35 %. In comparison to MI, NCC aims to closely match image intensities, and hence benefits from the usage of the intensity-modified images and the extended masks. The reason is that the borders of the CT and CBCT lung are forced to match as a result of the strong intensity gradients artificially generated by the intensity assignment procedure.

The result of nonrigid registration with NCC is shown in Fig. 2. Despite the satisfying quantitative measurements, a qualitative comparison of the deformed CT and the CBCT still reveals large misalignment. This can be seen throughout the lung parenchyma, where several internal structures are visible in only one of the images. Particularly, the landmarks placed on the nodule are 11.77 mm apart after nonrigid registration (51.1 mm after rigid registration), which is not within the clinical requirements. The registration problem at hand is a real challenge (*i.e.* very large deformations and low quality images). Although more sophisticated techniques do exist, the use of image intensity only to guide registration is possibly insufficient.

4 Conclusion

This preliminary study evaluated an intensity-based nonrigid registration approach for nodule localization during VATS. The results showed an error correction of 84.36 % when using NCC, although a closer qualitative analysis suggested unsatisfactory matching on some inner structures. We believe that intensity-based nonrigid registration only may be insufficient for nodule localization during VATS. Hence, hybrid approaches combining images and biomechanical models of pneumothorax deformation [8] will be explored.

Acknowledgments

This work was supported in part by the *Région Bretagne* through its *Allocations de Recherche Doctorale* (ARED) framework and by the French National Research Agency (ANR) through the frameworks *Investissements d'Avenir Labex CAMI* (ANR-11-LABX-0004) and *Infrastructure d'Avenir en Biologie et Santé* (ANR-11-INBS-0006).

References

[1] J. Keating and S. Singhal. "Novel methods of intraoperative localization and margin assessment of pulmonary nodules". en. *Seminars in Thoracic and Cardiovascular Surgery* 28.1 (2016), pp. 127–136.

[2] C. H. Park et al. "Comparative effectiveness and safety of preoperative lung localization for pulmonary nodules". en. *Chest* 151.2 (Feb. 2017), pp. 316–328.

[3] S. Rouzé et al. "Small pulmonary nodule localization with cone beam computed tomography during video-assisted thoracic surgery: a feasibility study". en. *Interactive CardioVascular and Thoracic Surgery* 22.6 (June 2016), pp. 705–711.

[4] H. Wada et al. "Thoracoscopic ultrasonography for localization of subcentimetre lung nodules". en. *European Journal of Cardio-Thoracic Surgery* 49.2 (Feb. 2016), pp. 690–697.

[5] A. Uneri et al. "Deformable registration of the inflated and deflated lung in cone-beam CT-guided thoracic surgery: Initial investigation of a combined model-and image-driven approach". *Medical physics* 40.1 (2013).

[6] Z. Wu et al. "Evaluation of deformable registration of patient lung 4DCT with subanatomical region segmentations: Evaluation of deformable registration of 4DCT with segmentations". en. *Medical Physics* 35.2 (Jan. 2008), pp. 775–781.

[7] S. Klein et al. "elastix: A toolbox for intensity-based medical image registration". *IEEE Transactions on Medical Imaging* 29.1 (Jan. 2010), pp. 196–205.

[8] P. Alvarez et al. "Biphasic model of lung deformations for Video-Assisted Thoracoscopic Surgery (VATS)". *IEEE 16th International Symposium on Biomedical Imaging.* 2019.

Additive Manufacturing of a Microbiota Sampling Capsule Based on a Bistable Mechanism

Mouna BEN SALEM [1,2]***, Guillaume AICHE*** [1]***, Lennart RUBBERT*** [2]***, Thomas SORANZO*** [3]***, Philippe CINQUIN*** [3]***, Donald K. MARTIN*** [3]***, Pierre RENAUD*** [2] ***and Yassine HADDAB*** [1]

[1] *University of Montpellier, LIRMM - UMR 5506*
161 Rue Ada, Montpellier, 34000 France - Tel : +33 (0)4 67 41 85 85
[2] *University of Strasbourg, ICube - UMR 7357, 67000 Strasbourg, France*
[3] *University of Grenoble Alpes, TIMC-IMAG - UMR 5525, F-38000 Grenoble, France*
Contact: bensalem@lirmm.fr

Diagnosis of gastrointestinal pathologies has considerably evolved with the introduction of wireless capsule endoscopy. As gastrointestinal diseases are often closely related to the microbiota, sampling of the bacterial flora using a capsule would be a powerful complementary tool for diagnostics compared to todays invasive surgeries. This paper aims to present the design of such a capsule based on a passive sampling technique and more precisely the modeling of the bistable mechanism used in the proposed device.

1 Presentation of the capsule

1.1 Capsule structure

Size is an obvious and major constraint in the capsule's design. The main challenge here is actually its integration while keeping a sufficient volume for the sample. As shown in the first picture of Figure 1, the proposed capsule is basically composed of a bistable mechanism which is a curved beam, a sponge [1], [2] and a soluble coating for the outer wall of the capsule to cover the orifice. The coating will be adjusted to dissolve in the small intestine where pH = 7 to 7.5 [3].

1.2 Operating mode

As described in the patents [1] and [2], when swallowed the capsule is carried through the gastrointestinal tract in a passive way. As soon as it reaches the desired area which is the small intestine, the coating dissolves, the capsule is thus open with the bistable mechanism preloaded in its second stable position as shown in Figure 1. The intestinal liquid is free to enter through the orifice, the sponge then absorbs the liquid [1] [2] and swells in order to trigger the bistable mechanism resulting in the closure of the capsule.

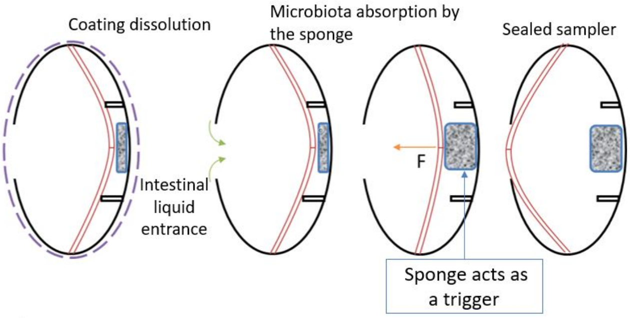

Figure 1: *The phases of the operating mode of the capsule*

One of the most important mechanical component of the capsule is the bistable mechanism because it ensures not only the opening and the closing of the device but also the sealing of the capsule to protect the sample from any contamination while exiting the human body by the anus.

The sizing of the bistable closing mechanism depends strongly on the maximum dimensions of the capsule which are a diameter of 10 mm and a length of 26 mm, the sample storage volume and integration of the sponge and the forces needed to trigger the snapping of the bistable mechanism (a minimum force delivered by the sponge to close the capsule and a maximum force to block the closure and seal the capsule).

An initial characterization shows that the actuator used to trigger the bistable mechanism can provide from 0.5 N up to 1 N of generated force when absorbing 0.20 mL of liquid which is enough for extracting diagnosis information from the collected sample [4].

2 Characterization of a small-sized bistable mechanism

2.1 Theoretical characterization

The bistable mechanism used in this paper is composed of the superposition of two preshaped curved beams. Each has the characteristics shown in Fig 2 : thickness t, depth b, length L, initial beam shape $\bar{w}(x)$ and initial height h [6] [7]. This configuration is essential to ensure the bistability of the structure in addition to a bistability ratio $Q = \frac{h}{t}$ that must exceed 2.31.

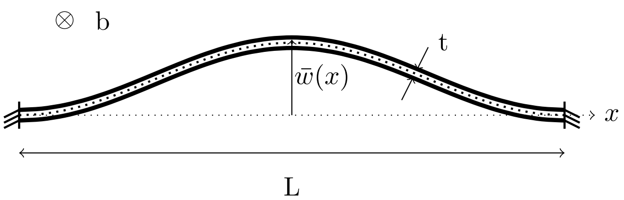

Figure 2: *Preshaped curved beam at the initial position*

Table 1: *Dimensions of the small-sized bistable mechanism*

Parameter	L	t	b	h
Value	20 mm	0.35 mm	2 mm	2.4 mm

Once the bistable behavior exists, it can be characterised by the evolution of the applied force f and the displacement d of its center as shown in Figure 4 where the analytical result is presented in a dashed line.

2.2 Experimental characterization

In order to characterize the bistable mechanism, a dedicated setup has been built. As shown in Figure 3, it is made up of a laser-based displacement sensor (Keyence LK-H152) that has a measuring range of ± 40 mm with a resolution of 0.25 μm, a force sensor (Sauter FK50) with a maximum force of 50 N and an accuracy of 0.02 N and a mounting bracket to fix the bistable mechanism and ensure the boundary conditions. A force is applied to the bistable mechanism by moving the linear table 1 on which the force sensor is mounted and the corresponding displacement is measured using the laser sensor mounted on the linear table 2 (see Figure 3).

For the experimental characterization, ten bistable mechanisms are manufactured with Fused Deposition Modeling (FDM) technology and used to determine the Force-Displacement curve. The result of this characterization is given in Figure 4 and presented in a continuous line.

The dispersion between the experimental tests at the extremum points of the force-displacement curve is 0.14 N for f_{max}, 0.32 mm for d_{max}, 0.09 N for f_{min}, 0.21 mm for d_{min}, 0.08 mm for d_{mid} and 0.25 mm for d_{end}.

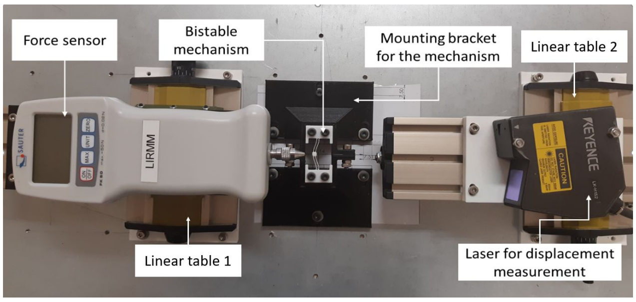

Figure 3: *Setup built for experimental characterization of the bistable mechanism*

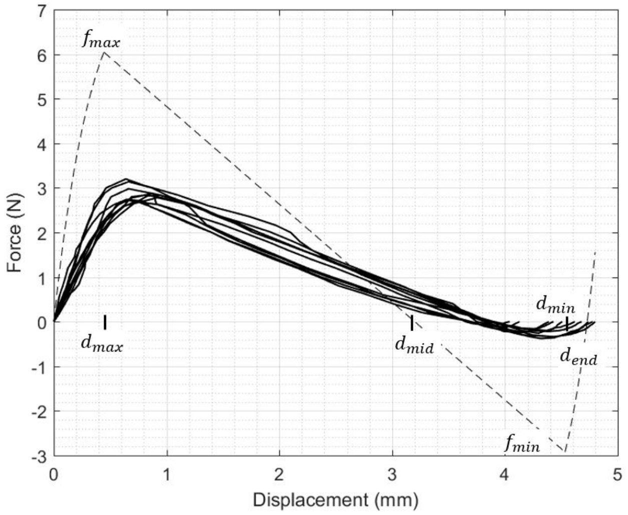

Figure 4: *Force-Displacement evolution for a bistable mechanism : the theoretical characterization is presented in a dashed line and the experimental one is presented in continious lines*

The difference between the average of the experimental values and the theoretical values for the extremum points is 3.16 N for f_{max}, 0.31 mm for d_{max}, 2.69 N for f_{min}, 0.34 mm for d_{min}, 0.59 mm for d_{mid} and 0.21 mm for d_{end}.

3 Conclusion

The comparison between the theoretical and experimental characterization of the bistable behavior shows a significant difference between the values of the maximum and minimum forces. The origin of such a quite large difference can be the scale of the bistable mechanism's geometrical parameters as well as the manufacturing technology which tends to produce parts with voids in the structure (lack of material). The mechanism manufactured with 3D printing technology needs a maximum value of 0.38 N to trigger the closure of the capsule, therefore the sponge is able to provide the force needed to trigger the snapping of the structure. After closing, the bistable mechanism resists up to 3 N which should be sufficient to prevent the reopening of the capsule and protect the sample from contamination.

Acknowledgements

The authors would like to thank TIMC-IMAG (UMR5525 UGA/CNRS), especially Jacques Thélu, Thomas Soranzo, Jean-Pierre Alcaraz, Thierry Alonso, Aziz Bakri, Sylvain Besson, Bertrand Favier, Ridha Frikha, Nawel Khalef, Jean-Marc Kweter, Audrey Le Goullec, Max Maurin, Dominique Schneider, Antonia Suau-Pernet, Bertrand Toussaint and Patrick Tuvignon for full access to the concepts of patents [1] and [2] and the corresponding results.

This work was supported by the Investissements dAvenir (Labex CAMI ANR-11-LABX-0004).

References

[1] Cinquin P., Favier D., Alonso T., Bakri A., Khalef N., Thélu J. , Besson S., Martin D. Dispositif de prise d'échantillon intestinal. Patent N° FR 1655187 filed by the UGA, 06/07/2016, 2016.

[2] Thélu J., Cinquin Ph., Martin D., Soranzo T., Alcaraz J.P., Kweter J.M. Device for intestinal fluid sampling. Patent N°FR1760069, 10/25/17, 2017.

[3] Nugent S. G., Kumar D., Rampton D. S., et al. Intestinal luminal pH in inflammatory bowel disease: possible determinants and implications for therapy with aminosalicylates and other drugs. Gut, 2001, vol. 48, no 4, p. 571-577.

[4] Berg R.D.: "The indigenous gastrointestinal microflora" Trends Microbiol., vol. 4, pp. 430–435, 1996.

[5] Vangbo M. An analytical analysis of a compressed bistable buckled beam. Sensors and Actuators A: Physical, 1998, vol. 69, no 3, p. 212-216.

[6] Qiu J. An electrothermally-actuated bistable MEMS relay for power applications. 2003. PhD thesis. Massachusetts Institute of Technology.

[7] Hussein H. Contribution to Digital Microrobotics: Modeling, Design and Fabrication of Curved Beams, U-shaped Actuators and Multistable Microrobots. 2015 PhD thesis. Bourgogne Franche-Comté University.

Towards a novel man-machine interface to speed up training on robot-assisted surgery

***Gustavo D. GIL*[1]*, Julie M. WALKER* [2]*, Nabil ZEMITI* [1]*, Allison M. OKAMURA* [2] *and Philippe POIGNET* [1]**

[1] LIRMM, University of Montpellier, CNRS, Montpellier, France

[2] Department of Mechanical Engineering, Stanford University, Stanford, CA 94305, USA

Tel : +33 (0)4 67 41 85 58

Contact: gustavo.gil@lirm.fr

New robotically-assisted minimally invasive surgery (RAMIS) systems make surgeries safer and reduce hospitalization time. Nevertheless, mastering the use of different surgical robotic tools requires demanding training and continuous practice as for an athlete. The final aim of our research is to shorten the training time for robotic surgery by developing a virtual mentor to provide haptic feedback. This paper presents a partial validation of a novel haptics device, designed to provide hand guidance (i.e., the device transmits commands to the user in order to direct his/her hand in the space).

1 Introduction

In comparison with open surgery, RAMIS systems can provide significant advantages. Current systems, like Da Vinci® robots, have been shown to reduce hospital stay [1-3], while avoiding large scars like laparoscopic surgery. Additionally, in certain type of surgeries, this technology enabled less blood losses [2], [4], and post-operative reduction in dose of analgesic and anti-inflammatory drugs [5].

The counterpart of this is that the new generations of surgeons must add an extensive training in robot teleoperation to their medical knowledge and skill set. The recommended training curricula progress from manipulation tasks to simulated surgical tasks [6-8], followed by often limited clinical exercises on cadavers [9]. Regrettably, trainees may not be ready for surgical independence at the end [10], [11].

To address these problems, we propose to integrate virtual reality together with haptic feedback in the surgical training sessions. In this paper we propose a portable haptic device that offers hand guidance while the user performs surgical gestures. The user will feel "as if" a force was directing his/her hand through of the surgical gesture. After a complete validation of our device, we plan to use the wearable haptic device with surgeon trainees to determine whether haptic guidance shortens the training time.

2 Definitions

Illustration of jargon for the actuation zones (Fig. 1).

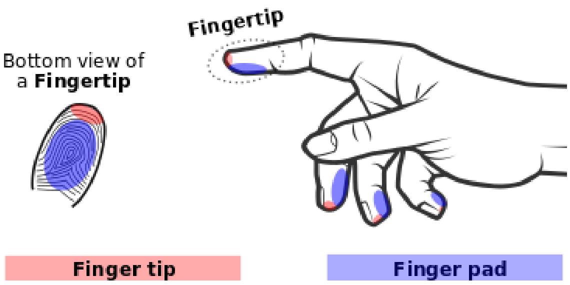

Figure 1: *The colors show the location terms of each zone.*

3 Materials

The device consists of a pair of servomotors mounted in a 3D printed handle, which has a similar design to the haptic device presented in [12]. Different views of the device are presented in Fig. 2. Each motor has a lever arm to stimulate the user's finger pad (Fig. 1) of the thumb/index distal phalanges by rotating through a semicircular arc (see schema in Fig. 2). The working principle of the device is to employ the lever arms to stretches the skin on the finger pads, giving the sensation that user's hand is being pulled.

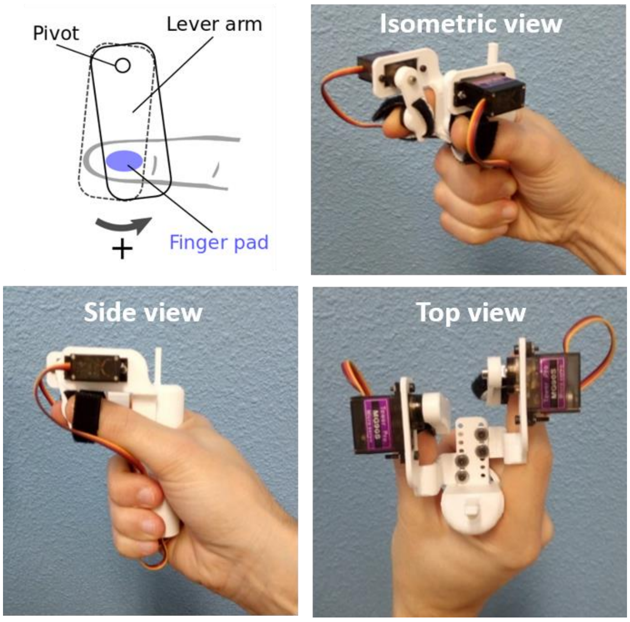

Figure 2: *Scheme for one actuator of the haptic device (working principle) and different views of the entire mechanism.*

The device has a range of motion of ± 20º for each finger. The contact of the fingers was ensured by fastening the distal phalange with Velcro® strips, similarly to those in the Da Vinci® master console.

4 Methods

The test method seeks to determine two key aspects: (1) if there is a common perception of tactile cues among different users; and (2) cues strength, which is related to stimulus-cue repeatability by user and intra-users. Thus, the haptic device stimulates user's finger pads and then, the user answered in which direction they felt a directing force. In essence, we execute a system identification procedure for the tactile sense of the user, aiming to identifying commands in 4 different directions or 2 degrees of freedom (DoF).

The experiment involved 6 right-handed users in a 2 trial tests on different days. 72 different stimuli were applied in a pseudorandom sequence of 360 stimuli per trial, totalizing 720 stimuli (each stimulus 10 times). In addition, the participant's visual and auditory sense were masked to capture the perceived commands only from the sense of touch.

For each stimulus, participants chose from five options: Left, Right, Twist Left, Twist Right, and Unclear. Therefore, if each user identifies a stimulus as the same direction many times, it means that this cue feels strongly (is clear) for a certain combination of servomotors actuation.

5 Results

The multidimensional nature of the results is expressed by marks in a two-dimensional map. In this map (Fig. 3), the colors encode the type of directional cue (e.g., Twist Left, Twist Right, Left, and Right), the X-Y location of each mark corresponds to an angular displacement for each servomotor (stimulus), and the mark size represents the saliency of this cue (big circle = intuitive cue). Examples of cue saliency cases are: (1) biggest circles = 100% stimulus-cue repeatability; (2) different color circles overlaid = intra-users cue mismatch; and (3) medium and small circles = not relevant stimulus for this application.

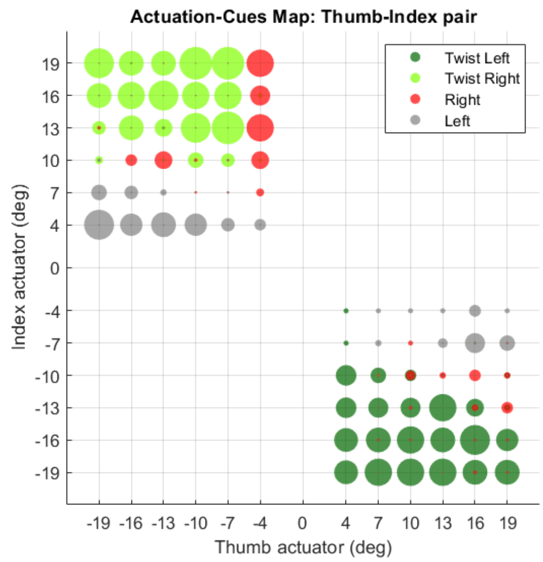

Figure 3: *Results of the partial haptics identification experiment (2nd and 4th quadrants). Marks diameter relates to directional cue saliency, color to cue type, and X-Y location in the map to a stimulus (motor movements).*

The results validate the possibility of delivering a strong feedback to the user in one DoF (Twist Left and Twist Right) because of several stimuli possibilities. These results also point out the feasibility to induce an additional DoF (translational Right and Left mouvements) by a reduced number of stimuli belonging to the 2nd quadrant.

The test is limited because of the low number of participants. The time required to conduct each trial was about 80 minutes. However, these results contain key information about an extensive variety of relevant stimuli. This data enable us to narrow the exploration space of additional commands that evoke hand movements (i.e., more DoFs), while shortening experiments time.

Acknowledgements

This work was supported by the French ANR within the Investissements d'Avenir Program (Labex CAMI, ANR-11-LABX0004), a Chateaubriand Fellowship, a National Science Foundation Graduate Research Fellowship, and a Stanford Graduate Fellowship.

References

[1] Daouadi M, Zureikat AH, Zenati MS, Choudry H, Tsung A, Bartlett DL, Hughes SJ, Lee KK, Moser AJ, Zeh HJ. (2013). Robot-Assisted Minimally Invasive Distal Pancreatectomy Is Superior to the Laparoscopic Technique. Annals of Surgery: January 2013 - Volume 257 - Issue 1 - p 128–132

[2] Lim PC, Kang E, Park DH. (2011). A comparative detail analysis of the learning curve and surgical outcome for robotic hysterectomy with lymphadenectomy versus laparoscopic hysterectomy with lymphadenectomy in treatment of endometrial cancer: A case-matched controlled study of the first one hundred twenty two patients. Gynecologic Oncology. Volume 120, Issue 3, March 2011, Pages 413-418

[3] Seamon LG, Cohn DE, Henretta MS, Kim KH, Carlson MJ, Phillips GS, Fowler JM. (2009). Minimally invasive comprehensive surgical staging for endometrial cancer: Robotics or laparoscopy? Gynecologic Oncology. Volume 113, Issue 1, April 2009, Pages 36-41

[4] Cardenas-Goicoecheaa J, Adams S, Bhat SB, Randall TC. (2010). Surgical outcomes of robotic-assisted surgical staging for endometrial cancer are equivalent to traditional laparoscopic staging at a minimally invasive surgical center. Gynecologic Oncology; Volume 117, Issue 2, May 2010, Pages 224-228

[5] Martino MA1, Shubella J, Thomas MB, Morcrette RM, Schindler J, Williams S, Boulay R. (2011). A cost analysis of postoperative management in endometrial cancer patients treated by robotics versus laparoscopic approach. Gynecol Oncol. 2011 Dec;123(3):528-31.

[6] Volpe A, Ahmed K, Dasgupta P, Ficarra V, Novara G, van der Poel H, Mottrie A. (2014). Pilot Validation Study of the European Association of Urology Robotic Training Curriculum. European Urology. Volume 68, Issue 2, August 2015, Pages 292-299

[7] Whitehurst SV, Lockrow EG, Lendvay TS, Propst AM, Dunlow SG, Rosemeyer CJ, Gobern JM, White LW, Skinner A, Buller JL. (2015). Comparison of Two Simulation Systems to Support Robotic-Assisted Surgical Training: A Pilot Study (Swine Model). Journal of Minimally Invasive Gynecology. Volume 22, Issue 3, March–April 2015, Pages 483-488

[8] Whittaker G, Aydin A, Raison N, Kum F, Challacombe B, Khan MS, Dasgupta P, Ahmed K. (2016). Validation of the RobotiX Mentor Robotic Surgery Simulator. Journal of Endourology. Volume 30, Number 3, March 2016

[9] Davies B. (2000). A review of robotics in surgery. Proc Inst Mech Eng., H, 214(1):129-40.

[10] Fabricius R, Sillesen M, Hansen MS, Beier-Holgersen R. (2017). Self-perceived readiness to perform at the attending level following surgical specialist training in Denmark. Dan Med J. 2017 Oct;64(10). pii: A5415.

[11] Lindeman BM, Sacks BC, Hirose K, Lipsett PA. (2014). Duty hours and perceived competence in surgery: are interns ready?. J Surg Res. 2014 Jul;190(1):16-21.

[12] Walker JM, Zemiti N, Poignet P, Okamura AM. (2019). Holdable Haptic Device for 4-DOF Motion Guidance. ArXiv [cs]

Percutaneous Osteoplasty

Julien GARNON, Laurence MEYLHEUC, Bernard BAYLE and Afshin GANGI

ICube - University of Strasbourg – UMR 7357 CNRS – INSA Strasbourg
1,place de l'Hôpital, 67091 Strasbourg - Tel:+33 (0)3 88 11 91 11
Contact: juliengarnon@gmail.com

The purpose of this work is to present one major technical problem associated with extraspinal cementoplasty, and to present one potential future solution using a dedicated robot.

1. Extraspinal cementoplasty

1.1 Definition

The percutaneous injection of polymethyl methacrylate into a vertebral body, also known as spinal cementoplasty or vertebroplasty, has been described since 1987 [1]. It has been applied to treat painful osteoporotic and malignant compression fractures of the spine for more than 30 years, with excellent antalgic and functional results.

The application of cementoplasty beyond the spine, also referred as extraspinal cementoplasty or osteoplasty, is also technically feasible and has been described to treat osteolytic lesions in various locations (pelvic girdle notably), with a double objective of pain palliation and bone consolidation [2]. Athough scarce and heterogeneous, there is a growing literature supporting the use of osteoplasty as a minimally invasive technique to treat painful osteolytic extra-spinal metastases in cancer patients.

1.2 Technical considerations

The key feature of a cementoplasty procedure is the possibility to deliver the PMMA bone cement within the osteolytic lesion while trying to fill not only the osteolysis but also the normal surrounding cancellous bone. Injection is performed under real-time image guidance (with fluoroscopy and/or CT-scan) in order to assess the proper repartition of cement and rule out any extra-osseous leakage, which is the most common complication of such intervention.

Currently, the maximal volume that can be injected with a single PMMA kit does not exceed 10 ml. If this quantity is appropriate for a spinal injection due to the relative small volume of a vertebral body, it is insufficient in many extra-spinal cases. The required volume in areas such as the acetabulum or the long bones can range from 10 to 50ml depending on the extension of the lytic process. Hence, performing extraspinal cementoplasty with such large volumes of cement requires modifying the technique of injection when compared to a standard spinal procedure

2. Solutions for the injection of large volumes of cement

2.1 Manual injection

Percutaneous injection of a large volume of cement can be achieved with different variations of the spinal technique. One solution, which seems to be the most frequently reported in the literature, consists to insert one additional needle inside the lesion after the previous injection has been completed, till optimal filling of the lesion has been reached. However, this increases the number of punctures, the time of the procedure and leads to different separated PMMA cement balls.

Another solution that we tend to favor in our clinical practice is to prepare sequentially several kits. As soon as the injection of a PMMA kit come to its end (around 8ml), another cement kit is prepared and immediately injected within the same bone trocar. This allows to reduce the number of needle, theoretically increases the chance of having one large cohesive PMMA ball, but is technically challenging because the time for injection of each cement is limited (around 10 to 15 minutes) and the countdown for cement preparation comes with little place for mistakes during preparation and connection.

2.2 Rationale for a robotic injection

Our team has developed a dedicated prototype for the robotic assisted injection of cement (S-tronic robot – figure1) [3]. With this system, is it possible to extend significantly the duration of injection, thanks to the thermic regulation of the cement viscosity just before it enters the cannula. The device is controlled remotely with a dedicated controller connected to the robot. In vitro tests have shown that the time could be prolonged up to 30 minutes, for cement that usually sets within 10 minutes. Theoretically, such device would be very well adapted for extraspinal cementoplasties, as it increases the time for injection and gives more time to the operator to properly fill the lesion through one bone trocar, while mitigating potentially the risks of leakages.

2.3 Preliminary results

Currently, the sheath of the robot has been designed to receive a standard 10ml syringe. On a cadaver study performed on 2 humerus with imaging (CT-scan) correlations, we were able to demonstrate that the robotic-assisted injection allowed us to inject as much as 40ml without multiple punctures, thanks to the preparation of several syringes of cement that were injected one after the other on the same needle. However, this was associated with multiple manipulations of the sheath and was not technically optimal. Hence, in one case the bone trocar had to be exchanged for another one after injection 20ml because of cement deposition within the cannula. This led to the lack of coalescence between the different cement streams (fig.2). Subsequent testing with a 3 points bending test (test speed 2mm/min) demonstrated that the fracture occured in front of that interface, suggesting the importance of having one single cohesive cement.

Because of the rheological properties of the PMMA bone cement, the injection of volume greater than 10ml comes with specific shear rates that need to be addressed in order to make it compatible with the heat exchanger.

Figure1 – SpineTronic Device

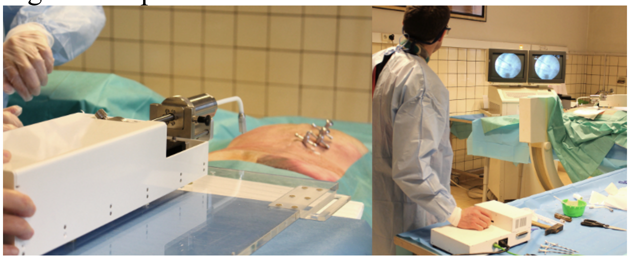

Figure2 – Robot-assisted injection of 4x10ml of cement in a humerus. Note the lack of cement cohesion at some points which likely represents the interface between two different cements

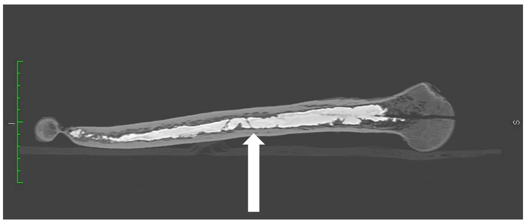

Figure3 – 3 points bending test of the same humerus showing a fracture occurring just a the site of cement interface. The flexural force at break is 3500 N.

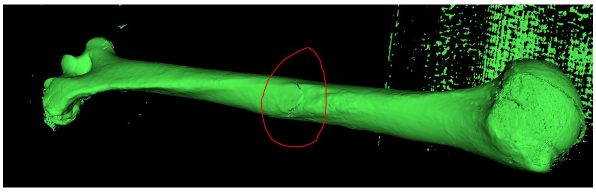

References

[1] Galibert P, Deramond H, Rosat P, Le Gars D. [Preliminary note on the treatment of vertebral angioma by percutaneous acrylic vertebroplasty]. Neurochirurgie. 1987;33(2):166-8.

[2] Wang Z, Zhen Y, Wu C, et al. CT fluoroscopy-guided percutaneous osteoplasty for the treatment of osteolytic lung cancer bone metastases to the spine and pelvis. J Vasc Interv Radiol. 2012 Sep;23(9):1135-42. doi: 10.1016/j.jvir.2012.06.007.

[3] Lepoutre N, Meylheuc L, Bara GI, Barbé L, Bayle B. Bone cement modeling for percutaneous vertebroplasty. J Biomed Mater Res B Appl Biomater. 2018 Sep 29. doi: 10.1002/jbm.b.34242.

Development of a finite element model of prostate validated by a realistic prostate phantom

Mohamed DIENG[1], Grégory Chagnon[1], Sandrine Voros[2]

[1]Univ. Grenoble Alpes, CNRS, Grenoble INP, TIMC-IMAG, 38000 Grenoble, France
[2]Univ. Grenoble Alpes, CNRS, Grenoble INP, INSERM, TIMC-IMAG, 38000 Grenoble, France

Tel : +33 (0)4 56 52 00 09 – Contact : sandrine.voros@univ-grenoble-alpes.fr

Anthropomorphic phantoms are often used in clinical applications of the prostate. These physical models show limitations of use when one want to test extreme conditions, e.g as of the permanent traces left by needle insertions. This is why there is a need to develop realistic numerical models that behave like physical models. This work concerns the development of a finite element method of a numerical prostate model based on a realistic prostate phantom.

Both physical and numerical models were developed based on the geometry of a resected prostate generated from MRI images of a patient. While an accurate mesh was realized for the FE model. Boundary conditions and mechanical properties were defined for each model. Then the molds were designed and manufactured to develop the prostate phantom.

The numerical model is validated by comparing with a prostate phantom results of compression test.

1 Introduction

Biomechanical models of the prostate have a number of potential applications in the diagnosis and management of prostate pathologies, including prostate cancer. These models based on Finite Element analysis (FE) can be used to supplement and / or replace the anthropomorphic phantoms of the prostate to predict deformities or prostatic mobility [1] [2]. Several studies showed that the use of anthropomorphic phantoms in prostatic applications is limited by: the development time of the phantom and the restriction of its use to a certain number of configurations such as needle insertions for example [3] [4]. If a strong correlation can be achieved between a realistic prostate phantom and a biomechanical model, all procedures for commonly performed prostate diseases (biopsies, surgery and radiotherapy) on phantoms could be improved by a FE model.

The aim of our study is to develop and validate a FE model of the prostate in a simple and effective way. To do this, the modeling was performed on the basis of a realistic prostate phantom [5] and a compression test bench was developed for validation by comparing the surface deformities of the prostate phantom and the FE model.

This article begins with a description of the procedure for developing the prostate phantom. It continues by presenting the necessary steps to obtain a faithful FE model. Subsequently, the test bench developed for the validation of the digital model by stereo correlation is presented. Finally, results as well as concluding remarks are detailed.

2 Materials and methods

2.1 Prostate phantom

The prostate and urethra were extracted from patient specific magnetic resonance imaging (MRI) data. These images were segmented manually on ITK-Snap. After a geometric reconstruction of the organs, the molds were designed on SpaceClaim and were printed in 3D. Three molds were printed, one core and two negative molds. For the molding of the resected prostate phantom and the urethra, two types of RTV (Room Temperature Vulcanizing) silicones were used. A thin layer (approximately 1 mm) of the RTV EC00 silicone was used to form the prostate capsule. On the other hand, prostate tissue was mimicked by the Wacker SilGel 612 (Wacker-Chemie GmbH, Germany). After mixing and degassing the mixtures, the solutions were poured into the molds. The crosslinking was performed at room temperature [5].

2.2 Stereo-correlation bench

To determine the surface deformations of the prostate phantom, a compression test bench coupled with a stereo correlation system (Vic-3DTM DIC System) was developed. The test bench is composed of two Plexiglas plates (130 × 130 × 5mm): a fixed plate that allows to put in place the phantom by the base and a sliding plate guided by steel rods. The conditions of non-arching are respected. In order to reduce the friction between the plate and the prostate phantom, the contacts are well lubricated. The value of the friction coefficient (0.2) was determined by conventional compression tests on a silicone cylinder.

The prostate phantom was covered with speckles and is placed between the two plates. Weights of 100 and then 200 grams were placed on the sliding plate to apply a compressive force. Thus, by means of the cameras, the surface displacements was recorded and the calculation of the deformation map is done.

2.3 Finite element model of prostate

After segmentation and geometry reconstruction, the model was imported into the ANSYS software as the initial step of the FE model. A volume structure was considered for the prostate. Thus, a volumetric mesh of the prostate was realized, using hexahedral and hybrid elements (10660 nodes and 9143 elements). A mechanical characterization of the Wacker SilGel 612 (behavior law, C1 = 7.71 kPa) representing the prostatic tissue made it possible to assume the hypotheses of elasticity, isotropy and incompressibility as true. Boundary conditions and changes were applied according to the test bench developed for the compression of the prostate phantom.

The compression test was modelled by a FE on ANSYS according to the test hypotheses, the boundary conditions and the loadings.

3 Results

In this section, the results of the simulation using the ANSYS model and the experimental results are compared. The results were compared using the MATLAB software. Two types of comparisons on the external surfaces of the models were made: a comparison of the deformation maps and an image registration of the point clouds after deformation.

Figure 1 shows the displacements maps (z axis - Fig1.a) and strains maps (maximum principal strain e1- Fig1.b) of the two models. The strain data for each model is reported in an average range of 0.001 to 0.007. Thus, it is possible to observe a very good correlation between the strain maps of the two models. Only one side of the prostate is illustrated here, however, it should be noted that similar results were found on the other side of the prostate.

In order to compare the experimental deformation data with FE deformation data, the ICP algorithm (Iterative closest point) was applied to perform the registration like in [4]. Figure 2a shows some corresponding points between points cloud and figure 2b is a view both point cloud after registration. The blue dots represent the points recorded with a good registration. While the red dots had a shift error of 1 mm. The average RMSE (Root-Mean-Square-Error) observed was 0.49 mm, which represents around 1% of the dimensions. It is low enough to consider it as a good image registration.

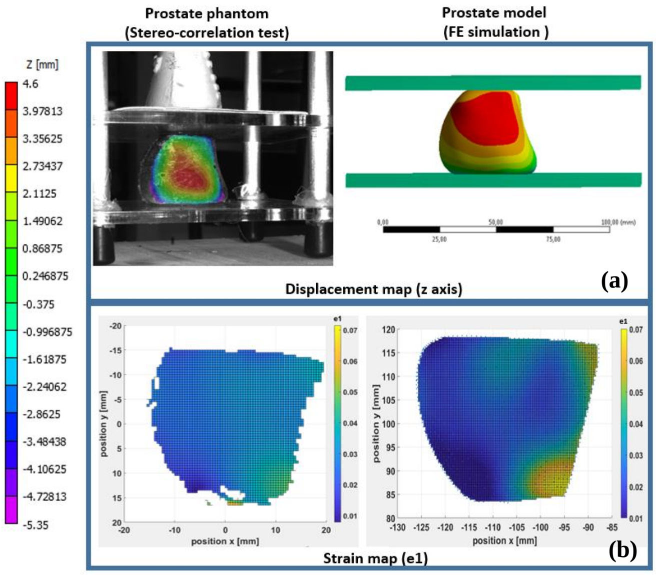

Figure 1: Displacement fields (a) and strain maps of the prostate models (b).

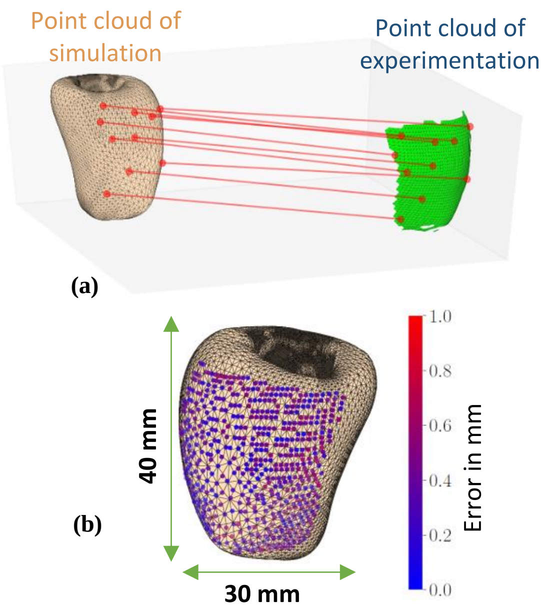

Figure 2: Image Registration (Iterative closest point), Root-Mean-Square-Error (RMSE): 0.49 mm

4 Conclusion

This study has presented the development of a prostate phantom and a biomechanical model for the simulation of prostate deformation using the ANSYS environment. The model is composed of a resected prostate and the urethra. The FE model was validated with two techniques: a comparison of the principal strain maps and an image registration between the physical and numerical model (RMSE = 0.49 mm). Based on these results, the FE model shows faithful behaviour with respect to the prostate phantom.

The integration of the other organs (bladder, rectum and pelvic floor) of the pelvic area into the model is another step that could be the subject of a later work. To this extent, a multi-organ phantom and biomechanical model could be designed. So a FE model validation will allow for getting more realistic in silico simulations.

Funding/Support and role of the sponsor:

This work was supported by French state funds managed by the ANR within the Investissements d'Avenir programme Labex CEMAM under reference ANR-10-LABX-44-01 and Labex CAMI under reference ANR-11-LABX-0004.

5 References

[1] Boubaker, M. B., Haboussi, M., Ganghoffer, J. F., & Aletti, P. (2009). Finite element simulation of interactions between pelvic organs: Predictive model of the prostate motion in the context of radiotherapy. Journal of biomechanics, 42(12), 1862-1868.

[2] Moreira, P., Peterlik, I., Herink, M., Duriez, C., Cotin,., & Misra, S. (2013). Modelling Prostate Deformation : SOFA versus experiments. Prostate, 17 (83.0),1-0

[3] Hungr, N., Long, J. A., Beix, V., & Troccaz, J. (2012). A realistic deformable prostate phantom for multimodal imaging and needle-insertion procedures. Medical physics, 39(4), 2031-2041.

[4] Li, P., Jiang, S., Yu, Y., Yang, J., & Yang, Z. (2015). Biomaterial characteristics and application of silicone rubber and PVA hydrogels mimicked in organ groups for prostate brachytherapy. journal of the mechanical behavior of biomedical materials, 49, 220-234.

[5] Dieng, M., Trezel, A., Chevrot, A., Chagnon, G., & Voros, S. (2017, November). Development of a biomechanical model and design of a realistic phantom for the evaluation of an innovative medical vacuum hemostasis device for the treatment of benign prostatic hyperplasia. In Surgetica 2017.

FEM-based confidence assessment of non-rigid registration

Paul BAKSIC[1,2], Hadrien COURTECUISSE[1], Matthieu CHABANAS[2] and Bernard BAYLE[1]

1 University of Strasbourg, CNRS, AVR-ICube, F67000 Strasbourg France
2 Univ. Grenoble Alpes, CNRS, Grenoble INP, TIMC-IMAG, F38000 Grenoble France
Contact: p.baksic@unistra.fr

Non-rigid registration is often used for 3D representations during surgical procedures. It needs to provide good precision in order to guide the surgeon properly. We propose here a method that allows the computation of a local upper bound of the registration confidence over the whole organ volume. Using a biomechanical model, we apply tearing forces over the whole organ to compute the upper bound of the degrees of freedom left by the registrations constraints. Confrontation of our method with experimental data shows promising results to estimate the registration confidence. Indeed, the computed maximum error appears to be a real upper bound.

1 Introduction

While performing a surgery, the surgeon's goal is to minimize the risk for the patient. For this purpose, minimally invasive surgery has been favored over traditional open surgery, especially in abdominal surgery. Such procedures can be very challenging for the practitioner to perform. It is mainly due to the fact that they don't see what they are doing through their own eyes. Views are often showed through a screen and captured either with an endoscope, Ultrasound probe or other devices. This is challenging because it forces the surgeon to mentally map what he sees to what he is doing. A way to help surgeons during the surgery is to add virtual information on the screen, for instance the 3D volume of a tumor into a liver. This should provide information allowing him to resect a minimum of healthy tissues.

To reach this objective, one first needs to make a registration of the organ that the surgeon is seeing through the measurement device. Combining a biomechanical model to data extracted from intraoperative images have yielded good results. This can be done either by using some points extracted from the surface [1, 2], the whole surface [3] or information on the organ volume extracted from ultrasounds [4]. Yet all the above methods are subject to errors. Through this method, we propose a tool providing an estimation of the confidence of a model-based registration method.

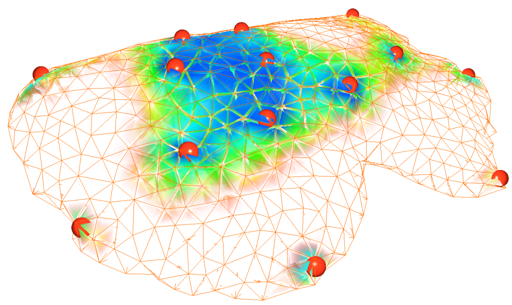

Figure 1: *High confidence (low mobility) areas are colored with shorter wavelength (blue). If the degree of confidence is lower than a threshold, the elements become transparent.*

2 Method

Our method takes as input the Finite Element mesh of the organ in the registered state. The registration can be performed by one of the method cited above or any method combining a biomechanical model with measured data. The method consists on evaluating the maximum mobility of the model at each point of its mesh, the confidence being high when the mobility of the point is low. The main assumption of the paper is that the deformation generated by the surgeon during the procedure does not damage tissues. Therefore, the maximum mobility is computed by applying an upper bound stress taken from the literature, known to cause irreversible deformations to the organ while satisfying the registration constraints into the simulation. This stress is successively applied along multiple directions on the model, in order to test each degree of freedom of the organ. Those directions are given by $\mathcal{D} = (\mathbf{x}, -\mathbf{x}, \mathbf{y}, -\mathbf{y}, \mathbf{z}, -\mathbf{z})$. The computation of the mobility $\mathbf{c}$ at each point i is formalized in the following equation :

$$\mathbf{c}_i = \max_f(||\mathbf{q}_i - C(\mathbf{d} \times f \times k)||) \quad \text{with} \quad \mathbf{d} \in \mathcal{D} \quad (1)$$

Where C is a non linear function providing the positions of the model at static equilibrium after the application the volume force f multiplied by the surrounding volume k. The rest positions of the model are considered to be the positions provided by the registration method. This may lead to more mobility of the model because of the lack of internal stress which usually rigidify the tissue. This way, the computed displacement remains an upper bound. The confidence map can be represented as shown on the figure 1.

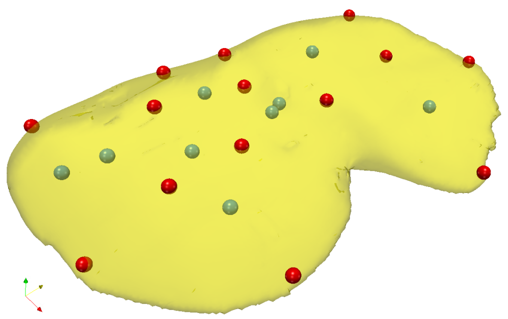

Figure 2: *Volume of a lamb liver with the outer markers in red and the inner ones in green.*

3 Confrontation to real data

Our method was tested on a data set of an ex-vivo liver of a lamb. External markers were put on the surface, which were then used to perform the registration along with internal markers that were used to evaluate the accuracy of the registration method. Then the volumes of the liver and the markers were segmented from CT-Scans in five different positions of the lamb liver.

Cross-registrations were performed between the different positions of the liver using external markers. We used a linear elastic model of the deformation along with a corotational finite element formulation [5] of the problem on tetrahedron elements. This formulation shows good results and gives good approximations of the non-linearity of the deformation while keeping low time complexity. The liver finite element model parameters are given by a Young modulus of $6kPa$ and a Poisson ration of 0.499 as found in the literature for healthy livers [8]. After the registrations, the distance between internal markers segmented from the CT images and the one provided by the model were considered as *ground truth* values of the registrations' accuracy. Our method was then applied on each configuration of the liver, in order to compute the theoretical upper bound of mobility. Given the material properties of the model described above, the force f used in the equation 1 is parameterized to reach 30% of strain. Indeed, despite the stress leading to tissue tearing vary amongst patients, this value is, according to the literature [6, 7], identified as an upper-bound value leading to irreversible deformations of the tissue.

4 Results

The mechanical study performed by our method takes into account the complex coupling between constraints provided by image data. Indeed, as shown in figure 1, the resulting confidence map provided by our method is not directly related to the distance with external markers. Instead, it provides complex shapes that cannot be generated with simple geometric primitives. Figure 3 shows that our method predicted 96.6% of the time a real upper bound of the registration accuracy.

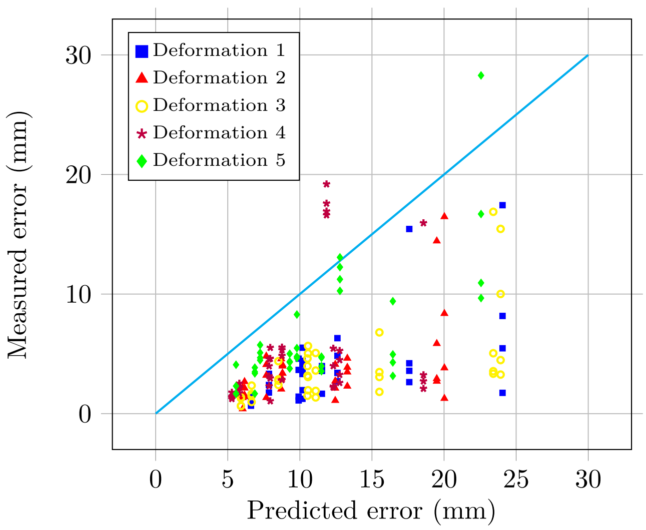

Figure 3: *Predicted error given by our method with respect to the measured error (given by the cross registrations) at each inner marker. Each label stands for a different target configuration.*

5 Conclusion

We proposed a method allowing to evaluate the registration accuracy of internal structures. The method provides an upper bound uncertainty of positions of a biomechanical model, that can be used to discriminate and display only the reliable parts of the model in the augmented view. Future works concern additional validation study with more data and registration methods.

References

[1] Plantefeve, R., Peterlik, I., Haouchine, N., & Cotin, S. (2016). Patient-specific biomechanical modeling for guidance during minimally-invasive hepatic surgery. *Annals of biomedical engineering*, 44(1), 139-153.

[2] Adagolodjo, Y., Golse, N., Vibert, E., De Mathelin, M., Cotin, S., & Courtecuisse, H. (2018, May). Marker-based Registration for Large Deformations-Application to Open Liver Surgery. *In International Conference on Robotics and Automation.*

[3] Peterlík, I., Courtecuisse, H., Rohling, R., Abolmaesumi, P., Nguan, C., Cotin, S., & Salcudean, S. (2018). Fast elastic registration of soft tissues under large deformations. *Medical image analysis*, 45, 24-40.

[4] Morin, F., Courtecuisse, H., Reinertsen, I., Le Lann, F., Palombi, O., Payan, Y., & Chabanas, M. (2017). Brain-shift compensation using intraoperative ultrasound and constraint-based biomechanical simulation. *Medical image analysis*, 40, 133-153.

[5] Müller, M., Dorsey, J., McMillan, L., Jagnow, R., & Cutler, B. (2002, July). Stable real-time deformations. *In Proceedings of the 2002 ACM SIGGRAPH/Eurographics symposium on Computer animation* (pp. 49-54). ACM.

[6] Brown, J.D. In-Vivo and Postmortem Biomechanics of Abdominal Organs Under Com- pressive Loads: Experimental Approach in a Laparoscopic Surgery Setup. *Doctoral dissertation*, University of Washington.

[7] Kerdok, A. E. (2006). Characterizing the nonlinear mechanical response of liver to surgical manipulation *Doctoral dissertation*, Havard University.

[8] Hudson, J. M., Milot, L., Parry, C., Williams, R., & Burns, P. N. (2013). Inter-and intra-operator reliability and repeatability of shear wave elastography in the liver: a study in healthy volunteers. *Ultrasound in medicine & biology*, 39(6), 950-955.

Tumor heterogeneity estimation from DW-MRI and histology data by linking macro- and micro-information in a quantitative way

Yi YIN [1,], Oliver SEDLACZEK [2], Kai BREUHAHN [3], Irene E. VIGNON-CLEMENTEL [1] and Dirk DRASDO [1]*

1. INRIA Paris, F-75589 Paris, France
2. Translational Lung Research Center Heidelberg (TLRC), University Hospital of Heidelberg, Thoraxklinik at University of Heidelberg and DKFZ, 69120 Heidelberg, Germany
3. Institute of Pathology, University Hospital Heidelberg, 69120 Heidelberg, Germany
(*) Current address: University of Oxford, John Radcliffe Hospital, Oxford, United Kingdom
Tel : +44 (0)1865 572259
Contact: yi.yin@wrh.ox.ac.uk

1 Introduction

Study of tumor heterogeneity, e.g. tumor cellularity and vasculature, can aid in better understanding of the cancer and designing effective treatment strategies. In the medical treatment of cancer, the histopathology of tumor specimens provides the basis for diagnosis and therapy-planning, including surgical resection. However, biopsies reflect only very restricted tumor areas, which might be unrepresentative of the whole tumor considering its size and location. Diffusion-weighted MRI (DW-MRI) is a clinically relevant and non-invasive imaging technique in cancer diagnosis, which measures the water molecule mobility in tissues [1]. DW-MRI provides indirect measures that reflect qualitatively the tumor microstructure. So far, only a few studies comparing DW-MRI and histological information have been performed. The quantitative interpretation of the tumor microstructure from DWI-MRI and the quantitative histological analysis of the tumor microstructure from many tissue slices are still challenging.

In this study, we analyzed the correlation of the non-invasive DW-MRI and the tumor histology data in a quantitative way, in order to explore the tumor heterogeneity. We proposed an image processing and analysis pipeline (Fig. 1), as a proof of concept, which is applied to a NSCLC (Non-Small Cell Lung Cancer) patient tumor to estimate the tumor cellularity and total cell load [2]. We selected several representative tumor samples. The integration of cell numbers information and DWI data derived from different tumor areas defined a negative correlation between cell density and D value. Besides, promising results were obtained in microvasculature estimation [3]. In summary, our results demonstrate that tumor cell count and heterogeneity can be predicted from DWI data, which may open new opportunities for personalized diagnosis and therapy optimization.

2 Method and Results

Primary human NSCLC tissue was obtained from a patient who underwent a lobar resection for lung cancer at the Department of Thoracic Surgery, Thoraxklinik Heidelberg-Rohrbach (Germany). Informed consent was obtained from the patient.

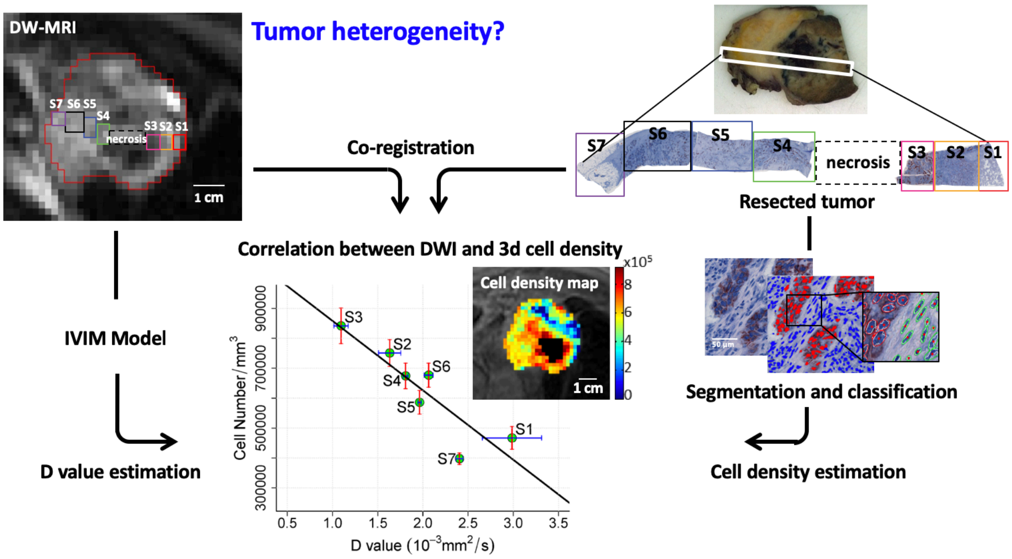

Figure 1. Scheme: tumor heterogeneity estimation from DW-MRI and histological images [2].

Before surgery, DW-MRI was performed on a 1.5 T MRI (Avanto, Siemens, Erlangen). By fitting the voxel signal S/S0 vs. the b-value to the intravoxel incoherent motion model (IVIM) [4],

$$\frac{S_b}{S_0} = (1-f)e^{-bD} + f\,e^{-b(D+D^*)} \qquad (1)$$

the diffusion coefficient D, pseudo diffusion coefficient D^* and parameter f can be obtained. D characterizes the restricted mobility of water molecules. D^* is related to blood flow in the capillary network. f is proportional to the blood vessel volume fraction.

After surgery, the resected tumor was cut, in parallel to the axial planes of MRI, into sections of thickness of approximately 1 cm. The one above the central cutting line of the tumor was selected for further analysis (top-right in Fig.1). Some representative tumor blocks were cut from the selected tumor section. Based on the axial cutting line, histological blocks were visually matched to fit the structures identified in MRI. This procedure was several times repeated ensuring reproducibility. The D, D^* and f were estimated for these blocks following Eq. (1).

In order to perform histological analysis of the selected tumor blocks, they were further sectioned into 1-2 µm thick tissue sections. The sections were stained and then were scanned by a Hamamatsu NanoZoomer 2.0-HT Scan System to generate high resolution digitized histological slides. Cell nuclei were segmented from the histological images to determine local and cell-type specific 2d densities. From these, the 3d cell density was inferred by a model-based sampling technique. The integration of cell numbers information and DWI data derived from representative tumor areas revealed a negative linear correlation between cell density and inferred diffusion parameter D (Fig 1.). Given the D value of each voxel in the tumor DWI data, the 3d cell density corresponding to each voxel was obtained by the mapping from the D value to the local cell density. The cell number of the whole tumor is the sum of the local cell numbers of all vital tumor voxel volumes excluding voxels dominated by necrosis.

In addition, we segmented and reconstructed the 3d vessel structures of the tumor based on the serial registered histological tumor slides. We compared the vessel area fractions for different tumor blocks with perfusion related parameters D* and f. High perfusion was observed in tumor block with high vessel area fraction. From the preliminary results, the process seems feasible and shows coherent results on two tumor blocks [3].

3 Conclusion

Exemplified for a NSCLC patient, we here present a new approach to estimate the tumor cell load in solid tumors based on the fusion of image processing techniques. As a result, tumor cell numbers may directly be inferred from the non-invasive DW-MRI data, which is clinically available for cancer patients. Our study may help to refine and adjust the patient-specific development of therapeutic strategies. In the future, more work needs to be carried out on different tumors. Further analyzing microvasculature may provide useful information to better understand the micro-perfusion, together with the cellularity, to reveal how far micro-architectural properties may be concluded from non-invasive image modalities.

4 References

[1] Le Bihan, D. (2013). “Apparent diffusion coefficient and beyond: What diffusion MR imaging can tell us about tissue structure”. *Radiology*, vol. 268, no. 2, pp. 318–322.

[2] Yin, Y. et al. (2018). “Tumor Cell Load and Heterogeneity Estimation from Diffusion-weighted MRI Calibrated with Histological Data: an Example from Lung Cancer”. *IEEE Transactions on Medical Imaging*, 37(1), pp.35-46, 2018.

[3] Yin, Y. et al. (2016). “Tumor Microvasculature in Lung Cancer and Diffusion-weighted MRI: Preliminary Results”. Proceedings of IEEE Nuclear Science Symposium and Medical Imaging Conference (NSS/MIC-2016).

[4] Le Bihan, D. et al. (1986). "MR imaging of intravoxel incoherent motions: application to diffusion and perfusion in neurologic disorder", *Radiology*, vol. 161, no. 2, pp. 401-407.

Improved prostate cancer radiotherapy planning with decreased dose in a rectal sub-region highly predictive for toxicity

Oscar ACOSTA, Caroline LAFOND, Anais BARATEAU, Baptiste HOUEDE, Axel LARGENT, Eugenia MYLONA, Nicolas PERICHON, Nolwenn DELABY, Pascal HAIGRON and Renaud de CREVOISIER
Univ Rennes, INSERM, LTSI – UMR 1099, F-35000 Rennes, France
Tel : +33 (0)2 23 23 53 34
Contact: oscar.acosta@univ-rennes1.fr

In this paper is presented a workflow for a modified planning in prostate cancer radiotherapy that includes the definition of a rectal sub-region, which has been proved to be predictive of rectal bleeding, and the application of dose constraints within a Treatment Planning System. Compared to a standard planning, a preliminary study showed that applying specific dose constraints to this region while preserving the dose to the target decreased the mean dose by 8 Gy and potentially decrease the risk of rectal bleeding by 23%. A developed computational platform will allow to confirm this hypothesis in similar external cohorts.

1 Introduction

Prostate cancer is among the most common types of cancer worldwide. One of the standard treatment methods is external radiotherapy, which involves delivering ionizing radiation to a clinical target, the prostate and seminal vesicles. Radiotherapy is conducted over several radiation sessions to complete a total dose of 70 to 80Gy. Radiation involves not only the target volume but also portions of healthy organs neighboring the prostate – the bladder and rectum – likely causing adverse toxicity related events that may be of sexual (erectile dysfunction), urinary (dysuria, incontinence, retention, hematuria, among others) or rectal (rectal bleeding, fecal incontinence, etc.) nature. Several studies have shown that increasing the dose to the prostate leads to improved local cancer control but at the expense of treatment-related organs at risk toxicity [1].

In order to reduce toxicity effects, the dose is limited to the organs at risk by applying some constraints during the planning based on the Dose Volume Histograms (DVH) as suggested by international recommendations. Some of the commercial Treatment Planning Systems (TPS) provide also a way to take into account predictive models constraints. Based on DVH studies, for instance, the French group « Groupe d'Études des Tumeurs Uro-Génitales » (GETUG) defined a set of recommendations for the rectum and bladder "dose-volume" values, nevertheless corresponding to a small number of parameters (only 2 DVH threshold values for the rectum).

Using a single DVH to generate constraints in the planning suffers from several drawbacks. DVH relate the 3D dose within a whole organ without any spatial consideration on intra organ dose variability or radio-sensibility. To cope with this problem there is a recent trend towards the identification of more predictive sub-organ regions which may lead to the definition of patient-specific constraints that should be spared during the treatment. Some works have raised this question and proposed sub-organs predictive models [2-3] who have demonstrated for example an anatomical dependence of specific

Gastro-Intenstinal (GI) toxicities by dividing the organs in standardized and reproducible regions. Going further, recent emerging voxel-wise population analysis have allowed to show evidence of local dose/toxicity relationships in prostate cancer radiotherapy [4-6]. Thus, some organs sub-regions have been identified as highly predictive of toxicity in Intensity Modulated Radiotherapy (IMRT). For the rectum, the identified sub-regions would potentially allow to produce a reduced toxicity plan without any modification to the target volume constraints as shown in [7-8]. From the works presented in [5] and in line with [7] a computer assisted planning tool has been developed that allows to define a rectal sub-region, which if used in the TPS could lead to a reduced rectal toxicity patient specific planning.

2 Methods

2.1 Definition of a generic rectal subregion

The definition of the rectal sub-regions was based upon the voxel-wise population study presented in [5] from 173 patients treated with IMRT and Image guided Radiotherapy (IGRT). Non-rigid registration [4] followed by voxel-wise statistical analysis of dose enabled to identify patient specific regions representing less than 4% of the absolute rectal volume. These were primarily located in the subprostatic anterior hemi-rectum and upper part of the anal canal. Drean et al. showed that in patients suffering from rectal bleeding the dose to these sub-regions was almost 4Gy greater (up to 6.8Gy) than for patients without any bleeding. From this work, a single reproducible Sub-Region (SRRg) was defined within 8x8 divided rectum subsections, with no registration method required (Figure 1). The identification of the SRRg is easily computed for a new patient with a low computational cost compatible with the clinical workflow.

2.2 Planning with SRRg constraints

Using the previously computed SRRg, a study presented in [7] where 60 patient data already treated for prostate cancer to a total dose of 78 Gy were used to evaluate the feasibility of decreasing the dose in this rectal sub-region while keeping a high coverage of the target volume (PTV). Thus, for each patient, 4 VMAT plans were generated with Pinnacle v9.10 (Philips) and compared. Lafond et al showed that compared to the standard protocol an improved plan can be obtained. This plan can also use the model proposed by Moore et al. [9] to determine an achievable mean dose in both the rectum and potentially in the SRRg. Indeed, Moore et al. [9] showed that by using a population model based on volume overlap between the PTV and an organ at risk, the mean rectal dose could be overall decreased.

2.3 Planning tool

Based on the previous feasibility study showing the benefit of the introduced SRRg within the planning, a web-based tool in python was developed. This cross-platform (linux, windows) user friendly interface tool allows to compute both the SRRg and the achievable dose based on Moore's model from a standard DicomRT structure file compatible across most of the TPSs. Figure 1 shows an example of planning without and with constrains to the generated SRRg.

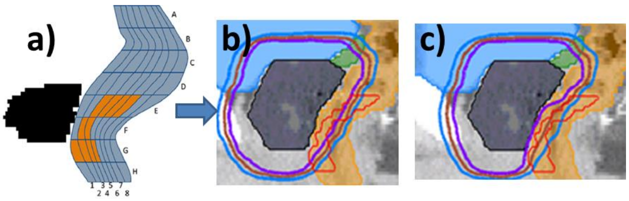

Figure 1. A) Generic Sub-Region. Planned dose b) without and c) with constraints.

3. Conclusion

Based on our previous studies on rectal bleeding toxicity in prostate cancer radiotherapy a workflow introducing a user friendly tool was proposed. The aim is to allow an improved IMRT/IGRT planning with a potential reduction on toxicity. This workflow relies on non-invasive tools which does not heavily increase the treatment workload. The approach can be transferred to the urinary toxicity as the symptoms associated sub-regions have already been identified in a further study [6]. This modified workflow can help tailoring personalized treatments by sparing different organ sub-regions highly predictive of toxicity.

4. Acknowledgements

This work was partially supported by the French National Research Agency (ANR) in the framework of the Investissement d'Avenir Program through Labex CAMI (ANR-11- LABX-0004) and CominLabs (ANR-10- LABX-07-01).

3. References

[1] Fiorino, C., R. Valdagni, T. Rancati, and G. Sanguineti. (2009). "Dose-volume effects for normal tissues in external radiotherapy: pelvis." *Radiother Oncol* no. 93 (2):153-67.

[2] Stenmark, Matthew H., Anna S. C. Conlon, Skyler Johnson, Stephanie Daignault, Dale Litzenberg, Robin Marsh, Timothy Ritter, Sean Vance, Nayla Kazzi, Felix Y. Feng, Howard Sandler, Martin G. Sanda, and Daniel A. Hamstra. (2014). "Dose to the inferior rectum is strongly associated with patient reported bowel quality of life after radiation therapy for prostate cancer." *Radiotherapy and Oncology* no. 110 (2):291-297.

[3] Ebert, Martin A., Kerwyn Foo, Annette Haworth, Sarah L. Gulliford, Angel Kennedy, David J. Joseph, and James W. Denham. (2015). "Gastrointestinal Dose-Histogram Effects in the Context of Dose-Volume Constrained Prostate Radiation Therapy: Analysis of Data From the RADAR Prostate Radiation Therapy Trial." *International Journal of Radiation Oncology • Biology • Physics* no. 91 (3):595-603.

[4] Drean, G., O. Acosta, C. Lafond, A. Simon, R. de Crevoisier, and P. Haigron. (2016). "Interindividual registration and dose mapping for voxelwise population analysis of rectal toxicity in prostate cancer radiotherapy." *Med Phys* no. 43 (6):2721-2730.

[5] Drean, G., O. Acosta, J. D. Ospina, A. Fargeas, C. Lafond, G. Correge, J. L. Lagrange, G. Crehange, A. Simon, P. Haigron, and R. de Crevoisier. (2016). "Identification of a rectal subregion highly predictive of rectal bleeding in prostate cancer IMRT." *Radiother Oncol* no. 119 (3):388-97.

[6] Mylona, Eugenia, Oscar Acosta, Thibaut Lizee, Caroline Lafond, Gilles Crehange, Nicolas Magné, Sophie Chiavassa, Stéphane Supiot, Juan David Arango Ospina, Borris Campillo-Gimenez, Joel Castelli, and Renaud de Crevoisier. (2019). "Voxel-based analysis for identification of urethro-vesical subregions predicting urinary toxicity after prostate cancer radiotherapy." *International Journal of Radiation Oncology • Biology • Physics*. doi: 10.1016/j.ijrobp.2019.01.088. In Press

[7] Lafond, C., J. N'Guessan, G. Dréan, N. Perichon, N. Delaby, O. Acosta, A. Simon, and R. De Crevoisier. (2017). "PO-0841: Feasibility of dose decrease in a rectal subregion predictive of bleeding in prostate radiotherapy." *Radiotherapy and Oncology* no. 123 (Supplement 1):S454-S455. doi: https://doi.org/10.1016/S0167-8140(17)31278-1.

[8] Lafond, C., J. N'Guessan, G. Dréan, N. Périchon, N. Delaby, O. Acosta, A. Simon, and R. de Crevoisier. 2017. "Faisabilité d'une diminution de dose dans une sous-région rectale hautement prédictive de saignement en radiothérapie prostatique." *Cancer/Radiothérapie* no. 21 (6):707.

[9] Moore, Kevin L., R. Scott Brame, Daniel A. Low, and Sasa Mutic. 2011. "Experience-Based Quality Control of Clinical Intensity-Modulated Radiotherapy Planning." *International Journal of Radiation Oncology*Biology*Physics* no. 81 (2):545-551.

Experimental test bench for the hemodynamic study of coronary arteries: bifurcation, stent, aneurysm

M. LAGACHE[2], R. COPPEL[1,2], A. GOMEZ[1], G. Finet[3] and J. OHAYON[1]

[1]TIMC-IMAG - Techniques de l'Ingénierie Médicale et de la Complexité - Informatique, Mathématiques et Applications (Grenoble), France
[2]SYMME - Laboratoire SYstèmes et Matériaux pour la MEcatronique (Chambéry), France
[3]Département de Cardiologie, Hôpital Cardiovasculaire et Université Claude Bernard(Lyon), France;
Tel : +33 (0)6 51 69 87 26
Contact : manuel.lagache@univ-smb.fr

Many models have been developed in recent years to study various phenomena related to cardiological interventions: stent deployment, serial coronary lesions in bifurcations, effect of the malapposition of a stent on the coronary flow, interaction between an endoprosthesis and the vascular structure, etc. These models are proving to be very interesting decision support tools for cardiologists. However, it is crucial to validate them with experimental tests. The best validation is *in vivo* but it is complex and parametric studies are very difficult to be conducted because of the diversity of patients' conditions. An interesting alternative is to develop an instrumented experimental bench to mimic, in the most realistic way, actual physiological conditions. This work presents an experimental bench with applications on the FFR measurement for coronary artery stenoses in complex configurations (multiple stenoses near a bifurcation with collateral circulation).

1 Experimental Bench and FFR Prediction Model

1.1 Experimental bench

A transparent artery phantom (polymer molding) was done to mimic the fractal nature of coronary bifurcations with multiple stenoses and collateral connections. The developed experimental bench (see Fig. 1) consists of a pulsatile pump, resistive elements and compliance chambers. A pulsatile hyperemic flow ($Q = 330 \pm 20$ ml min^{-1} at 70 beats/min.) is applied inside the artery phantom. Moreover, the bench is instrumented with flow and pressure sensors and it can be used with blood mimicking fluids such as water and glycerol mixtures. In the present study a realistic coronary geometry with a bifurcation is studied (LM coronary artery with LAD and LCx daughter branches). An acquisition device (based on Arduino cards) has been developed to read data from different types of sensors (medical catheters and others).

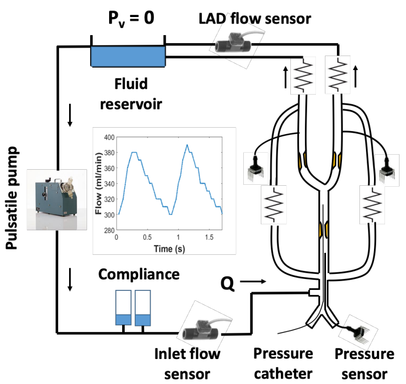

Fig. 1: Experimental test bench.

1.2 FFR Prediction Model

The Fractional Flow Reserve (FFR) is a clinical index of functional severity validated for isolated stenoses. For multiple-stenosis configurations, the measured FFR of the upstream lesion ($FFR_{App.}$) is not representative of the real significance of the stenosis (FFR_{True}) due to the interaction with concomitant lesions. In addition, it is known that collateral circulation tends to increase as atherosclerotic lesions get more severe [1]. A prediction model [2] was derived to estimate the true hemodynamic significance (FFR_{Pred}^{Model}) of the upstream stenosis after virtually removing the downstream lesion(s) taking into account their severities and the degree of collateral circulation. The model is fed with measurements that can be performed in daily clinical routine (FFRs, collateral flow indexes and vessel diameters). The aim of this study is to help interventional cardiologists during decision making for revascularization. Moreover, the accuracy of these predictions was validated with *in vitro* measurements conducted on our experimental bench.

2 Results and discussion

The study included 45 lesion configurations for which mean $FFR_{True} \pm SD$ was 0.73 ± 0.03 and ranged from 0.65 to 0.80.

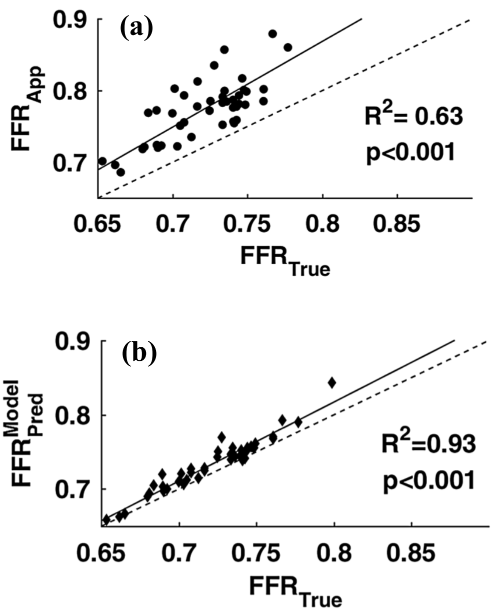

Fig. 2: Linear correlations for a) FFR_{App} versus FFR_{True} and b) FFR_{Pred}^{Model} versus FFR_{True}

Figure 2-a highlights the important difference between the FFR_{app} (measured by the cardiologist) and FFR_{True}, which can derive in diagnostic errors. The proposed model significantly improves the prediction of the true FFR value (Cf. Fig. 2-b). Considering the collateral contributions and the downstream lesions severities, the mean absolute FFR errors were significantly reduced: $|FFR_{App} - FFR_{True}| = 0.05 \pm 0.03$ and $|FFR_{Pred}^{Model} - FFR_{True}| = 0.01 \pm 0.01$.

3 Conclusions and perspectives

This study highlights the influence of collateral circulation and the presence of downstream stenoses on the FFR of the upstream lesion and proposes an efficient analytic model to evaluate the true FFR according to different measurements on the patient (before any clinical intervention). The experimental bench allowed to carry out a parametric study that would be very complex to perform *in vivo*.

This experimental bench allows to mimic realistic patient configurations and provides important information about hemodynamic parameters like pressure and flow. Different studies are currently being developed using this bench: One study will be the experimental validation of numerical models (CFD simulations) to evaluate the flow disturbance caused by arterial bifurcations and malapposed stents. Another study will examine the interaction between an endoprothesis and the vascular structure. For these studies, particles will be used to apply the Particle Image Velocimetry technique to measure the flow velocity fields and visualize potential recirculation regions.

Acknowledgments: This work was supported by the French National Research Agency (ANR) in the framework of the Investissement d'Avenir Program through Labex CAMI (ANR-11- LABX-0004) and the Mexican National Council for Science and Technology (CONACYT).

4 References

[1] Seiler, C., Stoller, M., Pitt, B., and Meier. The human coronary collateral circulation: development and clinical importance. European Heart Journal 34 (34): 2674–2682 (2013).

[2] Coppel R., Lagache M., Finet G., Rioufol G., Gomez A., Derimay F., Malve M., Yazdani S. Pettigrew R. and Ohayon J. Influence of Collaterals on True FFR Prediction for a Left Main Stenosis with Concomitant Lesions: An In Vitro Study. Annals of Biomedical Engineering (2019).

CAMI

COMPUTER ASSISTED
MEDICAL INTERVENTIONS